ÉCOLE DE TECHNOLOGIE SUPÉRIEURE
UNIVERSITÉ DU QUÉBEC

THESIS PRESENTED TO
ÉCOLE DE TECHNOLOGIE SUPÉRIEURE

IN PARTIAL FULFILLMENT OF THE REQUIREMENTS FOR
THE DEGREE OF
DOCTOR OF PHILOSOPHY
Ph.D.

BY
Mary Carmen BAUTISTA

TURBULENCE MODELLING OF THE ATMOSPHERIC BOUNDARY LAYER OVER COMPLEX TOPOGRAPHY

MONTREAL, "OCTOBER 19, 2015"

 Mary C. Bautista, 2015

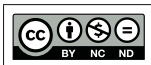

This Creative Commons license allows readers to download this work and share it with others as long as the author is credited. The content of this work cannot be modified in any way or used commercially.

BOARD OF EXAMINERS

THIS THESIS HAS BEEN EVALUATED

BY THE FOLLOWING BOARD OF EXAMINERS:

Prof. Louis Dufresne, Eng., Ph.D., Thesis Advisor
Département de génie mécanique, École de technologie supérieure

Prof. Christian Masson, Eng., Ph.D., Thesis Co-advisor
Département de génie mécanique, École de technologie supérieure

Prof. François Brissette, Eng., Ph.D., Committee President
Département de génie de la construction, École de technologie supérieure

Prof. Niels N. Sørensen, Eng., Ph.D., External Examiner
Department of Wind Energy, DTU Wind Energy, Technical University of Denmark

Prof. Julien Weiss, Eng., Ph.D., Examiner
Département de génie mécanique, École de technologie supérieure

THIS THESIS WAS PRESENTED AND DEFENDED

IN THE PRESENCE OF A BOARD OF EXAMINERS AND THE PUBLIC

ON "OCTOBER 5, 2015"

AT ÉCOLE DE TECHNOLOGIE SUPÉRIEURE

ACKNOWLEDGEMENTS

A grateful acknowledgement to my supervisor Prof. Louis Dufresne and co-supervisor Prof. Christian Masson. Thanks Christian for the financial support and for understanding straight away the problems behind my questions. Thanks Louis for encouraging me to ask the right questions. I learned a great deal from your complementary guidance. I also appreciate and thank in advance the thesis evaluation committee for their time, effort and comments.

This research was funded by the Fonds de Recherche du Québec - Nature et Technologies (FRQ-NT) and the Laboratoire de recherche sur l'Aérodynamique des Éoliennes en milieu nordique (AEMN). Their support was greatly appreciated.

All the numerical simulations were performed on the Guillimin and Colosse supercomputers managed by Calcul Québec and Compute Canada. These clusters are maintained by an awesome support team. Thank you very much for making many research projects possible. A special acknowledgement to all the OpenFOAM developers and community for their important contributions. In particular to the National Renewable Energy Laboratory (NREL) team for their outstanding job in the development of the SOWFA package. Matthew Churchfield, Sang Lee and Pat Moriarty, I am truly grateful for your help and friendship. The time I spend at NREL was extremely enriching and encouraging. Also thanks to Carlos Peralta because you always gave me the confidence to ask you questions.

An enormous thanks to all my friends at the ÉTS, in particular to Hugo, Jörn, Pascal and Louis-Étienne with whom I worked more closely. Thanks for your crucial help over the years and for being great teachers, but above all thanks for your constant encouragement and great friendship. To Jon, Simon-Phillipe, Nico, Yann-Aël, Jonathan, Sitraka, Salha, Alex, Joel, Marc, Hajer, Eric, Nacera, Cherif, Étienne, and Nico, thanks for making my days something worth remembering. A loving thanks to my family, you are always in my heart. I have come to realize how much each one of you have positively marked my life. Finally and most important, a huge thanks to ma petite famille, you are my love, my life and my greatest support. I accomplished this work and enjoyed these Ph.D. years because of you.

MODÉLISATION DE LA TURBULENCE DANS LA COUCHE LIMITE ATMOSPHÉRIQUE SUR TERRAINS COMPLEXES

Mary Carmen BAUTISTA

RÉSUMÉ

De nos jours, l'industrie de l'énergie éolienne emploie différents types de modèle de turbulence qui sont capables de reproduire correctement et de manière réaliste le comportement de divers écoulements relativement simples (par ex.: vent au dessus d'un terrain plat, homogène et sans obstacles). Cependant, l'augmentation de la complexité de l'écoulement (par ex.: dans le cas de topographies complexes) diminue grandement la précision des modèles de turbulence, tout en augmentant le coût des calculs. Par conséquent, les simulations précises et fiables des écoulements au-dessus des terrains complexes demeurent peu pratiques pour les applications du secteur éolien.

Afin d'améliorer les simulations d'écoulement du vent au-dessus des terrains complexes, deux des principales difficultés rencontrées dans ce domaine seront présentées dans cette thèse. La première difficulté est liée au fait que les traitements existants de modèles de surface ne sont valides que pour les terrains plats. Néanmoins, ces traitements sont fréquemment appliqués à des simulations d'écoulement au-dessus de terrain complexes. Cependant, le modèle de turbulence $k-\omega$ SST (shear stress transport) possède un traitement novateur de la surface qui le rend moins dépendant des suppositions de terrains plats. La seconde difficulté correspond aux coûts prohibitifs des simulations lorsque des statistiques précises et fiables sont requises. Cependant, les modèles hybrides de turbulence peuvent présenter un compromis idéal entre précision et coût de calculs. Prenant tout cela en compte, les travaux de cette thèse emploient un modèle de turbulence basé sur le modèle $k-\omega$ ainsi que sur la technique hybride dite "simplified improved delayed detached-eddy simulation" (SIDDES), afin d'adresser les besoins du secteur de l'énergie éolienne.

Pour valider ce modèle d'écoulement atmosphérique, une analyse détaillée d'écoulements typiques est effectuée. Cette validation rigoureuse permet de mieux comprendre les limitations intrinsèques du modèle de turbulence dans le cadre des calculs numériques effectués. Par la suite, des simulations de l'écoulement dans la couche atmosphérique neutre au-dessus d'un terrain plat et homogène sont conduites. Les résultats montrent que le modèle de turbulence $k-\omega$ SST-SIDDES reproduit de manière réaliste le comportement du vent au-dessus de terrains plats et complexes. La finesse verticale de la grille de calcul proche des limites du domaine requises par ce modèle présente un problème majeur pour la création du maillage. Cependant, malgré cette limitation, il est démontré dans cette thèse que le modèle de turbulence k-omega SST-SIDDES représente une approche appropriée à la modélisation de l'écoulement du vent au-dessus des terrains complexes, et ce, sans avoir à supposer que le terrain est plat et sans exiger d'importantes ressources de calculs.

Mot-clés: technologíe eolienne, couche limite atmospheric, modélisation de la turbulence, model hybride, terrain complexe, simulations microechelle

TURBULENCE MODELLING OF THE ATMOSPHERIC BOUNDARY LAYER OVER COMPLEX TOPOGRAPHY

Mary Carmen BAUTISTA

ABSTRACT

Nowadays, the wind energy industry employs different types of turbulence models which are capable of reproducing the correct and realistic behaviour of relatively simple flows (e.g. wind over flat, homogeneous and obstacle free terrain). However, as the complexity of the flow increases (e.g. wind over complex topography), the accuracy of the turbulence models may be greatly reduced, and in general, their computational cost rises significantly. Accurate and reliable flow simulations are still not practical for wind industry applications over complex terrain.

To improve wind flow simulations over complex terrain, two of the main challenges that the wind energy sector faces are addressed. The first challenge is related to the fact that ground surface modelling treatments are valid only on flat terrain. Nevertheless, it is a common practice to use those surface treatments on simulations over complex terrain. However, the $k-\omega$ SST (shear stress transport) turbulence model has a novel surface treatment that is less dependent on flat terrain assumptions. The second challenge is the high computational cost when accuracy and reliable turbulence statistics are needed. Nonetheless hybrid turbulence models could provide a good compromise between accuracy and computational cost. A turbulence model based on the $k-\omega$ SST model and the simplified improved delayed detached-eddy simulation (SIDDES) hybrid technique is proposed to address those needs.

To validate this model for atmospheric flows, first an extensive analysis of certain canonical flows was carried out. This rigorous validation helped understand the inherent limitations of the turbulence model within the specific numerical framework. Subsequently, computations of the neutrally stratified atmospheric flow over flat homogeneous terrain and then over complex topography were conducted. The results show that the $k-\omega$ SST-SIDDES turbulence model is able to predict realistic wind behaviour over flat terrain and more complex cases. The vertical grid refinement in the near-wall region required by this model poses a major challenge for the mesh generator. But despite this limitation, $k-\omega$ SST-SIDDES turbulence model proved to be a suitable approach for modelling the wind flow over complex terrain without relying on flat terrain assumptions or requiring substantial computer resources.

Keywords: wind energy, atmospheric boundary layer, turbulence modelling, hybrid model, complex topography, microscale simulations

TABLE OF CONTENTS

Page

LIST OF TABLES

LIST OF FIGURES

Page

LIST OF ABREVIATIONS

ABL	atmospheric boundary layer
AGL	above ground level
ASL	atmospheric surface layer
BL	boundary layer
CDS	central difference scheme
CFD	computational fluid dynamics
CFL	Courant–Friedrichs–Lewy stability condition
DES	detached-eddy simulation
DIT	decaying isotropic turbulence
DDES	delayed detached-eddy simulation
DNS	direct numerical simulation
FDS	*filteredLinear* discretization scheme
FVM	finite volume method
GIS	grid induced separation
HAT	homogeneous anisotropic turbulence
HSF	homogeneous shear flow
IDDES	improved delayed detached-eddy simulation
LES	large-eddy simulation
LLM	logarithmic layer mismatch

OpenFOAM	open source field operation and manipulation software
PISO	pressure implicit with splitting of operator algorithm
RANS	Reynolds-averaged Navier-Stokes simulation
sgs	residual or subgrid scale
SIDDES	simplified improved delayed detached-eddy simulation
SOWFA	simulator for wind farm applications
SST	shear stress transport
TI	turbulence intensity
UDS	upwind discretization scheme
URANS	unsteady Reynolds-averaged Navier-Stokes simulation
WRA	wind resource assessment
WRF	weather research and forecasting mesoscale model

LIST OF SYMBOLS AND UNITS OF MEASUREMENTS

General notation

$\langle a \rangle_t$, $\langle a \rangle_s$, $\langle a \rangle_N$	time, space and ensemble averaged quantity (Eq. 1.14, Eq. 1.15 and Eq. 1.16)
$\langle a \rangle$	time, space or ensemble averaged quantity
$\overline{a}$	filtered/resolved quantity (Eq. 2.6)
$\overline{a}'$	filtered/resolved fluctuating quantity ($\overline{a}' = \langle \overline{a} \rangle - \overline{a}$)
a or a_{sgs}	modelled/sgs value
a_0	initial value of a quantity
a_{total}	total value of a quantity ($a_{\text{total}} = \overline{a} + a$)
a_w	variable value at the wall
a^*	non-dimensional variable
a_i, a_{ij}	vector or tensor expressed in index notation
$\mathbf{a}$	vector or tensor expressed in vector notation ($\mathbf{a} = a_i \hat{e}_i$)

Upper-case Roman

B_{ij}	correlation function ($B_{ij}(\tau) = \langle u_i(t) u_j(t') \rangle$) [$\mathrm{m}^2/\mathrm{s}^2$]
D_h	hydraulic diameter [m]
$E(\kappa)$	three-dimensional energy spectra as a function of the wavenumber κ [$\mathrm{m}^3/\mathrm{s}^2$]
$E_{ii}(\kappa_j)$	one-dimensional spatial energy spectra (Eq. 3.6) [$\mathrm{m}^3/\mathrm{s}^2$]
$E_{ii}(f)$	one-dimensional temporal energy spectra (Eq. 4.6) [m^2/s]

F	external force/source term $[\mathrm{m/s^2}]$
F_C	Coriolis force term ($F_C = -2\boldsymbol{\Omega} \times \mathbf{u}$) $[\mathrm{m/s^2}]$
H	domain height $[\mathrm{m}]$
$\mathcal{L}$	side length of a cubic domain
L_i	domain length in the i direction $[\mathrm{m}]$
$L_{ij,\,k}$	integral lengthscale (Eq. 3.5) $[\mathrm{m}]$
N_i	number of cells in the i direction
R_{ij}	two-point correlation function ($R_{ij}(\mathbf{r},\,\mathbf{x},t) = \langle u_i(\mathbf{x},t)u_j(\mathbf{x}+\mathbf{r},t)\rangle$) $[\mathrm{m^2/s^2}]$
Re_{D_h}	Reynolds number based on D_h ($Re_{D_h} = U_{av}D_h/\nu$) $[-]$
Re_λ	Reynolds number based on λ ($Re_\lambda = u_{rms}\lambda/\nu$) $[-]$
Re_τ	Reynolds number based on τ ($Re_\tau = u_* H/\nu$) $[-]$
Ro_w	small scale Rossby number ($Ro = u_{rms}\kappa_p/w$) $[-]$
$Ro_{w,0}$	initial small scale Rossby number $[-]$
Ro_L	large scale Rossby number ($Ro_L = U_{ref}/\mathsf{f}L$) $[-]$
S	constant mean uniform shear ($S = \partial\langle\overline{u}\rangle/\partial z$) $[1/\mathrm{s}]$
S_{ij}	rate-of-strain tensor ($S_{ij} = 0.5(\partial u_i/\partial x_j + \partial u_j/\partial x_i)$) $[1/\mathrm{s}]$
$\mathcal{S}$	characteristic strain rate ($\mathcal{S} = \sqrt{S_{ij}S_{ij}}$) $[1/\mathrm{s}]$
T_0	longitudinal flow-through-times ($T_0 = L_x/\langle u\rangle$) $[\mathrm{s}]$
U_0	inertial frame velocity on DIT cases $[\mathrm{m/s}]$
U_{av}	averaged velocity for channel flow cases $[\mathrm{m/s}]$

U_{Defect}	velocity-defect $[\mathrm{m/s}]$
U_{ref}, u_{ref}	reference velocity $[\mathrm{m/s}]$

Lower-case Roman

d_w	distance to a solid wall $[\mathrm{m}]$
f	frequency $[1/\mathrm{s}]$
f	Coriolis parameter ($\mathsf{f} = 2w \sin\varphi$) $[1/\mathrm{s}]$
$\mathfrak{f}$	friction factor $[-]$
h	Askervein hill height [$h = 126\,\mathrm{m}$]
h_{max}	maximum edge length of the cell $[\mathrm{m}]$
h_{hw}	grid step normal to the wall $[\mathrm{m}]$
k	modelled turbulent kinetic energy per unit mass $[\mathrm{m}^2/\mathrm{s}]$
k_s	equivalent sand grain roughness $[\mathrm{m}]$
k_s^+	non-dimensional equivalent sand grain roughness ($k_s^+ = u_* k_s/\nu$) $[-]$
l_{RANS}	characteristic turbulent RANS lengthscale (Eq. 2.17) $[\mathrm{m}]$
l_{LES}	characteristic turbulent LES lengthscale (Eq. 2.18) $[\mathrm{m}]$
$\tilde{l}$	universal/hybrid turbulent lengthscale $[\mathrm{m}]$
$\tilde{l}_{xDES}$	hybrid lengthscale for the different DES approaches (Eq. 2.20- 2.23) $[\mathrm{m}]$
p	pressure per unit mass $[\mathrm{m}^2/\mathrm{s}^2]$
t	time $[\mathrm{s}]$
u_*	friction velocity ($u_* = \sqrt{\tau/\rho}$) $[\mathrm{m/s}]$

u_0	velocity at the top in velocity-defect study or initial velocity [$\mathrm{m/s}$]
u_g, v_g	geostrophic wind velocity components [$\mathrm{m/s}$]
u_{rms}	root-mean-square velocity [$\mathrm{m/s}$]
w	angular velocity [$\mathrm{rad/s}$]
w_{Earth}	Earth's angular velocity [$\mathrm{rad/s}$]
x, y, z	streamwise, spanwise and vertical direction coordinates [m]
z_0	aerodynamic roughness (Eq. 2.29) [m]
z_1	height of the first grid node [m]
z_1^+	non-dimensional distance of the first grid node ($z_1^+ = u_* z_1/\nu$) [$-$]
z_u	height at which the cells become cubic in the ABL simulations [m]

Greek

Δ	filter width ($\Delta = \max(\Delta_x,\, \Delta_y,\, \Delta_z)$) [$\mathrm{m}$]
Δ_i	cell length size on the i direction [m]
Δ_{IDDES}	IDDES filter with ($\Delta_{IDDES} = \min[\max(C_w d_w,\, C_w h_{max},\, h_{wn}),\, h_{max}]$) [$\mathrm{m}$]
Δ_u	uniform filter width [m]
ε	dissipation of specific turbulent kinetic energy ($\varepsilon = 2\nu_{eff} S_{ij} S_{ij}$) [$\mathrm{m^2/s^3}$]
ζ_1^+	non-dimensional outer-scale distance ($\zeta_1^+ = z_1/z_0$) [$-$]
θ	cross-isobaric angle [rad]
κ_1	wavenumber ($\kappa_1 = 2\pi/l$) [$1/\mathrm{m}$]
κ	von Kármán constant (Table I-1) [$-$]

λ	Taylor microscale (Eq. 3.3) $[\mathrm{m}]$
μ	dynamic viscosity $[\mathrm{Kg}/(\mathrm{s}\cdot\mathrm{m})]$
ν	kinematic viscosity ($\nu = \mu/\rho$) $[\mathrm{m}^2/\mathrm{s}]$
ν_t	turbulent viscosity $[\mathrm{m}^2/\mathrm{s}]$
ν_{eff}	effective turbulent viscosity ($\nu_{eff} = \nu + \nu_t$) $[\mathrm{m}^2/\mathrm{s}]$
ρ	mass density $[\mathrm{Kg}/\mathrm{m}^3]$
τ	time difference for temporal spectrum $[\mathrm{s}]$
τ	shear stress tensor $[1/(\mathrm{ms}^2)]$
τ_w	wall shear stress ($\tau_w = \mu\,(\partial u/\partial z)\vert_{z=0}$) $[1/(\mathrm{ms}^2)]$
ϕ_m	non-dimensional velocity gradient ($\phi_m = (\kappa z/u_*)\partial u/\partial z$) $[-]$
φ	latitude $[\mathrm{rad}]$
σ	total stress tensor $[1/(\mathrm{ms}^2)]$
σ_u	standard deviation of the velocity component u ($\sigma_u = \sqrt{\langle u'^2\rangle}$) $[\mathrm{m}/\mathrm{s}]$
σ_u^2	variance of the velocity component u ($\sigma_u^2 = \langle u'^2\rangle = (u - \langle u\rangle)^2$) $[\mathrm{m}^2/\mathrm{s}^2]$
ω	modelled dissipation rate per unit mass ($\omega = \varepsilon/(\beta_* k)$) $[1/\mathrm{s}]$
$\boldsymbol{\omega}$	vorticity ($\boldsymbol{\omega} = \nabla \times \mathbf{u}$) $[1/\mathrm{s}]$
$\boldsymbol{\Omega}$	angular velocity vector $[\mathrm{rad}/\mathrm{s}]$
Ω_{ij}	rate-of-rotation tensor ($\Omega_{ij} = 0.5(\partial u_i/\partial x_j - \partial u_j/\partial x_i)$) $[1/\mathrm{s}]$
Ω	characteristic rotation rate ($\Omega = \sqrt{\Omega_{ij}\Omega_{ij}}$) $[1/\mathrm{s}]$

Model constants

β_*, β, σ_k, σ_w, γ, a_1, c_1	$k-\omega$ SST model constants (Table I-1) [$-$]
F_1, F_2, ϕ	$k-\omega$ SST blending functions (Appendix I)
$C_{k-\varepsilon}$, $C_{k-\omega}$, C_w, C_{dt1}, C_{dt2}, C_t, C_l	hybrid model constants (Table I-1) [$-$]
C_{DES}, f_b, f_d, f_{dt}, $\tilde{f}_d$, f_e, f_l, f_t, r_d, r_{dl}, r_{dt}, α	hybrid blending functions (Appendix I and II)

*All units are expressed in SI system

INTRODUCTION

Wind is available and rather abundant almost everywhere on Earth. Recent studies estimated that around 95 TW of wind energy potential could be harvested worldwide, enough to cover several times the current world's total energy demand (Hossain and the WWEA Technical Committee, 2014). Nevertheless as of June 2014, the wind industry generated only around 4.0% of the global annual energy consumption (336 GW) (World Wind Energy Association, 2014). It has been shown that increasing the wind power capacity makes the energy market more resilient to fluctuating fossil fuel prices (Hossain and the WWEA Technical Committee, 2014). This directly reduces the dependence on local fossil fuel reserves or imports assuring a more secure energy market. Equally important, the electricity generated by the wind energy industry is renewable, sustainable and produces no greenhouse gases during operation. Therefore exploiting the wind potential can help tackle the global energy access, the energy security and the climate change challenges encountered today (Hossain and the WWEA Technical Committee, 2014).

To increase the wind energy potential and improve its reliability, the wind needs to be better understood. Accurate predictions of the wind behaviour should yield more trustworthy estimations of the expected energy production and the associated risks in wind farms, assuring a higher revenue and lower costs of operation and maintenance. In other words, it is crucial to know how much electricity can be generated at a certain location at any given time. A wind resource assessment (WRA) provides information of the wind speed and the energy that could be extracted. A complete WRA encompasses a macro or mesoscale study that analyzes the winds at a global or regional level taking into account the climate; and a microscale study which assesses the wind flow in a smaller area considering the local terrain characteristics among other things. The prediction of the wind flow properties at a microscale level (i.e. small meteorological scale with only local and short-lived atmospheric phenomena) is the focus of this research work.

The wind behaviour over flat and obstacle free terrain is fairly well understood and can be rather easily estimated. However the roughness and topography of the terrain induce important

changes on the wind properties. In particular, the wind flow over rough terrain or terrain with topographic features can present high turbulence, strong shear stresses and flow separation and reattachment. These phenomena are more difficult to assess. In this work, the term "complex terrain" will specifically refer to any terrain that could potentially induce flow separation.

Over complex terrain, the wind flow can have a considerable effect on the energy output of a wind park. For example, highly turbulent zones can greatly diminish or completely prevent the energy production. In addition, turbulence causes more stress and wear on the turbines. These effects will have a great impact on the operational cost, maintenance expenses, and revenue generation of a wind park. A site specific and exhaustive measuring campaign is costly and most likely not feasible because the wind velocity is a fluctuating quantity that presents a broad range of time and space scales (Ayotte, 2008). Therefore, considerable amounts of statistical data over long periods of time are needed to evaluate the local wind resources. For this reason, the wind industry relies on atmospheric flow modelling to understand and properly estimate the wind behaviour.

Motivation

Even with the current computational capacity, modelling the effects of the atmospheric turbulence represents a challenging problem. The complexity arises because turbulence is the result of the nonlinear convection terms in the Navier-Stokes equations (Pope, 2000). However, the standard computational approaches most commonly used by the wind industry are still based on linear simplifications of those convection terms (e.g. WaSP, MS-Micro, etc.). But in spite of all these simplifications, the linear turbulence models perform reasonably well on flat terrain. In addition, they are reliable, numerically stable, and computationally inexpensive (Petersen *et al.*, 1998). However, the accuracy of the simulations decreases as the terrain complexity increases.

Computational Fluid Dynamics (CFD) algorithms which solve the nonlinear convective terms are more computationally demanding. Nevertheless, CFD could in principle provide a more

complete description of the turbulent behaviour and consequently yield more accurate results in complex terrain. CFD is commonly used by the research community, and in recent years, the industry has also begun to be use it. However in some instances, the CFD calculation cost can be excessively high for routine and practical industrial applications. Numerous non-linear turbulence models have been proposed and used for complex terrain problems. In the wind community, the most widely studied Reynolds-Average Navier-Stokes (RANS) turbulence model has been the $k - \varepsilon$ closure scheme, but many other exist (e.g. Apsley and Castro (1997), Kim and Patel (2000), Castro *et al.* (2003), Hargreaves and Wright (2007), etc.). In general, RANS models yield acceptable results and have a relatively low computational cost; however, they cannot provide a full description of the turbulence quantities. On the contrary, the large-eddy simulations (LES) models can be more accurate and complete but they are too computationally demanding for practical wind energy applications (Ayotte, 2008) (e.g. Deardorff (1972), Mason and Thomson (1987), Sullivan (1994), Andren *et al.* (1994), etc.). However, LES might provide some insight and interesting facts about the turbulent behaviour of the local winds. Hybrid models (e.g. Bechmann (2006), Senocak *et al.* (2007), etc.), like the detached-eddy simulation (DES) approaches, incorporate RANS and LES characteristics, and they could potentially become a good prospect for wind energy simulations.

The wind industry needs accurate turbulence models to understand the wind behaviour over complex terrain. In addition, these models have to be robust (i.e. reliable and numerically stable) and practical (i.e. low computational cost). The challenge of this research project is to analyze a nonlinear turbulence model which could become a good alternative for wind energy studies over any type of terrain. To attain this goal, the OpenFOAM software has been chosen for this project (The OpenFOAM Foundation, 2013). This is a community developed CFD package that allows the users to have full access to the source code. Contrary to the commercial software, the OpenFOAM simulations are not limited or constrained by a predefined option. The possibility to modify the OpenFOAM code helps tackle specific atmospheric flow problems and improve the understanding of the wind behaviour.

Objectives

The main objective of this research is *to adapt OpenFOAM for practical wind energy simulations over complex terrain at a microscale level.*

In order to achieve the main goal, the research project is divided into four specific objectives:

1. To select an existing turbulence model that could potentially be a good candidate for neutral atmospheric boundary layer simulations over complex terrain. To implement the proposed model in OpenFOAM and to adapt it for wind flow modelling (Chapter 2).
2. To evaluate the advantages and limitations of the chosen turbulence model by analyzing rather simple but well-known canonical flows (Chapter 3).
3. To identify the appropriate boundary conditions required to correctly model the atmospheric boundary layer over an ideal flat terrain using the proposed turbulence model. To assess the model performance on flat terrain cases (Chapter 4).
4. To validate the turbulence model against complex flow cases including massively separated flows and natural "mildly" complex topography cases (Chapter 5).

Thesis overview

The motivation and detailed objectives of this work have been specified in this introduction. A literature review concerning the atmospheric boundary layer and its turbulent characteristics is given in Chapter 1. Subsequently, the current state of knowledge regarding atmospheric flow modelling and the adopted methodology for performing those type of simulations is presented in Chapter 2. More specifically, this chapter includes a review of the basic concepts of computational fluid dynamics within the context of the OpenFOAM package (Section 2.1), the atmospheric modelling techniques (Section 2.1.1), and the recognition of certain important challenges encountered on microscale simulations (Section 2.2). Taking all this into considera-

tion, the $k-\omega$ SST-SIDDES hybrid model is proposed to addressed some of those challenges. This turbulence model is described on Section 2.2.1.

In the present work, a rigorous validation of the turbulence model was performed using some well-known canonical flows. The results presented in Chapter 3 yield valuable information about the advantages and limitations of the turbulence model. Additionally, the model has been tested on atmospheric simulations over flat homogeneous terrain. The results are given in Chapter 4. Finally Chapter 5, presents complex flow simulations (i.e. massively separated flows and natural "mildly" complex terrain) using the SIDDES model. A summary of this work and the most important contributions is given in the conclusion section. To recapitulate, the turbulence models equations are summarized in Appendix I and Appendix II. Additionally, the main code lines used for the OpenFOAM v.2.2.2 implementation are described in Appendix III.

Original contributions

The original scientific contributions of this research project are in summary the following:

- The implementation of a hybrid turbulence model for atmospheric flows that
  - intrinsically avoids the logarithmic layer mismatch, a problem encountered by almost all hybrid models;
  - can yield more accurate results on adverse pressure gradients, a phenomenon frequently encountered in complex terrain;
  - and has a novel wall treatment which is less dependent on flat terrain assumptions (Section 2.2.1).
- The development of a complete benchmark to test turbulence models for atmospheric flows applications. This rigorous validation includes studies on canonical flows and on flat terrain to understand the inherit limitations and characteristics of a turbulence model (Chapters 3 and 4).

- The modelling of the neutral atmospheric boundary layer over complex flow cases (i.e. massively separated flows and natural "mildly" complex terrain) accomplished using the appropriate boundary conditions and the proposed turbulence model without relying on a wall function (Chapter 5).

CHAPTER 1

THE WIND AND THE ATMOSPHERIC TURBULENT FLOW

The success of the wind energy depends greatly on the proper understanding of the wind behaviour and its prediction. The global wind motion is the result of the balance between three main forces: the pressure differences in the atmosphere, the Coriolis force and the centrifugal force around zones of low and high pressure (Manwell *et al.*, 2002). In addition, the global wind patterns are locally modified by the terrain surface (i.e. surface roughness, terrain elevation, etc.). Hence, the wind speed and direction at a particular location is the sum of the prevailing global air flow and the local effects. The wind can be characterized and studied based on its meteorological scales as shown on Table 1.1 (Stull, 1988).

Table 1.1 Meteorological scales

Scale	Typical size (km)	Life span	Main forces involved
Macroscale	$\gtrsim 10^3$	Days to weeks	Pressure, Coriolis and centripetal
Mesoscale	$\sim 10^{-1}$ to 10^3	Minutes to hours	Pressure and Coriolis
Microscale	$\lesssim 10^1$	Few minutes or less	Friction

This research project will focus on the wind behaviour at a microscale level. At this scale, the air flow is highly affected by the roughness and complexity of the Earth's surface. The friction produced by the local geography becomes the predominant force that modifies the microscale wind patterns. Understanding these local winds is crucial to estimate the energy output of a turbine or a wind park.

1.1 Atmospheric boundary layer structure

The lowest layer of the atmosphere is called the troposphere. It comprises the first ~ 6 km above the surface at the poles and approximately the first 20 km at the equator. The global wind patterns happen in the upper part of the troposphere, commonly called free atmosphere (Stull,

1988). There, the wind is generally horizontal, non-turbulent and it does not dependent on the topography. On the contrary, the portion of the troposphere where the wind flow is influenced by the Earth's surface is known as the atmospheric boundary layer (ABL). Momentum and heat transfer processes take place in this layer; hence, the ABL is characterized by high levels of turbulence (Stull, 1988). It is also where the mesoscale and microscale processes take place. For wind energy purposes, the ABL is the central focus.

The ABL thickness varies from approximately hundreds of meters to a few kilometres depending on the terrain and wind speeds, and its variation time scale is of the order of few hours or less (Stull, 1988). For instance, at daytime the ABL thickness can reach 1-2 km, while at night with weak winds or coastal regions its thickness is generally around 100 m (Panofsky and Dutton, 1984). Based on the forces involved at different altitudes, the ABL is divided in three sublayers (Garrat, 1994):

- **Roughness or interfacial layer:** Just above the Earth's surface, molecular viscosity and diffusivity dominate over turbulent transport. Nevertheless, viscous effects are not significant in atmospheric flow due to their high Reynolds number.
- **Surface layer:** The Coriolis and the pressure gradient forces are negligible, while the friction force determines the turbulent air motion. The level of turbulence depends on the roughness of the terrain and on the obstacles present (i.e. vegetation, hills, buildings, etc.) The height of the surface layer is approximately 10% of the whole ABL.
- In the upper part of the ABL, the wind flow is influenced by the Earth's rotation and the surface friction forces.

Within all these layers, the velocity profiles and turbulence statistics of the wind flow over flat terrain are relatively simple. Overall, atmospheric turbulence is mainly produced by three phenomena: the surface shear stress, and the terrain roughness which cause mechanical turbulence, and the vertical heat flux that can produce convective or thermal turbulence. However if the terrain is not flat, other forces may arise. In uneven terrain, the velocity profiles be-

come more complex due to the viscous effects, pressure gradients and acceleration that occur when the wind flow encounters an obstacle. These phenomena generate additional mechanical turbulence.

Even though convective turbulence plays a rather important role in the production of atmospheric turbulence (see Panofsky and Dutton (1984) and Stull (1988) for further information regarding thermal turbulence and atmospheric stratification), this research project will focus on understanding only the mechanical turbulence caused by the terrain elevation. In other words, throughout this work it will be assumed that the atmosphere thermal stratification is always neutral and the surface heating plays a negligible role in the production of turbulence. For this reason, a temperature equation will not be considered. A neutral stratification happens when strong winds and overcast skies take place, often late in the afternoon (Stull, 1988). An exact neutral stratification is not a common occurrence in the atmosphere, however this assumption greatly simplifies the analysis of the atmospheric flow and allows to isolate and identify the effects of the mechanical turbulence.

1.1.1 Atmospheric surface layer

Modern wind turbines have a hub height of around 80 to 120 m, while the tip of its rotor blades can reach up to 120 to 180 m. For the most part, wind turbines reach only the atmospheric surface layer (ASL), thus understanding the effects that take place in this region is crucial. Within a neutrally stratified ASL over homogeneous flat terrain the vertical variations of the vertical momentum fluxes are considered negligible. But in fact, the momentum flux (shear τ) reaches a maximum at the ground surface and it is null at the top of the ABL. The shear decreases approximately in a linear manner with height. This means a momentum flux decrease of only 10% within the ASL (i.e. the 10% of the ABL). This 10% variation is often ignored or tolerated, thus the momentum flux is considered constant within the ASL (Panofsky and Dutton, 1984).

The surface shear stresses τ_w is commonly used to define a characteristic velocity u_* called friction velocity. This parameter is defined as

$$u_*^2 = \frac{\tau_w}{\rho} \tag{1.1}$$

where ρ is the air density. Based on the assumption that u_* is constant, the mathematical model most commonly used to approximate the velocity profiles is the logarithmic law of the wall (or simply log-law). This log-law defines the streamwise velocity u as

$$u = \frac{u_*}{\kappa} \ln\left(\frac{z + z_0}{z_0}\right) \tag{1.2}$$

where κ is the von Kármán constant, z the height and z_0 the aerodynamic roughness height. The surface ground is located at a height of $-z_0$ to assure that $u(z = 0) = 0$. This is illustrated in Figure 1.1. Notably, the logarithmic law is only valid to describe the surface layer in neutral conditions over flat and homogeneously rough terrain. Another consequence of the constant shear stresses, is that the non-dimensional wind shear or mean velocity gradient

$$\langle \phi_m \rangle = \frac{\kappa z}{u_*} \frac{\partial \langle u \rangle}{\partial z} \tag{1.3}$$

equals to 1.0 within the ASL. Here $\langle \cdot \rangle$ represents an averaged value.

To characterize the conditions of the ASL, the Monin-Obukhov or surface layer similarity theory defines different scaling parameters (like u_* and the Monin-Obukhov lengthscale L) and certain functions (like the logarithmic law and ϕ_m). These similarity parameters combine the effects of the mechanical and the convective turbulence (Panofsky and Dutton, 1984). However when neutral stratification is being considered, some parameters including the lengthscale L are not relevant (Stull, 1988). On the contrary, u_* is important and thus it is often used as a scaling parameter in surface layer relations.

For purely mechanical atmospheric turbulence, the Monin-Obukhov similarity theory estimates that the variance of the velocity components ($\sigma_u^2 = \langle u'^2 \rangle = \langle (u - \langle u \rangle)^2 \rangle$) is a constant value

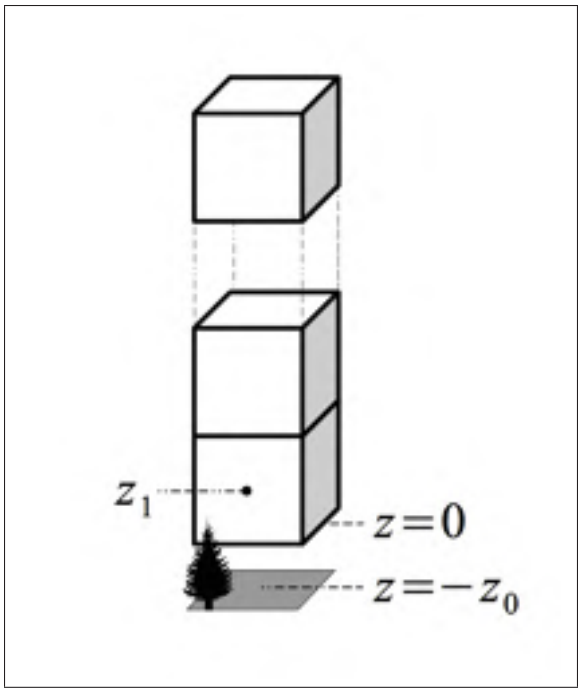

Figure 1.1 Illustration of grid cells position. The tree drawing is an approximate representation of the terrain roughness.

independent of height and roughness. Several experiments have measured the velocity fluctuations in a neutral ASL over flat homogeneous terrain. On average, those measurements yielded a standard deviation of the velocity components of $\sigma_u/u_* = 2.39 \pm 0.03$, $\sigma_v/u_* = 1.92 \pm 0.05$ and $\sigma_w/u_* = 1.25 \pm 0.03$ (Panofsky and Dutton, 1984). Therefore the variances in a neutral ASL are

$$\frac{\langle u'^2 \rangle}{u_*^2} = 5.71, \tag{1.4}$$

$$\frac{\langle v'^2 \rangle}{u_*^2} = 3.69, \tag{1.5}$$

$$\frac{\langle w'^2 \rangle}{u_*^2} = 1.56, \tag{1.6}$$

for the streamwise, spanwise and vertical components respectively. As in boundary layer flow laboratory experiments, the streamwise variance in the near-wall region is larger than the span-

wise and vertical variances (Grant, 1986). Stull (1988) has reported slightly different values where $\langle u'^2\rangle/u_*^2 = 6.1 - 6.5$, $\langle v'^2\rangle/u_*^2 = 2.9 - 6.1$ and $\langle w'^2\rangle/u_*^2 = 1.0 - 2.5$. Also Grant (1991) summarized other aircraft and surface measurements that have yield fairly consistent results for the ASL variances. Finally as a result of constant variances, the turbulent kinetic energy

$$k = \frac{1}{2}\left(\langle u'^2\rangle + \langle v'^2\rangle + \langle w'^2\rangle\right) \tag{1.7}$$

has also a constant profile within the ASL.

1.1.2 Above the atmospheric surface layer

The shear stresses are no longer considered constant above the surface layer. For this reason, the logarithmic law is not longer valid to describe the wind velocity. Vertical velocity profiles in the Ekman layer are more elaborated as summarized by Emeis (2013). The variances parametrization of the turbulent flow above the ASL depends on the height. The normalized ABL variances relationships are (Stull, 1988)

$$\frac{\langle u'^2\rangle}{u_*^2} = 6\left(1 - \frac{z}{H}\right)^2 + \frac{z}{H}\frac{\langle u_{top}'^2\rangle}{u_*^2}, \tag{1.8}$$

$$\frac{\langle v'^2\rangle}{u_*^2} = 3\left(1 - \frac{z}{H}\right)^2 + \frac{z}{H}\frac{\langle v_{top}'^2\rangle}{u_*^2}, \tag{1.9}$$

$$\frac{\langle w'^2\rangle}{u_*^2} = \left(1 - \frac{z}{H}\right)^{1/2}, \tag{1.10}$$

where H is the ABL height. The normalized variance at the top of the boundary layer $\langle u_{top}'^2\rangle/u_*^2$ and $\langle v_{top}'^2\rangle/u_*^2$ was defined as equal to 2.0 by an experiment carried out by Grant (1986), yet it can vary (Stull, 1988). In this work, $\langle u_{i,top}'^2\rangle/u_*^2 = 1.0$ as it is defined by Bechmann (2006).

1.2 Effects over complex topography

The description of the wind flow over inhomogeneous rough surfaces and over changing topography is extremely more complex. In nonuniform terrain, the effects of the wind shear stresses and turbulence levels depart from well-known equilibrium behaviour of the wind over flat terrain. Thus the homogeneous flat terrain assumptions need to be revised carefully over changing terrain. For instance, the logarithmic profile is not longer valid in such complex cases because u_* is highly dependent on height (Panofsky and Dutton, 1984). It is crucial to understand this flow behaviour in order to improve the potential of a wind park over nonuniform terrain. A historical perspective of this problematic is given in Wood (2000).

Reliable measurements of the surface fluxes over complex terrain are unfortunately not always available or complete. Numerous wind-tunnel experiments also have been carried out, but due to some conceptual limitations they are not always strictly representative of the ABL (i.e. the ratio between roughness elements and boundary layer height in the ABL and wind-tunnel experiments is not always comparable) (Kaimal and Finnigan, 1994). This indicates that our knowledge about the turbulent processes involved in complex topography is limited. Despite that, several theories based on linear simplifications have been developed to try to explain the flow behaviour over nonuniform terrain (including change of roughness and change of surface elevation). For instance, Jackson and Hunt (1975) derived a two-layer theory to explain the neutral atmospheric flow over hills. The mean flow around small hills with a downhill slope of 10° is well predicted, but the theory fails for steeper hills (Kaimal and Finnigan, 1994). A good survey of these linear theories can be found on Finnigan (1988) and Athanassiadou and Castro (2001). It has long been established that a more sophisticated turbulence model is required to have a quantitative and complete knowledge of the turbulence behaviour. Nonetheless, great progress has been made in the understanding of how turbulent flow dynamics are affected by the presence of changing roughness or changing terrain elevation.

When a change in surface roughness takes place over flat terrain, the surface momentum flux changes, then the air velocity changes and the local equilibrium is lost (Kaimal and Finnigan,

1994). To further illustrate this point, if the wind flow is moving from a grass field ($z_0 = 8$ mm) towards a dense forest region ($z_0 \sim 500 - 1000$ mm) (Panofsky and Dutton, 1984; Manwell *et al.*, 2002) the surface friction will increase so the flow will slow down. This deceleration only takes place in the near-wall region, but it is then progressively diffused vertically as the streamwise distance increases (Kaimal and Finnigan, 1994). Consequently an internal boundary layer is developed. The change in surface roughness will not be studied in this research project, the focus will concisely placed on terrain elevation changes.

The topography is vaguely classified as flat, hilly and mountainous (Petersen *et al.*, 1998). The flow around a large hill or a mountains range is predominantly driven by internal gravity waves. The study of gravity wave is beyond the scope of this work, because it is mostly a mesoscale phenomenon. As for smaller hills which are submerged within the ABL, the surface stresses, the flow blockage, and the large scale pressure field changes are more important. Terrain elevation can considerably increase the momentum exchange in the atmospheric flow (Athanassiadou and Castro, 2001). Additionally, in purely neutral stratification the vertical movement of an air parcel is only governed by the acceleration cased by terrain constrains; in reality buoyancy causes a gravitational restoring force that contributes to this vertical movement (Kaimal and Finnigan, 1994).

Neutral atmospheric flow accelerates when it encounters an obstacle because of the pressure gradients that developed around it. Downstream of the obstacle, wake vortices, separation, back-flow and reattachment regions could be present. Separation occurs when the flow direction reverses, namely when the velocity vertical gradient at the wall is

$$\left.\frac{\partial u}{\partial n}\right|_w < 0. \tag{1.11}$$

For laminar flows, the separation point takes place when the surface stress $\tau_w = \mu(\partial u/\partial z)|_w$ is zero. Nevertheless it is not evident when the separation point occurs for turbulent flow due to the complicated turbulent response (Kaimal and Finnigan, 1994). Scientists rely on empirical and qualitative data to predict a separation point. For a smooth slope hill, the critical slope angle

that will most likely produce separation is around 18°. Even when the topography effects are expected to dominate, the critical angle is highly dependent on the ground surface roughness. The angle for separation diminishes as the the surface roughness increases (Kaimal and Finnigan, 1994). Additionally, it has been observed that a separation region in turbulent flow is an unsteady process (Ayotte, 2008).

Other interesting phenomena take place when comparing the flow around two-dimensional hills (elongated ridges) against three-dimensional hills. When the wind flow encounters a two-dimensional hill, the flow decelerates at the foot of the hill, then accelerates and reaches a maximum at the top of the hill (Kaimal and Finnigan, 1994), finally if separation occurs one closed bubble is formed (Apsley and Castro, 1997). In contrast when the wind comes across a three-dimensional hill, the flow does not decelerate at the foot of the hill, instead the flow is redirected laterally. Also if a separation region develops, two counter-rotating vortices developed, and the separation bubble has a constant inflow and outflow (Kaimal and Finnigan, 1994).

Lastly, measurements show that the vertical velocity variance $\langle w'^2 \rangle$ at the ASL does not seem to be affected by the presence of uneven terrain. This is because the vertical velocity fluctuations are produced by small eddies that can rapidly adjust to the topography changes. On the contrary, the streamwise fluctuations are governed by large eddies that can only adjust slowly to the changing terrain. Compared to flat terrain, the streamwise variance $\langle u'^2 \rangle$ tends to be smaller (larger) when the locally surface stresses are larger (smaller) than the upstream conditions (Panofsky and Dutton, 1984). For instance on hilltops or in a smooth-to-rough transition, the local shear stresses are larger thus the streamwise variance will most likely be smaller than the flat terrain variances. For this same reasons, the vertical velocity spectra over flat and complex terrain are similar. As for the horizontal velocity spectra (refer to Section 1.3), they differ at the small wavelength (big eddies) between flat and complex terrain observations, but are similar in the high wavelength (small eddies) region (Panofsky and Dutton, 1984).

1.2.1 Turbine micro-siting

The placement of a turbine is a challenging problem but crucial for the proper operation of a wind park. The criteria used to define the ideal siting arrangement of the turbines is mainly based on the maximization of the total energy production. The power P produced by a wind turbine can be estimated by

$$P = \frac{1}{2}\eta_{mech} C_P \rho A u^3 \tag{1.12}$$

where u is the air velocity, ρ is the air density, A is the area swept by the turbine rotor, η_{mech} is the rotor mechanical and electrical efficiency, and C_P is the machine power coefficient (Manwell *et al.*, 2002). This evaluation of the turbine power, it based on the assumption that the air flow is always perpendicular to the rotor with a constant and uniform velocity, and that the turbulence intensity is low. The turbulence intensity is defined as $TI = u_{rms}/\langle u \rangle$, where u_{rms} is the root-mean-square of the velocity and $\langle u \rangle$ is the mean velocity. However in reality, a higher turbulence intensity may result in an increased energy output for smaller wind speed values, but in a reduction of the turbine power for faster winds (Langreder *et al.*, 2004). A more exhaustive analysis demonstrated that the parameters that affect the most the performance and power production of a turbine are: the wind speed at hub height, then the turbulence intensity and lastly the wind shear (Clifton *et al.*, 2014).

Furthermore higher turbulence levels, as well as the separation and reattachment of the air flow, can generate important vibrations on the turbine blades and several problems can arise. Specifically, those variable winds increase the mechanical stresses on a turbine, incrementing the fatigue loads, wear and possibilities of damages (Peinke *et al.*, 2004) (for a detailed study of the effects of turbulence intensity in the fatigue loads of turbines, refer to Riziotis and Voustsinas (2000)). These effects will have a great impact on the operational cost, maintenance expenses, and revenue generation of a wind park. For instance for the same wind speed, the damaged caused by the equivalent loads on the blade roots can increase up to three-times if the turbulence intensity varies from 10% to 25% (Clifton *et al.*, 2014). Another example is

a study carried out in an Austrian wind park located in a mountainous terrain. In this area, the turbulence intensity was more than 20% and the energy generation yield 25% less than the estimated calculation (Clifton *et al.*, 2014). Consequently, for wind turbine siting is essential to understand the magnitude of the wind acceleration and turbulence as well as the position where these phenomena take place (Kaimal and Finnigan, 1994).

1.3 Turbulence

Irregular motion, continuous instability, nonlinear behaviour and randomness are some of the essential features of turbulent flows. More precisely, the main turbulence characteristics are the efficient transport and high mixing rate of momentum, kinetic energy and matter through a fluid (Tennekes and Lumley, 1972). Additionally, turbulence is always a dissipative phenomenon (Wilcox, 2004).

A turbulent fluid presents a broad and continuous range of time and length scales (Wilcox, 2004). An approach to visualize these scales is to treat the local swirling motion of the fluid as turbulent structures, or eddies, with characteristic length and time scales. Overall, the large scales do most of the transport of momentum and the production of turbulent kinetic energy, which is then transferred to the smaller scales mainly by inviscid processes (i.e. vortex stretching, etc.) and finally the smallest scales dissipate that energy by viscous processes (Tennekes and Lumley, 1972). This concept is known as the turbulent energy cascade. The anisotropy of the turbulent eddies is another relevant parameter. Large eddies are generally anisotropic and highly dependent on the flow boundaries, while the small scale eddies are isotropic according to Kolmogorov's theory (Kolmogorov, 1941).

A Fourier analysis of a turbulent velocity field can be used to mathematically represent certain properties of the turbulent flow and visualize the energy cascade. For instance, the velocity spectrum $E(\kappa)$ represents the energy distribution over different lengthscales l characterized by the wavenumber $\kappa = 2\pi/l$. The spectrum of real physical turbulence at sufficiently high Reynolds number should display at least three distinct sections. The portion of the spectra at

small κ (or large l) represents the energy-containing eddies where the energy is produced, the middle section called the inertial subrange depicts the transfer of energy which is governed by inertial processes, and the dissipation range at the larger and isotropic κ where viscous effects are predominant. Additionally, the well-known Kolmogorov theory predicts that the inertial subrange on this spectrum has a slope of $-5/3$ (Kolmogorov, 1941).

According also to the Kolmogorov theory, the small eddies dissipation rate depends on the kinematic viscosity ν and on the rate at which the large eddies supply energy ε. Based on this principle, the characteristic scales of the smaller eddies can be defined. These parameters, called the Kolmogorov scales, are the length η, the time τ and the velocity υ. Hence,

$$\eta = \left(\frac{\nu^3}{\varepsilon}\right)^{1/4}, \quad \tau = \left(\frac{\nu}{\varepsilon}\right)^{1/2}, \quad \upsilon = (\nu\varepsilon)^{1/4}. \tag{1.13}$$

These parameters imply that the small turbulent scales are statistically similar and universal for high Reynolds flows (Kolmogorov, 1941).

Characterizing a random turbulent field can be mathematically complex. In experiments or simulations of turbulent flows, several types of averaging are defined in an attempt to get a global and more simplified picture of the turbulence. For example, statistically stationary flows can be described by the time average of its velocity field

$$\langle \mathbf{u}\,(t)\rangle_t = \frac{1}{T}\int_{t_0}^{t_0+T} \mathbf{u}\,(t')dt', \tag{1.14}$$

whereas a spatial average can be defined for homogeneous turbulence

$$\langle \mathbf{u}\,(t)\rangle_s = \frac{1}{V}\int_{0}^{V} \mathbf{u}\,(\mathbf{x},t)dV \tag{1.15}$$

in one, two or three dimensions. And finally, if a flow experiment can be replicated N times, an ensemble average

$$\langle \mathbf{u}\,(t)\rangle_N = \frac{1}{N}\sum_{n=1}^{N}\mathbf{u}^{(n)}\,(t) \tag{1.16}$$

can be used (Pope, 2000). For practical reasons, it is not always possible to repeat an experiment or a simulation, so $\langle u\rangle_N$ is rarely computed for atmospheric flows. Under certain circumstances, the ergodicity principle states that ensemble averages are equivalent to time averages. Similarly, $\langle u\rangle_t \approx \langle u\rangle_s$ for some cases based on the Taylor hypothesis[1] (Panofsky and Dutton, 1984). In this work, $\langle u\rangle_t$ and $\langle u\rangle_s$, $\langle u\rangle_N$ will be expressed as $\langle u\rangle$ to simplify the notation. However, the procedure used to compute the average values will always be clearly stated.

1.4 Microscale flow governing equations

In order to study the atmospheric flow at a microscale level, a mathematical description of the turbulent flow is needed. Using the Einstein notation[2], the unsteady behaviour of an incompressible fluid is described by the Navier-Stokes or momentum equations

$$\frac{\partial u_i}{\partial t} + \frac{\partial u_j u_i}{\partial x_j} = -\frac{1}{\rho}\frac{\partial \sigma_{ij}}{\partial x_j} + \frac{F_i}{\rho}, \tag{1.17}$$

and the mass continuity equation

$$\frac{\partial u_i}{\partial x_i} = 0. \tag{1.18}$$

Here ρ represents the constant density, u_i the velocity, t the time, and x_i the Cartesian coordinates. Additionally, $\partial\sigma_{ij}/\partial x_j$ characterizes the surface forces, while F_i the body forces acting on a fluid (Panton, 1995).

[1] The Taylor hypothesis is not quite valid for atmospheric flows since its basic assumptions are not entirely satisfied. First, the turbulence evolves over time so it is not frozen as assumed by the theory; secondly, the eddy convection velocity is not always precisely the local mean speed. Due to the lack of a better option, the Taylor hypothesis is widely used in atmospheric flows (Kaimal and Finnigan, 1994).

[2] $\mathbf{u} = u_i\widehat{e}_i = (u, v, w)$

The different surface forces are summed up in the total stress tensor σ_{ij}. It comprises the effects of the pressure p (a normal stress) and the shear stresses τ_{ij}, hence

$$\frac{\partial \sigma_{ij}}{\partial x_j} = -\frac{\partial p}{\partial x_j}\delta_{ij} + \frac{\partial \tau_{ij}}{\partial x_j} \tag{1.19}$$

where δ_{ij} is the Kronecker delta. Additionally, the shear stress or viscous stress are given by

$$\tau_{ij} = \mu\Big(\frac{\partial u_i}{\partial x_j} + \frac{\partial u_j}{\partial x_i}\Big) \tag{1.20}$$

where μ is the dynamic viscosity of the fluid. As for the body forces, F_i can represent the Coriolis force, the centrifugal force, a large scale pressure gradient, etc.

By substituting Equations 1.19-1.20 into Equation 1.17, the derivative form of the Navier-Stokes equations can be rewritten as

$$\frac{\partial u_i}{\partial t} + \frac{\partial u_j u_i}{\partial x_j} = -\frac{1}{\rho}\frac{\partial p}{\partial x_i} + \frac{\partial}{\partial x_j}\left[\nu\left(\frac{\partial u_i}{\partial x_j} + \frac{\partial u_j}{\partial x_i}\right)\right] + \frac{F_i}{\rho}, \tag{1.21}$$

where $\nu = \mu/\rho$ is the air kinematic viscosity. It is not easy to solve the turbulent momentum equations because of the nonlinear term $\partial(u_j u_i)/\partial x_j$, and the fact that the pressure and the velocity fields are coupled (Ferziger and Perić, 2002). In most cases, these equations cannot be solved analytically, therefore numerical methods are needed to model and to approximate the turbulent flow behaviour.

CHAPTER 2

MICROSCALE ATMOSPHERIC FLOW MODELLING

The partial differential equations that describe the atmospheric turbulent flow are rather complex and can only be solved numerically. Computational Fluid Dynamics (CFD) is a interdisciplinary branch of science which relies on numerical methods and algorithms to solve these type of equations through computer simulations. Special software, like OpenFOAM (Open Source Field Operation and Manipulation), have been designed to tackle CFD simulations and analyze fluid problems. In this section, only a brief summary of the basic aspects of CFD will be given. For a more complete reference see Ferziger and Perić (2002). This section will describe the basic concepts of CFD within the context of OpenFOAM and atmospheric flows at a microscale level. This chapter is also an attempt to gather the relevant information on the subject in one place and contribute to the OpenFOAM documentation for microscale atmospheric flows.

2.1 Basics aspects of computational fluid dynamics

A CFD analysis involves two fundamental aspects: the physical modelling (i.e. turbulence models) and the numerical techniques (i.e. effective, robust and reliable methods to discretize and solve the linear system of equations). More specifically, the CFD process starts by the derivation the partial differential (or integral) equations that govern a flow field (as done in Section 1.4). The resulting equations for the turbulent atmospheric flow are nonlinear, mathematically complex and computationally demanding to solve. A turbulence model is needed to approximate and simplify the physics, and to alleviate the computational cost. Additionally, a CFD computation depends on the discrete treatment of a continuous fluid. Consequently the space domain that represents the fluid volume is divided into cells or control volumes (CV) that form a grid or mesh. If required, the time domain is also divided in time steps. The partial differential equations are also discretized to obtain a set of approximate algebraic equations for each cell or control volume. Finally the discretized equations are then solved using numerical methods to find an approximate solution (Ferziger and Perić, 2002).

2.1.1 Physical modelling

As previously mentioned, turbulence models are required to approximate or estimate the nonlinear convective term present in the Navier-Stokes equations. Several classes of turbulence models have been developed. Here, only a brief description Reynolds-averaged Navier-Stokes (RANS) models, large-eddy simulation (LES) models and a hybrid technique called detached-eddy simulations (DES) will be given. A more complete description of turbulence models can be found in Pope (2000) and Wilcox (2004).

A turbulence model estimates the nonlinear term by making different assumptions about the turbulence characteristics and by computing additional turbulence quantities or transport equations. In general, the main difference between those turbulence models is the level of description of the turbulent flow, in other words, which turbulent scales are explicitly resolved by the equations and which ones are simply estimated or modelled.

Reynolds-averaged Navier-Stokes (RANS)

RANS models are based on the Reynolds decomposition of the turbulent velocity field. Consequently the instantaneous velocity u_i is expressed as the sum of the time-averaged velocity $\langle u_i \rangle$, and the instantaneous fluctuation u_i', thus (Reynolds, 1895)

$$u_i(\mathbf{x}, t) = \langle u_i \rangle(\mathbf{x}, t) + u_i'(\mathbf{x}, t) \tag{2.1}$$

Then the time-averaged flow Navier-Stokes equations used by any RANS model can be obtained by substituting Eq. 2.1 into the Navier-Stokes momentum expression (Eq. 1.21). This yields

$$\frac{\partial \langle u_i \rangle}{\partial t} + \frac{\partial \langle u_j \rangle \langle u_i \rangle}{\partial x_j} = -\frac{1}{\rho}\frac{\partial \langle p \rangle}{\partial x_i} + \frac{\partial}{\partial x_j}\left[\nu\left(\frac{\partial \langle u_i \rangle}{\partial x_j} + \frac{\partial \langle u_j \rangle}{\partial x_i}\right) - \langle u_i' u_j' \rangle\right] + \frac{F_i}{\rho}. \tag{2.2}$$

The term $\langle u_i' u_j' \rangle$ is called the turbulent stress tensor or the Reynolds stress tensor. The presence of these stresses in the equation show that the velocity fluctuations do have an impact on the mean velocity.

The time averaging procedures has introduced nine more variables (one for each Reynolds stress component) which are unknown (White, 1991). This system of four equations has more than four unknowns ($\langle u_i \rangle$, $\langle p \rangle$ and $\langle u_i' u_j' \rangle$), thus it is not mathematically closed. Therefore, a closure scheme is required to determine the nonlinear Reynolds stresses. One of the most common approaches is to use the turbulent viscosity or Boussinesq hypothesis which states that

$$-\rho \langle u_i' u_j' \rangle = \nu_t \left(\frac{\partial \langle u_i \rangle}{\partial x_j} + \frac{\partial \langle u_j \rangle}{\partial x_i} \right) - \frac{2}{3} k \delta_{ij} \tag{2.3}$$

where $k = 0.5 \langle u_i' u_i' \rangle$ is the modelled turbulent kinetic energy and δ_{ij} is the Kroneker delta (Boussinesq, 1897). Also the turbulent or eddy viscosity ν_t is a newly introduced variable can only be modelled or empirically approximated by introducing extra transport equations. For example, the $k - \omega$ SST RANS model uses the specific turbulent kinetic energy and the specific dissipation rate equations (k and ω respectively) to model ν_t. Finally, the time-averaged momentum equation is given by

$$\frac{\partial \langle u_i \rangle}{\partial t} + \frac{\partial \langle u_j \rangle \langle u_i \rangle}{\partial x_j} = -\frac{1}{\rho} \frac{\partial \langle p \rangle}{\partial x_i} + \frac{\partial}{\partial x_j} \left[(\nu + \nu_t) \left(\frac{\partial \langle u_i \rangle}{\partial x_j} + \frac{\partial \langle u_j \rangle}{\partial x_i} \right) \right] + \frac{F_i}{\rho}. \tag{2.4}$$

RANS models solve only the time-averaged velocity field and model the velocity fluctuations. For this reason they do not provide any information about the instantaneous behaviour of the flow nor about the turbulent structures, but the required computational power is relatively low. For steady RANS models the time derivative is zero. But if $\partial \langle u_i \rangle / \partial t \neq 0$, transient phenomena of a much bigger time scale than the turbulent fluctuations can be simulated. In other words, the low frequency variations in the diurnal cycle of the atmosphere can be estimated (Koblitz *et al.*, 2013), but not the turbulent fluctuations nor the intermittent separation bubble behind a hill. These transient models are called unsteady-RANS (URANS).

RANS and URANS simulations generate fairly accurate results for winds over flat terrain. However, the results obtained over complex terrain are not always reliable or numerically stable (Bechmann and Sørensen, 2010). In general, the flow patterns in adverse pressure regions are not well predicted. For instance, RANS models are not always able to reproduce the flow separation on the lee-side of a hill because they usually predict low velocity and low turbulence intensity (Bechmann and Sørensen, 2010). A RANS model called $k-\omega$ SST is commonly used for aerodynamic flows. It yields fairly accurate results on adverse pressure gradients and separation regions, and its results are more accurate on the viscous near-wall regions than for example the RANS $k-\varepsilon$ turbulence model (Menter, 1992). However, the $k-\omega$ SST model has rarely been used for atmospheric flows. In this thesis, the advantages of the model will be investigated in ABL simulations.

Large-eddy simulation (LES)

In LES a spatial filtering operation is carried out to decompose the velocity field as

$$u(\mathbf{x},t) = \overline{u}(\mathbf{x},t) + u_{sgs}(\mathbf{x},t). \tag{2.5}$$

$\overline{u}$ is the filtered or resolved component which represents the larger three-dimensional unsteady turbulent scales that will be explicitly solved; while u_{sgs} is the residual or subgrid component which will be modelled. The filtering is defined as

$$\overline{u}_i(\mathbf{x},t) = \int u_i(\mathbf{x}-\mathbf{r},t)G(\mathbf{r},\mathbf{x})d\mathbf{r} \tag{2.6}$$

where G is a normalized filter function (Leonard, 1974). Several types of filters exist (e.g. box, Gaussian, sharp spectral, Cauchy, and Pao), but most often the grid spacing Δ acts as the filter width (See Pope (2000) for details). Eddies which are twice as large as the cell size are explicitly solved. This is deduced from the Nyquist theorem (Kaimal and Finnigan, 1994). The filtered velocity equations can be found by filtering the Navier-Stokes equations. Analogous to the Reynolds decomposition, the filtering operation yields a residual (or sgs) stress tensor that

can only be modelled by a closure scheme. The LES momentum equation using a turbulent or eddy viscosity model are then given by

$$\frac{\partial \overline{u}_i}{\partial t} + \frac{\partial \overline{u}_j \overline{u}_i}{\partial x_j} = -\frac{1}{\rho}\frac{\partial \overline{p}}{\partial x_i} + \frac{\partial}{\partial x_j}\left[(\nu + \nu_t)\left(\frac{\partial \overline{u}_i}{\partial x_j} + \frac{\partial \overline{u}_j}{\partial x_i}\right)\right] + \frac{F_i}{\rho}. \tag{2.7}$$

This time the turbulent viscosity ν_t, represents the effects of the residual or sgs motions.

Solving the LES equations yields information about the unsteady filtered field. Then, the filtered velocity can be decomposed into a (time or spatial) average value $\langle \overline{u} \rangle$ and filtered fluctuations $\overline{u}'$; hence (Bechmann, 2006)

$$\overline{u} = \langle \overline{u} \rangle + \overline{u}'. \tag{2.8}$$

Consequently, the instantaneous velocity field is

$$\begin{aligned} u &= \overline{u} + u_{sgs}, \\ u &= \langle \overline{u} \rangle + \overline{u}' + u_{sgs}. \end{aligned} \tag{2.9}$$

Contrary to RANS, the LES models can give a more complete description of a turbulent flow. LES can provide information about the unsteady nature of the turbulence by resolving certain fluctuations in the flow. For example, LES can predict unsteady effects in wind flow over hills like the instantaneous and intermittent separation on the lee-side (Ayotte, 2008). This important phenomenon cannot be simulated using RANS models.

The grid used on LES cases should have near-cubic cells to avoid imposing non-physical effects to the large isotropic turbulence structures; however, close to the wall the flow is highly anisotropic, and the grid is usually refined (Wood, 2000). For the atmospheric flow in general, an appropriate LES grid can be relatively coarse far away from the Earth's surface (Bechmann and Sørensen, 2010). However, for resolving the near-wall eddies instead of just modelling them, a finer grid is needed. Since the grid resolution required to resolve these small-scale eddies increases approximately as the square of the Reynolds number, LES can be com-

putationally demanding (Gungor and Menon, 2010). The expensive computational cost makes, to this day, LES not suitable for industrial wind energy computations; however, LES can have important scientific implications thanks to the detailed flow behaviour that can be predicted.

Detached-eddy simulation (DES)

The standard detached-eddy simulation (DES) is a hybrid technique which uses a URANS model to solve the flow behaviour in the boundary layer and a LES model in regions of detached flow (Spalart *et al.*, 1997), as the sketch in Figure 2.1a shows. The DES technique can potentially improve the prediction of the flow behaviour with respect to a RANS models (Menter *et al.*, 2003), however, it has two well-known inherent deficiencies. First, the standard DES can sometimes predict unphysical separation regions in certain types of grids (Menter *et al.*, 2003). This phenomena is called grid-induced separation (GIS). Secondly, if the grid spacing (streamwise and spanwise) is much smaller than the boundary layer height, the DES model can act as a wall-modelled LES (WMLES) (Spalart *et al.*, 2006). In this case, the URANS branch of the hybrid model will solve the flow only in the near-wall region and not in the entire boundary layer, whereas the LES branch will compute the flow away from the wall but still inside the boundary layer. Figure 2.1b depicts the WMLES behaviour of the hybrid model. This not in agreement with the original formulation of the DES model[1]. It has been shown that a WMLES based on the DES equations is robust and able to sustain turbulence, however, it may lead to inaccurate velocity and stress values at the URANS and LES interface causing a log-layer mismatch (LLM) (Nikitin *et al.*, 2000).

A modification to the standard equations of DES was proposed to eliminate the hybrid model dependency on the grid density. This is achieved by using a shielding function that maintains the RANS behaviour within the boundary layer (Spalart *et al.*, 2006). This newer approach, known as the delayed detached-eddy simulations (DDES) model, solves the GIS problem but it does not address the disadvantages of the LLM. Fortunately, the improved delayed

[1]Rigorously, a WMLES based on the DES equations should not be called "DES" (Spalart *et al.*, 2006). Nevertheless for simplicity in this thesis, DES will refer to the model that uses the standard DES switch Equation 2.20 regardless of the type of mesh.

(a) Standard use of DES

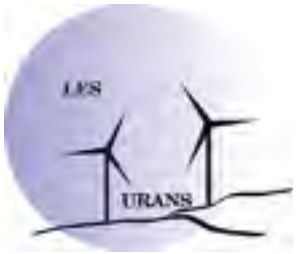

(b) WMLES usage

Figure 2.1 Sketch of DES applications. The extent of the boundary layer is represented by the colour blue. (a) The original DES was conceived to use URANS in the boundary layer, and LES everywhere else. (b) As a WMLES, the hybrid model employs URANS in the near-wall region, and LES far from the wall but within the boundary layer.

detached-eddy simulations (IDDES) model includes additional modifications that deal with the LLM (Shur *et al.*, 2008). The main disadvantage of IDDES is that the formulation increases considerably the complexity of the model. A simplified version of IDDES (hereafter SIDDES) has been recently proposed and successfully tested on aerodynamic flows (Gritskevich *et al.*, 2012). The SIDDES results are consistent with IDDES, hence the use of the simplified model is justified.

The wind energy microscale simulations are focused essentially only on the boundary layer; thus the hybrid model aim is to use URANS only in the near-wall region and LES away from the wall but still inside the boundary layer. In other words, the type of meshes needed (i.e. finer in the streamwise and spanwise direction compared to the height of the boundary layer) will force a standard DES model to always behave as a WMLES. Consequently, the use of the standard DES technique is not entirely adequate and it is extremely important to correct the LLM problem on ABL simulations. On the contrary, the GIS is not a relevant issue for atmospheric simulations. The performance and viability of the SIDDES turbulence model for neutral ABL cases will be analyzed. A full description of the proposed model will be given on Section 2.2.1.

Surface boundary conditions in atmospheric flows

Boundary conditions are required to solve a CFD simulation. They vary depending on the problem to be solved, but certain guidelines should be followed (Franke *et al.*, 2007). The boundary conditions for each simulated case will be specified in the following chapters. However, the solid surface boundary condition requires especial considerations.

The standard no-slip condition ($u_{wall} = 0$) can be defined on smooth surfaces for the velocity at the nearest wall node z_1 provided that the turbulence model equations can be accurately solved down to wall (Batchelor, 1967). However for high Reynolds flows, an extremely large number of cells are needed to solve the near-wall flow; for this reason, wall functions are usually imposed. For instance, a wall function imposes a value of the velocity at z_1 assuming a log-layer profile; thus, a wall function is valid only if the first grid node near the wall is located within the logarithmic region ($30 < z_1^+ = u_* z_1/\nu$) (White, 1991). As for rough surfaces in turbulent flows, the roughness has a great impact on the viscous sublayer and it rather increases the wall friction (White, 1991). If the terrain is considered to be rough, a wall function is commonly imposed to model the drag caused by this roughness.

It has been shown that adding a wall function generates accurate results on attached aerodynamic flows (Piomelli *et al.*, 1989), whereas their accuracy on separated flows has not been confidently established (Stoll and Porté-Agel, 2006). Notably in theory, a wall function is not longer valid and it might not yield accurate results in complex geometries or terrain were strong adverse pressure gradients, and separation, reattachment or recirculation regions exist (Patel, 1998; Ferziger and Perić, 2002).

The wall functions for RANS and LES vary slightly due to the computed variables (i.e. fluctuating vs. mean velocity), yet the basic principle is the same (Ferziger and Perić, 2002). Several approaches have been implement to model the atmospheric flows surface boundary conditions, Stoll and Porté-Agel (2006) provide a good summary of the most relevant wall functions used for LES. In essence, all of those wall functions relate the surface shear stresses to the velocity at the nearest node to the wall assuming a logarithmic-law velocity profile. Those wall func-

tions rely on the Monin-Obukhov similarity theory (i.e. log-law on rough flat terrain only and based on ensemble averages) to calculate the surface shear stresses, and it is not clear how these wall functions behave specially on complex terrain. Some studies have shown that for example the level of velocity fluctuations is underestimated for most of the wall functions used on flat terrain cases (Stoll and Porté-Agel, 2006). Those errors can be propagated throughout the surface layer. Due to the lack of a better solution, the use of standard wall functions is a common practice for ABL simulations over complex flows. The ability to compute a more reliable surface boundary condition for high Reynolds flows over rough and complex terrain is one of the biggest challenges that the CFD community currently faces (Piomelli *et al.*, 1989; Chow, 2004; Stoll and Porté-Agel, 2006).

A different approach to the standard wall function is explored within this work by using the $k-\omega$ SST turbulence model. This model chosen mainly for two reasons. First, the model can be integrated down to the wall (Menter, 1994) if a proper mesh is used; and secondly, the original turbulence model equations directly account for surface roughness (Patel and Yoon, 1996). These characteristics are particularly advantageous because the used of standard wall functions can be avoided.

2.1.2 Numerical techniques in OpenFOAM

The OpenFOAM software framework is used to perform all the atmospheric flow simulations of this work. A brief description of the numerical aspects of CFD concerning the atmospheric flow in the OpenFOAM context will be given. OpenFOAM uses one of the most common discretization approaches called Finite Volume Method (FVM) which solves the integral form of the momentum equations in each CV on the grid. This method relies on the fact that fluxes must be conserved in each control volume and hence conserved globally (Ferziger and Perić, 2002). Then by using the Gauss' divergence theorem, some of the volume integrals of these equations (i.e. the convective and diffusive term) are converted into surface integrals over the CV to estimate the fluxes (Versteeg and Malalasekera, 2007). Whereas the other terms in the equation (i.e. source terms) can easily be treated as volume integrals.

To compute exactly a surface integral, the value of the integrand quantity f needs to be known everywhere over such surface. Since this is not possible, an approximation is required. OpenFOAM assumes that the value of any quantity is constant over a surface (Churchfield *et al.*, 2010) and equivalent to the mean value over such surface. This is called the midpoint rule approximation and it provides a second-order accuracy (Ferziger and Perić, 2002). More specifically, the value of the surface integral at a CV face located at point 'e' is estimated as

$$F_e = \int_{S_e} f \, dS = \langle f \rangle \, S_e \approx f_e \, S_e, \tag{2.10}$$

thus the product of the integrand at the cell-face centre f_e times the cell-face surface area S_e. As for the volume integrals a similar approximation can be made, but in this case, the value of a variable q is computed at point 'p'- the CV centre. Therefore, the value of the volume integral is

$$Q_p = \int_V q \, dV = \langle q \rangle \, \Delta V \approx q_p \, \Delta V. \tag{2.11}$$

Here q_p is the known value of a quantity at the cell centre, so no interpolation is needed. Such volume integral is exact if q is constant or varies linearly within the CV, otherwise it becomes a second-order approximation (Versteeg and Malalasekera, 2007). For these reasons OpenFOAM has intrinsically a second-order spatial discretization.

Those surface and volume integrals need certain values of variables and/or gradients that are not always located at a central node, therefore, further interpolation from cell centres to cell faces values are required. Numerous interpolation schemes have been developed, for example: upwind interpolation (UDS), linear interpolation[2] (CDS), quadratic upwind interpolation (QUICK), etc.), which have different levels of accuracy (e.g. first-order, when the truncation error is the order of (Δx), second-order with a truncation error in the order of $(\Delta x)^2$, etc.). For specific details of each discretization scheme refer to Anderson (1995), Versteeg and Malalasekera (2007) and Ferziger and Perić (2002). Several interpolation schemes

[2]Linear interpolation corresponds to central difference approximation for finite difference methods, therefore the CDS label.

are already coded in OpenFOAM thus this research work will not focus on modifying or implementing new schemes. However, it will be verified that the schemes are stable and that the numerical dissipation is minimal leading to physical results. The interpolation methods and its particular parameters are specified in OpenFOAM simulation in the *fvSchemes* input file; an example of such file used for atmospheric flow simulations is shown on Appendix III.6.

The velocity and pressure discretized field are computed using the pressure-implicit split-operator (PISO) algorithm (Issa, 1985). PISO is a non-iterative method that solves the momentum-pressure coupling of the discretized flow equations implicitly in time. Several sets algebraic equations or matrices have to be solved within the different steps of the PISO algorithm. To find a solution for those matrices, numerous methods or techniques are already implemented in OpenFOAM. They will not be discussed here because the subject is extensive and numerous good reference exist including Ferziger and Perić (2002) and Versteeg and Malalasekera (2007). The solution techniques and its particular parameters are specified for an OpenFOAM simulation in the *fvSolution* input file; an example of such file used for atmospheric flow simulations is shown on Appendix III.7.

The PISO algorithm consist generally in one predictor step and two correctors steps which provides a velocity and pressure solution that are respectively third and second-order accurate. Adding another corrector loop will increase the accuracy by one order (Issa, 1985). Since OpenFOAM has a second-order spatial discretization, extra corrector loops might be unnecessary. However, it was observed that setting three corrector steps (*nCorrectors* variable in the *fvSolution* file) the solution converged faster and the number of total pressure iterations was greatly reduced. Additionally, the OpenFOAM structure is based on a collocated grid, thus all the variables are stored at the centre of the CV. This can generate unphysical pressure oscillations in the solution (Patankar, 1980). To avoid those oscillations, OpenFOAM uses a method similar to the Rhie-Chow correction within the PISO loop to obtain a oscillation-free field (Peng-Karrholm, 2006). This is one of the reasons why the PISO method in OpenFOAM (Peng-Karrholm, 2006; Churchfield *et al.*, 2010) varies slightly from the original PISO formulation (Issa, 1985) which was developed for staggered grids.

Systematic errors are always present in any numerical simulation. The accuracy of the solution depends on modelling, discretization and iteration errors (Ferziger and Perić, 2002). To correctly assess the modelling errors a comparison with experimental data has to be done. Unfortunately, precise measurements are essential and not always available. However the known inaccuracies or assumptions of the turbulence model that could lead to some modelling errors will be stated and a full validation of the turbulence model will be carried out. Concerning the discretization errors, all the discretization schemes used will be second-ordered accurate in time and space. Additionally, a grid independence and convergence should be verified; however, in wind engineering problems, this is not always attainable. Doing a grid-independence test with even finer grids is not always possible because the cost of coarse grid is already too high. In addition, a finer grid in LES will resolve smaller eddies and might yield a different solution. For these reasons, it is hard to judge the effect that these discretization errors have on the results (Bechmann, 2006). Finally to limit the iteration error, a convergence tolerance of at least 10^{-6} will be set in the *fvSolution* file for the normalized equation residual.

2.1.3 Additional details of the OpenFOAM framework

OpenFOAM software an open-source code developed in C++; in other words, the user can modify the code if necessary and adapt it to his or her needs. This is an important advantage of OpenFOAM, since the commercial software are not always as flexible.

In general, OpenFOAM works by creation of executable files called applications. The solver applications are used to solve a particular problem, while the data handling (pre-processing and post-processing) is done by the utility applications (The OpenFOAM Foundation, 2013). The user can select the grid discretization, the boundary conditions, the discretization schemes, the level of accuracy, and other parameters.

The software contains many features already defined and implemented (e.g. several turbulence models (RANS and LES), wall functions, boundary conditions, data sampling, etc.). Nonetheless, not all the requirements needed for the completion of this research project are satisfied.

Several aspects of the OpenFOAM code had to be modified for this project. These code changes are related to the improvement of ABL modelling, and the adaptation of the turbulence model and boundary conditions. The main code adaptations are described on Appendix III.

2.2 Challenges in microscale wind energy simulations

Now that the basis of CFD and the OpenFOAM framework have been discussed, a more informed and critical approach to solve some of the wind energy challenges can be taken. Two of the main challenges that the wind industry faces when doing microscale CFD simulations is the high computational cost, and the fact that most surface treatments are based theories developed for equilibrium boundary layer or flat terrain (i.e. the use of wall functions).

RANS turbulence models are the most sophisticated approaches used by the wind industry to simulate the atmospheric flow. As mentioned, RANS models have a relatively low computational cost, however, they do not provide a complete description of the unsteady turbulence behaviour and might not be capable of evaluating complex phenomena induced by the terrain. In order to have a detailed description of the turbulence characteristics, more advanced models are needed. LES models could potentially be a good alternative to RANS, but their computational cost is considerably higher. A compromise between the required accuracy and the need for affordable simulations for the wind industry is expected to be achieved with the use of hybrid models like the detached-eddy simulation (DES) approach. Bechmann (2006) used a hybrid model based on the DES approach and the $k-\varepsilon$ model for atmospheric flows. Other hybrid models that have been implemented include Sullivan (1994) and Senocak *et al.* (2007).

On the other hand, the wind energy predictions currently rely on numerical simulations that might not be accurate enough when complex topography is examined. Until now, it has been an accepted and frequent practice to impose a wall functions to model the ground surface; however, it is widely known that wall functions may not be valid for complex terrain where adverse pressure gradients or separation zones are highly probable. The RANS $k-\omega$ SST model could be used with a particular wall treatment that is less dependent on flat terrain

assumptions. In this manner, standard wall functions to model the Earth's surface, specially its roughness, can be avoided. Additionally, the $k-\omega$ SST model yields acceptable results in adverse pressure gradient and separations regions (Menter, 1992).

A turbulence model based on the $k-\omega$ SST Reynolds-averaged Navier-Stokes model and the simplified improve delayed-eddy simulation (SIDDES) hybrid technique is proposed to address those needs. This model was first formulated by Gritskevich *et al.* (2012); it was calibrated and used for aerodynamic flows. The hybrid model has been implemented in OpenFOAM v.2.2.2 and its performance will be tested.

2.2.1 Proposed hybrid model for atmospheric flow simulations[3]

The motion of a atmospheric flow is described by the incompressible and turbulent Navier-Stokes equations,

$$\frac{\partial \overline{u}_i}{\partial t} + \frac{\partial \overline{u}_j \overline{u}_i}{\partial x_j} = -\frac{1}{\rho}\frac{\partial \overline{p}}{\partial x_i} + \frac{\partial}{\partial x_j}\left[(\nu + \nu_t)\left(\frac{\partial \overline{u}_i}{\partial x_j} + \frac{\partial \overline{u}_j}{\partial x_i}\right)\right] + \frac{F_i}{\rho} \tag{2.12}$$

using the Einstein notation. In the case of the detached-eddy simulation approach, $\overline{u}_i$ represents the time-averaged velocity for the URANS region, while in the LES region this term is the filtered velocity (Bechmann and Sørensen, 2010). The pressure $\overline{p}$ is treated in a similar manner. Also ν_t represents the turbulent viscosity or the subgrid viscosity in the URANS and LES regions respectively. Lastly, F_i can represent all the external forces (e.g. large scale pressure gradient, Coriolis, etc.).

The proposed hybrid model uses the closure equations of the URANS model $k-\omega$ SST (Menter *et al.*, 2003)[4]. However a small modification is implemented in the equation of the turbulent kinetic energy. Specifically, the dissipation term ε of such equation is used to introduce a universal lengthscale $\tilde{l} = k^{1/2}/(\beta_*\omega)$. Hence, ε is substituted by $k^{3/2}/\tilde{l}$ in the

[3] A summary of the hybrid model formulae is given in Appendix I and II.

[4] As mentioned in *http://turbmodels.larc.nasa.gov/sst.html* a typographical error exists in the turbulent dissipation equation (Eq. 1) of that article. Future references use the corrected equation (e.g. Gritskevich *et al.* (2012)).

equations. The resulting closure equations to model the specific turbulent kinetic energy k, and the specific dissipation rate ω, used on all the DES approaches are (Gritskevich *et al.*, 2012)

$$\frac{\partial k}{\partial t} + \frac{\partial \overline{u}_j k}{\partial x_j} - \frac{\partial}{\partial x_j}\left[(\nu + \sigma_k \nu_t)\frac{\partial k}{\partial x_j}\right] = P_k - \frac{k^{3/2}}{\tilde{l}}, \tag{2.13}$$

$$\frac{\partial \omega}{\partial t} + \frac{\partial \overline{u}_j \omega}{\partial x_j} - \frac{\partial}{\partial x_j}\left[(\nu + \sigma_\omega \nu_t)\frac{\partial \omega}{\partial x_j}\right] = \frac{\gamma}{\nu_t}P_k - \beta\omega^2 + 2(1-F_1)\frac{\sigma_{\omega 2}}{\omega}\frac{\partial k}{\partial x_j}\frac{\partial \omega}{\partial x_j}, \tag{2.14}$$

where the production term is $P_k = \min(\nu_t \mathcal{S}^2, c_1\,\beta_*\,k\,\omega)$. Finally, the eddy viscosity is determined as

$$\nu_t = \frac{a_1 k}{\max(\mathrm{a}_1\omega, \mathcal{S}\mathrm{F}_2)} \tag{2.15}$$

regardless if it is a URANS or an LES region being solved[5]. Here $\mathcal{S} = \sqrt{S_{ij}S_{ij}}$ is the characteristic strain rate, a_1 is a constant, and F_1 and F_2 are blending functions defined as

$$\begin{aligned}
F_1 =& \tanh\left(arg_1^4\right),\\
arg_1 =& \min\left(\max\left(\frac{\sqrt{k}}{\beta_*\,\omega\,d_w}, \frac{500\,\nu}{d_w^2\,\omega}\right), \frac{4\,\rho\,\sigma_{\omega 2}\,k}{CD_{k\omega}\,d_w^2}\right),\\
CD_{k\omega} =& \max\left(2\,\rho\,\sigma_{\omega 2}\frac{\nabla k \cdot \nabla \omega}{\omega}, 10^{-10}\right),\\
F_2 =& \tanh\left(arg_2^2\right),\\
arg_2 =& \max\left(\frac{2\sqrt{k}}{\beta_*\,\omega\,d_w}, \frac{500\,\nu}{d_w^2\,\omega}\right).
\end{aligned} \tag{2.16}$$

F_1 equals 0.0 away from a solid surface and $F_1 = 1.0$ in the near-wall region (Menter *et al.*, 2003). While $F_2 = 1.0$ for boundary layers and $F_2 = 0.0$ in shear layers (Menter, 1994). Finally β_*, β, γ, σ_k and σ_ω are model constants. These constants, collectively represented as ϕ, are calculated by $\phi = F_1\phi_1 + (1-F_1)\phi_2$ based on the model constants from Table 2.1. As all the eddy viscosity models, this hybrid possesses all the known limitations of this type of

[5]Appendix III.1 shows how these equations were implemented in the OpenFOAM code.

models. Additionally, the hybrid could be highly dissipative and it only allows energy transfer from the filtered scales to the residual scales in a process called forward-scatter (Pope, 2000).

Table 2.1 Turbulence model constants.

$k-\omega$ SST constants for aerodynamic flows (Menter *et al.*, 2003):					
$\beta_1 = 0.075$	$\beta_2 = 0.0828$	$\sigma_{k1} = 0.85$	$\sigma_{k2} = 1.0$	$\kappa = 0.41$	$\beta_* = 0.09$
$\gamma_1 = 5/9$	$\gamma_2 = 0.44$	$\sigma_{\omega 1} = 0.5$	$\sigma_{\omega 2} = 0.856$	$a_1 = 0.31$	$c_1 = 10.0$
SIDDES constants for aerodynamic flows (Gritskevich *et al.*, 2012) (Travin *et al.*, 2002):					
$C_{k-\varepsilon} = 0.61$	$C_{k-\omega} = 0.78$	$C_w = 0.15$	$C_{dt1} = 20.0$	$C_{dt2} = 3.0$	
$k-\omega$ SST constants for atmospheric flow (Boudreault, 2011):					
$\beta_1 = 0.0236$	$\beta_2 = 0.0276$	$\sigma_{k1} = 0.85$	$\sigma_{k2} = 1.0$	$\kappa = 0.40$	$\beta_* = 0.03$
$\gamma_1 = 0.3255$	$\gamma_2 = 0.3011$	$\sigma_{\omega 1} = 0.5$	$\sigma_{\omega 2} = 0.67$	$a_1 = 0.31$	$c_1 = 10.0$
SIDDES constants for atmospheric flow:					
$C_{k-\varepsilon} = 0.61$	$C_{k-\omega} = 0.78$	$C_w = 0.15$	$C_{dt1} = 20.0$	$C_{dt2} = 3.0$	

Equations 2.13 and 2.14 are solved through the whole domain regardless if it is a URANS or LES region. It is the local and instantaneous value of $\tilde{l}$ that regulates if the k and ω equations will be solved in URANS or LES mode. Moreover, is the definition of the universal length-scale $\tilde{l}$ that makes the distinction between the different detached-eddy simulation approaches. SIDDES will be mainly used in this analysis, but for completeness and a better understanding of the model, the different definitions of $\tilde{l}$ will be explained.

The universal lengthscale is a function of the URANS and LES lengthscales, which are defined as

$$l_{RANS} = \frac{\sqrt{k}}{\beta_* \omega} \tag{2.17}$$

$$l_{LES} = C_{DES}\Delta \tag{2.18}$$

((Travin *et al.*, 2002) and (Spalart *et al.*, 1997) respectively). Additionally

$$C_{DES} = (1 - F_1)C_{k-\varepsilon} + F_1 C_{k-\omega} \tag{2.19}$$

where β_* and F_1 are the mentioned model constant and blending function from $k-\omega$ SST, $\Delta = \max(\Delta_x,\, \Delta_y,\, \Delta_z)$ is the filter width, $C_{k-\varepsilon} = 0.61$, and $C_{k-\omega} = 0.78$ (Travin *et al.*, 2002). The lengthscale describes the relative size of the modelled turbulence; hence l_{RANS} represents the eddies at a macroscale level, while l_{LES} refers to the grid size turbulence. In the same manner, the k and ω parameters represent different turbulent characteristics depending on the region, i.e. k in the URANS region defines the mean turbulent kinetic energy content of the flow, while in the LES region it refers only to the subgrid turbulent kinetic energy.

The transition between URANS and LES regions is then simply determined by the universal or hybrid lengthscale function. In the case of the standard DES approach, it is defined as

$$\tilde{l}_{DES} = \min(l_{RANS}, l_{LES}) \tag{2.20}$$

DES will behave as a URANS model close to the wall, where the l_{RANS} is generally smaller than l_{LES}. And so it will switch to LES mode far away from the wall, or in regions where the grid cells are refined (because the value of l_{LES} becomes small). On the other hand, the DDES switch is more complex since an empirical shielding function f_d was introduced to correct for the GIS (Spalart *et al.*, 2006). Thus,

$$\tilde{l}_{DDES} = l_{RANS} - f_d \max(0, l_{RANS} - l_{LES}) \tag{2.21}$$

(See Appendix II for a detail definition of f_d). The f_d value approaches 0.0 in the near-wall region up to the logarithmic part of the boundary layer (when $r_d = 1.0$), and $f_d = 1.0$ in the LES region (when $r_d \ll 1.0$) (Spalart *et al.*, 2006). Additionally f_d is a continuous function, therefore the transition between the LES and URANS region is smooth (contrary to the DES switch). This means that DDES can present URANS regions, LES regions, and a zone where a blend of URANS and LES mode is being solved, comparable to an under resolved LES. Likewise the IDDES lengthscale is defined as

$$\tilde{l}_{IDDES} = \tilde{f}_d\,(1 + f_e)\, l_{RANS} + (1 - \tilde{f}_d) l_{LES} \tag{2.22}$$

where $\tilde{f}_d$ is an empirical delay function similar to f_d, and f_e is introduced to diminish the RANS Reynolds stresses close to the wall (Shur *et al.*, 2008) (Expressions given on Appendix II). The function $\tilde{f}_d$ and f_e together with a redefinition of the filter width $\Delta_{IDDES} = \min[\max(C_w d_w, C_w h_{max}, h_{wn}), h_{max}]$ correct for the LLM (Shur *et al.*, 2008). Here, h_{max} is the maximum edge length of the cell, d_w is the distance to the nearest wall, h_{hw} is the grid step normal to the wall, and $C_w = 0.15$ (Shur *et al.*, 2008). Finally $f_e = 0$ for the definition of the universal lengthscale for the SIDDES.

Altogether the SIDDES lengthscale is given by

$$\tilde{l}_{SIDDES} = \tilde{f}_d\, l_{RANS} + (1 - \tilde{f}_d) l_{LES} \tag{2.23}$$

and

$$\begin{aligned}
\tilde{f}_d =& \max[(1.0 - f_{dt}), f_b], \\
f_{dt} =& 1.0 - \tanh\left[(c_{d1} r_{dt})^{c_{d2}}\right], \\
r_{dt} =& \frac{\nu_t}{\kappa^2 d_w^2 \sqrt{0.5(\mathcal{S}^2 + \Omega^2)}}, \\
f_b =& \min[2.0\, e^{-9.0\alpha^2}, 1.0], \\
\alpha =& 0.25 - d_w / h_{max}.
\end{aligned} \tag{2.24}$$

Here $\mathcal{S}$ and Ω are the magnitude of the strain rate tensor and the magnitude of the vorticity tensor respectively (Gritskevich *et al.*, 2012). $r_{dt} \ll 1.0$ on simulations with turbulent content, so f_{dt} is approximately 1.0 far from the wall; while $r_{dt} \sim 1.0$ in the logarithmic part of the boundary layer making $f_{dt} \sim 0.0$. On the other hand, f_b only depends on the mesh parameters and it has an extremely small value away from the wall (Shur *et al.*, 2008). Lastly $\tilde{f}_d = 1.0$ in the near-wall region solving the equations in URANS mode, and $\tilde{f}_d \sim 0.0$ as it transitions to an LES zone away from the surface. The behaviour of these blending functions is displayed in Figure 2.2 for an idealized ABL case described in Section 4.2.

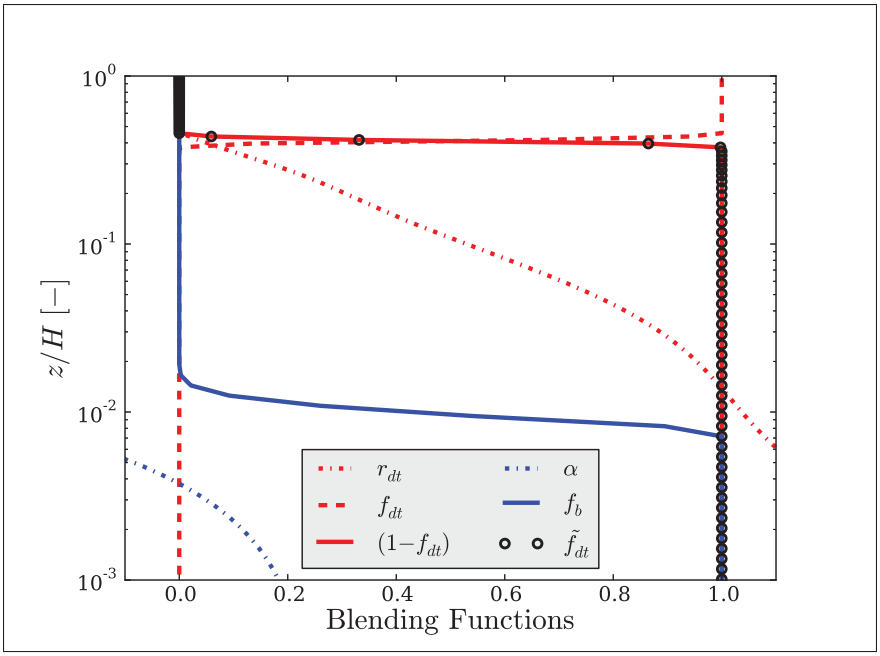

Figure 2.2 Value of the SIDDES blending functions for an ideal ABL case with $z_0 = 0.4$ m. Results shown correspond to instantaneous values at the centre line of the domain.

The original $k-\omega$ SST constants are calibrated for aerodynamic flows. These values are used only for the decaying isotropic turbulence and channel test flow cases in this thesis. Yet the $k-\omega$ SST constants have also been optimized for atmospheric flow based on purely RANS cases (Boudreault, 2011). Whereas the SIDDES constants have only been calibrated for the $k-\omega$ SST model with aerodynamic flows (Gritskevich *et al.*, 2012). A verification of the SIDDES constants will be performed for atmospheric flows on Section 4.2. The model constants used are summarized in Table 2.1.

2.2.1.1 Roughness extension and meshing

For smooth surfaces, the $k-\omega$ SST model is capable of resolving down through the viscous sublayer without the need of imposing a wall damping function. Studies with a similar hybrid model have shown that this technique yields consistently better results than if a wall function is used (Mockett *et al.*, 2012). If the wall is not smooth, the roughness has a significant effect on the whole boundary layer because the mass transport, the velocity, and the turbulence

characteristics in the near-wall region are altered (Patel, 1998). Most turbulence models, like the RANS $k-\varepsilon$, require certain modifications or extra terms inserted into the original equations, or the use of wall functions to properly deal with surface roughness. On the contrary, the $k-\omega$ SST model is capable of accurately describe the effect of a rough surface without any modifications to the original equations (Patel and Yoon, 1996).

The roughness effect for the $k-\omega$ SST model is simply taken into account through the wall boundary conditions. Thus, in this analysis the values of k_w and ω_w are based on the roughness extension proposed by Knopp *et al.* (2009). This roughness extension yields successful results for smooth ($k_s^+ < 2.25$), transitional ($2.25 \leq k_s^+ < 90$) and rough ($k_s^+ \geq 90$) surfaces (Blocken *et al.*, 2007). Here k_s represents the equivalent sand grain roughness height, thus, $k_s^+ = k_s u_*/\nu$.

The turbulent kinetic energy at the wall for any type of surface is then specified by

$$k_w = \phi_{r1} k_{rough} \tag{2.25}$$

where

$$\phi_{r1} = \min\left(1, \frac{k_s^+}{90}\right), \qquad k_{rough} \equiv \frac{u_*^2}{\sqrt{\beta_*}}. \tag{2.26}$$

Also u_* represents the friction velocity which is calculated based on the streamwise velocity gradient normal to the surface, therefore $u_* = (\nu + \nu_t)(\partial u/\partial n)$ (Knopp *et al.*, 2009). In a similar manner, the specific dissipation rate at the wall is

$$\omega_w = \min\left(\frac{u_*}{\sqrt{\beta_*}\kappa\ \tilde{z}_0}, \frac{60\nu}{\beta_1 z_1^2}\right). \tag{2.27}$$

Here, $\tilde{z}_0 = \phi_{r2} 0.03 k_s$, and z_1 denotes the distance between the wall and the centre of the first cell (Knopp *et al.*, 2009). Finally the blending function ϕ_{r2} is given by

$$\phi_{r2} = \min\left[1, \left(\frac{k_s^+}{30}\right)^{\frac{2}{3}}\right] \min\left[1, \left(\frac{k_s^+}{45}\right)^{\frac{1}{3}}\right] \min\left[1, \left(\frac{k_s^+}{60}\right)^{\frac{1}{4}}\right]. \tag{2.28}$$

The sand grain roughness is a measure of the surface roughness elements. For example as illustrated in Figure 2.3, k_s represents the diameter of roughness spheres packed closely together. This is an ideal representation of roughness, but in reality this is hardly the case and numerous surfaces types are possible. For this reason other definitions of roughness exists and the equivalence to the sand grain roughness has to be assigned. The surface roughness for atmospheric flow simulations is in general specified by z_0, the aerodynamic roughness height. The value of z_0 does not represent the actual or physical height of the roughness elements, it simply indicates at what height the logarithmic profile vanishes, and consequently the position of the coordinate system origin $z = 0$ (Schlichting and Gersten, 2000). This can also be seen in Figure 2.3. The relation between the aerodynamic and the equivalent sand grain roughness height can be approximated as (Blocken *et al.*, 2007)

$$z_0 = 0.03\, k_{s,\,ABL}. \tag{2.29}$$

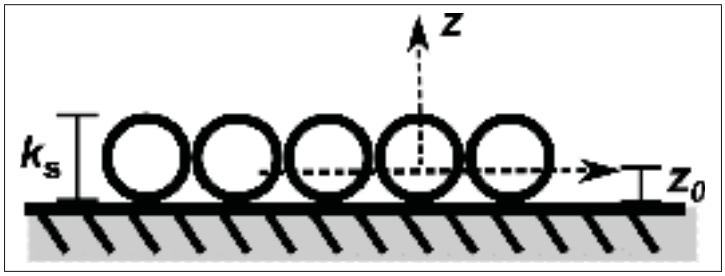

Figure 2.3 Surface roughness height illustration. k_s is the sand grain roughness and z_0 the aerodynamic roughness. Not to scale.

The value of z_0 can vary from approximately 0.00001 m on icy or muddy terrain to around 0.5 m for forest regions (Manwell *et al.*, 2002), then $k^+_{s,\,ABL} \gg 90$. Since the atmospheric flow is always considered in the fully rough turbulent regime (Blocken *et al.*, 2007), the roughness extension can be simplified to

$$k_{w,\,ABL} = \frac{u_*^2}{\sqrt{\beta_*}}, \qquad \omega_{w,\,ABL} = \frac{u_*}{\sqrt{\beta_*}\kappa\, z_0}. \tag{2.30}$$

It is true that these boundary values assume a logarithmic velocity profile, thus they are in fact based on flat terrain assumptions. However contrary to most common wall functions, k_w and ω_w will only constrain the eddy-viscosity value required to solve the momentum equation at the wall, they will not impose the wall velocity (or shear stress). Additionally, k_w and ω_w are calculated based on the local and instantaneous u_*. This allows the better representation of the unsteady local flow behaviour. Therefore, the $k-\omega$ SST-SIDDES wall treatment might be less dependent on flat terrain assumptions than most commonly used wall functions.

As previously mentioned, the use of wall functions can be avoided for the $k-\omega$ SST model, nevertheless it has been shown that a fine vertical grid refinement is needed for accurate results. The employed roughness extension requires the first cell centre to be located at a non-dimensional distance of $z_1^+ = u_* z_1/\nu \approx 0.3$ regardless of the roughness (Knopp *et al.*, 2009). This may represent a major drawback of the turbulence model, especially for high Reynolds number flows, since extremely fine meshes are needed. Furthermore within the current computational limitations, this demanding vertical grid refinement together with the relatively large simulation domains required to include the most energetic ABL eddies will most probably yield near-wall cells with a rather big aspect ratio. Complex topography meshes might represent a rather important challenge.

The modelling of a rough surface requires special attention. The flow behaviour computed at heights below the equivalent sand grain roughness is not entirely realistic (Patel, 1998). Therefore the simulations results for regions were $z^+ < k_s^+$ are not meaningful and should be neglected. For wind blowing over a rough surface of $z_0 = 0.4$ m, the value of the sand grain roughness corresponds to $k_s^+ \approx 10^5$. Then if the roughness extension mesh requirements are met, $z_1^+ \ll k_s^+$. This type of mesh can be considered a waste of computer resources since a rather large number of grid cells within the roughness height have to be computed and they give no relevant information about the physics of the flow. Nevertheless, the $k-\omega$ SST rough surface treatment does not rely on a wall function which may fail on complex and separated flows. Consequently, this RANS turbulence model (or any hybrid model based on it) may be

more appropriate for modelling complex flows (Patel, 1998) and a good candidates to simulate the ABL in complex terrain.

On the other hand, the atmospheric flow is an extreme case that has a high Reynolds number with a roughness height which is most likely always larger that the viscous scale $\delta_\nu = \nu/u_*$. In this situation, the drag caused by the rough surface is mainly due to pressure forces and not due to viscous stresses (Pope, 2000). Thus the viscosity should not be relevant when defining the height of the first node for high Reynolds flows. In wind energy simulations, it is a common practice to set the height of the first cell centre to at least the roughness height z_0 (Blocken *et al.*, 2007). In other words, z_1 is determined by a non-dimensional outer scale $\zeta_1^+ = z_1/z_0 \geq 1.0$. Following these mesh guideline makes the simulations considerably less computational demanding, but it does not satisfy the roughness extension requirements. For example, a z_1 computed based on an outer scale will correspond to an inner scale value of $z_1^+ \approx 10^4$ for ABL flows (assuming $z_0 = 0.4$ m). Some other examples are given in Table 2.2. The impact that the value of z_1 has on the simulations results will be analyzed in more detail for ABL flows in Section 4.2.1 (Figure 4.9).

Table 2.2 Examples of z_1 values

Definition of z_1 based on:	$z_0\,[\mathrm{m}]$	$z_1\,[\mathrm{m}]$
$z_1^+ = u_* z_1/\nu = 1$ ($u_* = 0.3880$ m/s and $\nu = 1.5 \cdot 10^{-5}$ m^2/s)	0.0002	$3.8 \cdot 10^{-5}$
	0.03	$3.8 \cdot 10^{-5}$
	0.4	$3.8 \cdot 10^{-5}$
$\zeta_1^+ = z_1/z_0 = 1$	0.0002	0.0002
	0.03	0.03
	0.4	0.4

2.3 Summary and subsequent tasks

The basic concepts of CFD have been explained within the OpenFOAM framework and within the microscale atmospheric modelling context. Furthermore, a hybrid model to undertake microscale simulations has been proposed and described in detail. The $k-\omega$ SST-SIDDES hy-

brid model is considered a good candidate for microscale simulations for the atmospheric flow because of two main reasons: its particular wall treatment is less dependent on flat terrain assumptions, and it could provide a good compromise between the higher accuracy and lower computer cost.

The $k-\omega$ SST model has rarely been used to model the ABL at a microscale level; while the SIDDES technique have never been utilized outside of aerodynamic flow studies. The possibility of avoiding the standard wall functions and the simpler roughness treatment provided by the $k-\omega$ SST, together with the LLM correction and probable computing time reduction (compared to a standard LES) offered by the SIDDES make this hybrid model a potential candidate for ABL simulations. To this end, a rigorous validation of the proposed hybrid model is performed using some well-known canonical flows. This process will yield valuable information about the advantages and inherent limitations of the turbulence model, as well as to explain certain modelling concepts often overlook in the literature. Consequently, the model validation will set solid bases to understand the flow behaviour computed by atmospheric simulations.

CHAPTER 3

TURBULENCE MODEL VALIDATION ON CANONICAL FLOWS

The $k-\omega$ SST-SIDDES model is carefully validated on canonical flows in this chapter. First, the LES behaviour of this hybrid turbulence model is compared against a well validated DNS of decaying turbulence. The objective is to test if the model can reproduce the transfer of energy between the different turbulent scales. Then, a homogeneous shear flow was simulated to study how the model behaves in the presence of rotation and mean shear. Finally, the half channel flow is analyzed to investigate the URANS and LES behaviour due to the presence of a wall. Additionally, the half channel test cases are analyzed for rather high Reynolds and extremely rough surfaces such as the ones required in atmospheric flows.

3.1 Decaying isotropic turbulence flow

Decaying isotropic turbulence (DIT) is the most simple and fundamental turbulent flow[1]. It is an unbounded flow characterized by the absence of mean velocity gradients, so there is no turbulence production or shear stresses. As a result, the turbulence merely decays over time. The time evolution of the total turbulent kinetic energy (i.e. filtered plus modelled) is simply equal to the total dissipation, thus

$$\frac{dk_{\text{total}}}{dt} = -\varepsilon_{\text{total}}. \tag{3.1}$$

Decaying isotropic turbulence is an ideal and theoretical flow, but it can be fairly well approximated by a grid turbulence experiment (Comte-Bellot and Corrsin, 1971). This experiment consist of a flow with a streamwise velocity U_0 which encounters a grid. Behind this grid, on the laboratory frame the turbulence decays in x, the direction of the flow. However, on an inertial frame moving at U_0 the turbulence statistics evolve over time as $t = x/U_0$ (Pope, 2000). Based on the Taylor hypothesis the time-evolving velocity fluctuations of a DIT can

[1] In the literature it is sometimes referred as homogeneous isotropic turbulence (HIT) (Sagaut and Cambon, 2008).

be interpreted as a frozen flow field advected by the uniform steady flow of the experiment. Mathematically this means (Sagaut and Cambon, 2008)

$$[u(x,t)]_{DIT} = [u(x - U_0 t, 0)]_{Exp}. \tag{3.2}$$

The decaying turbulence processes are not completely understood, nevertheless this flow has been studied extensively and it is well documented. Numerically, DIT is used as benchmark to test the transfer of kinetic energy between the different turbulent scales in LES models, as well as in the LES mode of a hybrid model. A DIT case modelled using a DES approach should not present any URANS regions since there are no solid surfaces. Therefore all the DES approaches should have $\tilde{l} = l_{LES}$ and compute identical results. However to properly model a DIT case using IDDES and SIDDES, the LES mode has to be enforced. The reason for this is that the definition of the Δ_{IDDES} is based on a distance to a non existing surface. In this case, OpenFOAM erroneously yields $\Delta_{IDDES} = C_w h_{\max}$, underestimating the lengthscale. To force the LES mode in the DIT case, the value of the constant C_w was set to a high enough value that will trigger the correct filter width (i.e. $\Delta_{IDDES} = h_{\max}$) and consequently the proper lengthscale.

Most importantly the DIT flow case is crucial to calibrate the model constant $C_{DES} = C_{DES}(C_{k-\varepsilon}, C_{k-\omega})$ within the specific numerical framework (i.e. interpolation schemes, software, etc.) (Bunge *et al.*, 2007). The $k-\omega$ SST-DES has been calibrated previously for a different numerical framework (Travin *et al.*, 2002), thus those constants were taken as a initial reference to calibrate the proposed model implementation in OpenFOAM (refer to SIDDES constants in Table I-1). Those constants will be adjusted later if needed.

The LES mode of the $k-\omega$ SST-DES and $k-\omega$ SST-SIDDES will be validated against the well-known Comte-Bellot and Corrsin's grid turbulence experiments at a Reynolds number of $Re_\lambda = u_{rms}\lambda/\nu \approx 70$ (Comte-Bellot and Corrsin, 1971), and against Wray's DNS results at

$Re_\lambda \approx 945 - 58$ (Jimenez J. (Ed.), 1997). The Taylor microscale is defined as

$$\lambda = 15\nu u_{rms}^2/\varepsilon_{\text{total}}, \tag{3.3}$$

where u_{rms} is the rms velocity, and the total dissipation $\varepsilon_{\text{total}}$ is the sum of the filtered $\overline{\varepsilon}$ and subgrid ε contributions. The simulations were performed in a cubic domain of size $\mathcal{L} = 2\pi$ and periodic boundaries. The transport and turbulence model equations were discretized using a second-order central interpolation scheme for the divergence terms (unless otherwise noticed), while a backward second-order implicit scheme was used for the time derivative term. The pressure-implicit split-operator (PISO) algorithm was used for the velocity-pressure coupling (Issa, 1985). A maximum Courant-Friedrichs-Lewy (CFL) number of 0.1 and the aerodynamic constants from Table I-1 were imposed.

Starting the simulation with a realistic turbulent field prove to be extremely crucial. For this reason the velocity field was initialized using the DNS data set provided by A. Wray in the AGARD database (Jimenez J. (Ed.), 1997) for a 128^3 mesh with a $Re_\lambda \sim 104$. This field was projected on physical space for the coarser meshes. Unfortunately, at those Re_λ the inertial range slope of $-5/3$ is not distinguished as clearly as it does for higher Reynolds number. To generate the proper initial fields for k, ω and specially ν_t, a simulation of the "frozen" initial velocity field was carried out following the work of Bunge *et al.* (2007). This computation solves only the steady turbulence model equations without solving for the velocity and pressure. The converged simulation yields the initial fields of all the variables which are consistent with the given velocity field. The "frozen" turbulence technique is not needed for other models like Smagorinsky because the ν_t field is calculated directly from the velocity field, but this is not the case for the DES approaches. Finally, this robust initial turbulent field is let to decay freely. Figure 3.1 depicts the time evolution of the vorticity field.

The total turbulent kinetic energy k_{total} should decay as a power-law in the DIT case. Hence,

$$k_{\text{total}}(t) = k_0 \left(\frac{t}{t_0}\right)^{-n}. \tag{3.4}$$

(a) $t^* = 0.0$ (b) $t^* = 2.0$ (c) $t^* = 5.0$

Figure 3.1 Vorticity contours at different non-dimensional times for the DIT 64^3 case. The contour levels are the same in all figures and are colour by the magnitude of the velocity (Units: [m/s]).

Consequently, the dissipation should behave as $\varepsilon_{\text{total}} \sim t^{-(n+1)}$ and the integral scale as $L \sim t^{(1+n/2)}$ (Pope, 2000). The turbulent nonlinear effects are more predominant when Re_λ is high, as Re_λ decreases the inertial effects become negligible and the viscous linear effects dominate. For this reason, two different decaying regimes could be distinguished (Sagaut and Cambon, 2008). For the first regime, the decay coefficient measured by several experiments falls in the range of $6/5 \leq n \leq 4/3$ (Sagaut and Cambon, 2008), while simulations have yield $n = 1.25$ (Kang *et al.*, 2003). On the other hand the decay rate for the second regime increases up to $n \sim 2.0 - 2.5$ (Sagaut and Cambon, 2008; Pope, 2000). To this day, it is still extremely difficult to achieve the second regime in experiments and in simulations due to the extremely low Reynolds numbers involved (Sagaut and Cambon, 2008). Therefore no much details about this second regime are available in the literature. Hence, this validation test will only focus on the first decay regime.

Figure 3.2 gives the turbulent kinetic energy decay. The results show a volume average, hence $k_{total} = \sum_i (k_{total,\,i} * \Delta \mathrm{v}_i)/V_{total}$. The decaying rate is practically the same for DES and SID-DES as expected, and consistent with the Smagorinsky model. Additionally, the calculated value of n is approximately 1.25 using a 32^3 mesh, which agrees with the literature and with the DNS data also provided in the AGARD database (Jimenez J. (Ed.), 1997). Simulations with 128^3 cells and 64^3 cells yield consistent results as Figure 3.3 demonstrates. A decay exponent

of $n \approx 1.25$ was also obtained for the dissipation and integral scale power-law decays. In Figure 3.4a, the volume average of the dissipation was calculated based on $\varepsilon_{\text{total}} = -\Delta k_{\text{total}}/\Delta t$.

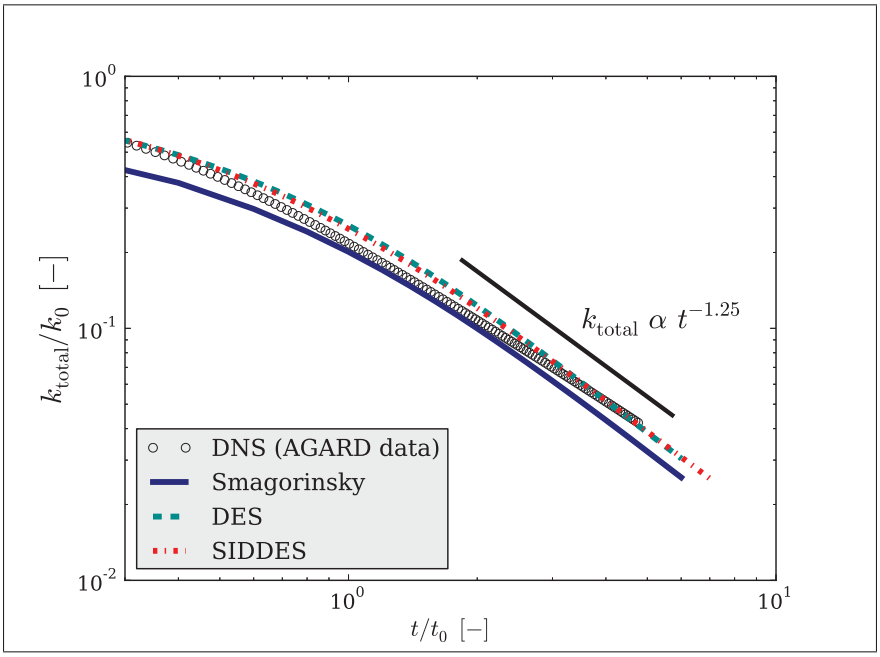

Figure 3.2 Turbulent kinetic energy decay over time employing different turbulence models with 32^3 cells. The total kinetic energy k_{total} is the sum of the turbulent kinetic energy from the filtered resolved scales $\overline{k}$ plus the modelled k for the hybrid models. Smagorinsky results are shown for reference, but only the $\overline{k}$ is plotted.

The integral scale time evolution shown in Figure 3.4b, the results were computed using the velocity two-point correlations $R_{ij}(\mathbf{r},\, \mathbf{x},\, t) = \langle u_i(\mathbf{x}, t) u_j(\mathbf{x} + \mathbf{r}, t) \rangle$. For homogeneous turbulence the two-point correlation function does not depend on the position $\mathbf{x}$; thus the integral lengthscale is calculated as

$$L_{ij,\,k}(t) = \frac{1}{R_{ij}(0,\, t)} \int_0^\infty R_{ij}(\mathbf{e_k} r_k,\, t)\, \mathrm{d}r_k. \tag{3.5}$$

where $\mathbf{e_k}$ is the unit vector in the x_k direction (Pope, 2000). The notation $L_{ij,\,k}(t)$ represents the lengthscale calculated based on the one-dimensional two-point correlation function be-

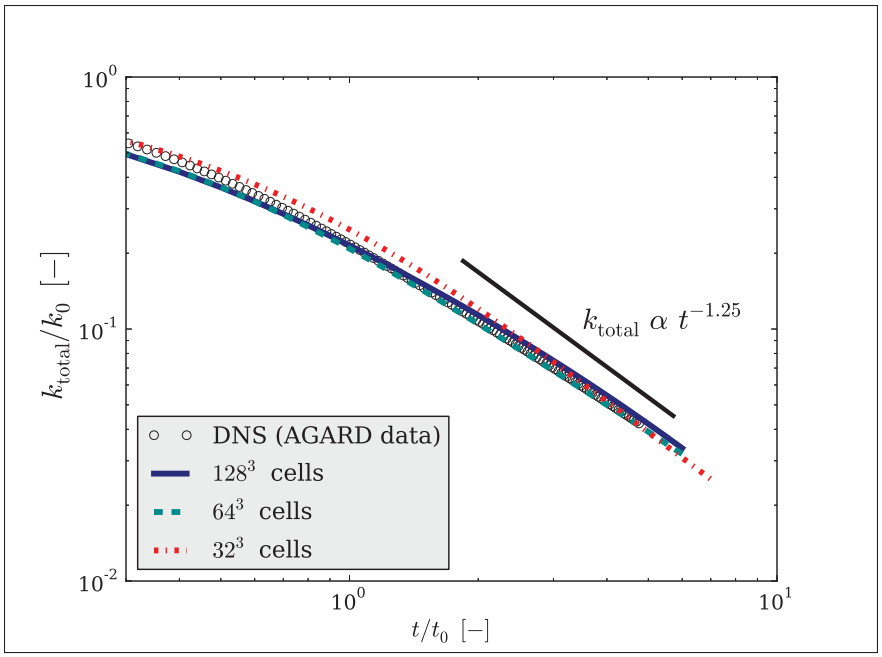

Figure 3.3 Turbulent kinetic energy decay for different meshes using SIDDES

tween the u_i and u_j velocity component in x_k direction. Since integrating to infinity might not be practically possible, the two-point correlation function is integrated just to the first zero crossing (Kaimal and Finnigan, 1994).

The turbulence energy spectrum represents the amount of energy contained by the different turbulent scales. It depicts the energy cascade process and how the energy from the large structures (or small wavenumber κ) is transfer to the smaller scales (large κ). Three dimensional spectra are in practice difficult to measure; most of the time experiments only gather data along one direction. Therefore one-dimensional spectra are computed directly from the measured data. A one-dimension spectra is defined as twice the Fourier transform of the two-point correlation function (Pope, 2000), hence

$$E_{ij}(\kappa_k,\, t) = \frac{1}{\pi}\int_{-\infty}^{\infty} R_{ij}(\mathbf{e_k} r_k,\, t) e^{-i\kappa_k r_k} \mathrm{d}r_k. \tag{3.6}$$

The notation $E_{ii}(\kappa_k)$ represents the one-dimensional spectrum of the u_i velocity component computed on the x_k direction. The largest eddies that can be resolved with a domain size of $\mathcal{L}$

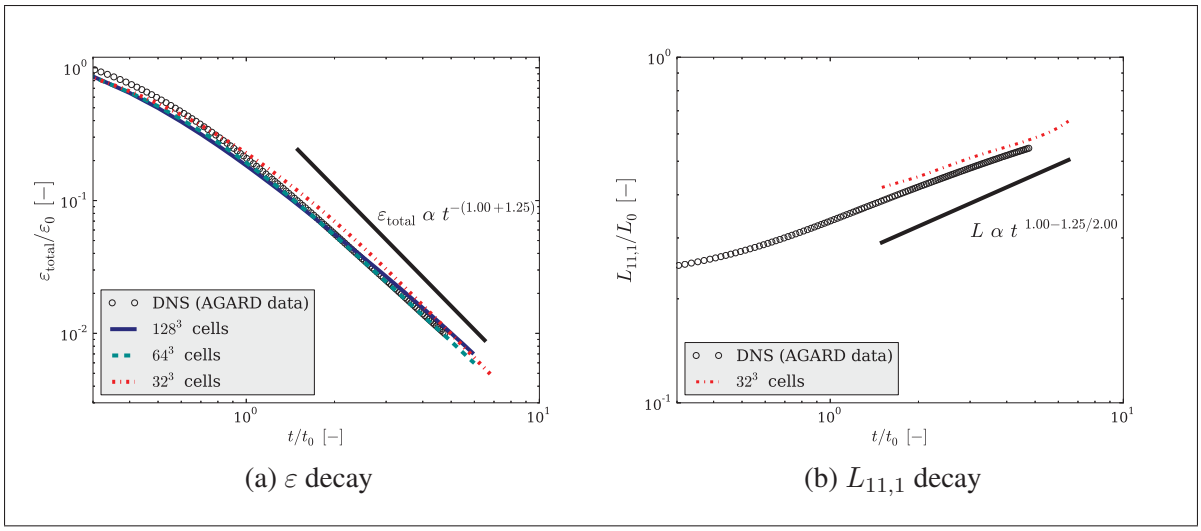

(a) ε decay (b) $L_{11,1}$ decay

Figure 3.4 Time evolution using $k-\omega$ SST-SIDDES compared against the results provided in the AGARD database (Jimenez J. (Ed.), 1997).

have a wavenumber of $\kappa_{min} = 2\pi/\mathcal{L}$. On the other hand, the smallest eddies that can be theoretically resolved depend on the grid resolution Δ and the Nyquist theorem; hence $\kappa_{max} = \pi/\Delta$. Figure 3.5 shows the one-dimensional spectra computed with the $k-\omega$ SST-SIDDES model compared to the DNS one-dimensional spectra computed by Wray. The hybrid model spectra are estimated based on the Welch method (Welch, 1967). The hybrid model reproduces fairly well the spectrum slope in the inertial range, as well as the time evolution of such energy spectra. However it can be seen that the non-dimensional longitudinal spectra $E^*_{11}(\kappa^*_1)$ do not perfectly match the DNS results at smaller wavenumbers. This discrepancy diminishes over time. A small cusp is visible at high wavenumbers, this phenomenon is well known for eddy viscosity models (Lesieur and Métais, 1996). Additionally in Figure 3.6 it can be observed that $E^*_{ii}(\kappa^*_i) \approx 3/4\, E^*_{jj}(\kappa^*_i)$ as expected for the inertial range dynamics of an isotropic turbulent field (Pope, 2000).

The spectra normalized by the Kolmogorov scale η are given in Figure 3.7. The non-dimensional longitudinal energy spectra from the hybrid model computations compare well with the grid turbulence experiments and DNS results. As expected the $k-\omega$ SST-DES and $k-\omega$ SST-SIDDES results are equivalent. The mentioned small cusp is visible at high

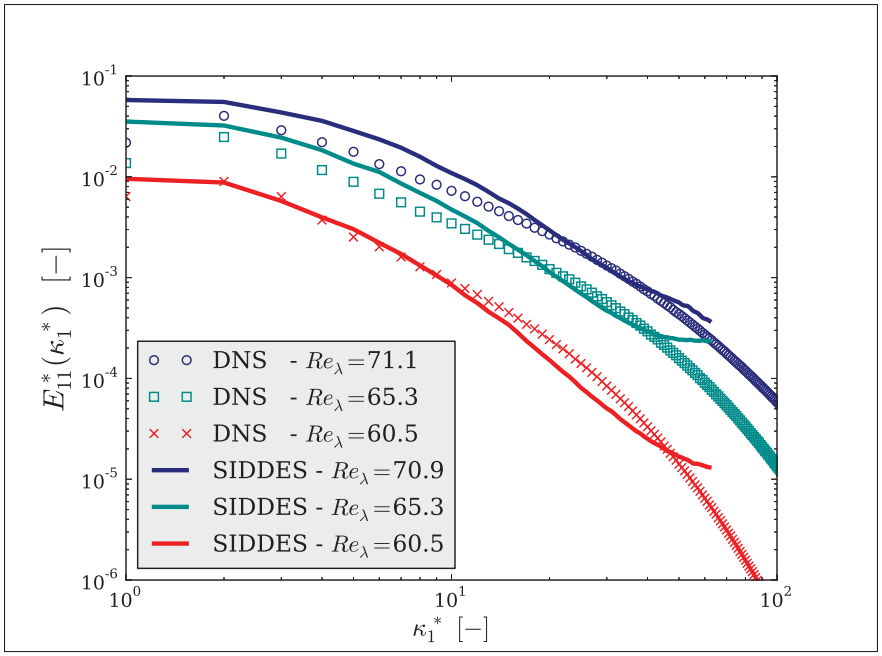

Figure 3.5 Non-dimensional longitudinal energy spectra. The DNS spectra computed by Wray (Jimenez J. (Ed.), 1997) is compared against the $k-\omega$ SST-SIDDES results from the 128^3 mesh.

wavenumbers, but it can be seen that all spectra collapse at the smaller scales. This results are in agreement with the assumption that the high wavenumber structures are universal (Pope, 2000).

Since the energy spectra and the turbulent kinetic energy decay results are in fairly good agreement with DNS and the theory, the C_{DES} model constant within this specific numerical framework does not require a calibration. The constant values from the literature will be used in this study. It is important to recall that this analysis is highly dependent on the discretization of the flow equations.

Discretization schemes are essential to accurately reproduced the turbulence characteristics. Therefore to conclude this validation case, the convective term discretization was analyzed. On average, the convective term is zero for the decaying isotropic turbulence case, however the local instantaneous convective terms are active. Figure 3.8 shows the longitudinal energy

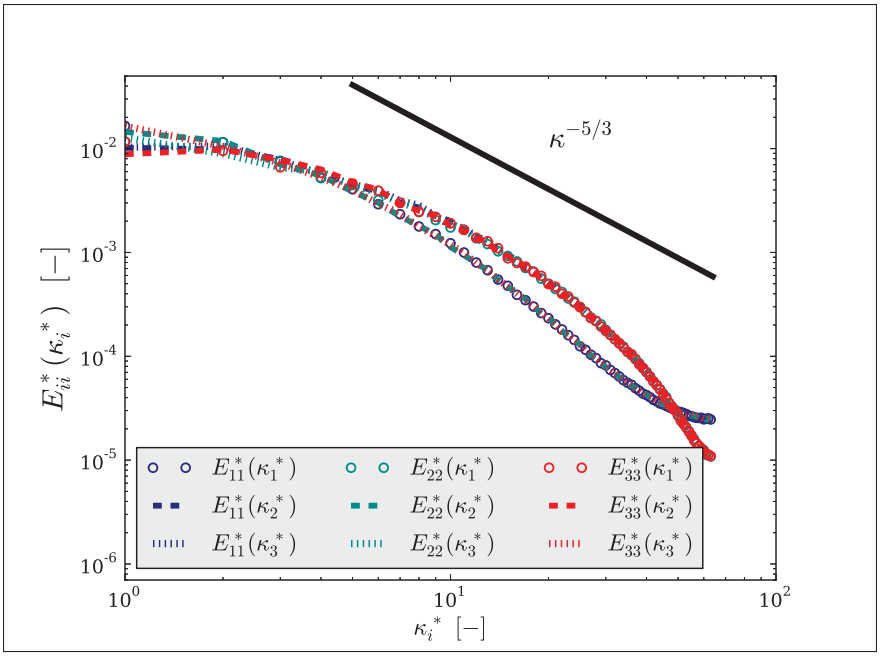

Figure 3.6 Non-dimensional one-point energy spectra of a DIT simulation using the $k-\omega$ SST-SIDDES model. The computation was carried out on a 128^3 grid. Results shown have a $Re_\lambda \approx 62$.

spectra from DIT simulations using several discretization schemes. The slope of the energy spectrum is reproduced correctly (except for the small cusp which is typical of eddy viscosity models) when second-order central schemes (*linear* using the OpenFOAM terminology) are used to discretized the convective terms of the momentum equation regardless of the schemes used for the turbulence model equations. In other words, the schemes used for the convective terms in the k and ω equations are apparently not as significant. Additionally, a mixed discretization scheme specific of OpenFOAM was also tested. This scheme called *filteredLinear* (hence FDS) introduces locally some upwind components to avoid unphysical oscillations (The OpenFOAM Foundation, 2013). The FDS is slightly more dissipative than pure central. It can also be seen in the same figure, that using a QUICK scheme (Ferziger and Perić, 2002) or a first-order upwind scheme results in a spectrum which decays more rapidly and its inertial range slope is not correct. Based on these findings, central schemes should be used with the hybrid model.

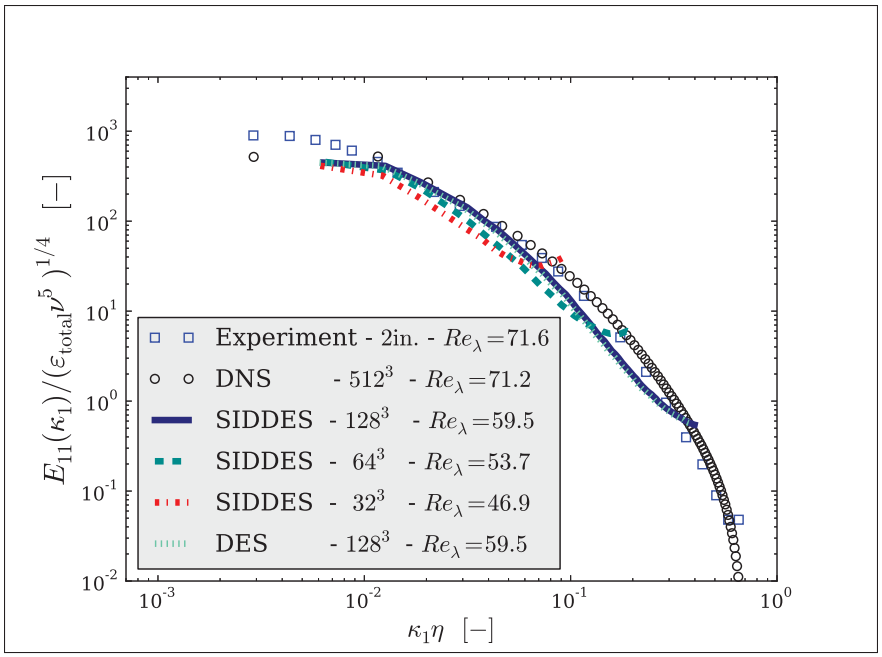

Figure 3.7 One-dimensional energy spectra for different mesh resolutions compared against experimental data (Comte-Bellot and Corrsin, 1971) and DNS (Jimenez J. (Ed.), 1997).

The DIT test case only has a LES region, but more complex cases will include a URANS region. In terms of discretization schemes, URANS and LES have different requirements. RANS simulations are more stable if an upwind discretization scheme is used, but for LES, the numerical dissipation introduced by these upwind schemes is excessive (Ferziger and Perić, 2002) (as shown previously). Thus the choice of discretization schemes is not simple for hybrid models when URANS and LES regions are present. However Figure 3.8 results indicate that FDS could be employed if a complex case simulation proves to be too unstable without affecting considerably the transfer of energy between the different turbulent scales. Alternatively, upwind schemes can be used only for the turbulence model equations. Another possibility is to define a blended scheme. This last option will be explained in more detail in Section 3.4 when URANS/LES regions are studied.

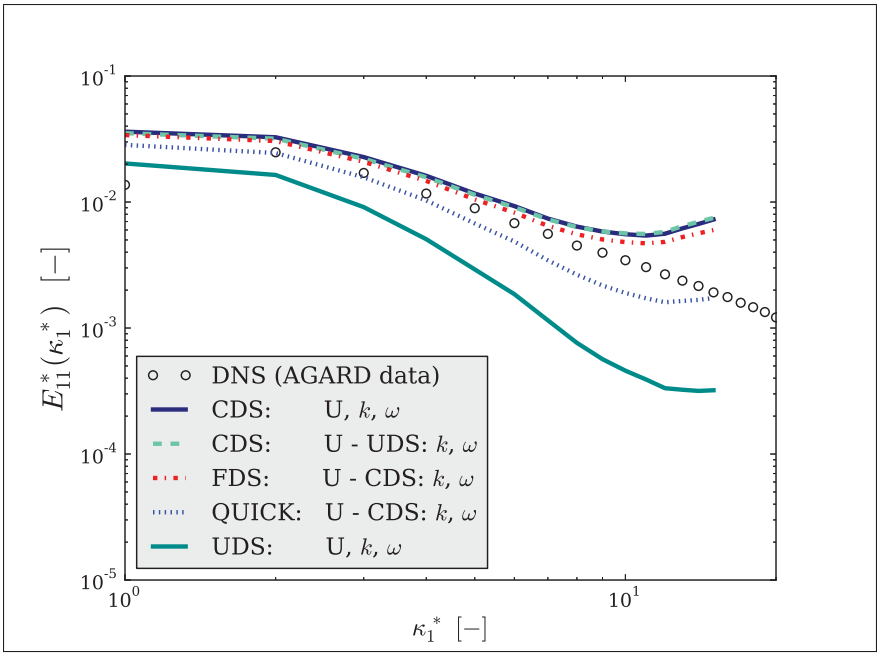

Figure 3.8 DIT one-dimensional spectra using SIDDES and 32^3 cells. Different discretization schemes are set for the convective terms in each of the equations. CDS: 2nd-order central, FDS: *filteredLinear* and UDS: 1st-order upwind. Results have $Re_\lambda \approx 65$ and were taken at the non-dimensional time $t^* = 0.5$.

3.2 Decaying turbulence with rotation effects

The presence of any external body force could have important effects on a turbulent flow. In the study of geophysical flows, the Earth's rotation produces an external acceleration that could play an important role in the dynamics of the turbulence. The aim of this validation case is to study the effects that rotation has on a turbulent flow, while at the same time test the proposed hybrid model behaviour under rotation.

In a non-inertial reference frame rotating with a constant angular velocity vector $\mathbf{\Omega}$, centrifugal and Coriolis forces are present. Normally, the centrifugal forces are combined with the pressure term in the momentum equations, hence p in Equation 2.12 represents $0.5\rho\,|(\mathbf{\Omega} \times \mathbf{r})|^2 + p_0$ when rotation is included (Bardina *et al.*, 1985). Regarding the Coriolis force, it is considered an external force. Then $\mathbf{F}_c = 2\mathbf{\Omega} \times \mathbf{u}$ in Equation 2.12. The Coriolis force adds no energy

to the turbulence, in other words, it produces no work. However, the energy is redistributed among the Reynolds stresses (Bardina *et al.*, 1985), which can increase the anisotropy of the turbulent structures and affect the energy cascade (Sagaut and Cambon, 2008). To study how the flow is distorted by rotation an initially isotropic turbulent field is subjected to different rotation rates and analyzed. This validation test case is known as homogeneous anisotropic turbulence (HAT) under pure rotation (Sagaut and Cambon, 2008).

The HAT in a rotating frame test case is setup in exactly the same manner as the DIT case from the previous section (i.e. domain size, mesh resolution, boundary conditions, initial field, numerical parameters, etc.). The only difference is that the Coriolis force $\mathbf{F}_c$ is added to the momentum equation. The Coriolis term is treated explicitly (See Appendix III.4 for code details) which enforces a small time step, especially when the rotational force dominates (Bartello *et al.*, 1994). It was observed that on fast rotating frames, simulations tend to become unstable and yield erroneous results even for CFL values of 0.1. For this reason a CFL$= 0.01$ was imposed. Different rotation rates around the vertical axes are studied, thus $\mathbf{\Omega} = (0, 0, w)$. This yields different Rossby numbers.

The Rossby number Ro_w is a non-dimensional quantity that describes the ratio between the inertial to the rotational forces. The rotational forces can be neglected when the Rossby number is large, and are relevant when the Rossby number is small. For the HAT cases, the Rossby number is calculated as

$$Ro_w = \frac{\kappa_p u_{rms}}{w} \tag{3.7}$$

where $\kappa_p = (\kappa_{max} - \kappa_{min})/2$ represents the energy containing wavenumber at the initial time as in the original reference (Yu *et al.*, 2005). Since the initial field used in the current simulations does not have a clear inertial range, the whole range of resolved scales was used to calculate k_p. As the turbulent field decays the u_{rms} value diminishes, thus the Rossby number also decreases. Throughout this section, the $Ro_{w,0}$ refers to the initial value Ro_w for each

simulation. Its it important to mention that the Rossby number Ro_L used for atmospheric flow cases is defined differently; it is based on the large scales (See Section 4.2.2).

As the Coriolis force does not generate energy, the initial unbounded isotropic turbulent field subjected to rotation will also decay. Nevertheless, the energy decay rate decreases as the $Ro_{w,0}$ increases (Bardina *et al.*, 1985). This can be seen in Figure 3.9. Simulations with initially isotropic turbulent fields that are subjected to the Earth's rotation rate do not show any significant difference from the freely DIT case ($Ro_{w,0} = \infty$). This effect is also negligible even when the inertial forces are fifty times greater that the rotational forces, $Ro_{w,0} = 50$. The simulations for an initial $Ro_{w,0} = 1$ start to become unstable; this is probably because the time step is not small enough as explained previously. To emphasize the effect that rotation has on the decay rate, the spectra for different angular velocities is given in Figure 3.10. As Yu *et al.* (2005), the rotation inhibits the energy cascade, and that energy tends to accumulate on the small wavenumbers as $Ro_{w,0}$ increases. Also, the $\kappa^{-5/3}$ is no longer followed; in other words, the turbulence is not described by the Kolmogorov theory.

Another important characteristic of the rotation effects on an isotropic field is the generation of anisotropic structures. This can be observed in Figure 3.11 where the different components of velocity are equal for high values of $Ro_{w,0}$, but are altered as $Ro_{w,0}$ decreases. This anisotropy can be better perceived in the integral lengthscales for the various velocity components. For instance, Figure 3.12 shows that for a case without rotation or with w_{Earth}, the lengthscales are $L_{ii,i} \approx 2L_{jj,i}$ ($i \neq j$) as expected for isotropic turbulent fields. This is no longer valid for the case with initial $Ro_{w,0} = 5$, where the lengthscales calculated along the rotation axis grow faster as observed by Bardina *et al.* (1983). This result show that the turbulent vortices are elongated along the axis of rotation (Godeferd, 2012) and the flow tends to become two-dimensional.

As expected, the results show that the Earth's angular velocity has a negligible effect on the dynamics of the turbulence for the HAT validation case. This is also valid for $Ro_{w,0} = 50$. As it will be explained later in Section 4.2.2, the large scale Rossby number Ro_L obtained

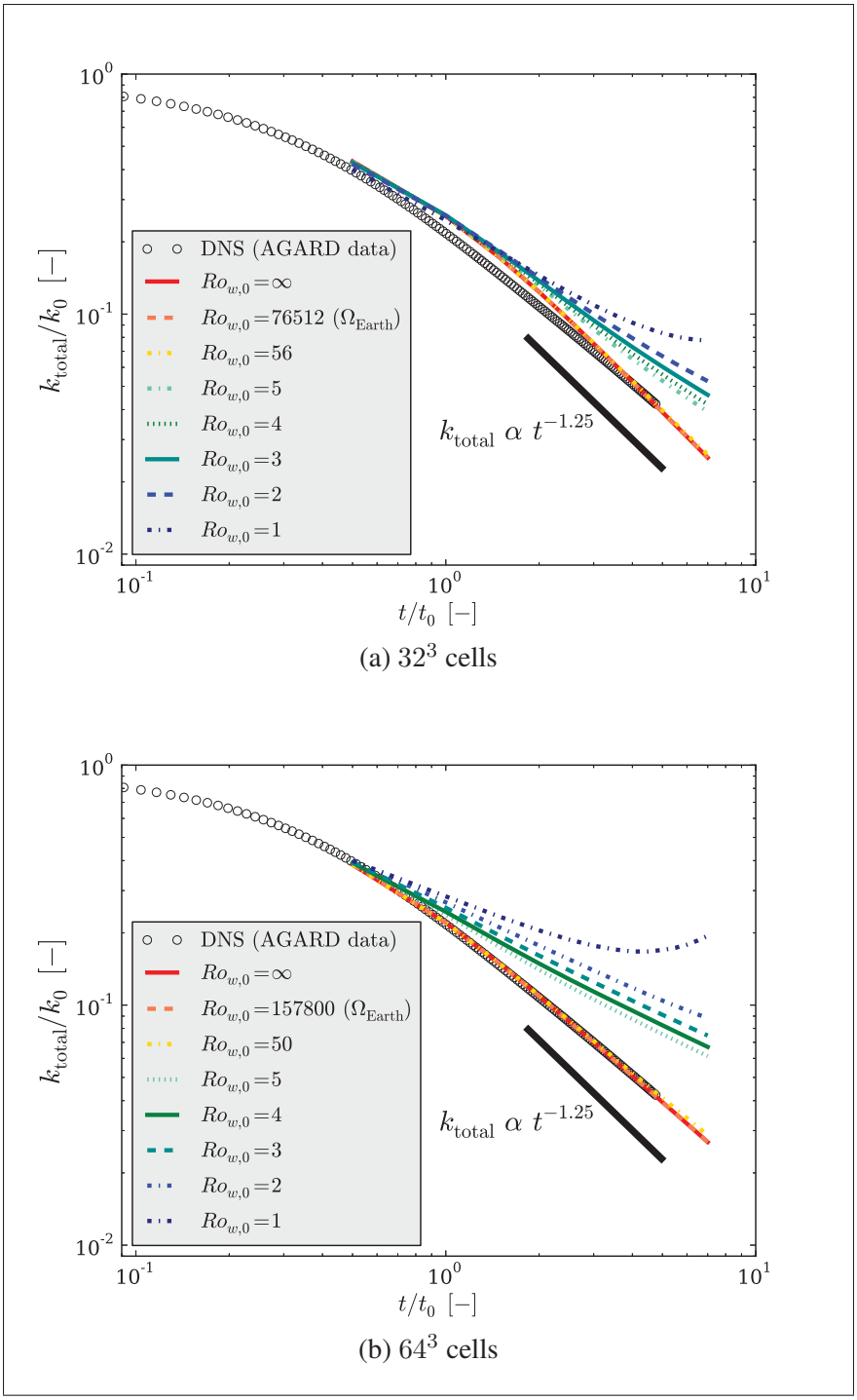

Figure 3.9 Total turbulent kinetic energy decay for different Rossby numbers $Ro_{w,0}$.

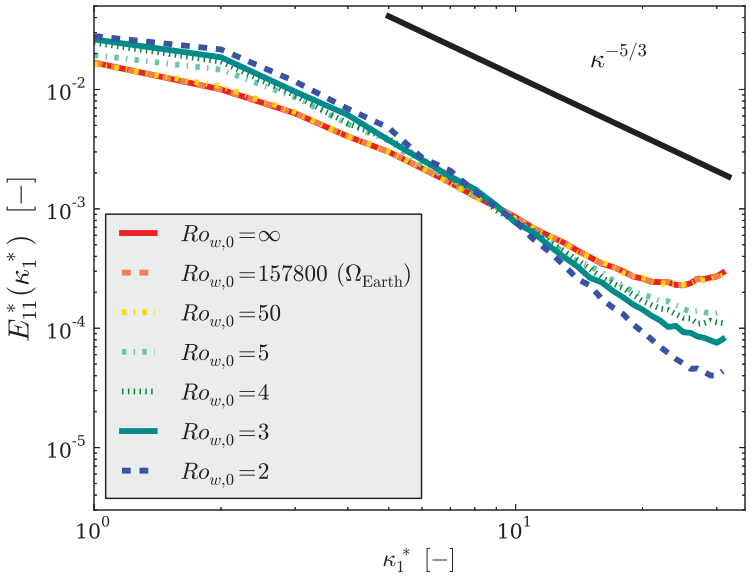

(a) Longitudinal spectra

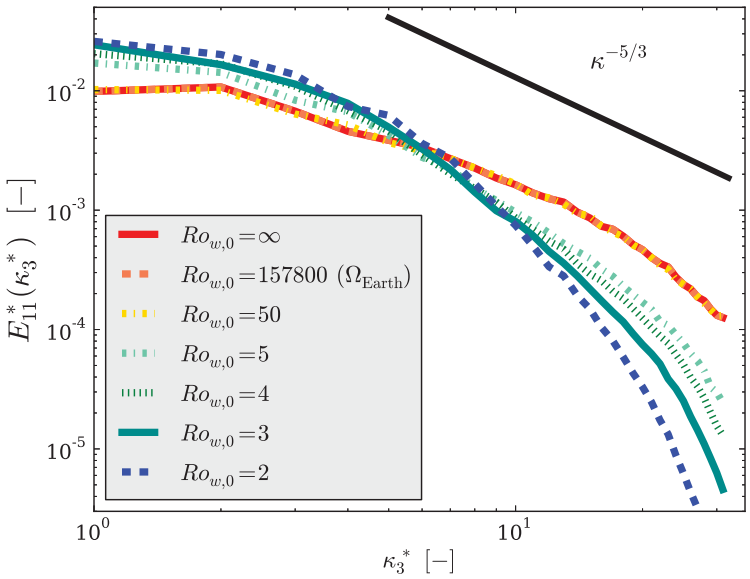

(b) Vertical spectra

Figure 3.10 One-dimensional energy spectra for different Rossby numbers taken at a non-dimensional time $t^* = 2.0$ for the 64^3 mesh.

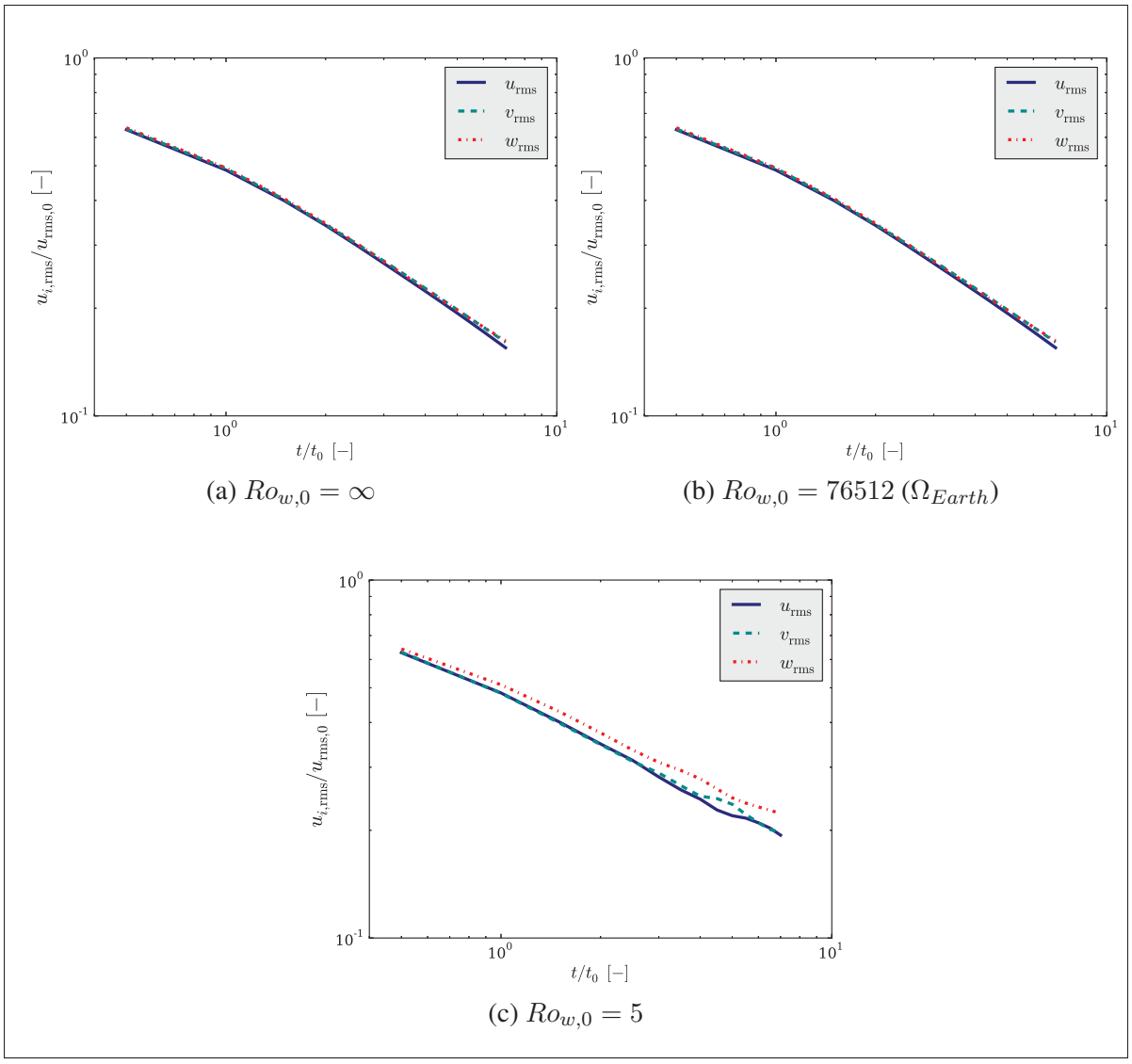

(a) $Ro_{w,0} = \infty$

(b) $Ro_{w,0} = 76512$ (Ω_{Earth})

(c) $Ro_{w,0} = 5$

Figure 3.11 Time evolution of the $u_{i,rms}$ components for different angular velocities using the 32^3 mesh.

on microscale simulations is of that same order. Hence, the Coriolis force does not alter the atmospheric turbulent structures in a crucial manner. For this reason, in the atmospheric flow literature there is no mention about the effects of rotation on the turbulent structures. Nevertheless it is important to be aware of its subtle effects. First, because a mean curvature or the advection by a large eddy can have the same repercussions (Sagaut and Cambon, 2008). Secondly, it is relevant to understand that small eddies might not always be isotropic. Eddy viscosity models might not be able to properly account for that anisotropy. Furthermore since

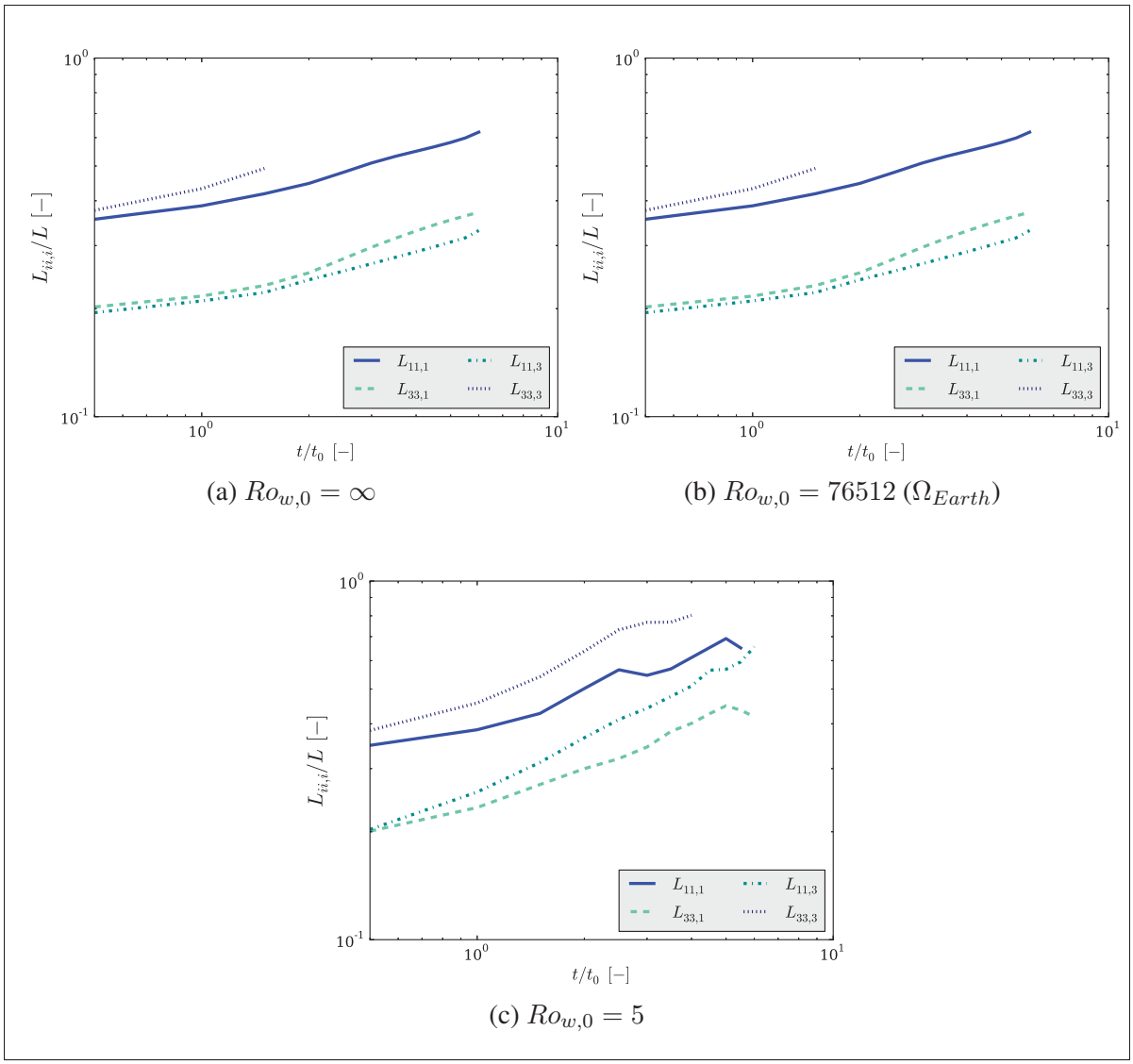

(a) $Ro_{w,0} = \infty$

(b) $Ro_{w,0} = 76512$ (Ω_{Earth})

(c) $Ro_{w,0} = 5$

Figure 3.12 Time evolution of the lengthscale for different angular velocities using the 32^3 mesh.

the Coriolis force produces no work, the turbulent kinetic energy in a rotating case is described by $dk_{\text{total}}/dt = -\varepsilon_{\text{total}}$. There is no explicit term that takes the rotation effects into account (Sagaut and Cambon, 2008), thus this relation is identical to the DIT turbulent kinetic energy evolution given in Equation 3.1.

3.3 Free homogeneous shear turbulence

The next step on the validation process is the simulation of an unbounded homogeneously sheared flow, also referred as a HAT under pure shear or uniform sheared turbulence in the literature (Hinze, 1975; Sagaut and Cambon, 2008). The aim here is to study the interaction between turbulence and mean shear without the complexity of a solid boundary. The simplest homogeneous mean shear is imposed for this test case as shown in Figure 3.13. Such velocity gradient only adds a level of complexity to the flow with respect to the DIT case; yet this case has proven to be more problematic than it appears. There are several fundamental questions that still remain unanswered, and often experiments and numerical simulations give conflicting results (Sukheswalla *et al.*, 2013).

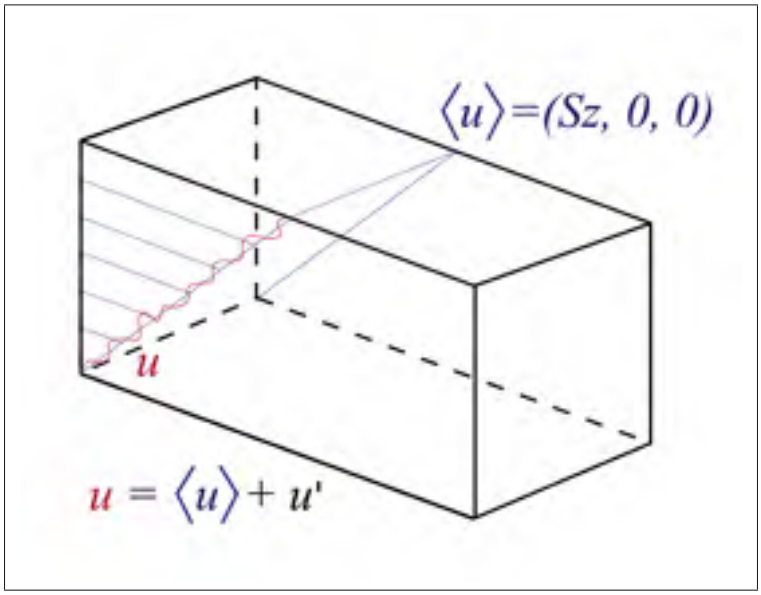

Figure 3.13 Graphic representation of the free homogeneous shear case.

The instantaneous velocity u_i is expressed as the sum of the mean velocity $\langle u_i \rangle$ and the instantaneous fluctuations u_i'. The mean velocity is determined based on the imposed mean shear $S = \partial \langle u \rangle / \partial z$, hence $\langle \mathbf{u} \rangle = (Sz, 0, 0)$. Such imposed shear is temporally and spatially uniform. Shear generates energy and continuously produces turbulence (Hinze, 1975). Therefore

the turbulent kinetic energy evolves in time as

$$\frac{dk_{\text{total}}}{dt} = -S\langle u'w'\rangle - \varepsilon_{\text{total}}. \tag{3.8}$$

Contrary to the previous validation cases, there is the energy production term $P = -S\langle u'w'\rangle$ in the equation (Sagaut and Cambon, 2008). A self-similar state is attained if the turbulence production is compensated by the local dissipation (Davidson, 2004). Most experiments (Tavoularis and Karnik, 1989) and numerical studies (Rogallo, 1981; Rogers and Moin, 1987; Lee *et al.*, 1990) suggest that the turbulent kinetic energy in unbounded shear flows grows exponentially in time. It has been observed that the production term equals the dissipation term ($P/\varepsilon \sim 1$) only when a low-shear is imposed; hence a steady state regime is found for these cases. However high-shear cases converge to an asymptotic regime where $P/\varepsilon > 1$ (Tavoularis and Karnik, 1989). It appears that the $P \sim \varepsilon$ balance can only be achieved on confined cases (Pumir, 1996).

A DNS numerical study performed by Lee *et al.* (1990) was chosen to validate the $k-\omega$ SST-SIDDES hybrid model. The results of this test case are also available on the AGARD database (Jimenez J. (Ed.), 1997). In this case, the unbounded computational domain consists of a periodic box and an initial isotropic field which is subjected to a high mean shear. The hybrid model will yield only LES regions due to the absence of solid walls. The domain size is $(L_x, L_y, L_z) = (8\pi, 2\pi, 2\pi)$. It is larger in the streamwise direction to allow for the elongated turbulent scales that will developed due to the shearing action. The SIDDES mesh has $(128 \times 32 \times 32)$ cells while the referenced DNS have four times more cells in each direction. A shear of $S = 10$ (with units of 1/time) is defined as well. The initial field was generated based on the DNS data set provided by A. Wray (Jimenez J. (Ed.), 1997) for DIT cases. This data set was concatenated four times in the streamwise direction and then mapped to the shear flow mesh. Subsequently it was let to decay freely until the required initial $Re_\lambda \sim 50$ was attained. Once a mean shear is imposed, the velocity field is no longer periodic in the vertical direction. Consequently to simulate this unbounded computational box, the flow equations have to be slightly rearranged.

As most of the numerical studies of unbounded homogeneous shear flow, Lee *et al.* (1990) DNS test cases have been performed using a non-dissipative pseudo-spectral method and the re-meshing algorithm developed by Rogallo (1981). The re-meshing methodology allows for the use of periodic boundaries in spectral methods. Due to the nature of the SIDDES turbulence model, a different technique has to be used. However this technique is also based on the Reynolds decomposition. Consequently, the Navier-Stokes equations for free, homogeneous (temporally and spatially uniform) shear flow can be written as

$$\frac{\partial\langle u_i\rangle}{\partial t}+\frac{\partial u_i'}{\partial t}+\frac{\partial\langle u_j\rangle\langle u_i\rangle}{\partial x_j}+\frac{\partial\langle u_j\rangle u_i'}{\partial x_j}+\frac{\partial u_j'\langle u_i\rangle}{\partial x_j}+\frac{\partial u_j'u_i'}{\partial x_j}= \\ -\frac{1}{\rho}\frac{\partial p}{\partial x_i}+\nu\frac{\partial^2\langle u_i\rangle}{\partial x_j\partial x_j}+\nu\frac{\partial^2 u_i'}{\partial x_j\partial x_j} \tag{3.9}$$

Because mean velocity is steady and homogeneous, the previous equation can be written as

$$\frac{\partial u_i'}{\partial t}+\frac{\partial u_j'u_i'}{\partial x_j}=-\frac{1}{\rho}\frac{\partial p}{\partial x_i}+\nu\frac{\partial^2 u_i'}{\partial x_j\partial x_j}-\frac{\partial\langle u_j\rangle\langle u_i\rangle}{\partial x_j}-\frac{\partial\langle u_j\rangle u_i'}{\partial x_j}-\frac{\partial u_j'\langle u_i\rangle}{\partial x_j} \tag{3.10}$$

However $\langle u_i\rangle$ is an imposed and known value. This implies that the only unknowns in Equation 3.10 are the velocity fluctuation u_i' and p. Contrary to the u_i field, the statistically homogeneous fluctuations u_i' are periodic in all directions. Consequently Equation 3.10 can be solved implicitly for u' and p using periodic boundaries. This methodology to solve the homogeneous shear flow cases was implemented in OpenFOAM as explained in Appendix III.2. Plane averages of the instantaneous velocity profiles are shown in Figure 3.14 to help visualize the test case.

Some practical numerical constrains need to be carefully addressed; for instance the effects regarding the lengthscale growth. In theory, the lengthscale grows continuously since there is no external delimitation (Rogallo, 1981). In practice, the periodic boundaries restrict the size at which the lengthscale can adequately grow. For this reason simulations cannot run indefinitely in time and they need to be stopped. It is a common practice to terminate the simulation around the time when $L_{xx,x}/L_x < 0.1$ or at the moment where unusual behaviour takes place such as $dL_{xx,x}/dt \leq 0$ (Sukheswalla *et al.*, 2013). For this DNS test case, the maximum non-

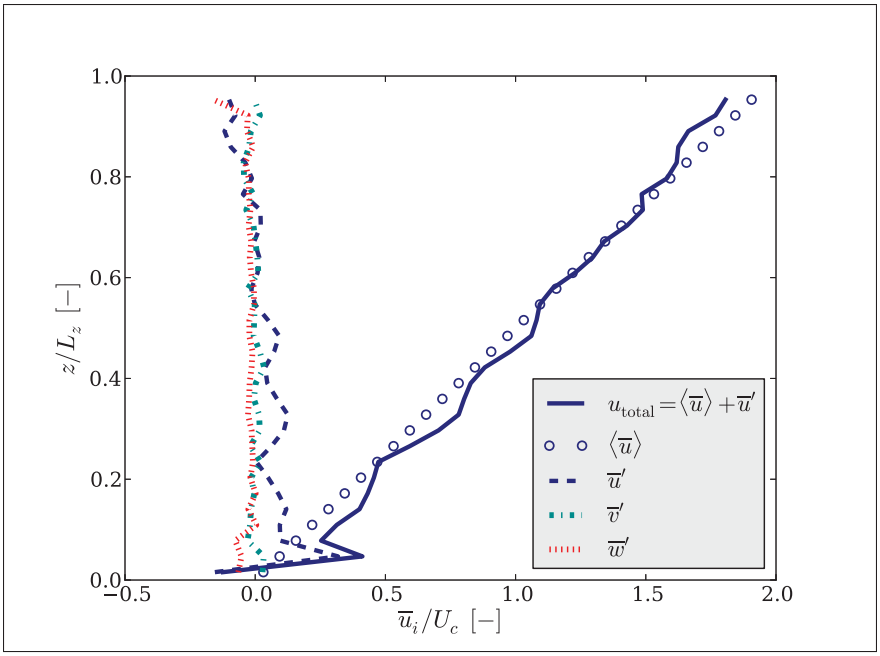

Figure 3.14 Plane averages of the instantaneous velocity profiles for the shear flow case at a particular time. $\langle\overline{u}\rangle$ is an imposed value, while $\overline{u}_i'$ is obtained by implicitly solving Equation 3.10

dimensional time St (i.e. time t normalized by the mean shear stress S) allowed was 16 (Lee *et al.*, 1990). However, with the SIDDES model only a non-dimensional time $St = 12$ was attained before anomalous behaviour occurred as it can be appreciated in Figure 3.15. The results display a volume average (Equation 1.15) taken from the centre $x - z$ planes. The top and bottom 25% of the domain was neglected due to some instabilities that developed, as it will be shown later.

Figure 3.15 clearly shows that all the rms velocity components grow with time. Hence the turbulent kinetic energy and the turbulence intensity also increase. Up to $St = 12$, the SIDDES results are in rather good agreement with the DNS data obtained from the AGARD database (Jimenez J. (Ed.), 1997). It is not clear why a non-dimensional time of $St = 16$ was not reached as in the DNS simulations. The different turbulence models compared, the different initial fields, or the different used meshes might be the main factors for this discrepancy, but a further investigation is needed to certainly conclude the cause of this behaviour. Regard-

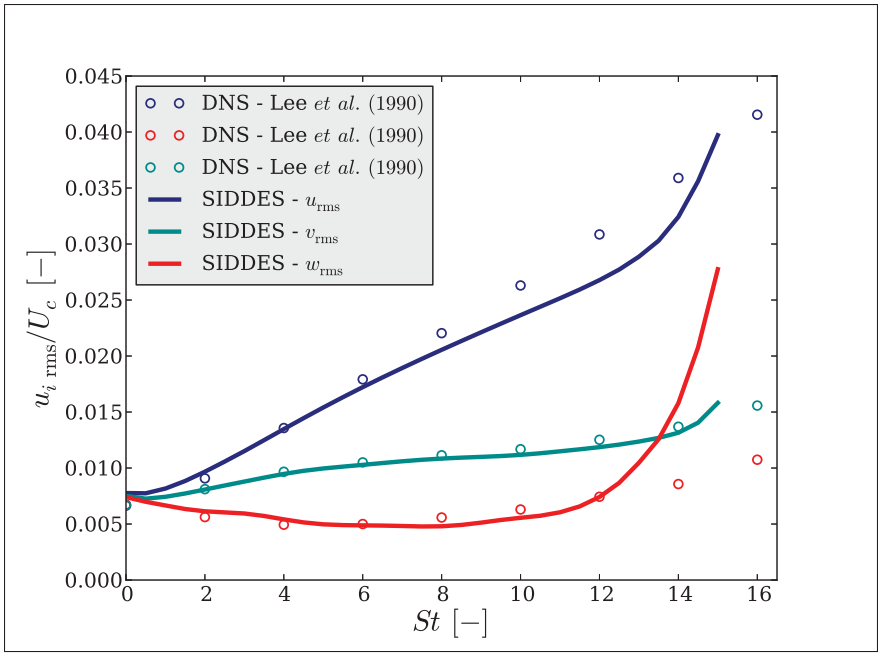

Figure 3.15 History of the velocity for homogeneous shear flow simulations

ing the initial velocity field used in SIDDES, it was observed that Wray's data set which was copied four times remained distinguishable throughout the shear flow simulation. For instance, the correlation function of the streamwise velocity clearly displays four peaks at every time step (not shown here). This makes the initial field not ideal and this could explain the unusual behaviour that prevented a longer and accurate simulation. Nevertheless the SIDDES model yield insightful results that are worth investigating.

It is known that the shear has a tendency to stretch the vortex lines of the turbulence structures in certain direction. This generates anisotropic eddies with increasing turbulent kinetic energy as seen in Figure 3.16. On the other hand, the dissipation takes place at the smallest and isotropic scales. This implies that the energy is redistributed between the different turbulence components (Davidson, 2004) as seen in Figure 3.17.

The shear stress alone produces turbulence, thus the presence of a solid wall is not necessary. Nevertheless the turbulence behaviour on shear flows is extremely similar to the near-wall turbulence. For example, the peculiar hairpin vortices and other streaky turbu-

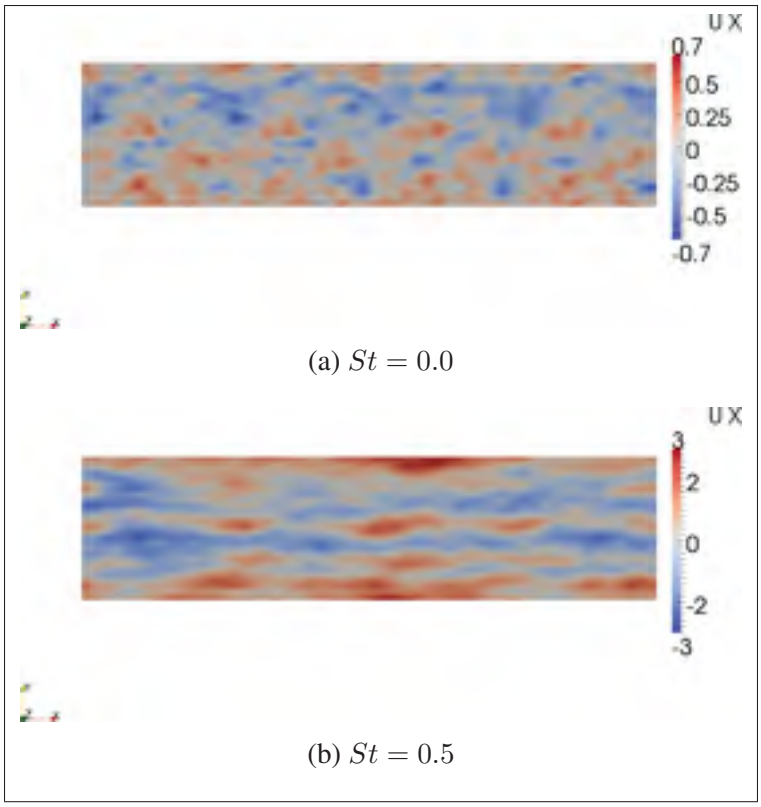

(a) $St = 0.0$

(b) $St = 0.5$

Figure 3.16 Streamwise velocity contours on the $x - y$ plane. Units: [m/s].

lence structures found on wall-bounded flows are also characteristic features of turbulent shear flows (Rogers and Moin, 1987; Lee *et al.*, 1990). This phenomena was also observed on the SIDDES results. Figure 3.18 shows snapshots of the vorticity of the fluctuating velocity field ($\overline{\boldsymbol{\omega}} = \nabla \times \overline{\boldsymbol{u}'}$). The isotropic initial field is seen at $St = 0$, but at later times the elongated turbulence structures are clearly distinguished. Surely in real flows, the shear is mostly generated by a solid surface (i.e. no-slip condition) (Sagaut and Cambon, 2008). However certain cases like the velocity deficit on a turbine wake could be characterized as a unbounded shear flow.

Finally, the production to dissipation ratio in this highly-sheared turbulent flow is displayed in Figure 3.19. The SIDDES simulation results are consistent with the DNS; furthermore $P/\varepsilon > 1$ as the experimental results from Tavoularis and Karnik (1989) concluded. Once again this plot shows that the SIDDES are presents a higher turbulent kinetic energy production than it can be locally compensated by dissipation.

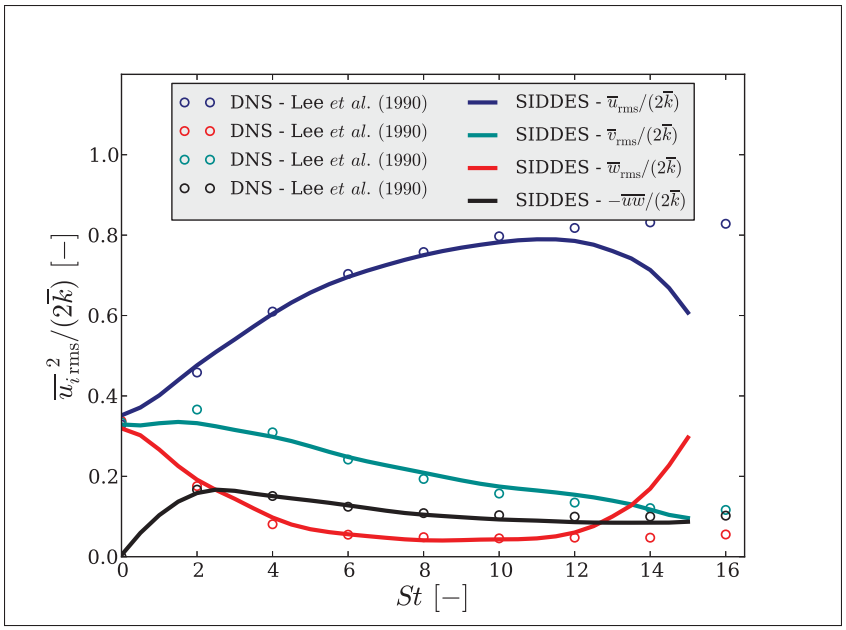

Figure 3.17 Energy components evolution in homogeneous shear turbulence

Peculiarly uniformed shear flow simulations prove to be quite unpredictable and hard to reproduce with other mesh refinement or other flow parameters (i.e. different CFL). It is not clear why this happens, but other authors have also experience similar unstable simulations (Sukheswalla *et al.*, 2013). Nevertheless the achieved hybrid and DNS results are consistent and in agreement with other experimental findings. This indicates that the hybrid model was able to reproduce the interaction between turbulence structures and mean shear correctly. Despite the good results, one must be aware that all eddy viscosity models, including the $k-\omega$ SST-SIDDES, only evaluate the turbulence locally without taking the neighbouring cells or the time history into account. This assumption can lead to erroneous results in cases where the flow is subjected to sudden changes of shear whether in space or in time (Davidson, 2004). Similarly, eddy viscosity models cannot accurately account for the dynamics of severe anisotropy structures produced by strong shear or a strong rotation (Pope, 1975). For the hybrid model in the LES region, the advantage is that the eddy viscosity assumptions concern only the small subgrid scales (Bechmann, 2006).

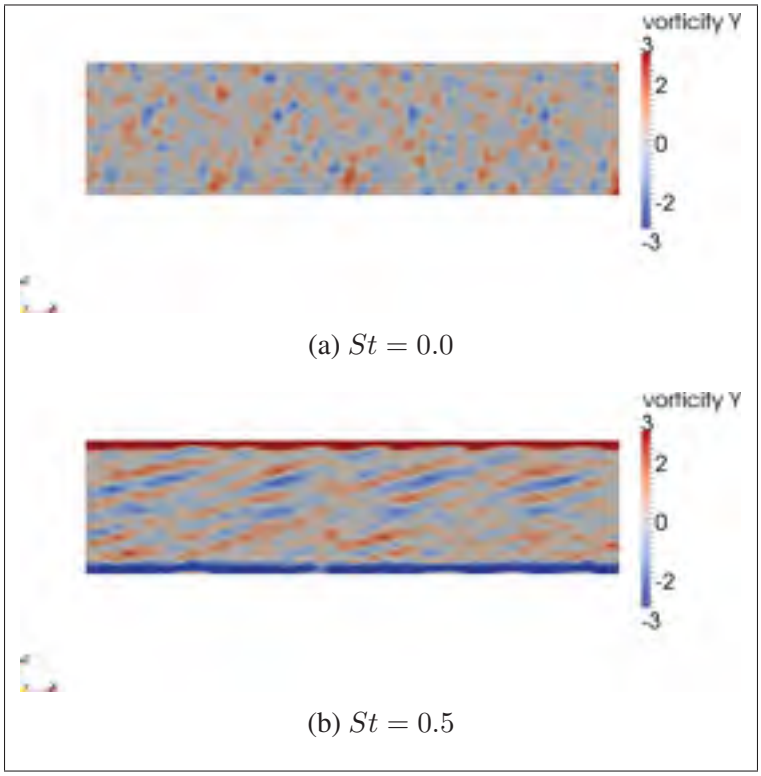

(a) $St = 0.0$

(b) $St = 0.5$

Figure 3.18 Fluctuating vorticity contours (ω_y) on the $x - y$ plane. Undesired instabilities are seen at the top and bottom boundaries. Units: [1/s].

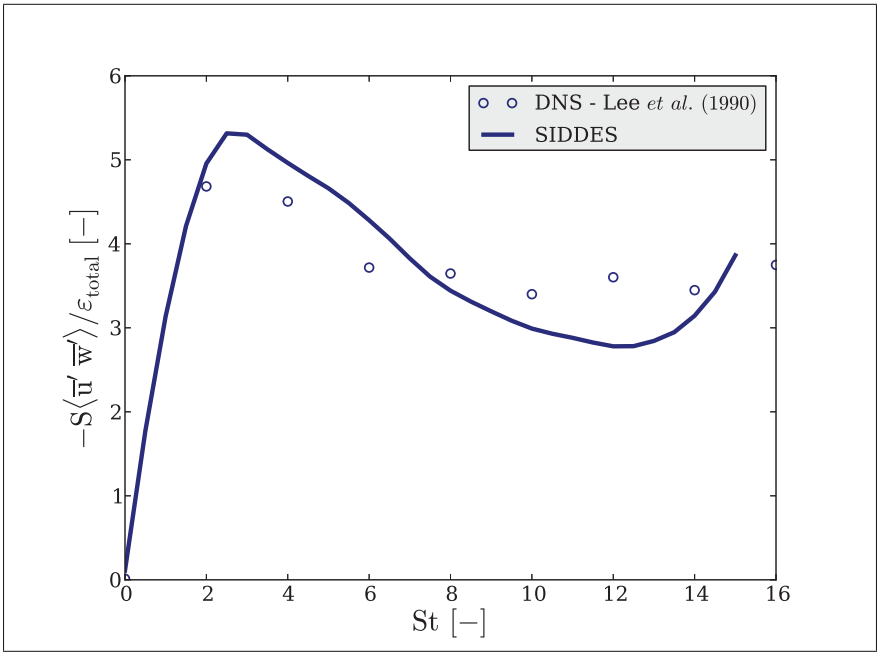

Figure 3.19 Production to dissipation ratio

3.4 Channel flow

The widely studied half channel flow was chosen as the last validation test for the proposed hybrid model. This is a rather simple flow, however it introduces a non-trivial wall interaction that entails significant challenges for the numerical simulations. Moreover, the hybrid model should this time present a URANS and a LES region.

To verify that the $k-\omega$ SST-SIDDES hybrid model was correctly implemented in OpenFOAM, the half channel case from previous studies (Shur *et al.*, 2008; Gritskevich *et al.*, 2012) was reproduced. This test case has a $Re_\tau = u_* H/\nu = 1.8 \cdot 10^4$ where H is the half channel height. The computational domain size is $(L_x,\, L_y,\, L_z) = (8H,\, 3H,\, H)$ which represent the streamwise, spanwise and vertical directions respectively. The grid refinement is uniform for $\Delta_x/H = 0.1$ and $\Delta_y/H = 0.05$, while an expansion ratio of $\Delta_{z_{i+1}}/\Delta_{z_i} = 1.14$ starting at $z_1^+ \sim 0.3$ are used in the vertical direction. This mesh has $(80 \times 60 \times 64)$ cells. The channel is periodic in the streamwise and spanwise direction, a no-slip boundary condition with the roughness extension (Section 2.2.1.1) was set at the wall, and a stress-free boundary ($\partial\overline{u}/\partial z = \partial\overline{v}/\partial z = 0,\, \overline{w} = 0$) was defined at the top. These boundary conditions required an added pressure gradient term to drive the flow. Also, the aerodynamic flow constants from Table I-1 were used. The internal velocity was initialized with a mean logarithmic profile plus approximately $\pm 20\%$ of random fluctuations. Finally, the simulations ran for approximately 30 longitudinal flow-through-times ($T_0 = L_x/\langle u \rangle$); then for the following $60T_0$ the time-averaged statistics were calculated. The results shown as $\langle \cdot \rangle$ represent the time and space average.

The flow is driven by a constant pressure gradient in the streamwise direction. This force term is added to compensate the shear stresses at the wall and ensure a statistically stationary flow in a periodic domain; in other words, to assure that velocity profile does not decay over time due to the friction at the wall. For steady and horizontally homogeneous flow, the hybrid model mean momentum equation is (in the x direction) (Bechmann, 2006)

$$\frac{1}{\rho}\frac{\partial\langle\overline{p}\rangle}{\partial x} = \frac{\partial}{\partial z}\left(\nu\frac{\partial\langle\overline{u}\rangle}{\partial z} + \langle\overline{u}'\overline{w}'\rangle\right) = \frac{1}{\rho}\frac{\partial\langle\overline{\tau}\rangle}{\partial z}. \tag{3.11}$$

By integrating this equation over the whole domain height, and assuming that $\tau = 0$ at the top ($z = H$), it is found that

$$\langle \overline{\tau} \rangle = H \frac{\partial \langle \overline{p} \rangle}{\partial x} \left(\frac{z}{H} - 1 \right). \tag{3.12}$$

At $z = 0$, the shear stresses are $\tau_w = -\rho u_*^2$, hence

$$\langle \overline{\tau}_w \rangle = -H \frac{\partial \langle \overline{p} \rangle}{\partial x} = -\rho u_*^2. \tag{3.13}$$

Thus the force term imposed in the Equation 2.12 corresponds to

$$F_x = \frac{\partial \langle \overline{p} \rangle}{\partial x} = \frac{\rho u_*^2}{H}. \tag{3.14}$$

It is sometimes referred as the large scale pressure gradient.

The large scale pressure gradient was implemented in OpenFOAM as a steady value based on an imposed u_* (Refer to Appendix III.3 for code details). On the contrary, the *channelFoam* solver and a possible option on the SOWFA[2] solvers use an imposed value of velocity at the top of the domain to calculate and correct an unsteady large scale pressure gradient at each time step to ensure the correct velocity at the top boundary. However an unsteady pressure gradient might cover up the LLM that could occur when using the $k - \omega$ SST-SIDDES.

OpenFOAM has a second-order spatial discretization (See Section 2.1.3), therefore the schemes used in the model implementation are all second-order. On the contrary the original reference case uses fourth-order central schemes. For this reason, it is expected that the shear stresses from the OpenFOAM implementation will not be as precise as the reference case (for the same mesh refinement). This is shown in Figure 3.20. Additionally it was observed that when a URANS region is present, these hybrid simulations become more unstable and tend to diverge more easily if only central schemes are used to discretized the divergence terms of

[2]Wind energy software toolbox developed by Matt Churchfield and Sang Lee of the National Renewable Energy Laboratory. It is based on OpenFOAM. More details can be found at NWTC Information Portal (SOWFA). *https://nwtc.nrel.gov/SOWFA*.

the equations. For this reason blended discretization schemes are chosen; they are called *local-Blending* in the OpenFOAM code. A *blendingFactor* is defined based on the local and instantaneous URANS and LES regions in the domain. For cells located in pure URANS regions, the *blendingFactor* is defined as 0 and the second-order upwind (*linearUpwind*) scheme is chosen; while for cell in pure LES zones, the *blendingFactor* equals to 1.0 and the second-order central (*linear*) scheme is used. Consequently a scheme with some upwind and central components is used for the blended URANS/LES regions (For a detailed explanation of the implementation and use in OpenFOAM see Appendix III.5 and III.6). To be consistent, second-order backward scheme is always employed for the temporal discretization.

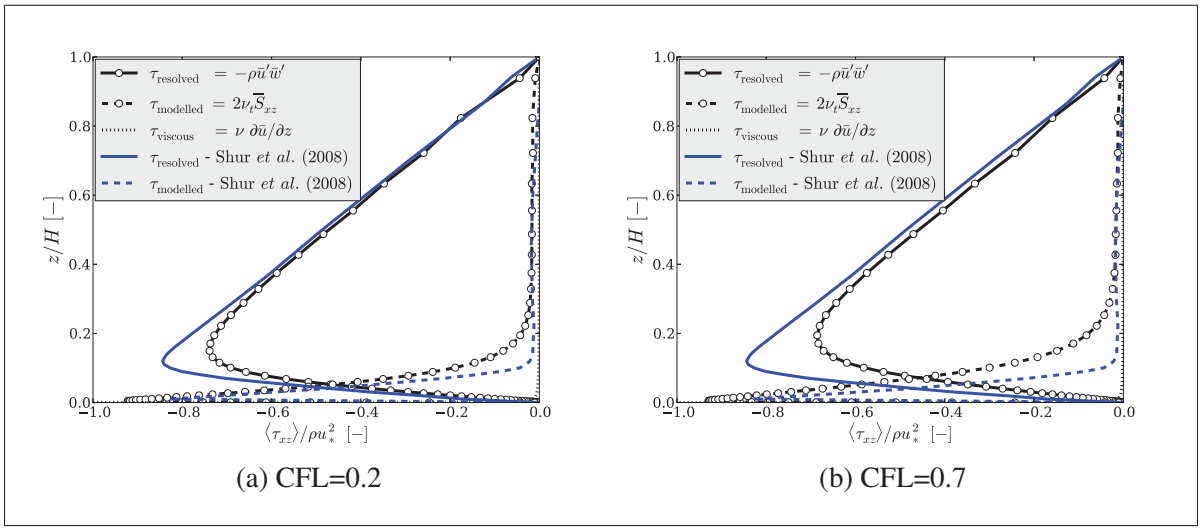

(a) CFL=0.2

(b) CFL=0.7

Figure 3.20 Averaged shear stresses for a smooth half channel flow using central discretization schemes for the divergence term on the transport and model equations. These SIDDES results are compared against the reference article data (Shur *et al.*, 2008).

Figure 3.21 shows the viscosity ratio $\langle\nu_t\rangle/\nu$ for half channel simulations using different discretization schemes for the convective terms. The turbulent viscosity increases in the URANS regions, then around $z^+ \approx 10^3$ the hybrid switches to LES and the eddy viscosity starts diminishing. The discretization schemes do not have an impact on the height at which the URANS zones transition to LES. However, the results that agree better with the benchmark case use pure central schemes to discretized the convective terms in the momentum equation

and blended schemes for the divergence terms in the k and ω equations. Additionally, the simulations prove to be more stable with this type of locally and instantaneous blended schemes. This combination of schemes is going to be employed from this point forward.

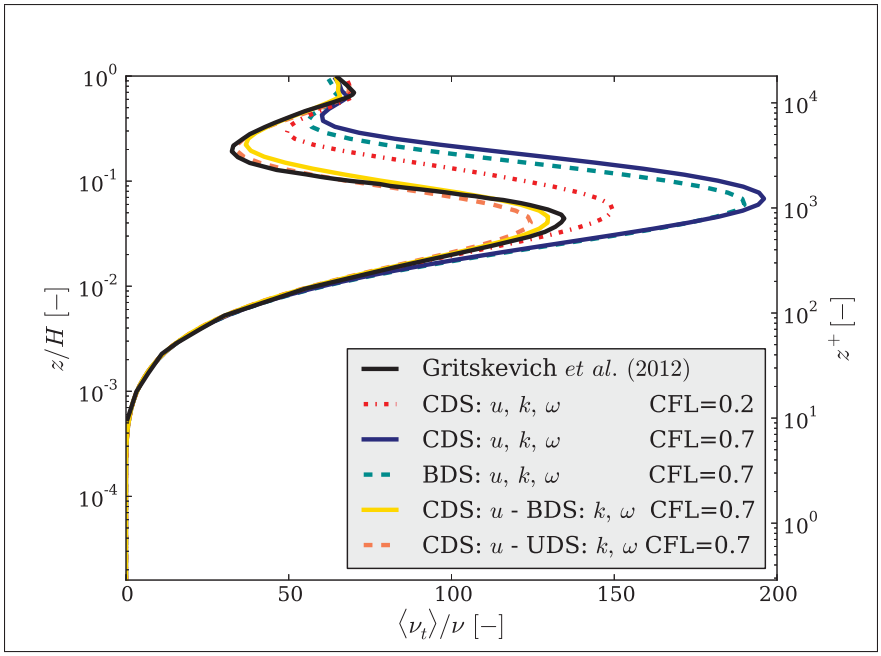

Figure 3.21 Viscosity ratio for half channel simulations. Different schemes are used for each of the transport and model equations. CDS: 2nd-order central, UDS: 2nd-order upwind, and BDS: 2nd-order blended schemes (described in the text). Gritskevich *et al.* (2012) data has been obtained from that article.

With the appropriate schemes for the half channel reference case, the velocity profile is in agreement with Reichardt's law (Reichardt, 1951) and the LLM is not observed in Figure 3.22a. Additionally using only second-order schemes, the shear stresses obtained are in good agreement with the previously mentioned studies (Shur *et al.*, 2008) that use fourth-order central schemes as it can be seen in Figure 3.22b.

All the DES models were developed and validated for aerodynamic applications, namely flows with a relatively low Reynolds number and rather smooth walls. For exam-

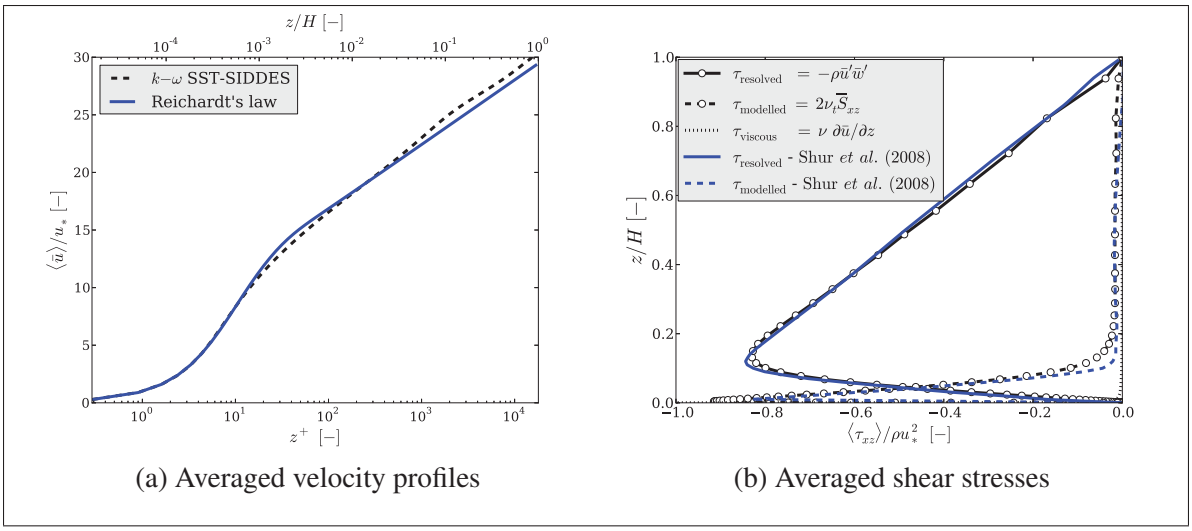

(a) Averaged velocity profiles

(b) Averaged shear stresses

Figure 3.22 Half channel flow at $Re_\tau = 1.8 \cdot 10^4$ using blended schemes for the divergence terms in the k and ω equations and imposing a maximum CFL=0.7. Shur *et al.* (2008) data has been digitized.

ple, the IDDES model has been validated for smooth channel flow simulation up to $Re_\tau = u_* H/\nu = 1.8 \cdot 10^4$, where u_* is the friction velocity and H represents the half channel height (Shur *et al.*, 2008); the same for SIDDES (Gritskevich *et al.*, 2012). On the contrary, the ABL simulations required by the wind energy industry involve extremely high Reynolds numbers ($Re_\tau \sim 10^7 - 10^9$) and exceedingly high roughness ($z_0 \sim 0.00001 - 0.5$ m depending on the terrain (Manwell *et al.*, 2002)). Therefore, the behaviour of the DES hybrid models still need to be validated for the ABL specifications.

To this end, SIDDES half channel flow simulations were performed for a series of higher Reynolds numbers[3] $Re_{D_h} = U_{av} D_h/\nu$ and then for rough walls covering all across the available data in the Moody chart (White, 1991). $D_h = 4H$ represents the hydraulic diameter of a channel with a height of $2H$ and periodic lateral boundaries, and U_{av} is the average velocity. The aim is to verify if the LLM correction is still valid for other parameters not tested by (Gritskevich *et al.*, 2012). As a reference, Shur *et al.* (2008) case has a $Re_{D_h} = 1.9 \cdot 10^6$ and a relative pipe roughness $k_s/D_h = 0$, while a typical ABL simulation could reach $Re_{D_h} = 1 \cdot 10^8$ and relative pipe roughness of $k_s/D_h = 30 z_0/4H = 3 \cdot 10^{-3}$ for a

[3] A $Re_\tau \sim 10^7$ corresponds to $Re_{D_h} \sim 10^8 - 10^9$

$z_0 = 0.4$ m and a $H = 1000$ m. These half channel simulations were carried out using the same domain and boundary conditions as in the previous channel verification test. The same meshing guidelines were used also, but since U_{av} varies per case, the value of z_1 and the number of cells in the vertical direction changes. The driving pressure gradient was adjusted for each case based on the friction factor ƒ obtained from the Moody chart, then the imposing forcing term is $F_x = \partial\langle p\rangle/\partial x = \Delta p/\Delta x = \rho\, ƒ\, U_{av}^2/2D_h$ (Munson *et al.*, 2006).

The results of all the channel cases carried out are shown in Figure 3.23. The four smooth wall cases results are consistent with Reichardt's law and no LLM is observed. Thus, the use of the SIDDES model can be extended for much higher Reynolds flow that the original articles suggest (Shur *et al.*, 2008; Gritskevich *et al.*, 2012). Concerning the rough cases, the logarithmic layer is well modelled and in agreement with the theory. But it is evident that a slight deviation from the logarithmic law of the wall exists and that it becomes more pronounced as the roughness height increases. It is important to confirm if this deviation is simply the defect layer or is due to the unphysical LLM caused by the hybrid model.

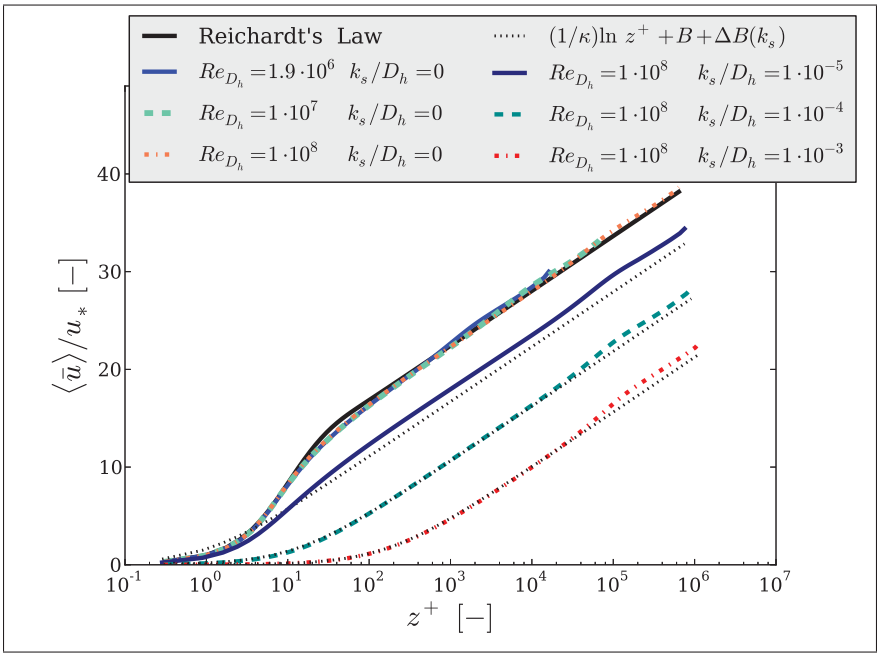

Figure 3.23 Averaged velocity profiles for different Re_{D_h} and various surface conditions using SIDDES

The defect layer behaviour

$$u_{Defect} = \frac{\langle u_0 \rangle - \langle u \rangle}{u_*} \tag{3.15}$$

has been studied in the past for smooth and rough turbulent pipe flow. Here $\langle u_0 \rangle$ is the mean velocity at the top of the half channel. Coles' law of the wake as well as the velocity-defect distribution obtained from Laufer's experimental data describe this deviation from the logarithmic layer (Hinze, 1975). It is known, that the logarithmic layer exist up to a height of $0.15H$ for boundary layers and pipe flows (Hinze, 1975), but the behaviour above that height has not been thoroughly studied especially on channel flow. The velocity-defect for the channel cases is shown in Figure 3.24. Regardless of the type of surface, all the velocity-defect curves collapse, confirming that the wall roughness does not have an impact on the defect layer (White, 1991). However, the velocity profiles start deviating from the log-law slightly below $0.1H$, and also, there is a disagreement between Laufer's measured velocity distribution and the simulations results. For the lack of more exhaustive studied on the defect law, it is a hard task to distinguishing if the observed deviation is related to the hybrid model or to the defect layer behaviour. However, this findings may suggest that there is still a slight LLM for all the channel flow simulations done using the $k-\omega$ SST-SIDDES model. Another possibility to explain these results might be an speed up effect caused by the domain size. This effect was observed for the pressure driven atmospheric boundary simulations carried out in Section 4.2.

3.5 Summary

A step by step validation of the $k-\omega$ SST-SIDDES model has been carried out on canonical flows. The investigation of this mostly theoretical cases provide the opportunity to examine certain turbulence properties in an isolated manner. In other words the development of isotropic or anisotropic eddies, the effect that rotation or shear forces have on the overall flow, and finally the impact of a solid wall were analyzed independently. This particular understanding is highly detailed and theoretical, but it will certainly be advantageous when more complex flows are modelled.

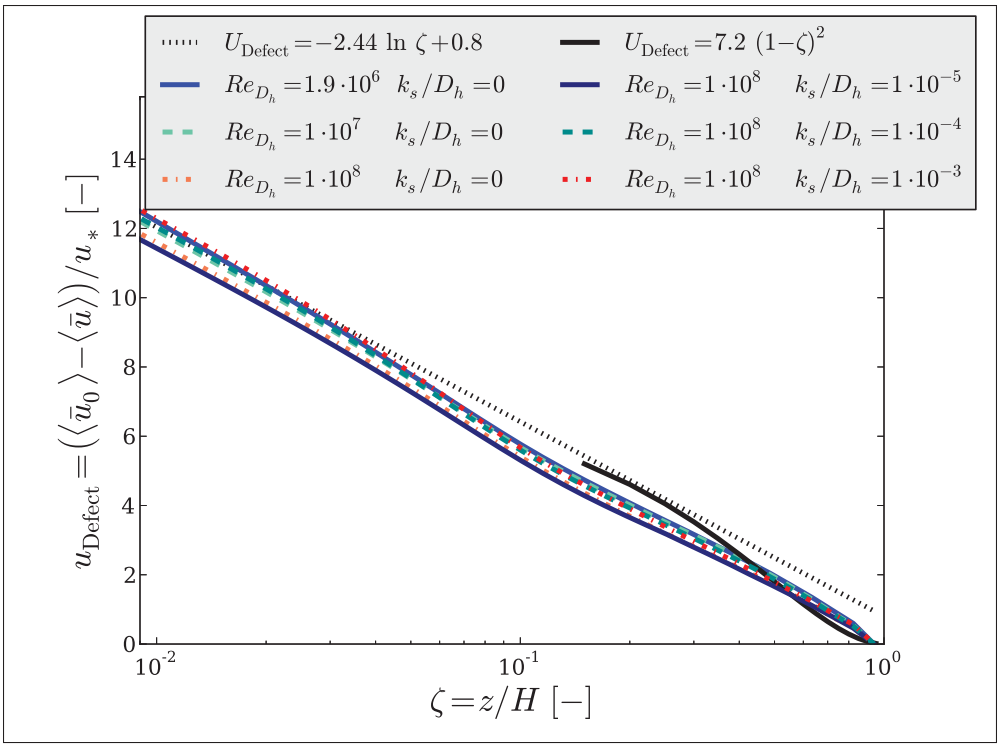

Figure 3.24 Averaged velocity-defect profiles for different Re_{D_h} and surface conditions using the SIDDES turbulence model compared against Laufer's measured velocity-defect distributions.

Concerning the hybrid model, it was demonstrated that it reproduces all tested the canonical flows correctly. But most importantly, this validation helped determine the proper discretization schemes. These chosen schemes allow the proper modelling of the turbulent flow and at the same time ensure the stability of the simulations. Now, the hybrid model can be used with confidence for flat terrain simulations.

CHAPTER 4

MICROSCALE ATMOSPHERIC FLOW SIMULATIONS OVER FLAT TOPOGRAPHY

Neutrally-stratified "ideal ABL" simulations were performed to test the capabilities of the hybrid model on homogeneous flat terrain. In these simulations, the velocity profile is not imposed and it is rather a natural consequence of the flow conditions. It is a common practice for atmospheric flow RANS simulations focus only on the atmospheric surface layer (ASL) and drive the flow by imposing a constant velocity or shear at the top boundary of the domain (Richards and Hoxey, 1993). In this case, the Monin-Obukhov similarity theory is valid in the whole domain height (i.e. the velocity profile is logarithmic and the turbulent kinetic energy profile is constant) (Monin and Obukhov, 1954). However, imposing a total fixed shear (in particular the resolved stresses) for an inherently unsteady LES or hybrid model is not trivial as it will be explained in Section 4.1. For this reason, the majority of atmospheric flow LES and hybrid simulations model the whole atmospheric boundary layer (ABL) in which the flow is driven instead by a mean constant pressure gradient. In this case the simulation yields a logarithmic velocity profile and a constant turbulent kinetic energy profiles only in the bottom $\sim$10$\%$ of the domain (Porté-Agel *et al.*, 2000) or $\sim$15-20$\%$ according to other references (Brasseur and Wei, 2010). Essentially, this represents a channel flow (if no Coriolis or buoyancy forces are taken into account), hence the term "ideal ABL". The differences between the two techniques to drive the flow for ASL and ABL, as well as the other numerical aspects involved, make a RANS and hybrid/LES atmospheric flow simulations not so easily comparable.

Furthermore the shear stresses above the ASL are smaller than the wall shear stresses, as in the defect layer for aerodynamic flows. As a consequence, turbulent viscosity diminishes and the value of the lengthscale is less than κz in this region (Detering and Etling, 1985). Most eddy viscosity RANS models, assume that the lengthscale, namely the size of the eddies, increases indefinitely and linearly above the surface. To correct this issue, lengthscale delimiters are needed for ABL simulations. Several lengthscale delimiters have been successfully proposed

mostly for $k-\varepsilon$ models (Sumner and Masson, 2012) but not for $k-\omega$ SST. This problem is not present in the hybrid models since the RANS region does not generally extend above the surface layer.

Considering these issues, several simulations of the atmospheric flow in flat and homogeneously rough terrain will be performed in this chapter. First the neutral atmospheric surface layer will be studied. Then the neutrally stratified boundary layer will be characterized as a pressured-driven flow. Then, the effects of the Coriolis force will also be analyzed for the ideal ABL. To conclude this validation process, a field measurement campaign over a natural flat terrain will be studied. The current flat terrain study attempts to anticipate and eliminate the forthcoming problems that might be encounter in other types of terrain.

4.1 Atmospheric surface layer [1]

The atmospheric surface layer represents approximately 10% of the atmospheric boundary layer. It is characterized by constant shear stresses on the vertical direction and a logarithmic velocity profile. To model this region three turbulence models are investigated to model the ASL: the RANS $k-\omega$ SST, and the hybrids $k-\omega$ SST-DES and $k-\omega$ SST-SIDDES.

For these simulations, a domain of size of $(L_x,\, L_y,\, L_z) = (3H,\, 3H,\, H)$ where $H = 1000$ m is used. The bottom boundary is placed at the roughness height of $z_0 = 0.1$ m as illustrated in Figure 1.1. A $z_1^+ \sim 1.0$ is implemented instead of 0.3 as required by the roughness extension. This compromise was necessary to alleviate the constrains on *blockMesh*, the OpenFOAM mesh generator, which was not giving accurate results (i.e. the lowest row of cells was too small and could not achieve a constant height possibly due to round off errors). These tests brought forward the fact that the model requires a good quality mesh generator capable of properly defining the height of the fist node and handling high aspect ratio near-wall cells. From the wall surface, an expansion ratio of $\Delta z_{i+1}/\Delta z_i \sim 1.15$ is set up until the size of the cell Δz

[1] Preliminary results of this section were published as the conference article: Bautista. M. C., Dufresne L., and Masson C. "Hybrid turbulence models for atmospheric flow. A proper comparison with RANS models". In *The Second Symposium on OpenFOAM ® in Wind Energy*. (Boulder, CO., USA) May 19-21, 2014.

reaches 20 m; from there, cubic cells with a uniform filter width $\Delta_u/H = 0.020$ are specified. The mesh has approximately $3 \cdot 10^6$ cells where $(N_x,\, N_y,\, N_z) = (150,\, 150,\, 130)$. Periodic boundary conditions are defined on the streamwise and spanwise directions, the bottom wall is define as no-slip, and a fixed shear stress is imposed at the top boundaries. The initial velocity field consists of a mean logarithmic velocity profile plus some random fluctuations ($\pm 20\%$). As explained in Section 3.4, local and instantaneous blending discretization schemes are used. The $k-\omega$ SST model atmospheric constants summarized in Table I-1 are used. Finally, a CFL~ 0.7 was set, and the simulations ran for the equivalent of 20 longitudinal flow-through-times ($T_0 = L_x/\langle u \rangle$); then, the time-averaged statistics were gathered for at least the following 20 flow-thought-times. Lastly, the mean results $\langle \cdot \rangle$ represent again a time and space average.

To have a constant shear stress throughout the domain as in the ASL, the value of the wall shear stress $\tau_0 = \rho u_*^2$ could be imposed as the top boundary condition, thus $\tau_{top} = \rho u_*^2$ (Jimenez *et al.*, 2010; Hargreaves and Wright, 2007). To correctly estimate the shear, τ_{top} has to represent the total stresses, hence

$$\tau_{total} = \tau_{viscous} + \tau_{modelled} + \tau_{resolved}. \tag{4.1}$$

For the RANS simulations the resolved part is absent so the top boundary implementation is simple. However for hybrid or LES models this implies that

$$\tau_{top} = \rho\nu \frac{\partial \bar{u}}{\partial z} + \rho\nu_t \frac{\partial \bar{u}}{\partial z} - \rho \bar{u}' \bar{w}' \tag{4.2}$$

where $\bar{u}'$ and $\bar{w}'$ represent the fluctuations of the resolved filtered velocity field. The last term, the resolved shear stresses, is the most relevant contribution to the total shear stresses. However, the vertical boundaries are not true free boundaries, thus the movement of the eddies is constrained and the resolved fluctuations close to those boundaries are damped. For this reason the resolved stresses are incorrectly estimated at the top boundary and become negligible. On the contrary, far from the wall the total stresses can be correctly computed. The total stresses

at the centre of the domain correspond mainly to the resolved stresses, since the viscous and subgrid stresses are negligible in this region (Jimenez *et al.*, 2010). Hence $\langle \tau_{ij} \rangle \sim -\rho \langle \bar{u}_i' \bar{u}_j' \rangle$.

Figure 4.1 shows the model comparison of the mean velocity profiles and the mean turbulent kinetic energy. It is evident that the RANS $k-\omega$ SST model agrees with the Monin-Obukhov theory. However for the hybrid models, the resolved shear stresses erroneously tends to zero at the top due to damping and the velocity increases. Hence, the hybrid models do not represent the profiles correctly but they are consistent with other published results (Jimenez *et al.*, 2010). Additionally as expected, the LLM is clearly observed on the DES velocity profile.

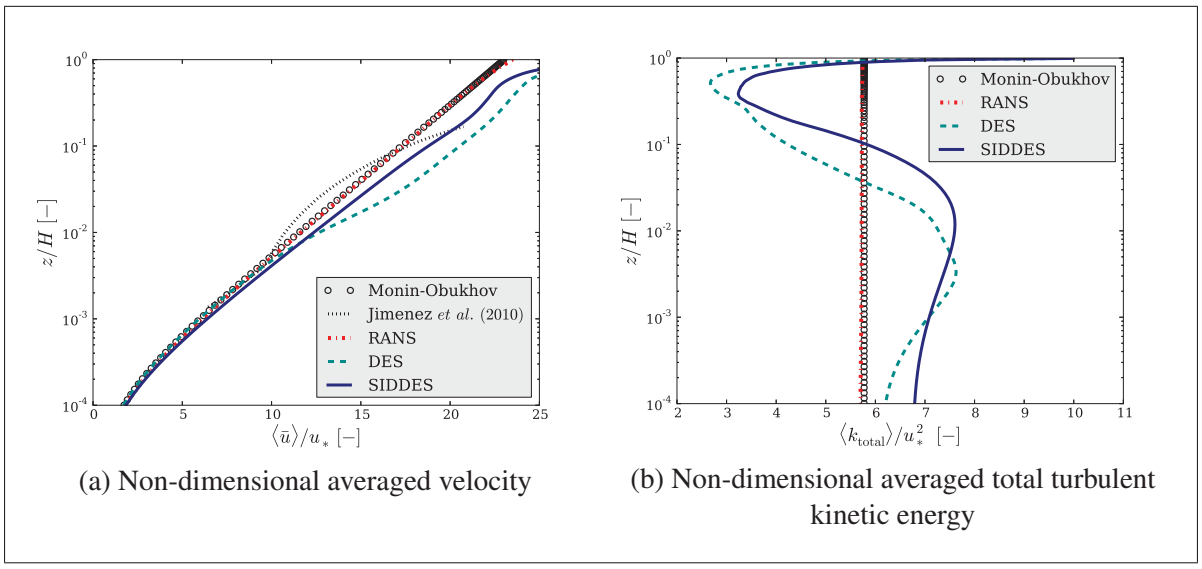

(a) Non-dimensional averaged velocity

(b) Non-dimensional averaged total turbulent kinetic energy

Figure 4.1 Atmospheric surface layer case with $z_0 = 0.1$ m. The $k-\omega$ SST, $k-\omega$ SST-DES and $k-\omega$ SST-SIDDES results are compared to the Smagorinsky results obtained from the Jimenez *et al.* (2010) figures.

The standard deviation of the velocity fluctuations ($\sigma_u = \sqrt{\langle (u - \langle u \rangle)^2 \rangle}$) is on average $\sigma_u/u_* = 2.39 \pm 0.03$, $\sigma_v/u_* = 1.92 \pm 0.05$ and $\sigma_w/u_* = 1.25 \pm 0.03$ as explained on Section 1.1.1 (Panofsky and Dutton, 1984). Subsequently, the atmospheric stress tensor com-

ponents are approximated as

$$\langle \tau_{xx} \rangle = -5.71 \ \rho u_*^2, \tag{4.3}$$

$$\langle \tau_{yy} \rangle = -3.69 \ \rho u_*^2, \tag{4.4}$$

$$\langle \tau_{zz} \rangle = -1.56 \ \rho u_*^2. \tag{4.5}$$

While the rest of the stress tensor components are determined by the imposed boundary conditions, thus $\langle \tau_{xy} \rangle = 0$, $\langle \tau_{yz} \rangle = 0$ and $\langle \tau_{xz} \rangle = \rho u_*^2$ (Jimenez *et al.*, 2010). Figure 4.2 shows the averaged stress tensor profiles obtained for the ASL flow. The top region where the fluctuations are damped could be considered as a buffer layer and it is ignored. It is also worth mentioning that for the SIDDES model, around 20-30% of the domain is not solved by pure LES; therefore, the resolved shear stresses close to the wall are small. In the LES region, these stresses are underestimated compared to the atmospheric measurements as it is expected for any eddy viscosity model (Pope, 1975), but they are in agreement with other eddy viscosity model results of similar cases in the literature (Jimenez *et al.*, 2010).

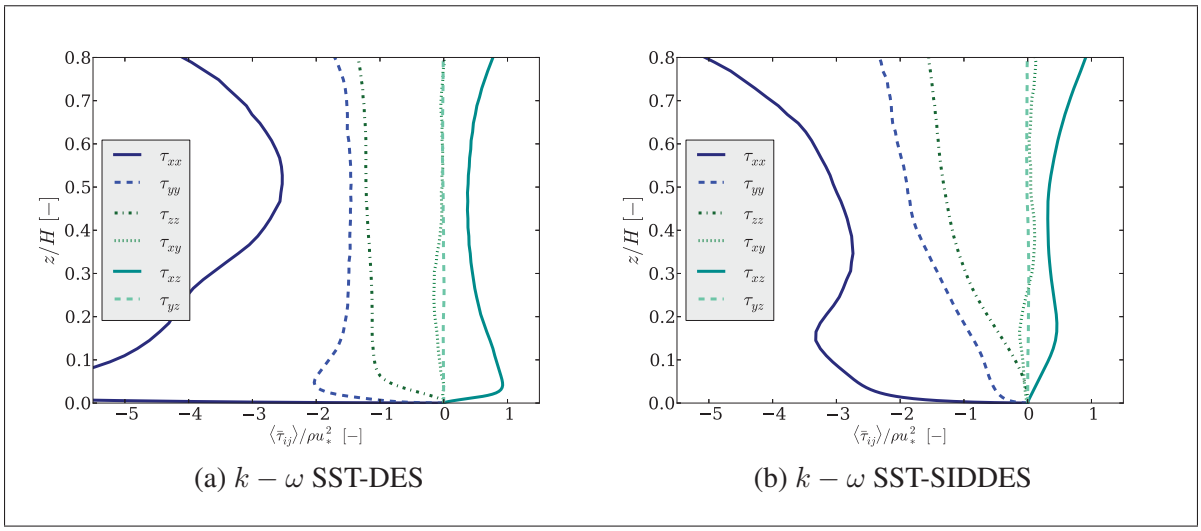

(a) $k-\omega$ SST-DES (b) $k-\omega$ SST-SIDDES

Figure 4.2 Components of the averaged resolved stress tensor for the ASL flow

Certain authors have taken advantage of the somewhat constant shear stresses obtained with these boundary conditions to analyze turbine wakes (Jimenez *et al.*, 2010). However, these boundary conditions and the technique to drive the flow might not be suitable for atmospheric flow simulations. Notably, a sophisticated unsteady boundary condition that does not constrain the eddies movement would have to be implemented to correctly simulate the resolved stresses. However, this is a complex task and not easy achievable. To bypass this problem, a pressure driven flow is commonly enforced and the entire atmospheric boundary layer is simulated.

4.2 Idealized neutral atmospheric boundary layer

It was demonstrated that solving only the atmospheric surface layer using a hybrid model does not yield ideal results due to the required boundary conditions. Therefore, the next step is to simulate the whole yet simplified representation of the atmospheric boundary layer, as the majority of LES and hybrid simulations do. In ABL simulations, the mechanisms that drive the flow and the top boundary conditions are different from the previous ASL case. Hence, ABL simulations should yield a logarithmic velocity profile and a constant turbulent kinetic energy profiles only in the bottom $\sim 10 - 20\%$ of the domain (Porté-Agel *et al.*, 2000; Brasseur and Wei, 2010) if a well-behaved LES or hybrid model is used. However if an eddy viscosity RANS model is employed, a lengthscale delimiter most be added to the original equations to account for the unphysical and unlimited increase of the calculated length scale (Sumner and Masson, 2012). Only the length scale delimiter for $k - \varepsilon$ models has been published in the literature, and the extrapolation to the $k - \omega$ SST might not be as straightforward nor the objective of this work. Therefore, the RANS ABL simulation will not be presented here.

4.2.1 Pressure driven atmospheric flow

A simplified neutral ABL simulation is carried out as a pressure driven flow, which is equivalent to a channel flow. As in Section 3.4 a large pressure gradient source term is added to the Navier-Stokes equations, thus $F_x = \rho u_*^2 / H$ in Equation 2.12. A stress-free boundary condition is imposed at the top of the domain, while periodic boundaries are specified for the stream and

spanwise directions (Franke *et al.*, 2007). The domain size is $(L_x,\, L_y,\, L_z) = (3H,\, 3H,\, H)$ defining $H = 1000$ m. A nominal value of $u_* = 0.3880$ m/s is always chosen and several roughness are studied. For comparison, the equivalence of the roughness values are given in Table 4.1.

Table 4.1 Equivalence of roughness values

$z_0\,[\mathrm{m}]$	$z_0^+\,[-]$	$k_s\,[\mathrm{m}]$	$k_s^+\,[-]$	$k_s/D_h\,[-]$
0.0002	5	0.006	165	$1.5 \cdot 10^{-6}$
0.03	825	0.9	24 766	$2.2 \cdot 10^{-4}$
0.1	2 752	3	82 553	$7.5 \cdot 10^{-4}$
0.4	11 007	12	330 212	$3.0 \cdot 10^{-3}$

The griding guidelines for DES (Spalart, 2001) are respected in all the meshes used, thus most cells are cubic. However to respect the $k-\omega$ SST roughness extension, the cells are not cubic close to the wall. Those cells can even have really high aspect ratios as it is common for this RANS model. The bottom of the computational domain starts at the roughness height, implying that the ground surface is located at $z = -z_0$ as it has been shown in Figure 1.1. A $z_1^+ \leq 1$ with an expansion ratio of $\Delta z_{i+1}/\Delta z_i \sim 1.15$ is imposed up to the height z_u at which the cells become cubic. Above z_u the mesh becomes uniform in all directions. The meshes studied have cubic cells with a side length of $\Delta_u/H = 0.010, 0.0125, 0.015, 0.020, 0.025$; its characteristics are summarized on Table 4.2 and the a lateral picture of the grid is given in Figure 4.3. As well, a variable time step that yield a CFL~ 0.7 was assigned (except when spectra are computed). After several longitudinal flow-through-times ($\sim 20 L_x/\langle u \rangle$) when the simulations reach statistical convergence, the time-averaged values were computed for at least the following 20 flow-thought-times. Then an average in space is calculated to improve the statistics. Figure 4.4 illustrates the magnitude velocity computed by the $k-\omega$ SST-SIDDES.

Significant random fluctuations ($\pm 20\%$) are added to a mean logarithmic velocity profile to generate the initial field. It was observed that if these initial fluctuations are absent or too small,

Table 4.2 Mesh properties of the atmospheric boundary layer simulations

Δ_u/H [−]	z_u/H [−]	N_z below z_u [−]	N_z above z_u [−]	N_x [−]	N_y [−]	N_z [−]	N_{Total} [−]
0.0250	~ 0.192	91	29	120	120	123	1 771 200
0.0200	~ 0.155	88	42	150	150	130	2 925 000
0.0150	~ 0.115	87	59	200	200	146	5 840 000
0.0125	~ 0.096	85	72	240	240	157	9 043 200
0.0100	~ 0.077	84	92	300	300	176	15 840 000

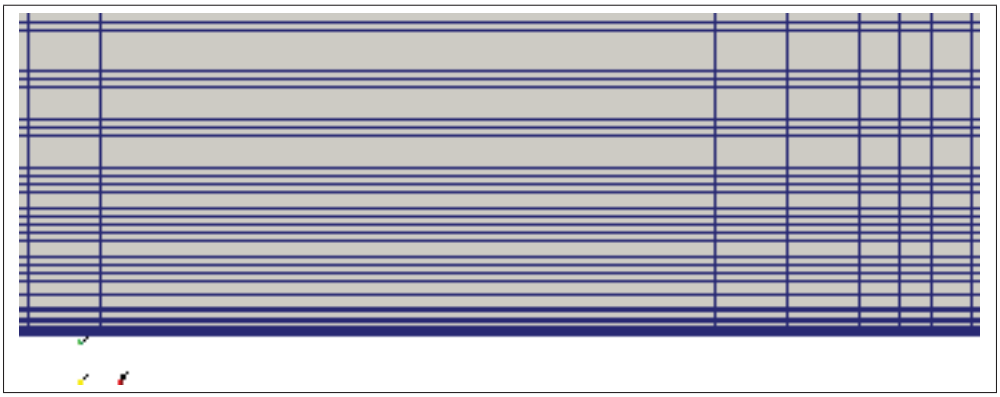

Figure 4.3 A diagram of the grid used on the ABL cases

the SIDDES model will not develop turbulent content and it will behave as an URANS model. This is an inherent characteristic of this hybrid model (Shur *et al.*, 2008), yet it was observed that it is not as critical for the DES cases. Additionally, excessive numerical dissipation can also trigger the SIDDES model to transition to pure URANS. As on Section 3.4 local and instantaneous blending discretization schemes are used based on the URANS/LES regions.

Domain dimensions

In LES, the domain size has to be big enough to contain the largest turbulent scales. Hence, the biggest turbulent scales that could develop in these simulations are of the order of H. The value of H was chosen as 1000 m because it about the height of the ABL with neutral stratification, but mostly for simplicity. Additionally, it is necessary to verify that the results obtained by a simulation are domain independent. To this end, several simulations with varying domain

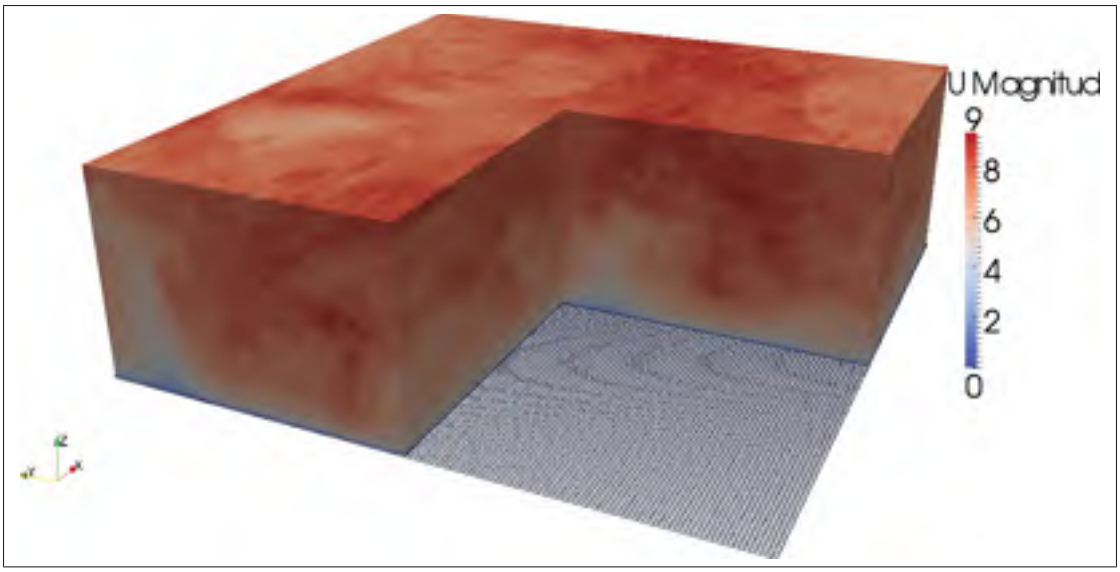

Figure 4.4 Magnitude of the filtered instantaneous velocity field computed for an ideal ABL simulation ($\Delta_u/H = 0.020$ and a $z_0 = 0.4$ m). The domain dimensions and turbulent nature of the flow can be appreciated. Units: [m/s].

width were carried out while keeping the streamwise length as $L_x = 3H$ and the height as $L_z = H$. The results are compiled in Figure 4.5. When the domain width is smaller than $3H$ a speed-up effect can be seen. This could be misinterpreted as being caused by the LLM. When $L_y = 3H$, the simulations are not strictly domain independent. Nevertheless, the different in the results is minimal and at the same time, the computational cost is kept low. Additionally, other authors have used this domain size for ABL simulations (Brasseur and Wei, 2010).

SIDDES model constants calibration

The $k-\omega$ SST model constants for atmospheric flows given in Table I-1 are employed on these cases. These constants have not been used in combination with DES and SIDDES, therefore their overall effect on the results had to be studied. In has been shown for a similar DES hybrid model, that the LES results do not depend on the RANS constant C_μ (equivalent to β^*) (Bechmann and Sørensen, 2010), suggesting that the value of such constant is not relevant in the LES region. Likewise for the $k-\omega$ SST-DES it was verified that the LES results are not affected by the choice of RANS constants and the height at which URANS switches to

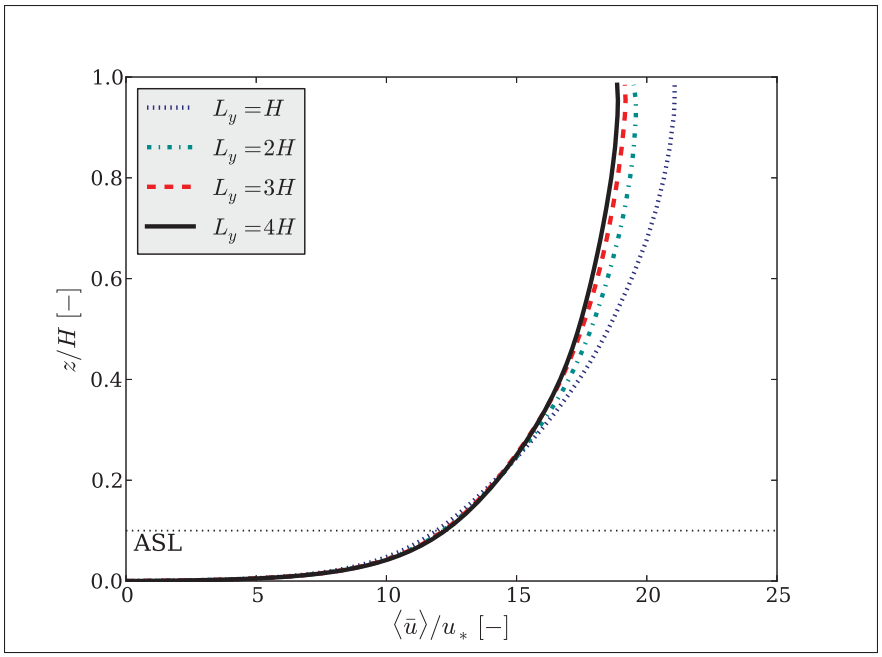

Figure 4.5 Averaged velocity profiles for ideal ABL simulations for varying domain widths. A $\Delta_u/H = 0.025$ and a $z_0 = 0.4$ m was used.

LES remains roughly the same. On the other hand, the effect that the SIDDES model constant c_{d1} has on the URANS and LES regions is shown in Figure 4.6a. Only the results with a $\Delta_u/H = 0.020$ mesh are shown but other meshes were investigated and similar results were obtained. It was found that by decreasing the value of c_{d1} the URANS region becomes smaller, however, the LLM correction becomes less effective and the results worsen. For example, the velocity profile (not shown) and turbulent kinetic energy profile (Figure 4.6b) are also affected by this small value of c_{d1}. The possible LLM becomes slightly more prominent and the turbulent kinetic energy results are not accurate within the ASL. Based on these findings, it was determined that the SIDDES constants for aerodynamic flow are also valid for atmospheric simulations. Then if the size of the URANS region wants to be reduce and at the same time keep the logarithmic profile valid, the mesh has to be refined.

Using the $k - \omega$ SST model constants for atmospheric flows has a considerable impact on the URANS to LES zone ratio. For example, in all the channel flow cases from Section 3.4 the URANS region only covered at the most 10% of the computational domain, and it does

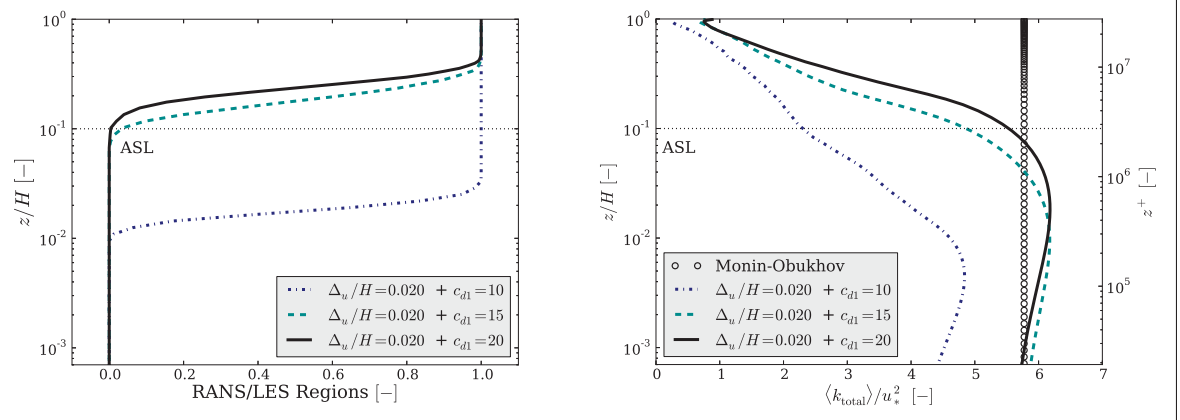

(a) Time-averaged URANS/LES regions taken at the mid-plane for c_{d1} constant calibration. A region of 1.0 is equivalent to pure LES, while a region of 0 represents pure URANS.

(b) Averaged total turbulent kinetic energy

Figure 4.6 SIDDES model constant verification for atmospheric flows with the $\Delta_u/H = 0.020$ mesh and $z_0 = 0.1$ m

not seem to depend on the Re_{D_h} or the wall roughness. However for the pressure driven atmospheric flow cases, the URANS region increased to 20-40% of the domain depending on the mesh refinement. The reason for this is the smaller value of β_* used on the atmospheric flow cases. A smaller β_* causes a considerable increase on the modelled turbulent kinetic energy k, and consequently on l_{RANS}. Notably, this yields a larger value of l_{SIDDES} and a larger URANS zone.

DES vs. SIDDES results

The advantages of SIDDES over DES can be appreciated in Figure 4.7. The LLM is evident in the DES results and it worsens as the roughness increases; whereas the SIDDES is able to predict a logarithmic profile in the ASL region. Another approach to avoid the LLM using DES could be to add a backscatter model (Bechmann and Sørensen, 2010). The DES are more computationally expensive, e.g. the $z_0 = 0.4$ m case model with DES and no backscatter model required more than twice the CPU time than a SIDDES on the same grid. The reason for the difference on the computational cost is the extent of the URANS regions which are less

expensive compared to an LES in the near-wall region. In SIDDES simulations, the URANS regions are relatively big compared to DES simulations where only a couple of cells in the near-wall region are solved in URANS mode. This can be seen in Figure 4.8.

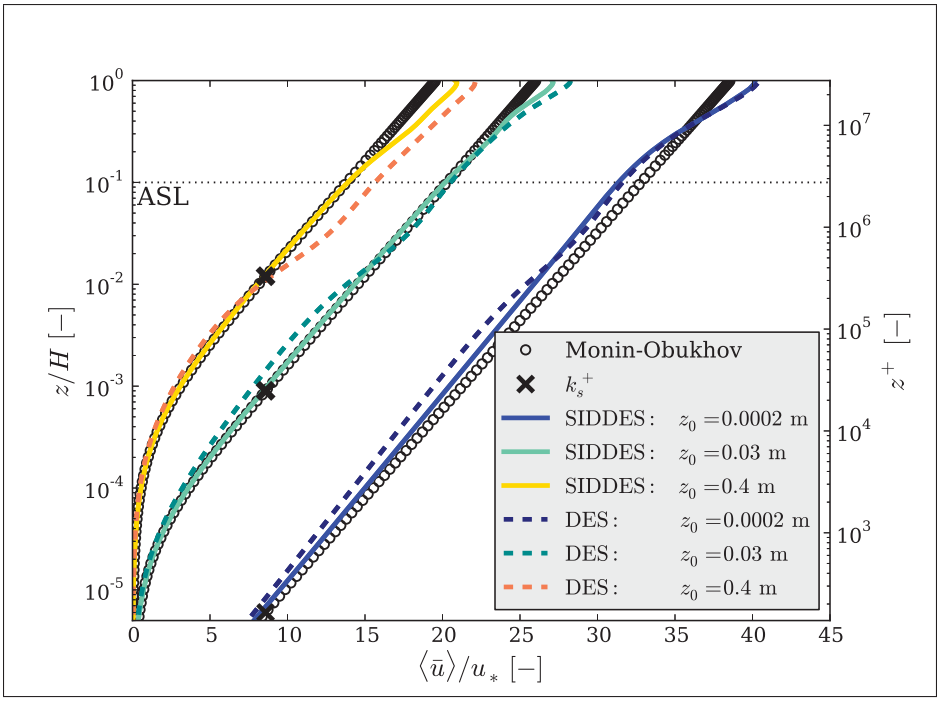

Figure 4.7 DES vs. SIDDES velocity profiles for the $\Delta_u/H = 0.015$ mesh.

Height of the first cell

All the simulations carried out so far have a z_1 which is defined based on a inner scale $z_1^+ = u_* z_1/\nu$ of the order of 1.0 as required by the roughness extension (Section 2.2.1.1). However, it is a common practice in ABL simulations to use the outer scale $\zeta_1^+ = z_1/z_0 \sim 1.0$ to define the first node. The impact of defining z_1 based on z_1^+ or ζ_1^+ will be analyzed using a $\Delta_u/H = 0.020$ mesh. On the analysis carried out previously for the different roughness heights cases, the same mesh was always used because z_1^+ does not depend on z_0. On the contrary, a different mesh will be required of each roughness value if z_1 is defined based on the outer scale. The meshing technique is the same for all cases.

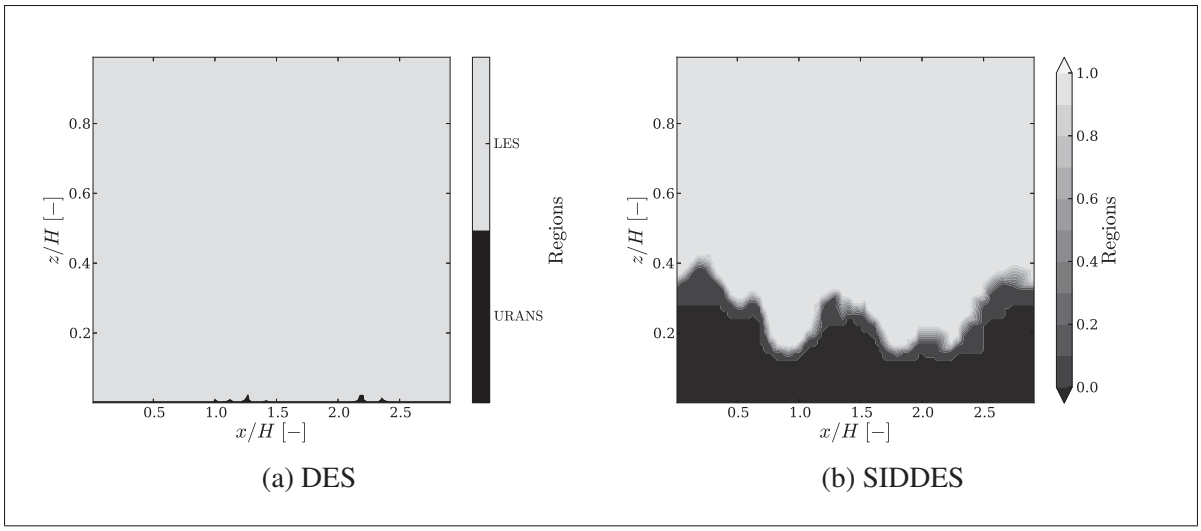

(a) DES (b) SIDDES

Figure 4.8 Instantaneous URANS/LES regions taken at middle plane. A region which is light grey (or has a value of 1.0) is equivalent to pure LES, while a black region (or has a value of 0) represents pure URANS. The plots show the results from the $\Delta_u/H = 0.020$ mesh and the $z_0 = 0.4$ m case. Axes are not to scale.

As mentioned in Section 2.2.1.1, $k-\omega$ SST simulations with a roughness extension and no wall function do not yield accurate results if $z_1 \sim z_0$. However this is not what it was observed in this SIDDES implementation. Possibly the negligible viscous stresses in high Reynolds and extreme roughness values present in the atmospheric flows allow the relaxation of the roughness extension requirements. Results in Figure 4.9a show that the velocity profiles for the mesh with $\zeta_1^+ \sim 1.0$ are almost identical to the $z_1^+ \sim 1.0$ results. However the former mesh has significantly less cells especially for the $z_0 = 0.4$ m case which has only $(150 \times 150 \times 66)$[2] making it more practical for ABL simulations. On the other hand, the turbulent kinetic energy results shown in Figure 4.9b present a non physical peak close to the wall. This is a known phenomena on under resolved ABL grids (Sumner *et al.*, 2010). The peak per se may not be a problem since it is located below physical height of k_s, but that might not always be the case. Nonetheless, the computation of u_* at the first node is highly overestimated (e.g. up to 40% for the $z_0 = 0.4$ m case) on those under resolved meshes. Still the $\zeta_1^+ \sim 1.0$ meshes only require around 15% of the running time needed for the $z_1^+ \sim 1.0$ meshes and the URANS/LES region ratio is rather the same. For the remaining simulations in this work, a $z_1^+ \sim 1.0$ will be used.

[2]Compared to the $z_1^+ \sim 1.0$ mesh that has $(150 \times 150 \times 130)$.

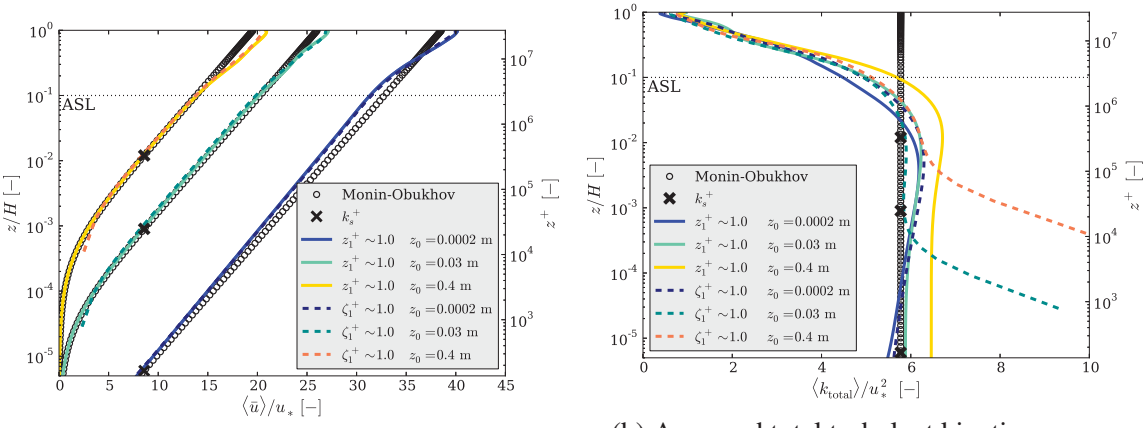

(a) Averaged velocity profiles

(b) Averaged total turbulent kinetic energy profiles

Figure 4.9 Idealized ABL velocity profiles for different roughness lengths using the $\Delta_u/H = 0.020$ mesh.

SIDDES mesh study

Finally, different mesh resolutions have to be investigated. Figure 4.10 compares the velocity results of the five grids given in Table 4.2. For all meshes the mean velocity profile follows the logarithmic law in the ASL up to $\sim 20\%$ of the domain, which is consistent with other LES of ideal ABL cases in the literature (Porté-Agel *et al.*, 2000). However if a slight LLM is still present (as shown in Section 3.4), it may appear to move towards the wall as the mesh is refined. On the other hand, a finer mesh resolves smaller eddies and gives more information about the turbulence flow and its particular characteristics. This can be visualized in Figure 4.11 where the instantaneous filtered velocity fluctuations are presented.

In Figure 4.12, the total mean kinetic energy is constant inside the ASL as predicted by the Monin-Obukhov theory. Nevertheless, the simulations do not agree with the turbulent kinetic energy calculated using the empirical velocity variances of the neutral ABL (given in Eq. 1.10). But these simulations are just an approximation of the real ABL which could explain in part that discrepancy.

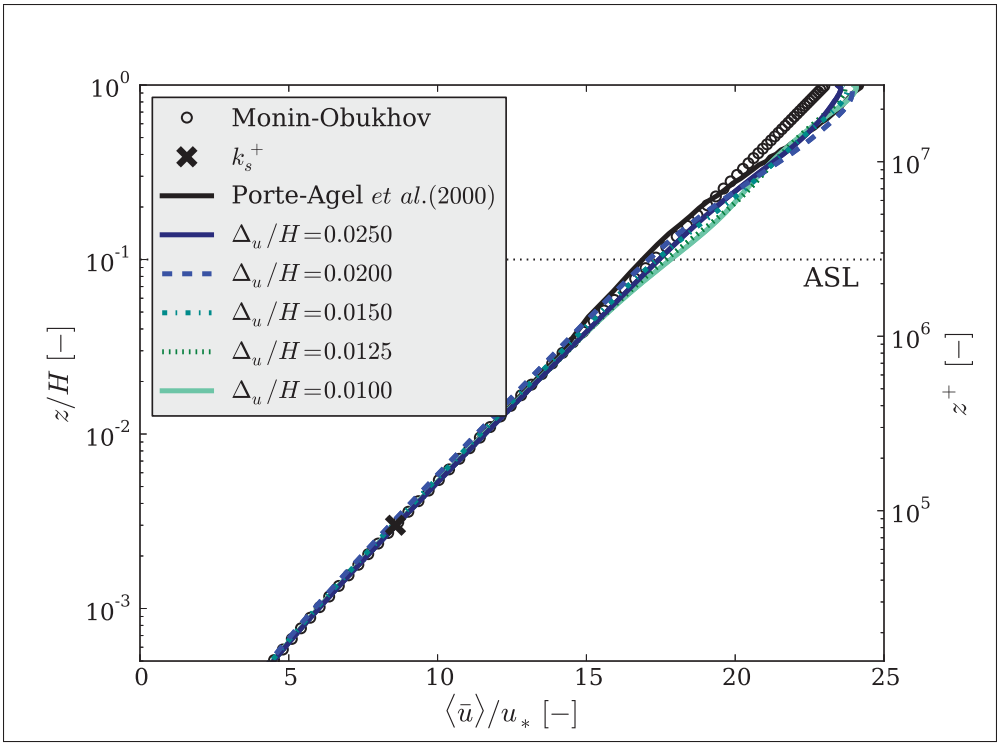

Figure 4.10 Averaged velocity profiles for ideal ABL simulations with the SIDDES model and a $z_0 = 0.1$ m for different mesh resolutions. Porté-Agel *et al.* (2000) data corresponds to the standard dynamic Smagorinsky model results from such article.

The turbulent kinetic energy obtained by a hybrid model is also highly dependent on the mesh resolution as well as the distance to the solid wall as expected. The modelled and resolved components of the turbulent kinetic energy for two different resolutions are presented in Figure 4.13. The modelled turbulent kinetic energy k predominates close to the wall and it is negligible far from it. It is crucial to be aware that the value of k depends on the $k-\omega$ SST model constants. On the other hand, the resolved component $\overline{k}$ behaves in the opposite manner, and the model constants do not have a direct impact on its value. It can also be observed that $\overline{k}$ starts to increase or developed closer to the wall for the finer mesh. This same phenomenon can also be verified in Figure 4.14 which displays the variance of each velocity component. From here it can be deducted that the velocity fluctuations tend to zero close to the wall, but they start to developed away from it. Additionally, it can be see that the finer mesh velocity variance results are in closer agreement than the coarsest mesh.

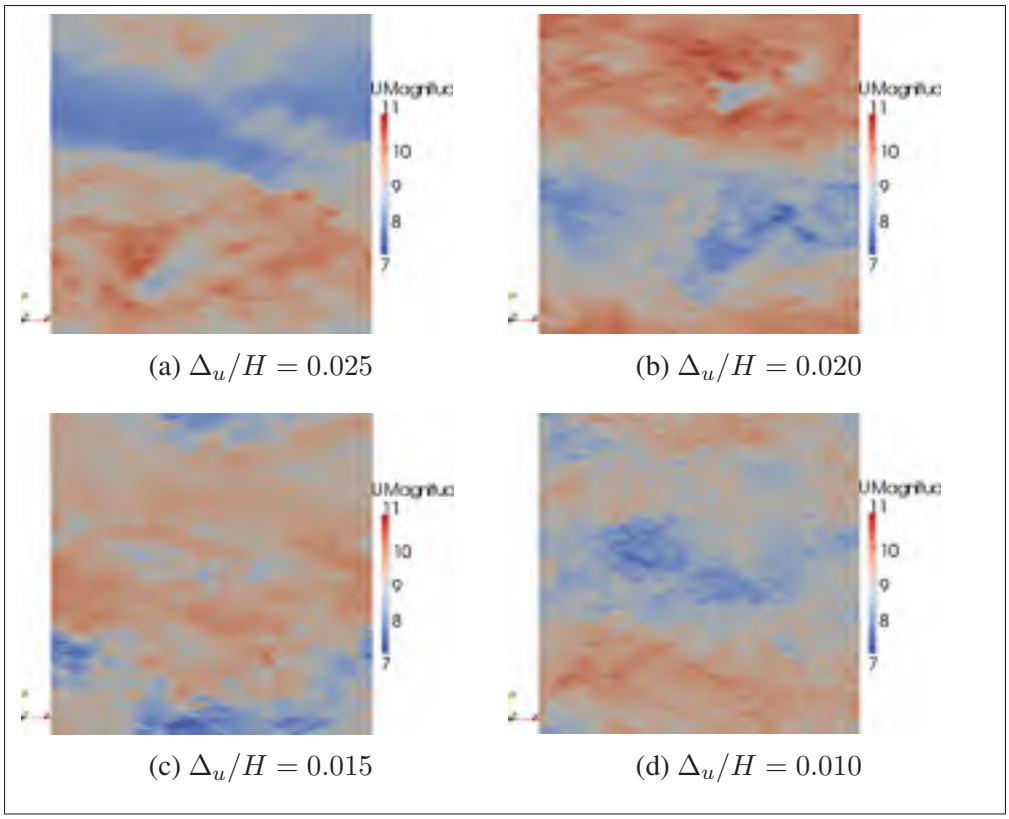

(a) $\Delta_u/H = 0.025$ (b) $\Delta_u/H = 0.020$

(c) $\Delta_u/H = 0.015$ (d) $\Delta_u/H = 0.010$

Figure 4.11 Magnitude of the instantaneous filtered velocity field yielded by different mesh resolutions at $z/H = 0.8$. Units: [m/s]

Figure 4.15 shows unequivocally how the time-averaged URANS region diminishes as the mesh resolution increases. The same effect can be visualized on the time and space averaged value of the URANS and LES regions displayed in Figure 4.16. The considerable URANS region that needs to be solve to avoid the LLM is a great advantage because it provides a good surface model to treat the wall effects, and it reduces greatly the computer cost. At the same time, this URANS region could also be a main drawback. In certain cases, for example in a turbine wake analysis where it is advantageous to solve the wake in a LES region, the required mesh resolution to push the LES zone closer to the ground might be too demanding[3].

[3]Preliminary results of this subject were presented as a conference proceeding paper: Nathan J., Bautista M.C., Masson C. and Dufresne L. "Study of the near wake of a wind turbine in ABL flow". In *The Science of Making Torque with the Wind*. Technical University of Denmark (Copenhagen, Denmark.) June 18-29, 2014.

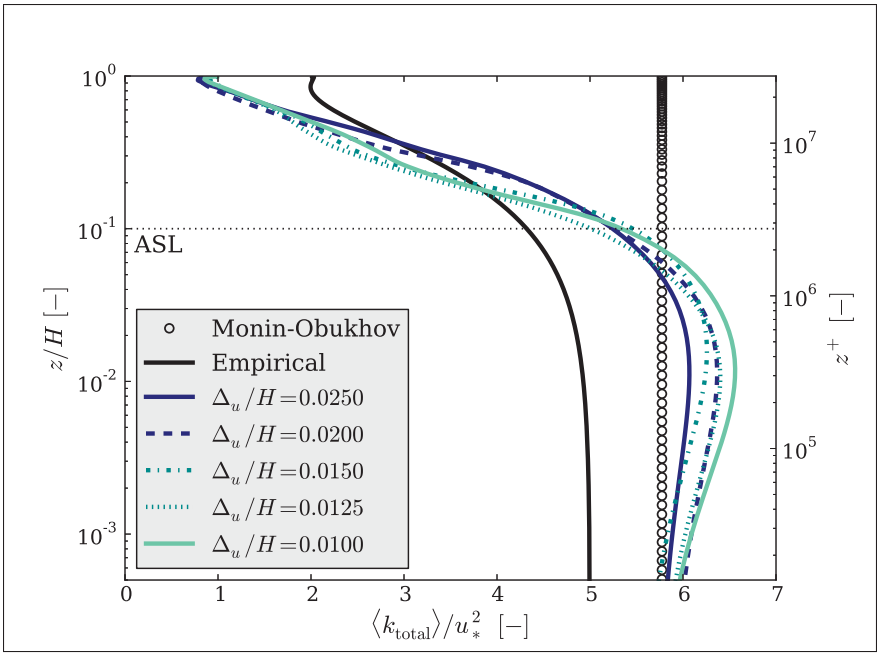

Figure 4.12 Averaged total kinetic energy for ideal ABL simulations with the SIDDES model and a $z_0 = 0.1$ m. The empirical value was calculated based on the ABL variances (Stull, 1988).

Another crucial parameter that needs to be discussed is the non-dimensional mean velocity gradient $\langle\phi_m\rangle = (\kappa z/u_*)\partial\langle\overline{u}\rangle/\partial z$. The Monin-Obukhov theory predicts that $\langle\phi_m\rangle = 1.0$ inside the ASL, but ABL simulation using LES models do not always achieve this conclusion. Most often, a peak or "overshoot" is seen on LES simulation, and this has been a subject of great debates and struggles. The SIDDES results are compiled in Figure 4.17.The results show an excellent agreement with the theory, but these results might be misleading. The reason for the absence of the overshoot is due to the large URANS region that cover almost all the ASL. It is also evident that the larger URANS zone, the higher the $\langle\phi_m\rangle$ remains equal to 1.0.

Brasseur and Wei (2010) developed certain criteria for atmospheric LES simulations to properly remove the overshoot in $\langle\phi_m\rangle$, satisfy the logarithmic law scaling in the ASL, and ensure that a simulation is moved to what the authors called the "high accuracy zone". These criteria include the adjustment of the number of cells in the vertical direction, the model constant and the grid aspect ratio. In this reference, it is mentioned that these criteria could also be used for

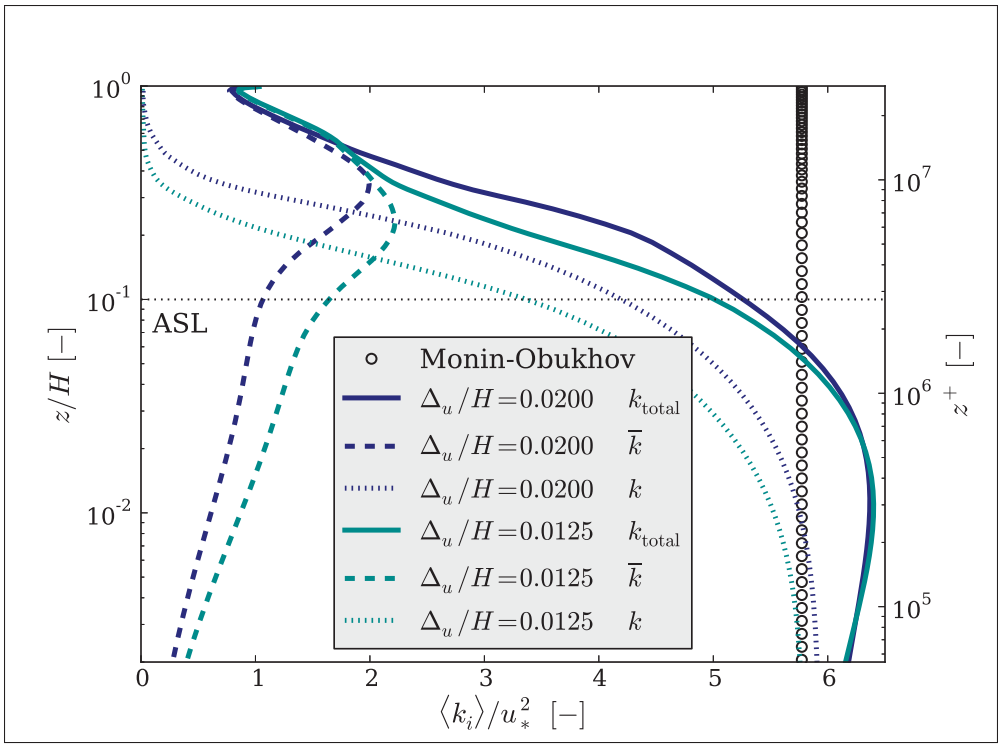

Figure 4.13 Averaged turbulent kinetic energy components for the ideal ABL with $z_0 = 0.1$ m.

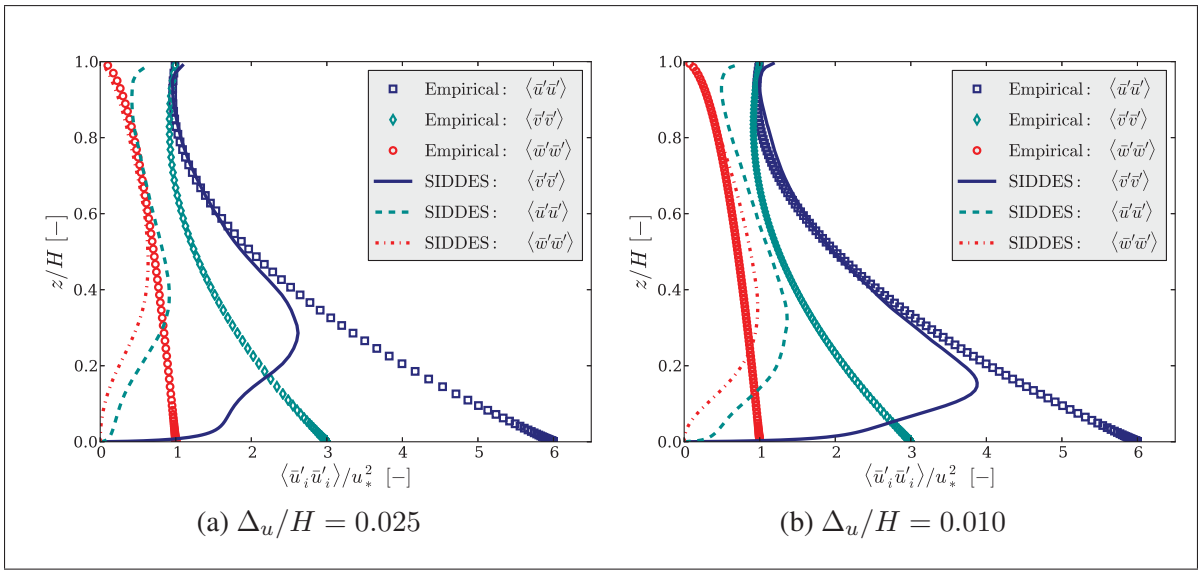

(a) $\Delta_u/H = 0.025$ (b) $\Delta_u/H = 0.010$

Figure 4.14 Velocity variances for the ideal ABL with $z_0 = 0.1$ m.

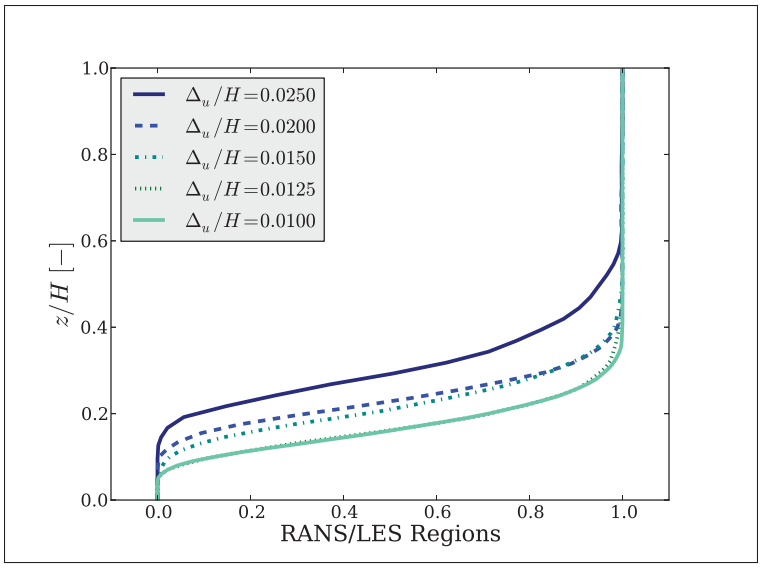

Figure 4.15 Time-averaged URANS/LES regions at mid-plane in an ideal ABL simulation with a $z_0 = 0.1$ m. A pure LES region is represented as 1 and a pure URANS is 0.

hybrid models to avoid the LLM when the URANS region is taken as the fist "effective grid cell". Carrying out the exact process to guarantee that the SIDDES test cases are located within the high accuracy zone is not as straight forward because the URANS to LES transition height is not fix in space nor in time. However the calibration verification of the SIDDES model constants demonstrated that with a c_{d1} value of 20.0, the LLM is minimum, the turbulent kinetic energy peak is not existent (when $z_1^+ \sim 1$) and the $\langle \phi_m \rangle = 1.0$ in the surface layer.

Finally to complete this study, the filtered velocity spectra are investigated. Since ABL measurement campaigns provide time series of the velocity value at a particular location (e.g. with an anemometer at a fixed position), a temporal spectrum is often computed. A spectra from a time series is defined as

$$E_{ij}(f) = \frac{1}{T} \int_{-\infty}^{\infty} B_{ij}(\tau) e^{-i2\pi f \tau} \mathrm{d}\tau, \tag{4.6}$$

where the correlation function $B_{ij}(\tau) = \langle u_i(t) u_j(t') \rangle$ depends only on $\tau = t - t'$. Also the frequency f equals to $1/\tau$. To make a more strict comparison to the one-dimensional *spatial*

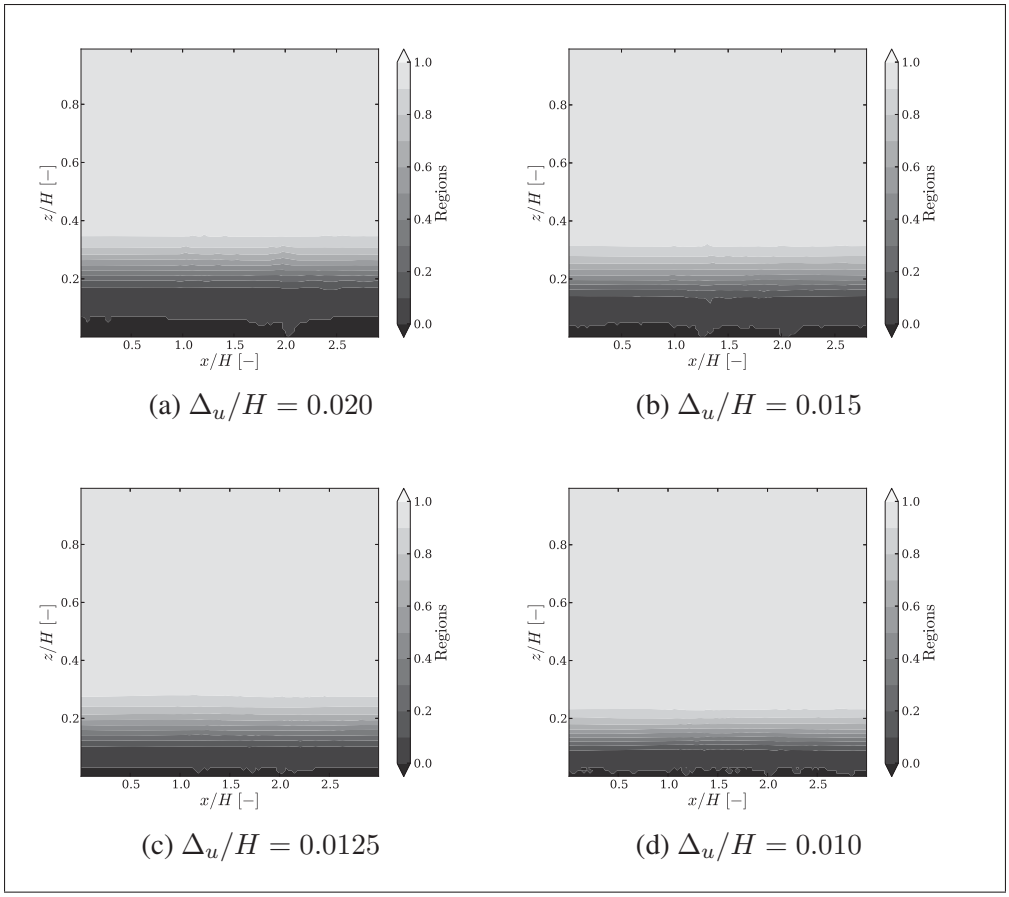

(a) $\Delta_u/H = 0.020$ (b) $\Delta_u/H = 0.015$

(c) $\Delta_u/H = 0.0125$ (d) $\Delta_u/H = 0.010$

Figure 4.16 Averaged URANS/LES regions. The snapshots are taken at the middle vertical plane. Pure LES equals 1.0 and pure RANS is 0.0.

spectra calculated on Section 3.1, the Taylor hypothesis and $\kappa_1 = 2\pi f/\langle\overline{u}\rangle$ will have to be employed (Drobinski *et al.*, 2007). However, the main concern of this test is to validate the results with numerical and experimental studies of the ABL, hence only the $E_{ii}(f)$ will be computed using the Welch method.

The longitudinal $E_{11}(f)$ and vertical $E_{33}(f)$ power spectra are presented in Figure 4.18. They are normalized in the same manner as Drobinski *et al.* (2004). The spectra computed at the lower region of the domain have much lower resolved energy and decay rapidly. This is expected because those spectra are located on URANS regions. For this reason unfortunately the whole layered structured of the ASL cannot be verified. For example, $E_{11}(f)$ in the near-wall region should vary from $E_{33}(f)$ and from the spectra farther from the ground; this is due most

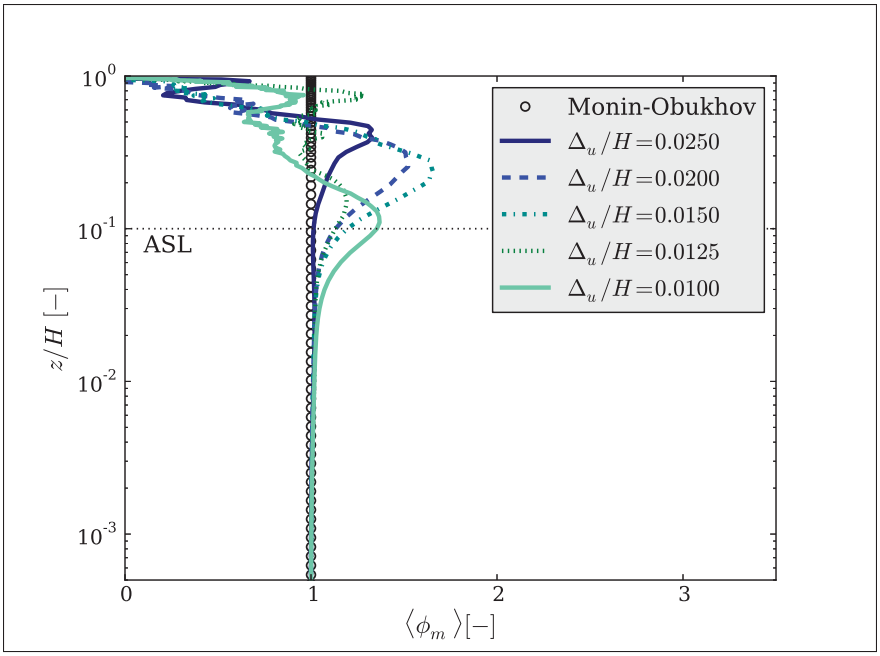

Figure 4.17 Non-dimensional mean velocity gradient for an ideal ABL simulation with the SIDDES model and a $z_0 = 0.1$ m.

probably to blockage mechanisms (Drobinski *et al.*, 2004). This cannot be appreciated with the SIDDES results. Nevertheless in the mentioned figures, it is evident that as the height increases and the LES regions are reached (above $z/H = 0.20$) the spectra follow the correct behaviour. In other words, a -1 power-law is clearly visible at the intermediate frequency range (displayed as a 0 power-law in the plot due to the normalization), while the high frequency range presents the characteristic $-5/3$ slope ($-2/3$ in the plot due to the chosen normalization) of the inertial subrange.

The eddies included in the spectra intermediate frequency range are bigger and have a larger time scale, and because those large eddies are affected by the shear, they are highly anisotropic. Additionally, this region is where the turbulence is generated (Drobinski *et al.*, 2004). On the other hand, the high frequency slope of $-5/3$ is consistent with nearly isotropic eddies that have an almost constant transfer of energy across the different turbulent frequencies (Drobinski *et al.*, 2004). Shorter lived eddies can be resolved by finer meshes. But since the inertial range is clearly present on Figure 4.18, it can be concluded that the spatial resolution of the mesh and

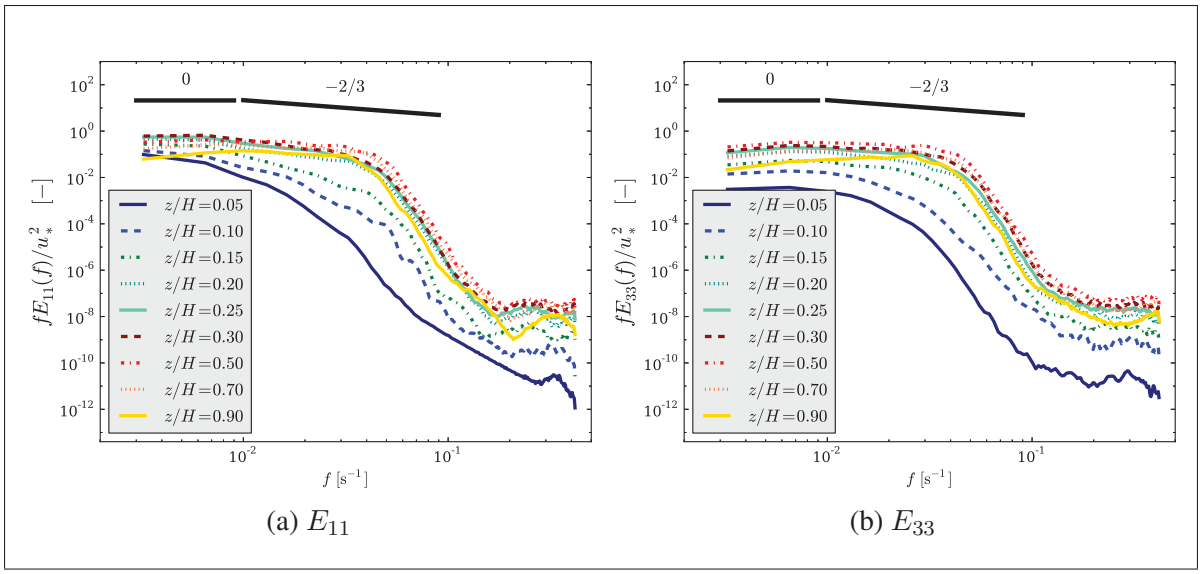

(a) E_{11} (b) E_{33}

Figure 4.18 Longitudinal and vertical spectra of the ideal ABL with $z_0 = 0.4$ m and $\Delta_u/H = 0.020$ resolution.

the subgrid model discretization are appropriate (Drobinski *et al.*, 2004). The energy contained at the highest frequencies is several orders of magnitude smaller than on other frecuencies. Therefore, this can be considered simply as noise, and most reference do not show this portion of the spectrum. Figure 4.19 shows once more that shorter lived eddies can be resolved by finer meshes. Lastly, the inertial range is clearly present on the LES regions (here shown at $z/H = 0.5$) for all the cases. Thus, it can be concluded that the spatial resolution of the simulations and the subgrid model discretization are appropriate (Drobinski *et al.*, 2007).

4.2.2 Pressure driven atmospheric flow with Coriolis force

Lastly, the effect of taking the Earth's rotation into consideration is investigated. The microscale simulations that have been performed through this study have a $U_{ref} \approx 10$ m/s in the streamwise direction and a domain size of $L = 3000$ m. Assuming a latitude of $\varphi = 45°$ and the angular velocity of the Earth $w_{\text{Earth}} = 2\pi/24\,\text{hours} = 7.27 \cdot 10^{-5}\,\text{s}^{-1}$, the Coriolis parameter $\mathsf{f} = 2w_{Earth}\sin\varphi$ will be approximately $1 \cdot 10^{-4}\,\text{s}^{-1}$. This yields a large scale Rossby number of $Ro_L = U_{ref}/\mathsf{f}L \approx 30$. Therefore the inertial forces are rather significant compared to the Coriolis forces, and the later could be neglected. Nevertheless, it has become a common

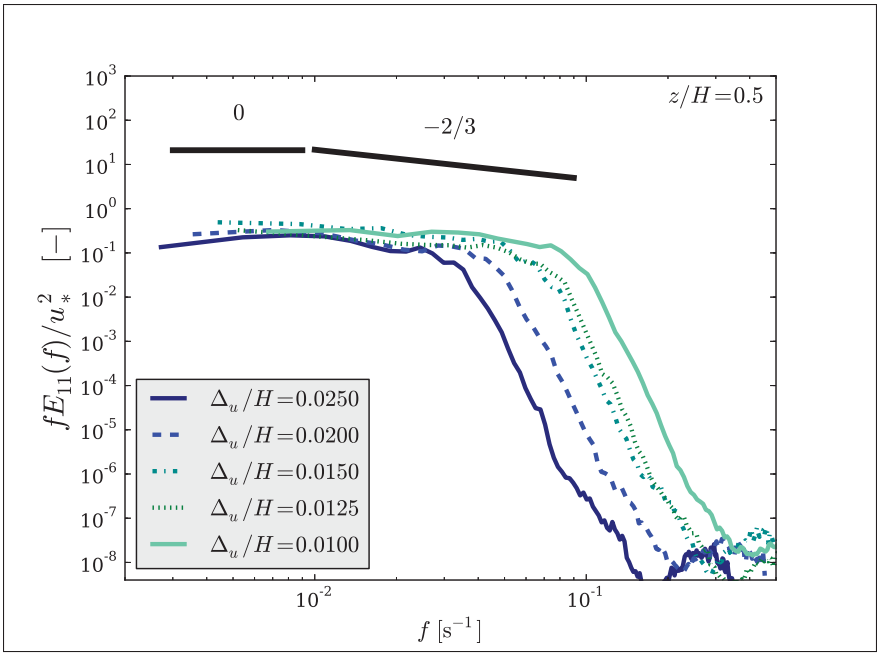

Figure 4.19 Spectra from ideal ABL simulations with the SIDDES model and a $z_0 = 0.1$ m.

practice to include the rotation effects at a microscale level (e.g. Churchfield *et al.* (2014)), possibly in an attempt to merge microscale and mesoscale software.

To include the Coriolis force in the ABL simulations two important steps have to be followed. First the Coriolis force term $\mathbf{F}_C = -2\boldsymbol{\Omega} \times \mathbf{u}$ has to be added to the momentum equation. Here $\boldsymbol{\Omega} = (0,\, w_{\text{Earth}} \cos\varphi,\, w_{\text{Earth}} \sin\varphi)$ represents the Earth's angular velocity vector at a latitude φ. Second the large scale pressure gradient term that drives the flow has to be adjusted with respect to previous simulations. The computation of this driving pressure gradient is once again calculated following the procedure shown in Section 3.4. But for a steady and horizontally homogeneous flow that includes the Coriolis force, the hybrid model momentum equations become

$$\frac{1}{\rho}\frac{\partial\langle\overline{p}\rangle}{\partial x} = +\,\mathsf{f}\langle\overline{v}\rangle + \frac{1}{\rho}\frac{\partial\langle\overline{\tau}_{xz}\rangle}{\partial z} \tag{4.7}$$

$$\frac{1}{\rho}\frac{\partial\langle\overline{p}\rangle}{\partial y} = -\,\mathsf{f}\langle\overline{u}\rangle + \frac{1}{\rho}\frac{\partial\langle\overline{\tau}_{yz}\rangle}{\partial z} \tag{4.8}$$

for the streamwise and spanwise direction respectively. This balance between pressure, Coriolis and frictional forces describe the Ekman layer. At the top of the atmosphere, the geostrophic wind is the result of only the Coriolis and pressure forces, since at that height the frictional forces are negligible. Following the procedure given in Bechmann (2006), this simplifies to

$$\frac{1}{\rho}\frac{\partial\langle\overline{p}\rangle}{\partial x} = +\,\mathsf{f}\langle v_g\rangle \tag{4.9}$$

$$\frac{1}{\rho}\frac{\partial\langle\overline{p}\rangle}{\partial y} = -\,\mathsf{f}\langle u_g\rangle \tag{4.10}$$

Therefore for a geostrophic wind that drives the flow in the streamwise direction $(u_g, v_g, w_g) = (u_g, 0, 0)$, the large scale pressure gradient is given by

$$\mathbf{F} = \left(\frac{\partial\langle\overline{p}\rangle}{\partial x}, \frac{\partial\langle\overline{p}\rangle}{\partial y}, \frac{\partial\langle\overline{p}\rangle}{\partial z}\right) \tag{4.11}$$

$$\mathbf{F} = (0,\ -\rho\mathsf{f}\langle u_g\rangle,\ 0) \tag{4.12}$$

When the Coriolis force is being considered at a microscale level only some minor differences are perceived. Figure 4.20 shows two simulations with and without Coriolis forces. The choice of mesh resolution for this simulations is not ideal, a better conclusion could have been reached if a finer mesh had been used. In spite of this it can be observed that the spanwise velocity is different than zero only for the Coriolis case, thus the Ekman layer forms. On the other hand, the streamwise velocity component is not really affected. To emphasize this findings, Figure 4.21 illustrates a snapshot of the velocity field at a certain height. If observed in detail, it can be seen that the Coriolis case presents velocity streaks that are not aligned with the streamwise direction, while this orientation offset is not visible in the case without Coriolis. Also because of the large URANS zones, the near-wall streaks studied by Drobinski and Foster (2003) could not be compared with this coarse mesh. Finally based in Section 3.2, it is expected that the Earth's rotation does not affect the turbulence statistics.

Results show that the roughness height is a relevant factor in the development of the Ekman spiral. Figure 4.22 displays the averaged velocity profiles computed by simulations of the ABL

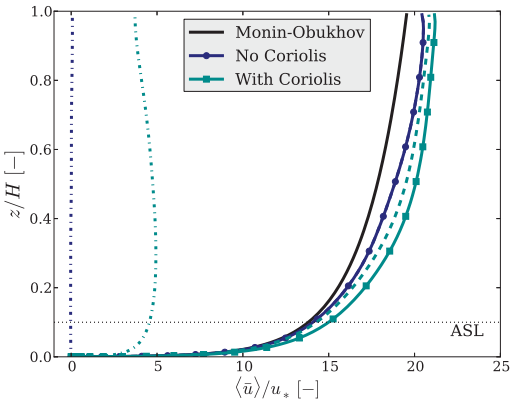

(a) Averaged velocity profiles. −−: $\overline{u}$-component, −. : $\overline{v}$-component and −: $U = \sqrt{\overline{u}^2 + \overline{v}^2}$.

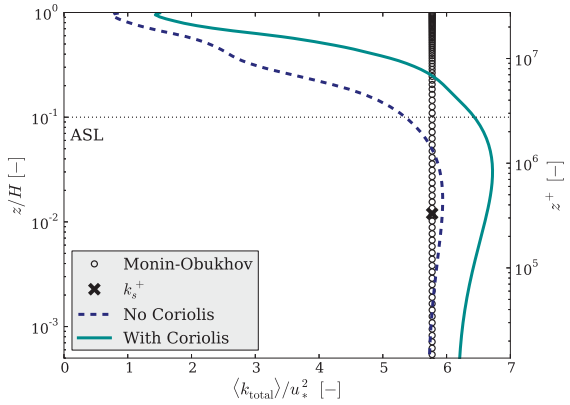

(b) Averaged total kinetic energy

Figure 4.20 ABL simulations with the SIDDES model, a $z_0 = 0.4$ m and $\Delta_u/H = 0.020$ mesh. The effects of the Coriolis force are explored. Different scales are chosen for each plots to better highlight the discrepancies.

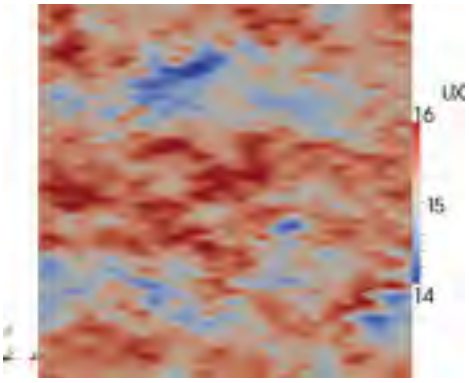

(a) No Coriolis

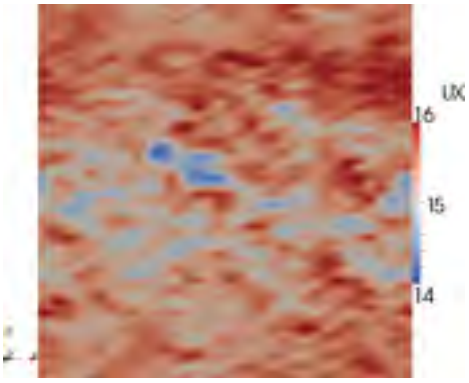

(b) With Coriolis

Figure 4.21 Instantaneous velocity field taken at $z/H = 0.8$. Simulations used the SIDDES model, a $z_0 = 0.0002$ m and $\Delta_u/H = 0.020$ mesh. Units: [m/s].

with different roughness z_0, nevertheless this effect can be better appreciated in Figure 4.23. It can bee concluded that the cross-isobaric angle θ of the Ekman spiral increases as the roughness increases, as reported by other references (Bechmann, 2006).

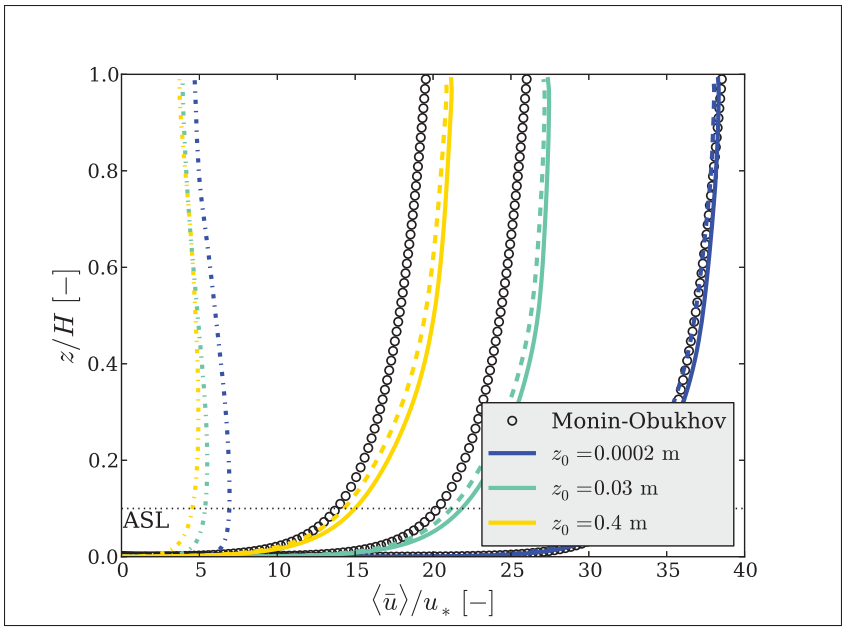

Figure 4.22 Averaged velocity profiles.
−: without Coriolis −−: with Coriolis force

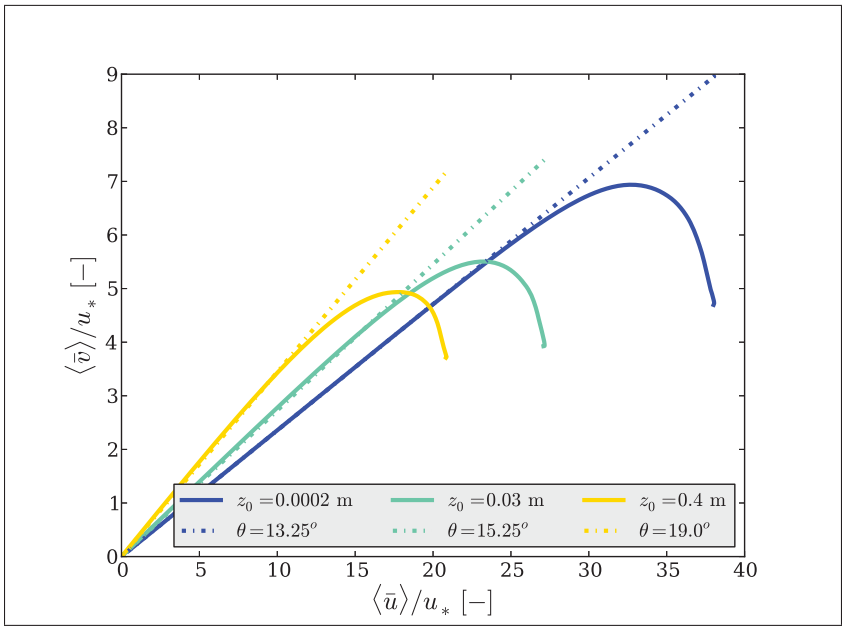

Figure 4.23 Ekman spiral generated by different roughness length simulations

4.3 Høvsøre field measurement campaign: neutral case

One of the most recent and complete field measurement campaign was carried out in Høvsøre, Denmark (Peña *et al.*, 2014). Accurate observations with modern instrumentation were performed for a period of 1-year over nearly homogeneous flat terrain under various stratification conditions. Peña *et al.* (2014) clearly indicates all the ABL conditions during each observation period and it provides a thorough explanation of the data analysis. Additionally WRF (Weather Research and Forecasting mesoscale model (The WRF community, 2015)) simulations were performed for the different observed stratification cases. Such experimental measurement as well as the WRF modelling results are accessible online. The neutral stratification case (refer to Case 5 on the mentioned reference) is simulated using the $k-\omega$ SST-SIDDES hybrid microscale model. The comparison of the results will determine the accuracy of the hybrid model implementation over a "real and full-scale" natural flat terrain.

The microscale simulation is performed on a domain of size of $(L_x,\, L_y,\, L_z) = (3H,\, 3H,\, H)$ where $H = 1150$ m. Such height is chosen to be consistent with the ABL height obtained by the WRF simulation (i.e. 1120 m). Additionally the measured terrain roughness is $z_0 = 0.015$ m. The mesh contains about $8.2 \cdot 10^6$ cells and it follows the same meshing technique as the previous cases. The cells have an expansion ratio of 1.15 up to a height of $z_u/H = 0.1$, from there all the cells are cubic with a $\Delta_u/H = 0.013$. The domain boundary conditions are the same as for the previous flat terrain cases. The large scale driving pressure gradient is calculated as on Section 4.2.2 based on the velocity measured at H, thus $(u_g,\, v_g) = (17.81,\, 7.83)$ m/s. Also a latitude of $\varphi = 56.43°$ is used to calculate the Coriolis factor. The velocity field is initiated with a logarithmic profile for the streamwise component, a linear slope profile for the spanwise component, and some added random fluctuations on all three components. Because the value of v_g is non zero in this case, the initial spanwise component is computed a bit differently than previously done. Thus the velocity streamwise component was initiated with a logarithmic profile as before, but the spanwise component was defined by a linear profile. Lastly, $\pm 20\%$ of random fluctuations were added to all three initial velocity components.

The resultant averaged URANS region represents only 20% of the domain, thus around 200 m. The measured friction velocity is $u_* = 0.70$ m/s (Peña *et al.*, 2014) while the microscale simulation yield a value of $u_* = 0.66$ m/s. The measured velocity is in agreement with the logarithmic profile for the entire ABL, as mentioned by Peña *et al.* (2014). The WRF mesoscale simulations as well as the $k - \omega$ SST-SIDDES microscale results predict the streamwise velocity field correctly as it can be seen in Figure 4.24. However, the spanwise velocity component is rather overestimated by the hybrid microscale model. While a neutral ABL is the simplest stratification case, the $k - \omega$ SST-SIDDES model together with the microscale simulation implementation yield accurate results for the magnitude of the velocity.

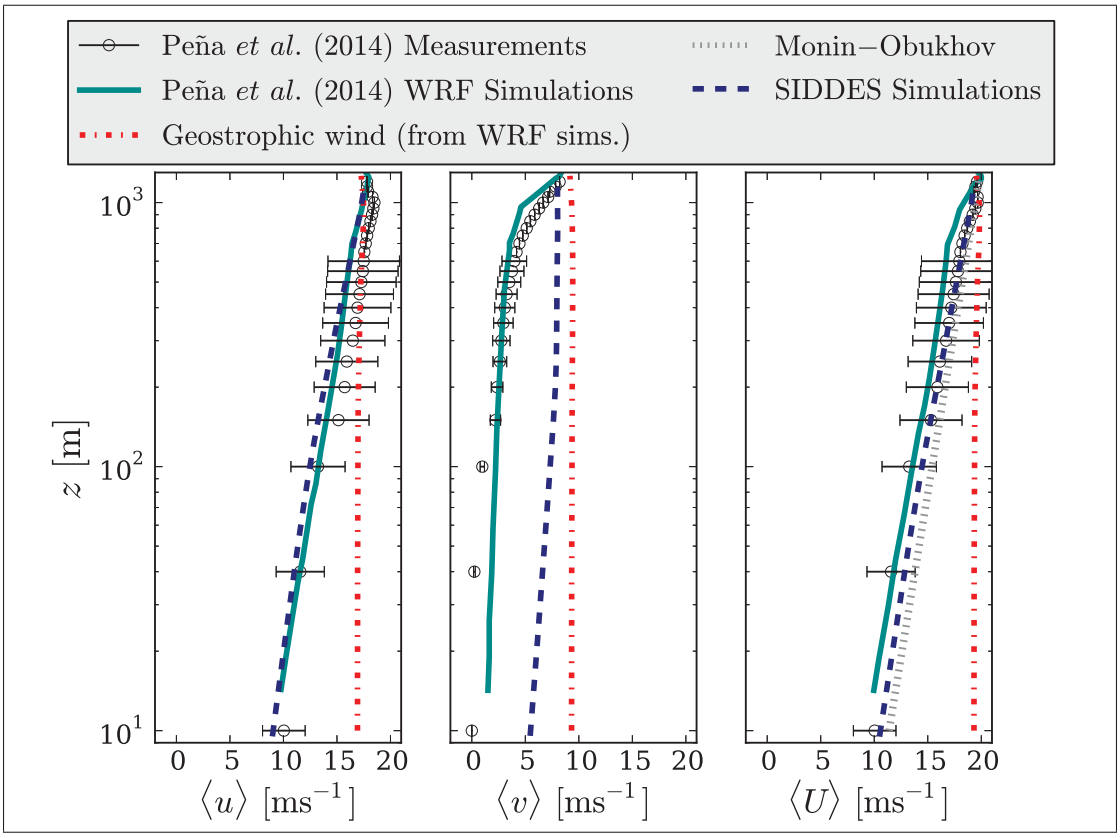

Figure 4.24 Averaged velocity profiles of the Høvsøre neutral case

4.4 Summary

The $k-\omega$ SST-SIDDES hybrid model is thoroughly validated for neutral atmospheric flows over flat and homogeneously rough terrain. To this end, microscale ASL and ABL simulations were performed. A summary of their boundary conditions and other parameters are given in Table 4.3.

Table 4.3 Boundary conditions for atmospheric flow cases without Coriolis

	ASL	**ABL**
bottom:	no-slip + roughness ext. (Eq. 2.30)	no-slip + roughness ext. (Eq. 2.30)
top:	fixed shear stress	stress-free (*slip*)
streamwise:	periodic	periodic
spanwise:	periodic	periodic
F (in Eq. 2.12):	0	$F_i = \partial P/\partial x = u_*^2/H$
$\overline{u}_0$:	logarithmic + random fluctuations	logarithmic + random fluctuations

The neutral ASL case was simulated using the RANS $k-\omega$ SST model and the $k-\omega$ SST-DES and $k-\omega$ SST-SIDDES hybrid models. A simple model comparison proved to be not an easy task due to the different techniques used to drive the flow in RANS and hybrid models. The results for the ASL case show that the RANS model agrees with the theory, while the velocity and turbulent kinetic energy profiles computed with the hybrid models are not accurate. Therefore, it is not ideal to model the ASL using hybrid/LES models.

As for the microscale neutral ideal ABL case, only the hybrid models were studied. The RANS simulation was not carried out for the lack of a lengthscale delimiter. It was observed that the SIDDES model compensates for the LLM correctly thus it provides more acceptable results than DES. Nevertheless in atmospheric cases, the URANS region is much bigger for the SIDDES model. This large URANS zone might be an important drawback of this model. The study of other flow characteristics and turbulence statistics yield results that are in agreement with the literature. It can be concluded that this type of boundary conditions and method to drive the flow give accurate results for hybrid simulations.

The $k-\omega$ SST-SIDDES model behaviour is better understood as a result of the flat terrain study. It has been demonstrated that the hybrid model captures the correct features of a simplified atmosphere model when the Coriolis effects are neglected and when they are included. Additionally, it has been verified that the hybrid model yields results of the velocity magnitude which are in agreement with the neutral case of the Høvsøre measurement campaign and WRF simulations. Nevertheless, the major achievement of this analysis is the development of a turbulence model with the following characteristics:

- The wall treatment is less dependent on flat terrain assumptions (i.e. no wall function required nor a velocity or a shear value is imposed to the first cell)
- The description of the turbulent flow that could be attained is more detailed and complete due to the LES methodology.
- The computer cost might be reduced without highly compromising the accuracy of the results because of the hybrid approach.

Consequently the SIDDES hybrid model based on the $k-\omega$ SST equations is expected to be a good candidate for complex terrain simulations.

CHAPTER 5

MICROSCALE ATMOSPHERIC FLOW SIMULATIONS OVER COMPLEX TOPOGRAPHY

To conclude the analysis of the ABL using the hybrid model $k-\omega$ SST-SIDDES, the flow behaviour will be studied over complex terrain. When heterogeneous terrain or an obstacle is modelled, the boundary conditions on the streamwise direction need to be redefined. Contrary to the flat terrain cases, a simple periodic condition might not be accurate for complex terrain cases. An obstacle will most likely influence the nature of the flow for a considerable distance far downstream. Then if periodic boundaries are used and the domain is not sufficiently long, the effects of the obstacle will be wrongly reintroduce at the inlet. Alternatively an inlet profile and an outlet boundary condition have to be defined.

A simple mean logarithmic profile at the domain entrance is not sufficient for LES test cases. Inlet flows must include the unsteady and turbulent flow behaviour, as well as other special considerations to reproduce the natural characteristics of the wind (Uchida and Ohya, 2003). Numerous methods exist to generate these realistic inflows. For instance, randomly generating isotropic fluctuations in the velocity components and adding them to the mean velocity profile at the inlet (Troldborg, 2008), increasing the computational domain and defining buffer zones between the inlet and the region of interest to allow for the flow to become turbulent (Uchida and Ohya, 2003), or using a precursor simulation (e.g. Bechmann (2006) or as done by Churchfield *et al.* (2014)). This latest method computes first a streamwise periodic simulation of the wind flow over flat terrain, then for every time step, the resulting flow field at a particular plane is mapped to the inlet of the complex terrain simulation (Castro *et al.*, 2003). A simple analysis of some methods to generate an inflow will be done.

Neumann boundary conditions will be used for the outlet, meaning that $\partial\phi/\partial x = 0$ for any variable ϕ. Then in order to avoid having a singular solution, the value of the pressure must be set at a certain location. However, it has been observed (e.g. (Bechmann, 2006)) that this type of condition could sometimes yield a non-physical flow behaviour near the outlet. Another

solution can be to increase the computational domain and simply disregard a buffer zone close to the outlet, or to apply a convective outflow (Uchida and Ohya, 2003).

The complex terrain analysis will include the simulation of simplified test cases that represent idealized complex terrains. Typically such simplified cases are carried out experimentally in a wind-tunnel and include detailed measurements of the flow characteristics. Thus, a thorough comparison of the fluid behaviour in the experimental measurements and the modelling results can be done. Nevertheless quantifying the error and uncertainties of those comparisons is not simple (Oberkampf and Trucano, 2002).

Lastly, the final challenge is to use the hybrid turbulence model to predict the actual three dimensional complex flow induced by a full scale terrain. The wind industry uses field measurements, like the ones taken at Askervein hill in Scotland (1982-1983) (Salmon *et. al.*, 1988) and the peninsula of Bolund in Denmark (2007-2008) (Berg *et al.*, 2011) as reference real validation test cases. Nevertheless, the data obtained in a field campaign is not as detailed as the ones from a wind-tunnel experiment. In real terrain, a couple measuring masts are placed strategically at different places and at different heights, but the horizontal and vertical resolution of this data is very limited. Based on so few data points, it is hard to critically qualify the performance of a turbulence model; nevertheless, it is now the only viable option to validate real terrain.

Following all these considerations, the simplified test case of square-section cylinder will be modelled. This case was chosen mainly because of the detailed and recent wind-tunnel measurements that are available for comparison. Lastly, a simulation of the Askervein hill case will be carried out and compare against measurement obtained in full scale complex terrain.

5.1 Flow around a square-section cylinder

Complex phenomena arises when a fluid encounters an obstacle like a 3D square-section cylinder mounted on a smooth surface. The flow can exhibit unsteadiness, separation and reattachment points, wake formation, vortex shedding, and a non-trivial wall interaction that entails

significant challenges for the numerical simulations. Several experiments have shown that the nature of the flow and wake formation depends on the Reynolds number (Lim *et al.*, 2007), the surfaces condition (Lim *et al.*, 2009) and aspect ratio of the square-section cylinder (Sakamoto, 1983), as well as the characteristics of the approaching flow (i.e. the turbulence intensity and the boundary layer height relative to the obstacle height) (Castro and Robins, 1977; Wang *et al.*, 2006).

Numerous attempts to model the flow around other similar square cylinder cases have been carried out using different turbulence models, but the results are not been fully consistent with the experimental measurements (Sagaut, 2006). In this section, numerical simulations of the flow around a square-section cylinder are undertaken. The focus of these simulations is not be to carry out a complete and through comparison against all the available experimental results. Instead, the purpose is simply to verify if the hybrid model can reproduce some of the phenomena already seen by the mentioned authors.

The numerical simulations were defined based on the CFD Society of Canada 2012/2013 Challenge wind-tunnel experiment (http://www.cfdcanada.ca/challenge). The details about the experimental setup and results can be found on Bourgeois *et al.* (2011) and Sattari *et al.* (2011). Essentially the computational case-study includes a square cylinder with a cross-section of $d = 12.7$ mm and a height of $h = 50.4$ mm (aspect ratio $h/d \approx 4$). The domain size is $(L_x,\, L_y,\, L_z) = (9h,\, 4h,\, 3h)$ which represent the streamwise, spanwise and vertical directions, respectively. The mesh is centred at the obstacle which is placed at a distance of $4h$ from the inlet. In order to better reproduce the turbulent flow, and at the same time, to save on computing cost, the grid is divided in three regions with different refinements as seen in Figure 5.1. Therefore, close to the wall and the obstacle, and in the wake formation zone the cells are smaller in size. Additionally, four layers of cells with an expansion ratio of $\Delta\mathfrak{z}_{i+1}/\Delta\mathfrak{z}_i = 1.15$ where added close to the bottom and obstacle walls. $\mathfrak{z}$ represents the perpendicular direction to the nearest wall; thus a vertical refinement is set close to the bottom wall and the top face of the obstacle, and a streamwise and spanwise refinement is imposed around the obstacle sides. The purpose of these layers is to attain as much as possible the $\mathfrak{z}_1^+ = \mathfrak{z}_1 u_*/\nu \approx 1$ as required by

$k-\omega$ SST for smooth walls (Knopp *et al.*, 2009), where u_* is the friction velocity, and z_1 is the perpendicular distance from any wall to the nearest cell centre. Most cell are cubic following the mesh guidelines for DES (Spalart, 2001), except in the interface between the refinement regions and close to the walls. These meshing procedure yields a mesh with approximately $1 \cdot 10^6$ cells. The number of cells might not be notable with current computers resources. However attaining the $z_1^+ \approx 1$ posses a great challenge for the mesh generator in particular at the square cylinder edges. For this reason around the obstacle, the z_1^+ requirement was relaxed to around 10 to avoid faulty meshes (due to the limitations of the mesh generator). While z_1^+ was relaxed up to 2 in the bottom wall. A CFL of 0.7 was used. Lastly, no space averages can be computed in complex terrain cases. In this chapter $\langle\cdot\rangle$ represents a time-averaged value only.

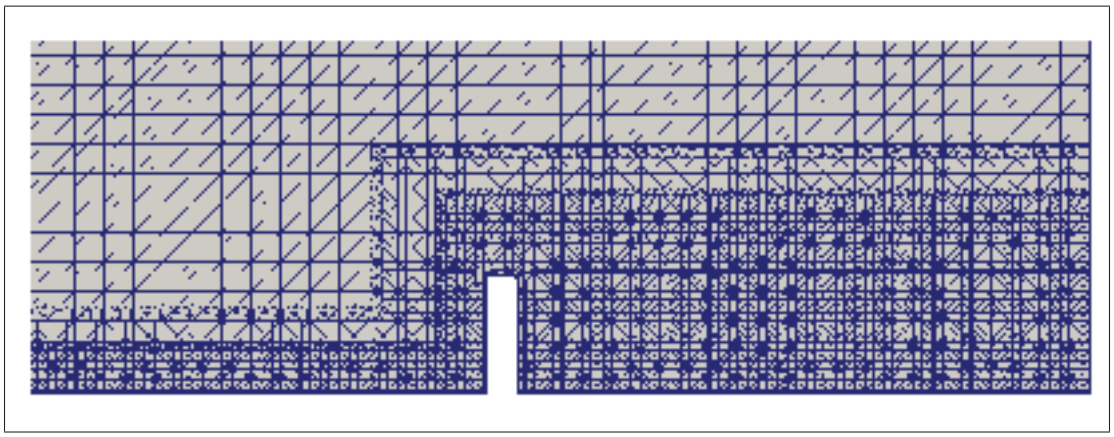

Figure 5.1 Vertical plane of the mesh with three refinement regions. Layers of cells were added close the bottom and obstacle walls to achieve a smaller z_1^+.

The wind-tunnel experiment was carried out with an upstream thin boundary layer flow, in other words, the approaching flow presents a boundary layer which is small compared to the size of the obstacle ($\delta < h$). This is an ideal case to validate the performance of the hybrid models within its original formulation (i.e. solving only the boundary layer with URANS, and using LES everywhere else); but at the same time, this is hardly the case in ABL flows where most likely $\delta > h$. A proper hybrid model validation will require an experiment that comprises measurements where the approaching boundary layer height is small relative to the obstacle

as depicted in Figure 5.2a, and simultaneously where the obstacle is completely immersed on the boundary layer as in Figure 5.2b. It was found that only Castro and Robins (1977) and Castro and Dianat (1983) have performed such experiments for a cubic obstacle. However the experiments are not recent, and most important, only the limited data presented on such articles is publicly available. On the other hand, the experimental results provided by the CFD Society of Canada are complete, detailed and available. For these reasons, the wind-tunnel thin boundary layer data from the CFD Society of Canada 2012/2013 Challenge will be used to verify and analyze the performance of the DES and SIDDES approaches in complex flows. This case will be referred as case A from now on. Furthermore, a thick boundary layer upstream flow case will be studied where $\delta > h$, and it will be labelled as case B. This represents a hypothetical case that was not performed in such wind-tunnel and no experimental data exists. The thick boundary layer case will be examined for two main reasons; first to study the atmospheric flow behaviour on complex cases, and second to investigate how the DES and SIDDES approaches perform when used as WMLES (as explained on the detached-eddy simulation segment found in Section 2.1.1).

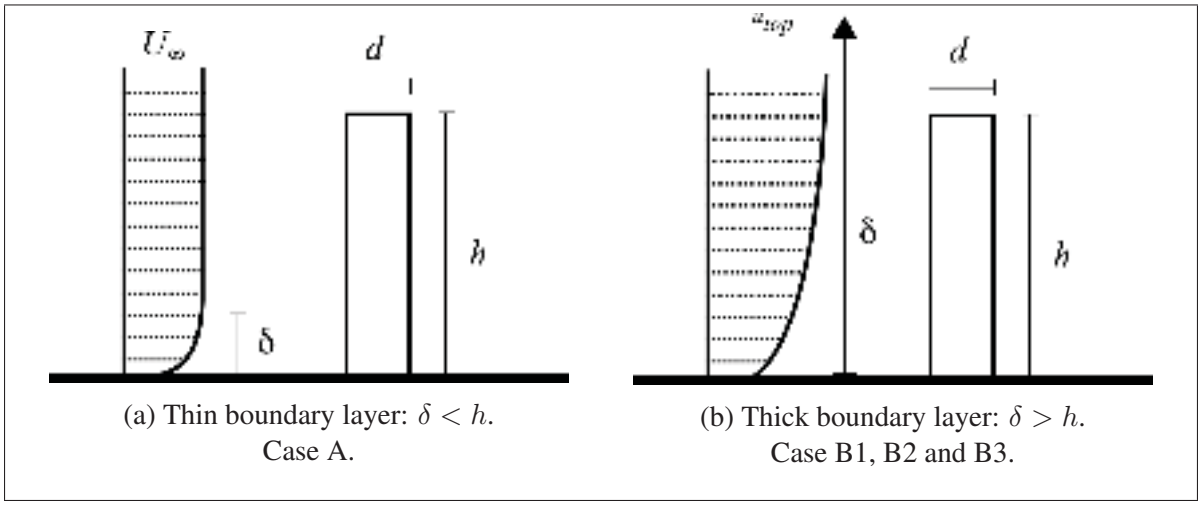

(a) Thin boundary layer: $\delta < h$. Case A.

(b) Thick boundary layer: $\delta > h$. Case B1, B2 and B3.

Figure 5.2 Upstream boundary layer schema (not to scale)

5.1.1 Case A: Approaching thin boundary layer flow[1]

As in the experiment, the free-stream velocity U_∞ is 15 m/s, and the Reynolds number is $U_\infty d/\nu = 11\,000$. The wind-tunnel experiment test without the obstacle yielded a boundary layer with a height of $0.18h$ at a streamwise distance of $4h$, exactly where the obstacle was supposed to be located. Additionally, a free-stream resolved turbulence intensity $\mathrm{TI} = u_{rms}/U_\infty \approx 1\%$ was measured at this same location.

Regardless of all these measurements, attaining a correct inlet boundary condition is a challenging but crucial task. Having a uniform velocity upstream will produce very different results compared to a case with an approaching turbulent shear flow (Castro and Robins, 1977). In this case, the inlet boundary condition was defined by adding some time-correlated random fluctuations to the measured unperturbed velocity profile obtained at $x = 0$ (the obstacle position). These added fluctuations are scaled accordingly to attain the 1% averaged turbulence intensity measured at the obstacle location. Nevertheless, a thorough study was not carried out to verify if this inlet boundary condition generates truly physical turbulence fluctuations. As for k at the inlet, the OpenFOAM boundary condition *turbulentIntensityKineticEnergyInlet* with a intensity of 0.01 was used; while a Dirichlet boundary condition was specified for ω.

A no-slip boundary condition (without a wall function) was set at the bottom and obstacle smooth walls, while $k_w = 0$ and $\omega_w = 60\nu/(\beta_1 \mathfrak{Z}_1^2)$ (using the aerodynamic constants) were calculated following the $k-\omega$ SST recommendations for smooth walls (Menter, 1993). The top boundary condition was defined as a stress-free ($\partial\overline{u}/\partial z = \partial\overline{v}/\partial z = 0$, $\overline{w} = 0$). The lateral boundaries were designated as periodic to avoid constraining the turbulent structures and because the domain is considered sufficiently wide. A Neumann boundary condition (zero-gradient) was imposed at the outlet, such that, $\partial\phi/\partial x = 0$ for any variable ϕ. As for the internal

[1] Preliminary results of this section were published as the conference articles:

- Bautista M. C. Nathan J., Olivares-Espinosa H., Dufresne L., and Masson C. "Flow around a square-section cylinder using $k-\omega$ SST delayed detached-eddy simulation". In *20th Annual Conference of the CFD Society of Canada*, (Canmore, AB, Canada). Mary 9-11 2012.

- Bautista M. C. Nathan J., Olivares-Espinosa H., Dufresne L., and Masson C. "Detached-eddy simulations for complex flow. Analysis of the flow around a square cylinder.". In *21th Annual Conference of the CFD Society of Canada*, (Sherbrooke, QC, Canada). Mary 7-9 2013.

field, it was initialized with the measured unperturbed velocity profile and some added random fluctuations. The simulations ran for at least 15 longitudinal flow-through-times (L_x/U_∞). Then, the time-averaged statistics were gathered for the following 15 flow-through-times or more. Finally, the discretization schemes used are the same as for the flat terrain cases (Appendix III.6), with the exception of the velocity divergence term. It was observed that using *linear* yield unphysical velocity field variations upstream of the obstacle, but the velocity field becomes smoother and the simulation more stable if *filteredLinear* is used instead. The reason for this is that *filteredLinear* introduces locally some upwind components (The OpenFOAM Foundation, 2013).

Before beginning the square-section cylinder simulations, it was necessary to verify that the turbulence models and the boundary conditions selected could correctly represent the flow behaviour in the absence of the obstacle. An empty domain simulation was studied. Its mesh is analogous to the square-section cylinder case; thus it presents the same three refinement regions but without conforming to the obstacle. The time-averaged resolved velocity and $\overline{u}_{rms}$ profiles at the location where the obstacle should be placed are given in Figure 5.3. It is evident that the inlet boundary condition reproduces correctly the time-averaged velocity field at the obstacle location for DES and SIDDES. Figure 5.3a also confirms that the LLM phenomena is not present in any of the hybrid simulations. This was expected because the empty domain case (as well as the square cylinder case) has a grid which is in agreement with the original formulation of the DES model approaches. In other words, the boundary layer height is thin with respect to the domain and the obstacle. As for the resolved turbulence intensity, Figure 5.3b shows that added fluctuations at the inlet ($x/d = -16.0$) need to be slightly higher than 1% to assure the correct turbulence intensity at the obstacle location. Also if these fluctuations are too small, the SIDDES simulations will not always develop a LES region. Additionally, the SIDDES presents larger URANS regions than DES which grow downstream. This can be seen by the reduced amount of resolved velocity fluctuations close to the wall. Finally in Figure 5.4, it can be verified that the Neumann (zero-gradient) boundary condition at the outlet does not generate spurious unphysical behaviour for this case as it has been observed (Bechmann, 2006).

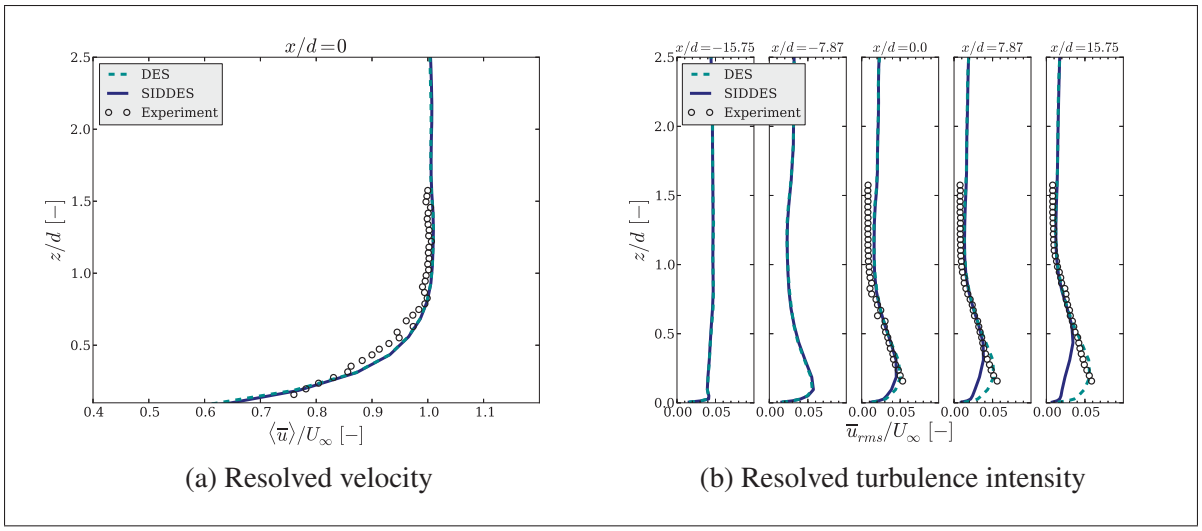

(a) Resolved velocity

(b) Resolved turbulence intensity

Figure 5.3 Case A empty domain case profiles

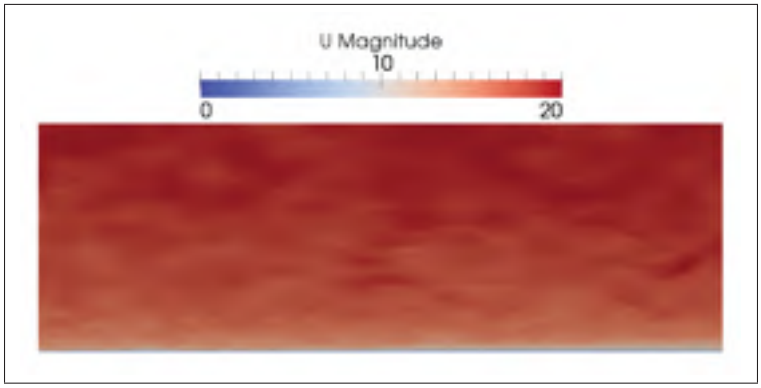

Figure 5.4 Instantaneous velocity for case A. No anomalous behaviour is observed when a zero-gradient boundary condition is imposed at the outlet. Units: [m/s].

Once the boundary conditions were verified on the empty domain, the square-section cylinder simulations were performed using DES, SIDDES and URANS. The first key point that needs to be addressed is the URANS/LES regions on the hybrid models. For complex cases like the square-section cylinder, the switch between regions is not always evident, and the visualization of these regions can provide an insightful perspective about the hybrid model behaviour. Figure 5.5 displays an approximate visualization of these instantaneous regions at the centre plane. With DES only the first few cells close to the wall are solved by URANS, thus, the

URANS regions are hardly visible in Figure 5.5a. As for the SIDDES case, Figure 5.5b shows a slightly larger URANS region close to the walls and a small URANS zone in the upstream region. This is due to the fact that there is not enough turbulent fluctuations and/or the mesh is not fine enough to trigger the development of LES content. As previously mentioned, the URANS/LES regions vary slightly over time.

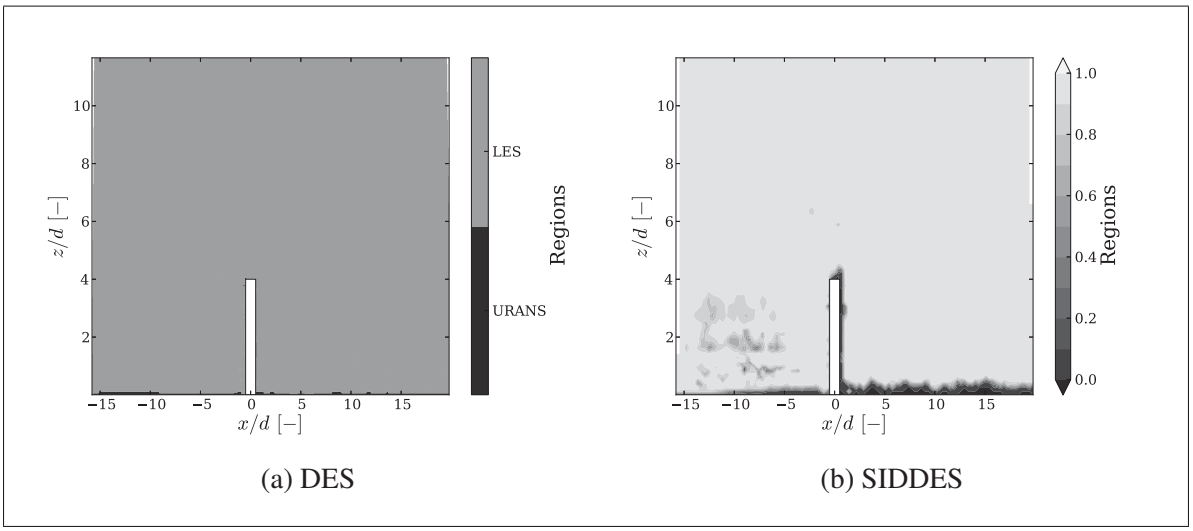

(a) DES (b) SIDDES

Figure 5.5 A snapshot of the URANS and LES regions for case A. A region of value 1 (or grey) represents a pure LES zone, while, a region with a value of 0 (or black) shows a pure URANS zone.

The resolved velocity statistics for the upstream thin layer simulation (case A) are displayed in Figures 5.6 and 5.7. The shape of the time-averaged velocity profile differs slightly from the experimental value close to the wall, nevertheless they are consistent elsewhere. The large z_1^+ value could explain the discrepancy close to the wall. The results obtained by the hybrid approaches are notably similar between them. This is due to the fact that the LES region behind the obstacle is almost the same for both cases, thus the models behaviour should be practically identical. As for the URANS simulations, the obstacle wake presents a larger deviation from the experimental results at mid-obstacle height. The root-mean-square of the resolved velocity fluctuations agrees well with the experimental data close to the wall, but it is slightly overestimated by the hybrid approaches above $z/d \sim 3.0$.

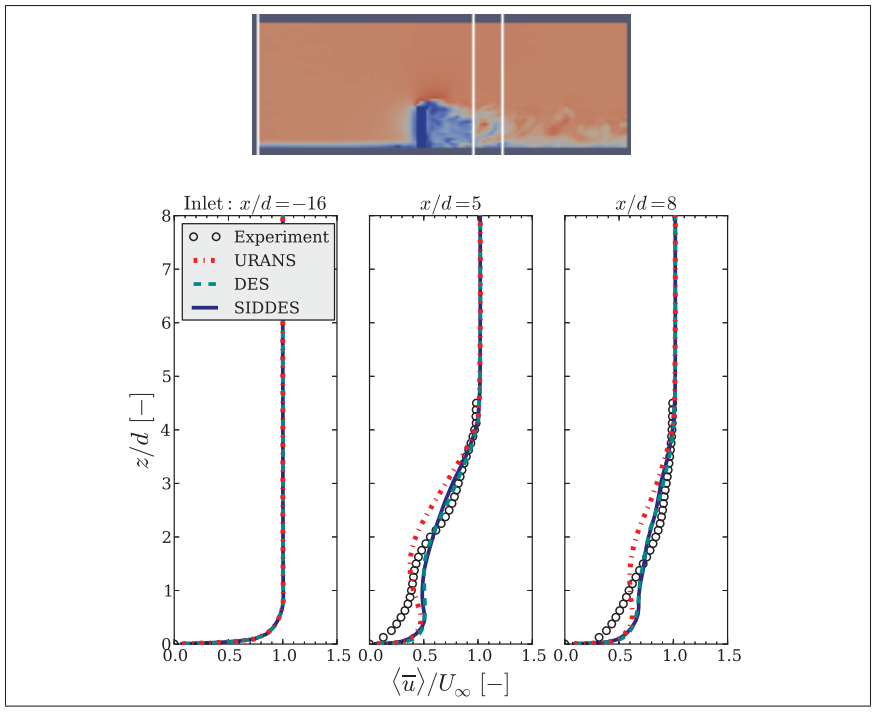

Figure 5.6 Time-averaged velocity at the centre plane for case A. The top schema depicts a cross-section of the instantaneous velocity field and he location of the profiles (white line).

The width of the time-averaged velocity deficit at the wake is shown in Figure 5.8. Only the near-wake region is analyzed as a precaution since zero-gradient boundary condition is imposed at the outlet. The hybrid models yield a slightly slender and smaller wake than the wind-tunnel data, yet the two hybrid models results are in agreement. The URANS simulations also predict a thinner wake. The time-averaged downstream velocity at the wake is displayed in Figure 5.9. The hybrid approaches capture a downstream recirculation zone, but it is not entirely in agreement with the experimental results. This is an important achievement, since it has been shown that steady RANS models ($k - \omega$ SST and Spalart-Allmaras) could fail to reproduced this wake behaviour (Roy *et al.*, 2003). The hybrid models yield similar results, and they slightly underpredict the size of recirculation bubble behind the obstacle. As for the wake predicted by the URANS simulations, it takes it a longer distance to achieve and recover the free-stream velocity observed in the experiments.

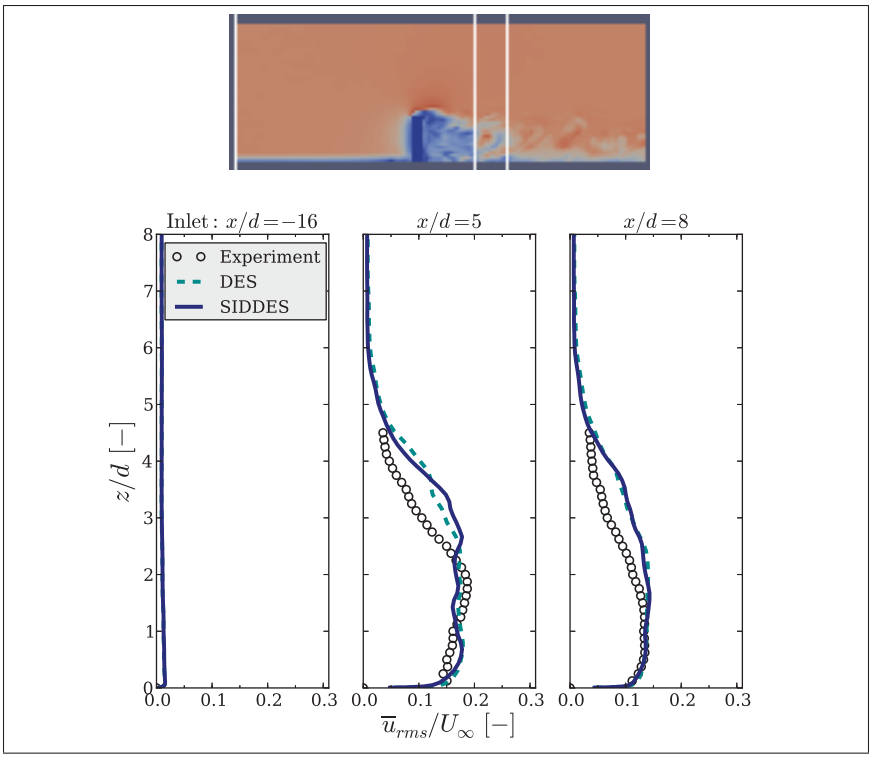

Figure 5.7 $\overline{u}_{rms}$ at the centre plane for case A. The schema shows the position of the profiles (white lines).

To better comprehend the wake, the time-averaged streamwise resolved velocity is displayed on Figures 5.10 at a plane $x = 5d$ downstream of the obstacle. In addition the time-averaged resolved velocity at the horizontal plane $z = 2h$ is compared in Figure 5.11; while Figure 5.12 shows the resolved shear stresses at $x = 5d$. In this last figure it can be appreciated that the DES and SIDDES contour plots are not smooth; this might indicate that a longer time period is required for the averaging process. However in all the planes the numerical and experimental results present a good qualitative agreement overall, but the wake velocity is slightly overpredicted and slender compared to the measured one. This thinner wake does not seem to be the result of blockage effects induced by a domain that is too small. For instance, in Figure 5.8 the velocity at the domain edges is not overpredicted confirming that the domain does not constrain the flow nor causes it to speed-up. A possible explanation to the slender wake could lie on the size of the turbulent scales on the incident flow. For atmospheric flows it has been shown that the wake behaviour, in particular the transverse and vertical movement, is

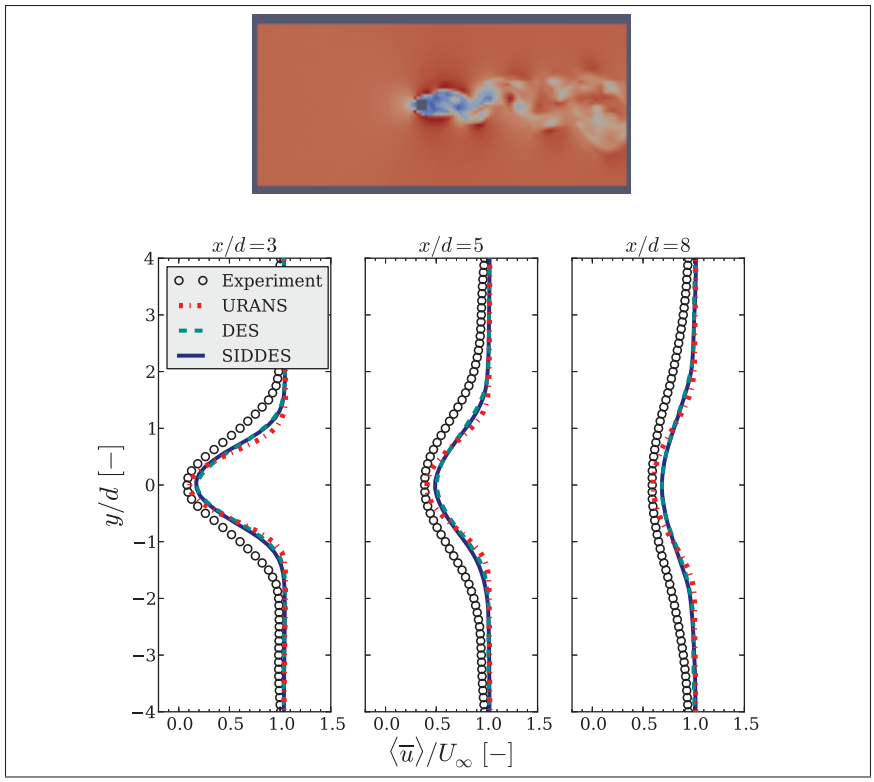

Figure 5.8 Time-averaged wake deficit velocity at a height of $z = d$ for case A. The schema displays the instantaneous velocity and the position of the profiles (white lines).

highly influenced by the large turbulent eddies approaching the obstacle (Muller *et al.*, 2013). The defined inlet boundary condition might not accurately reproduce all the physical turbulent scales required to model the wake correctly, in particular, it may lack appropriate large scale eddies.

The complexity of the wake can be observed in Figure 5.13a and in Figure 5.13b where the vorticity contours clearly show the Kármán-type vortex formation. This type of vortices occur behind square-section cylinder obstacles when $h/d > 2$. The shedding vortices behind obstacles with this large aspect ratio are dominated by the flow coming from the obstacle sides thus asymmetric vortices are generated. On the contrary when the obstacle aspect ratio is smaller, the flow separation at the top of the obstacle dominates and symmetric or arc-type vortices developed (Sakamoto, 1983). By looking at the instantaneous shear stresses at the bottom wall

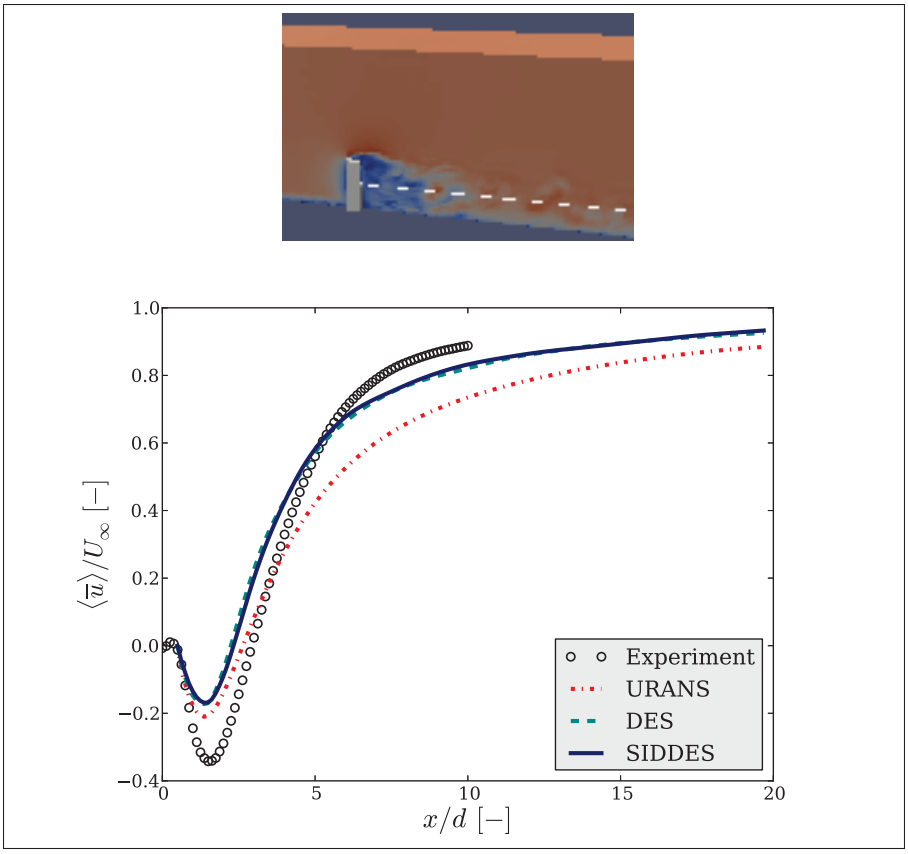

Figure 5.9 Time-averaged velocity of the wake centre-line at a height of $z = 2d$ for case A. The schema displays the instantaneous velocity and the position of the profiles (white lines).

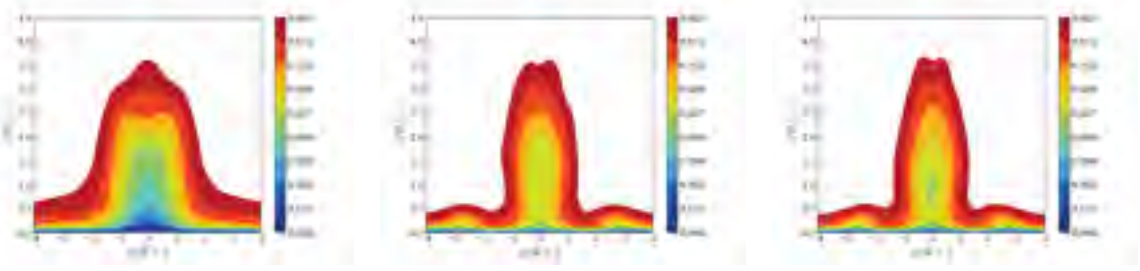

(a) Exp: $\langle u \rangle / U_\infty$ (b) DES: $\langle \overline{u} \rangle / U_\infty$ (c) SIDDES: $\langle \overline{u} \rangle / U_\infty$

Figure 5.10 Comparison of the normalized time-averaged velocity at a plane $x = 5d$ downstream from the obstacle for case A.

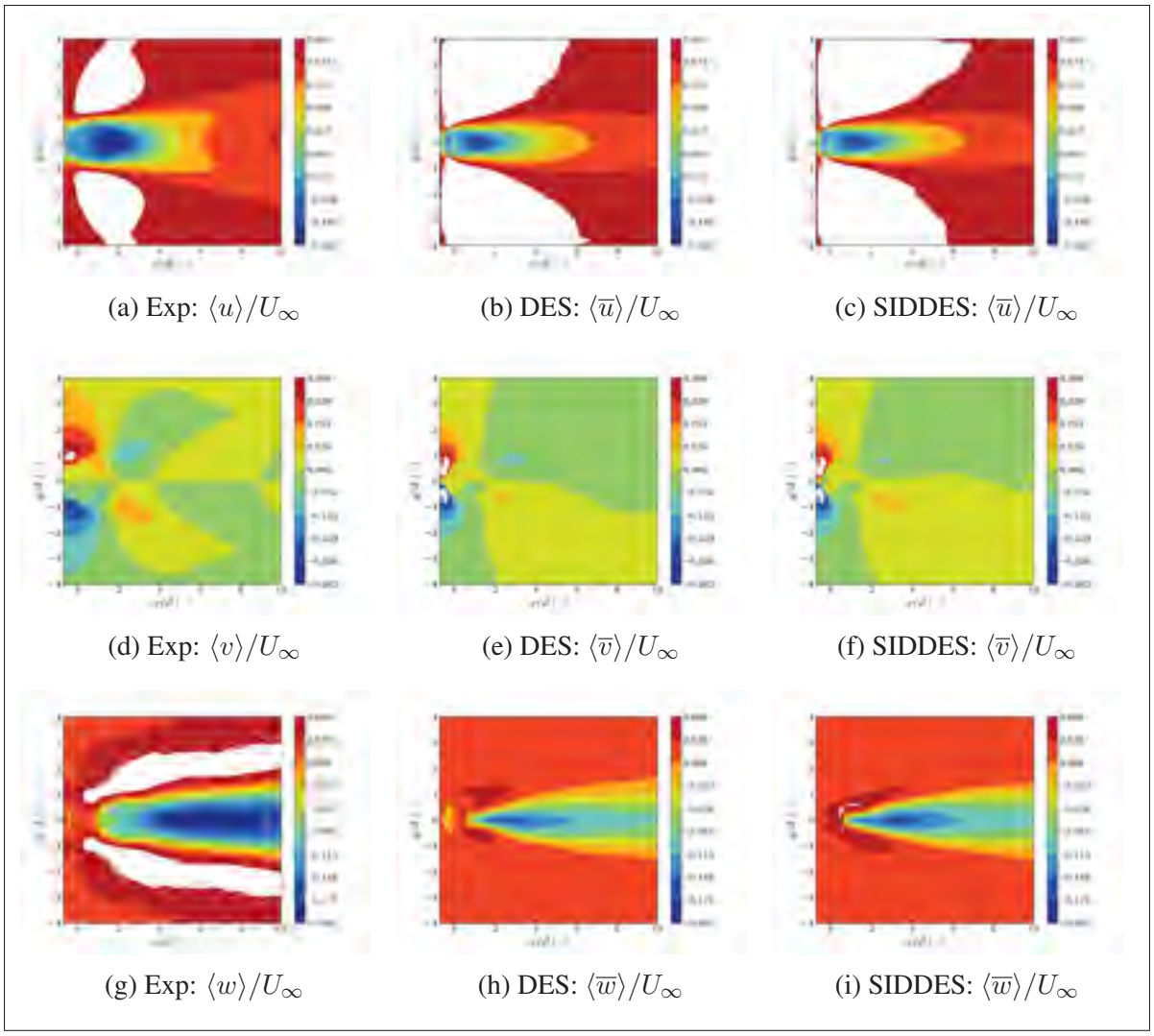

(a) Exp: $\langle u \rangle / U_\infty$ (b) DES: $\langle \overline{u} \rangle / U_\infty$ (c) SIDDES: $\langle \overline{u} \rangle / U_\infty$

(d) Exp: $\langle v \rangle / U_\infty$ (e) DES: $\langle \overline{v} \rangle / U_\infty$ (f) SIDDES: $\langle \overline{v} \rangle / U_\infty$

(g) Exp: $\langle w \rangle / U_\infty$ (h) DES: $\langle \overline{w} \rangle / U_\infty$ (i) SIDDES: $\langle \overline{w} \rangle / U_\infty$

Figure 5.11 Upstream thin boundary layer case wake comparison at $z = 2d$. Case A.

in the hybrid simulations, the Kármán-type vortex can also be seen as display in Figure 5.14. However, the time-averaged shear stresses give a different perception of the flow behaviour.

A visualization of the time-averaged velocity streamlines also sheds further insight of the wake dynamics. In Figure 5.15, two recirculation bubbles are seen; one behind the obstacle and another smaller one located in front at the obstacle's base. A really interesting phenomena is that the reverse flow region behind the obstacle does not reattached at the bottom wall. However, shorter square-section cylinders ($H/d << 3-4$) do reattach at the wall (Wang *et al.*, 2006). This mentioned phenomena can be better perceived in Figure 5.16 where the time-

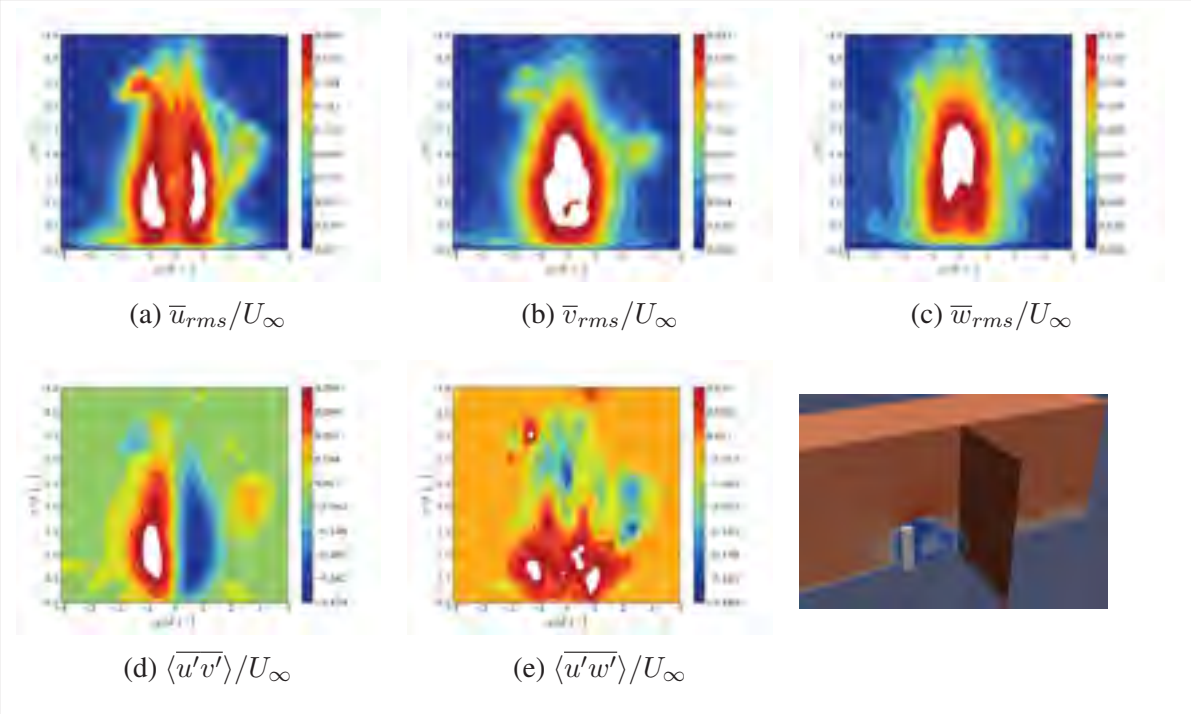

(a) $\overline{u}_{rms}/U_\infty$ (b) $\overline{v}_{rms}/U_\infty$ (c) $\overline{w}_{rms}/U_\infty$

(d) $\langle\overline{u'v'}\rangle/U_\infty$ (e) $\langle\overline{u'w'}\rangle/U_\infty$

Figure 5.12 $\overline{u}_{i,\,rms}$ and shear stresses at the wake using SIDDES for Case A. The location of the plane $x = 5d$ is shown in the bottom right schema.

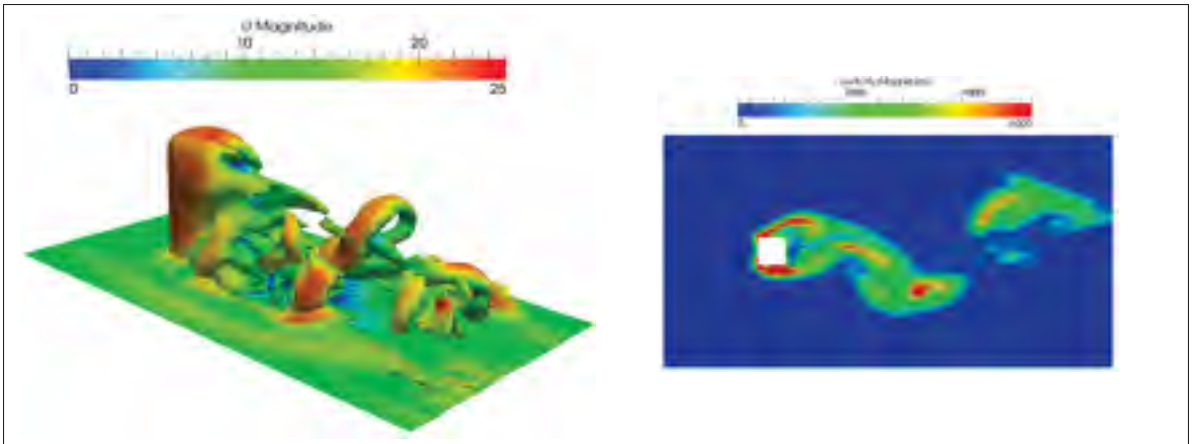

(a) The vorticity structures at the wake. Units: [m/s].

(b) Vorticity contours at $z \approx 3d$. Units: [1/s].

Figure 5.13 Vortex shedding visualization for case A with SIDDES

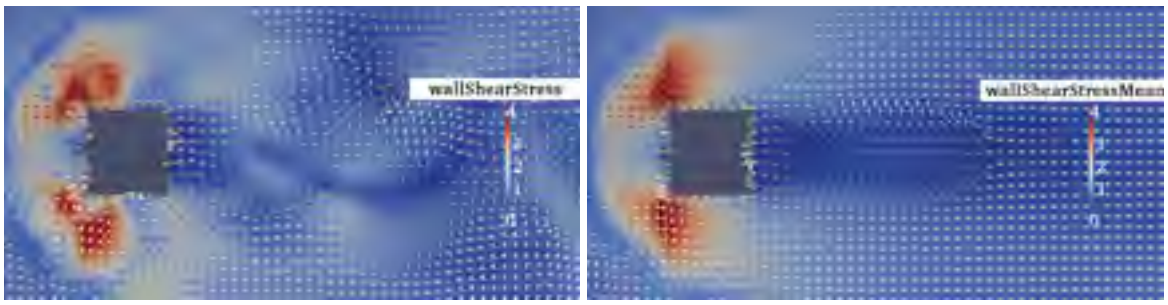

(a) Instantaneous (b) Time-averaged

Figure 5.14 Wall shear stresses at the bottom boundary for case A with SIDDES. The colour bar represents the magnitude. Units: $[\mathrm{m}^2/\mathrm{s}^2]$.

averaged velocity vectors clearly show upwash and a downwash region behind the obstacle. Where the two regions collide a saddle point is present. The reverse flow regions can also be distinguished by analyzing the wall shear stresses on the cylinder wall as in Figure 5.17. On the front face, near the base of the obstacle a downwash flow (wall shear stress vectors pointing upwards) confirms the existence of a recirculation bubble. Further from the cylinder base, the flow just travels to the sides, around the obstacle. While on the back face, a region of upward facing shear stress vectors is present at the base of the obstacle, and downward wall shear stress vectors are located at the top. The change in flow direction is clearly seen.

Qualitatively, the resulted modelled wake displays the turbulent nature and vortex characteristics described in the literature for this type of obstacles. Additionally, the results obtained by the hybrid approaches are consistent with each other, and they show a fairly good agreement with the wind-tunnel data. The computing time is somewhat smaller for the SIDDES cases because of the slightly larger URANS regions. For case A, the SIDDES simulations required only around 70% of the computing time needed for the DES simulations. However, the computing time difference might not that relevant and the simpler DES could just be sufficient for a case where the boundary layer is of the order of the grid spacing (streamwise and spanwise). The increased complexity of the SIDDES might not be necessary for thin boundary layer cases. Nevertheless, the GIS phenomena might arise for certain meshes, and it is not well handled by DES.

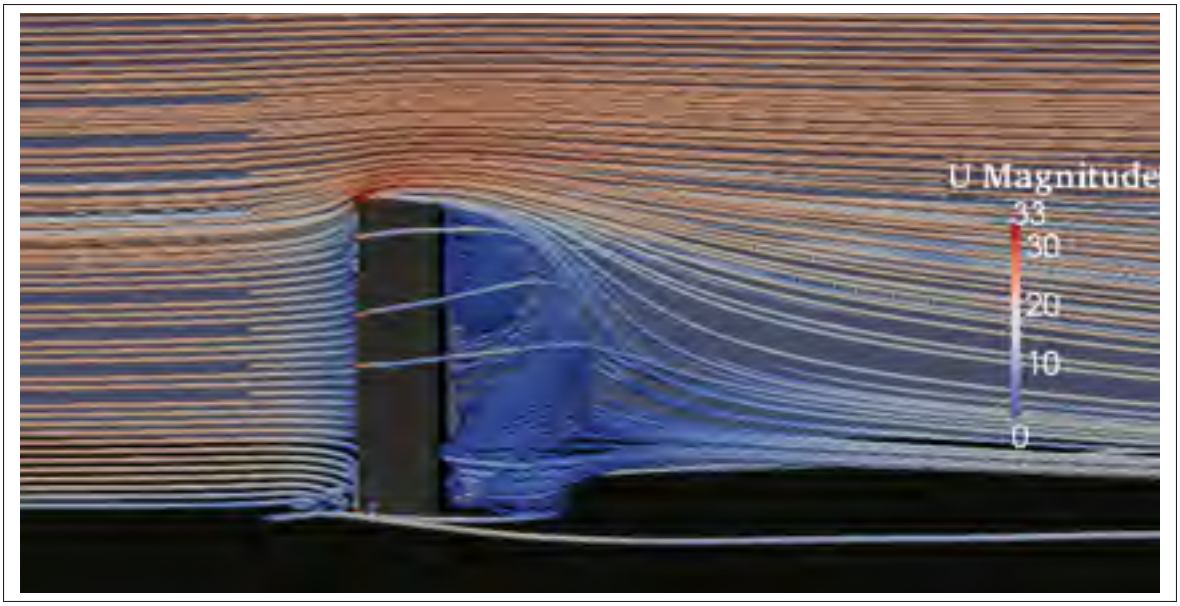

Figure 5.15 Time-averaged velocity streamlines visualization with SIDDES for case A. Units: [m/s].

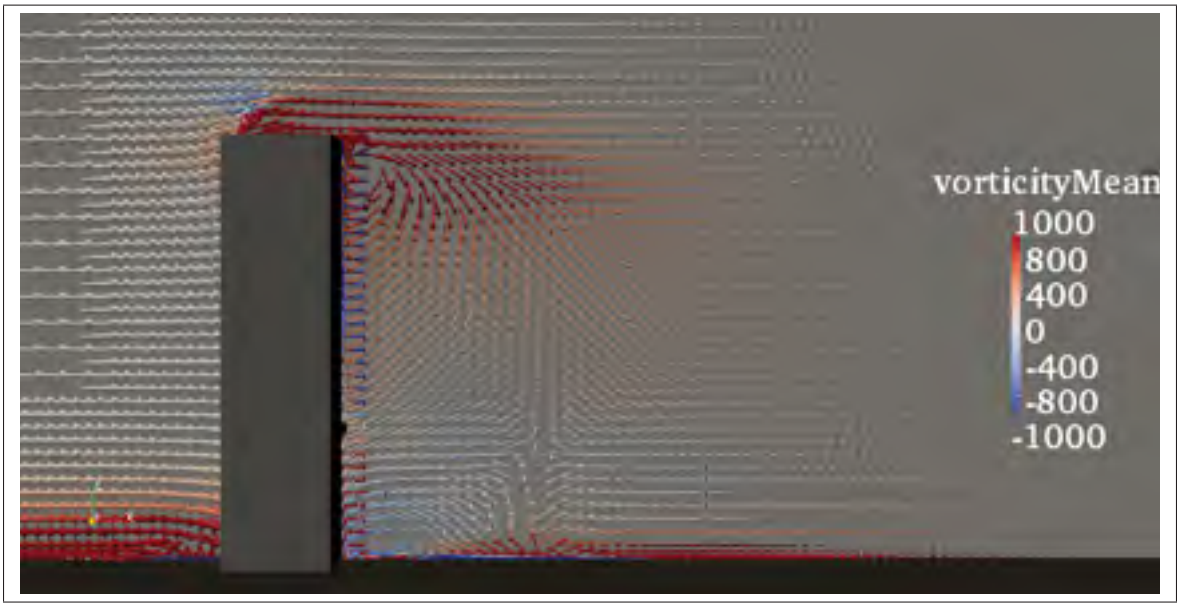

Figure 5.16 Time-averaged velocity vectors for case A at the centre plane coloured by averaged spanwise vorticity on the SIDDES computation. Units of colour bar: [1/s].

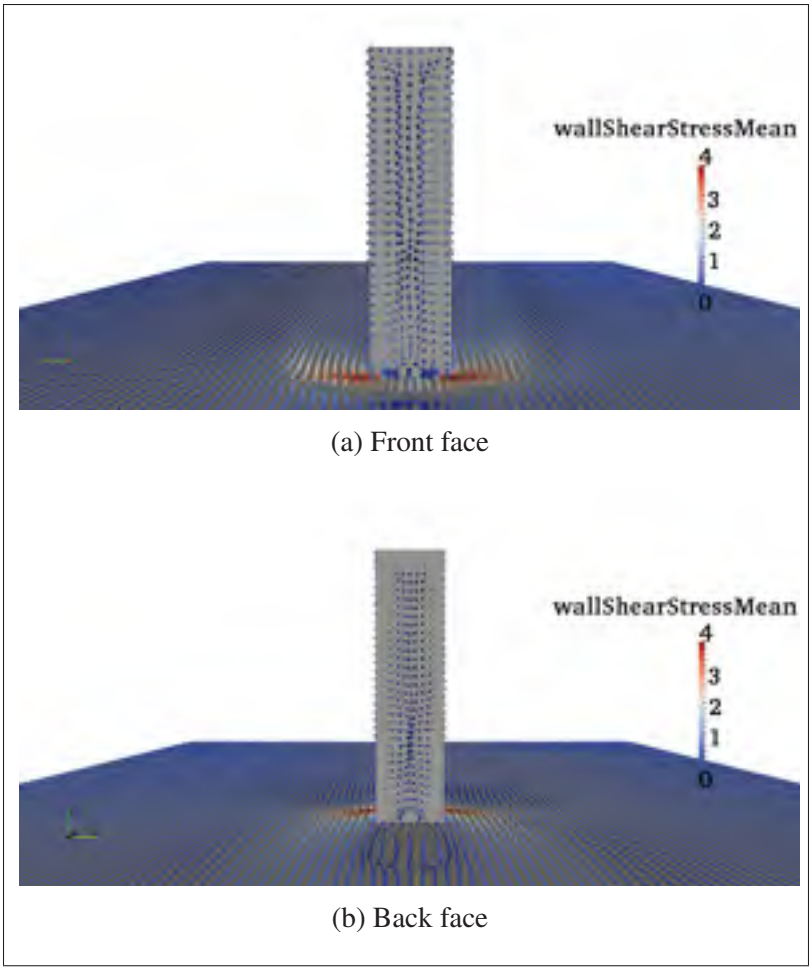

(a) Front face

(b) Back face

Figure 5.17 Time-averaged shear stresses vectors from case A with SIDDES. Colour scale represents their magnitude. Units: $[\mathrm{m}^2/\mathrm{s}^2]$.

5.1.2 Case B: Approaching thick boundary layer flow

Subsequently, simulations where the approaching boundary layer height is larger than the obstacle height, as in Figure 5.2b, will be performed using the hybrid models. The objective of the following studies is to verify and extend the application of the hybrid approaches to cases like atmospheric flow where the thickness of the atmospheric boundary layer is most likely larger that the size of any obstacle. For such cases, the grid spacing is considerably smaller than the boundary layer height. Thus, the URANS/LES switch behaviour might be affected and the presence of LLM phenomena could become important.

Three different cases will be analyzed. Their characteristics are summarized in Table 5.1 and they will be explained with more detail in this section. From the beginning, it is worth mentioning that case B1 and B2 do not represent a entirely valid nor physical test case. This will become more apparent in the following paragraphs. However, it was deem important to show these results in order to do a smooth transition between case A and B3.

Table 5.1 Square-section cylinder cases

	A	**B1**	**B2**	**B3**
approaching BL:	thin	*thick*	*thick*	*thick*
inlet:	imposed profiles	imposed profiles	imposed profiles	*mapped precursor*
outlet:	zero-gradient	zero-gradient	zero-gradient	zero-gradient
spanwise:	periodic	periodic	periodic	periodic
top:	stress-free	stress-free	stress-free	stress-free
solid walls:	no-slip + rough ext.	no-slip + rough ext.	no-slip + rough ext.	no-slip + rough ext.
model constants:	aerodynamic	aerodynamic	*atmospheric*	*atmospheric*

5.1.2.1 Case B1: Imposed inlet profiles

The domain size, mesh resolution and boundary conditions are defined as in the previous case A. The only difference is the profile defined at the inlet which in this case consist of the sum of a mean logarithmic profile and time-correlated random fluctuations. The nominal friction velocity was kept the same as in the previous case to keep the same mesh (since z_1^+ depends on u_*). This yields a $u_{top} = 19.6$ m/s. The empty domain simulation results given in Figure 5.18 show the resolved velocity and the resolved turbulence intensity profiles. The plots for this case are still normalized by $U_\infty = 15$ m/s for easier comparison. Surprisingly, the LLM is not present in this case as it was expected. Further comments will be given about this issue on Section 5.1.2.3. The resolved turbulence intensity is similar to case A.

The URANS/LES regions in the square-section cylinder approached by a thick boundary layer flow simulations (case B1) are really similar to the previous case as it can be seen in Fig-

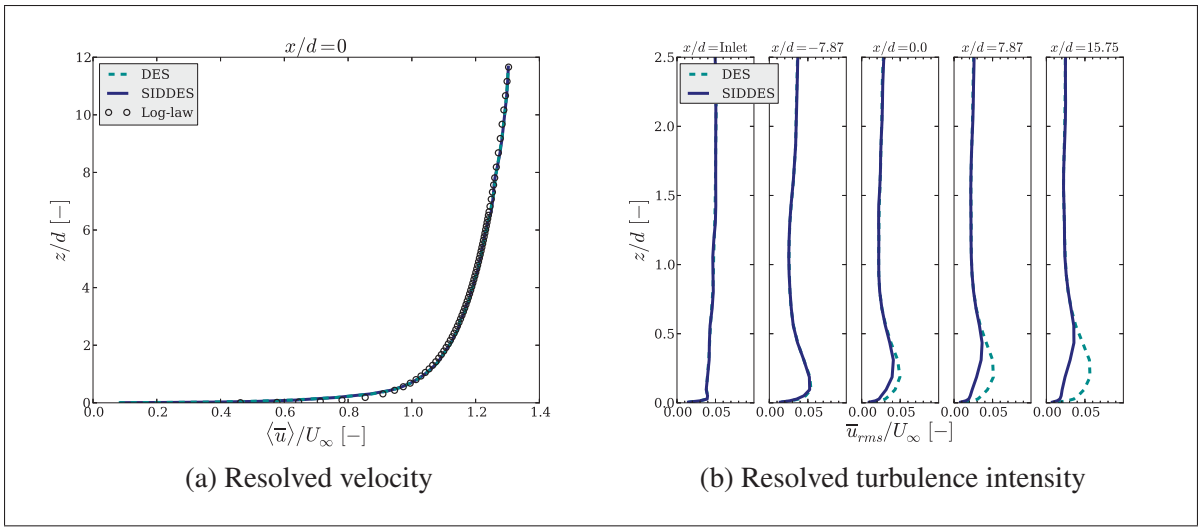

(a) Resolved velocity (b) Resolved turbulence intensity

Figure 5.18 Empty domain profiles for the thick boundary layer case (B1).

ure 5.19. Correspondingly, Figure 5.20 and Figure 5.21 display the velocity wake deficit and the velocity downstream of the obstacle respectively. Notably, all the plots show that the DES and SIDDES results are almost identical. This result was not at all expected for the fully immersed obstacle case and seems to contradict the claim that thick boundary layer cases require SIDDES to correct for the LLM.

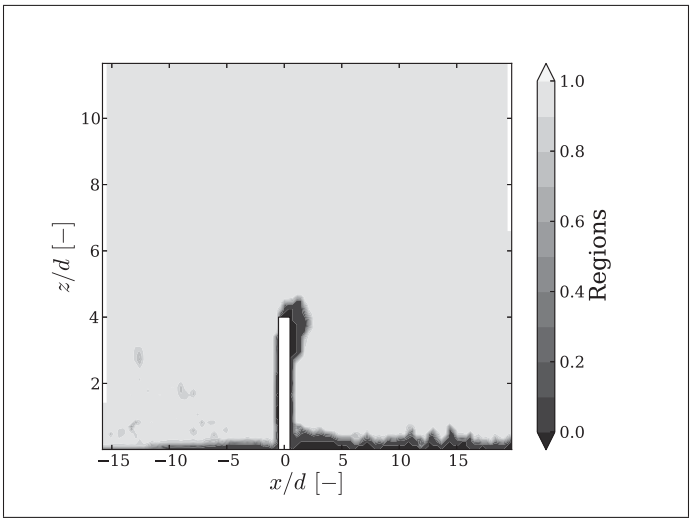

Figure 5.19 Case B1 instantaneous regions using SIDDES. A pure LES region is identified as 1 and a pure URANS as 0.

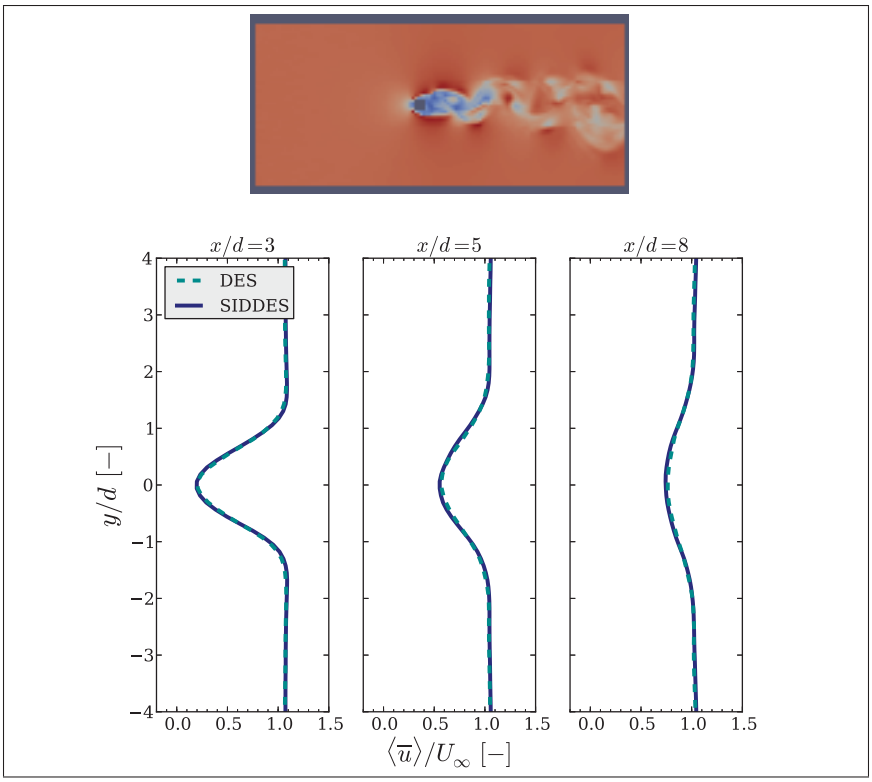

Figure 5.20 Time-averaged resolved velocity at a height of $z = d$ for the thick boundary layer case (B1). The top schema depicts the instantaneous velocity and the profiles location (white lines).

Figure 5.22 compares the average results from the approaching thin (case A) and think boundary layer (case B1) flows. The profile discrepancy at the top of the domain is expected because of the different velocity on the incident flows. However, behind the obstacle the wake behaviour does not appear to be distinct between the two cases. Castro and Robins (1977) measured more pronounced discrepancies on the wake region of a surface-mounted cube which was approached by two different boundary layer thickness flows. Wang *et al.* (2006) square cylinder simulations also show that the boundary layer thickness has stronger effect on the wake than the computed by this analysis.

All these discrepancies (i.e. the lack of LLM and the small effect that the boundary layer thickness has on the wake compare to other results in the literature) might indicate that the

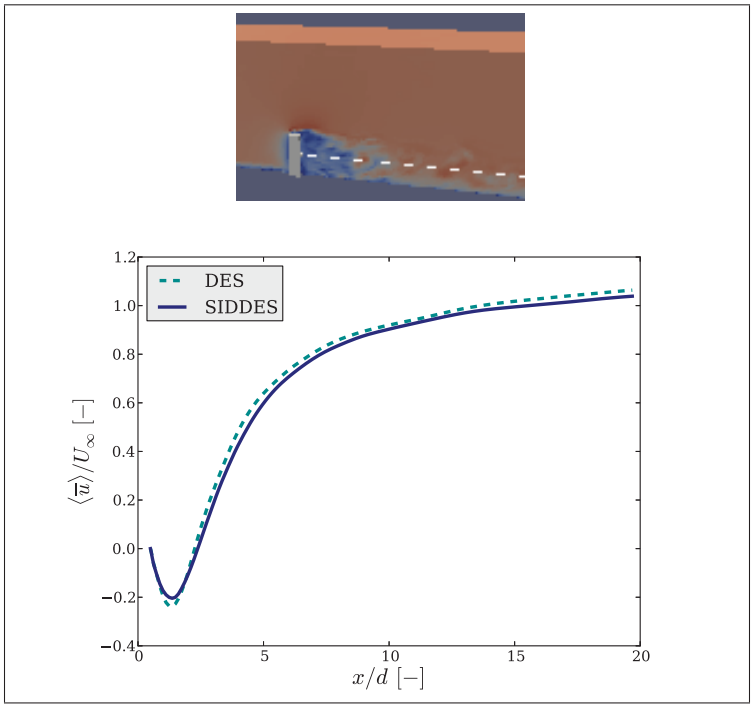

Figure 5.21 Time-averaged downstream velocity at the centre-line and at a height of $z = 2d$ for the thick boundary layer inflow case (B1).

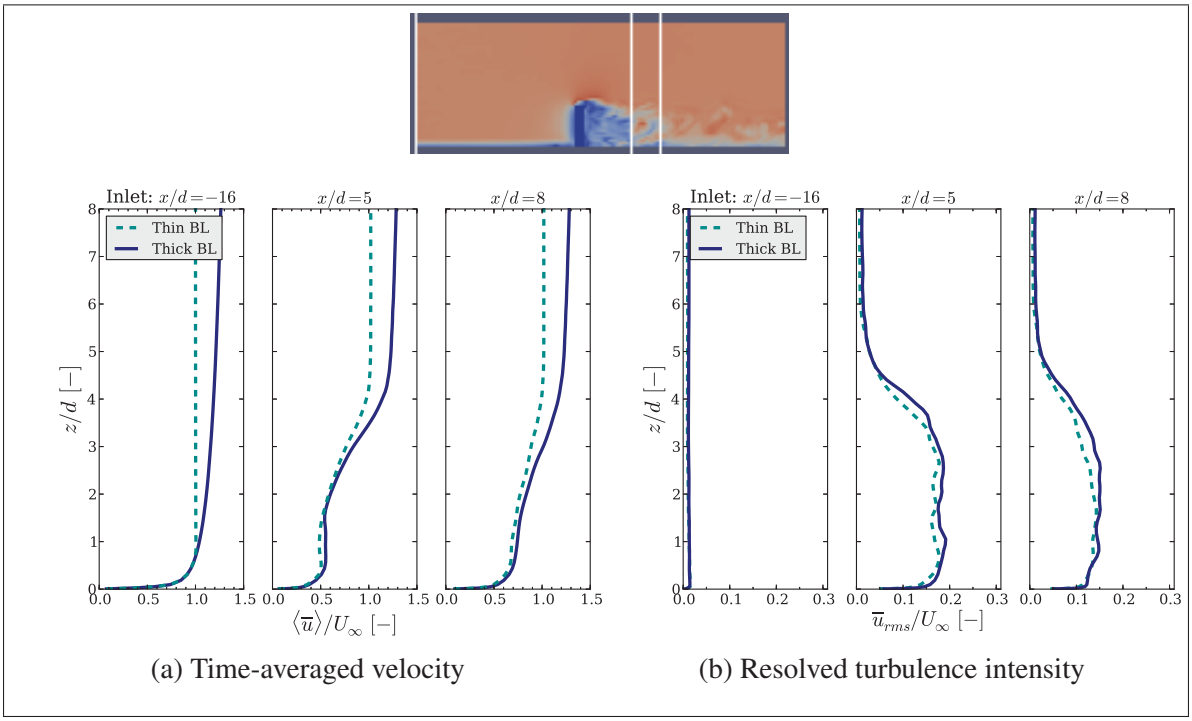

(a) Time-averaged velocity

(b) Resolved turbulence intensity

Figure 5.22 Case A and B1 profiles comparison

inlet boundary condition is not entirely correct nor physical. By comparing Figure 5.3b against Figure 5.18b it can be seen that the resolved turbulence intensity in the absence of the obstacle is similar for both cases. In reality, a thick boundary layer should present a higher turbulence intensity as measured by Castro and Robins (1977). The empty domain simulation results indicate that the flow is constrained and the boundary conditions not ideal, therefore the resolved turbulence intensity for the thick boundary layer case does not evolve naturally nor attains the correct turbulence. Unfortunately, this inconsistency at the inlet does not allow to make any accurate conclusions about the effect that the approaching boundary layer thickness has on the wake.

5.1.2.2 Case B2: Approaching thin boundary layer flow with imposed inlet profiles and ABL constants

Disregarding the inaccurate inlet boundary for the moment, it is interesting to study the effect that the model constant have on the simulations results. The flow around a square-section cylinder was simulated using the same parameters as in case B1, except that this time the atmospheric model constants from Table I-1 are employed. Figure 5.23 displays the computed URANS/LES regions which are consistent with previous cases (A and B1). Contrary to the channel and ABL over flat terrain cases, the use of the atmospheric constants do not have an impact on the URANS/LES regions. Figure 5.24 shows that the resolved turbulence intensity behind the wake is slightly more elevated when the atmospheric constants are used. The same behaviour can be appreciated in Figure 5.25. The velocity deficit is larger for the atmospheric constants, however the wake spread is the same for both cases. Finally Figure 5.26 demonstrates that the recirculation bubble for the atmospheric constant case is considerably larger.

Due to the lack of experimental data it is not possible to determine which set of model constants reproduces the flow more accurately. However the objective of this comparison exercise is to discern the important repercussions and effects that the calibration of a turbulence model can have on the computations.

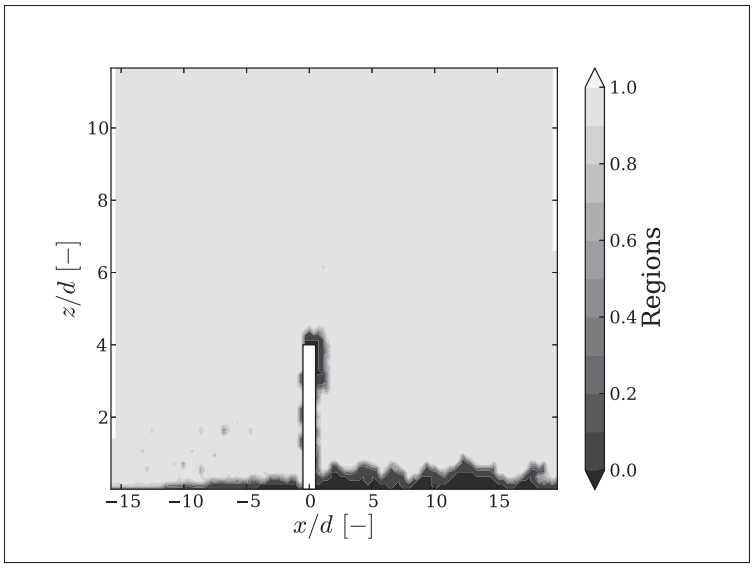

Figure 5.23 Time-averaged regions for the SIDDES case B2. A pure LES region is identified as 1 and a pure URANS as 0.

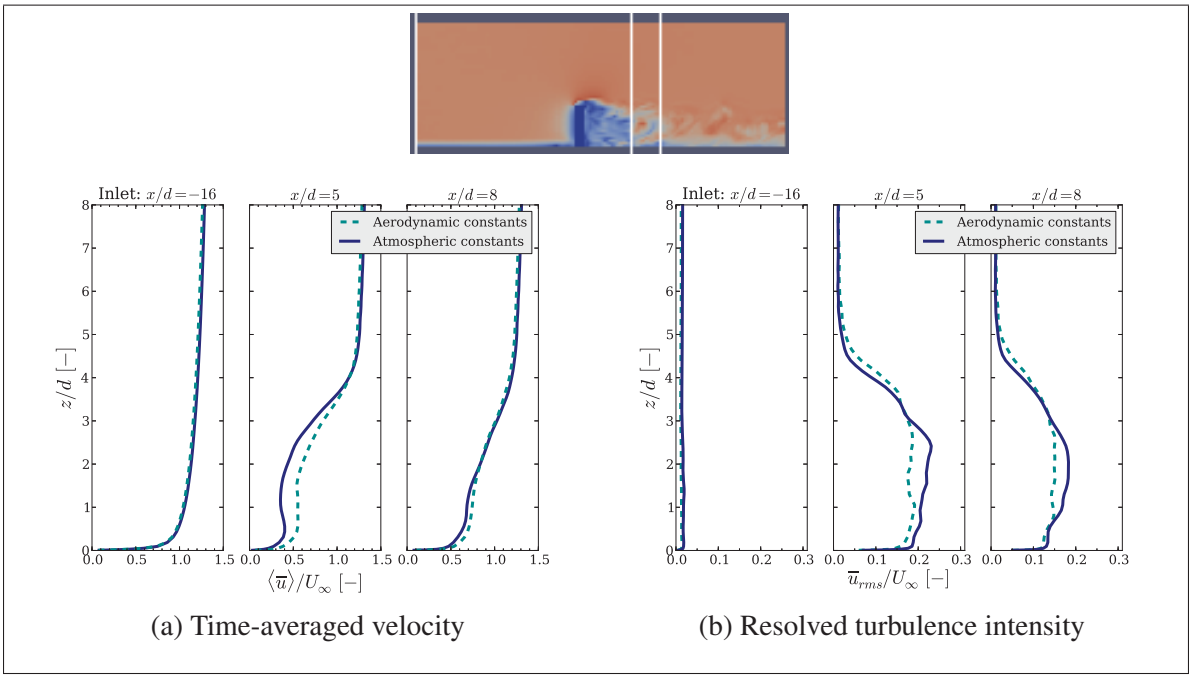

(a) Time-averaged velocity

(b) Resolved turbulence intensity

Figure 5.24 Case B1 (aerodynamic constants) and B2 (atmospheric constants) comparison using SIDDES.

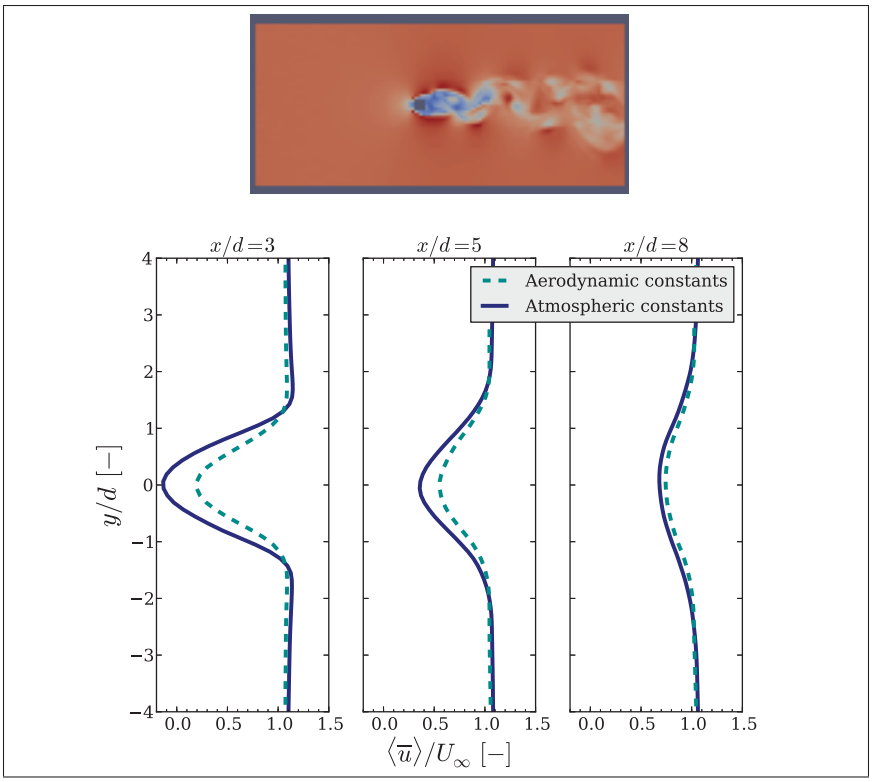

Figure 5.25 Time-averaged resolved velocity at a height of $z = d$ for the thick boundary layer. Case B1 (aerodynamic constants) and B2 (atmospheric constants) using SIDDES.

5.1.2.3 Case B3: Approaching thick boundary layer flow with mapped inlet from a precursor simulation

A precursor simulation is employed to appropriately model a square-section cylinder submerged in a ABL, in particular to correctly represent the inlet flow. As shown in Figure 5.27, an empty domain with periodic boundary conditions and a thick boundary layer driven by a constant large pressure gradient is computed first. A precursor simulation is basically a ABL simulation over flat terrain. Within the precursor simulation the flow naturally develops the turbulence structures and turbulence intensity. Once the simulations has reach statistical convergence ($\sim 20 - 30$ flow-through times), the flow characteristics (i.e. $\overline{u}$, k and ω) are saved every time step at the outlet plane and used as a inlet boundary condition for a successor simulation. Contrary to the previous cases B1 and B2, a precursor simulation will yield an inlet where all the flow properties (i.e. velocity, turbulence intensity, eddy size, etc.) are in agree-

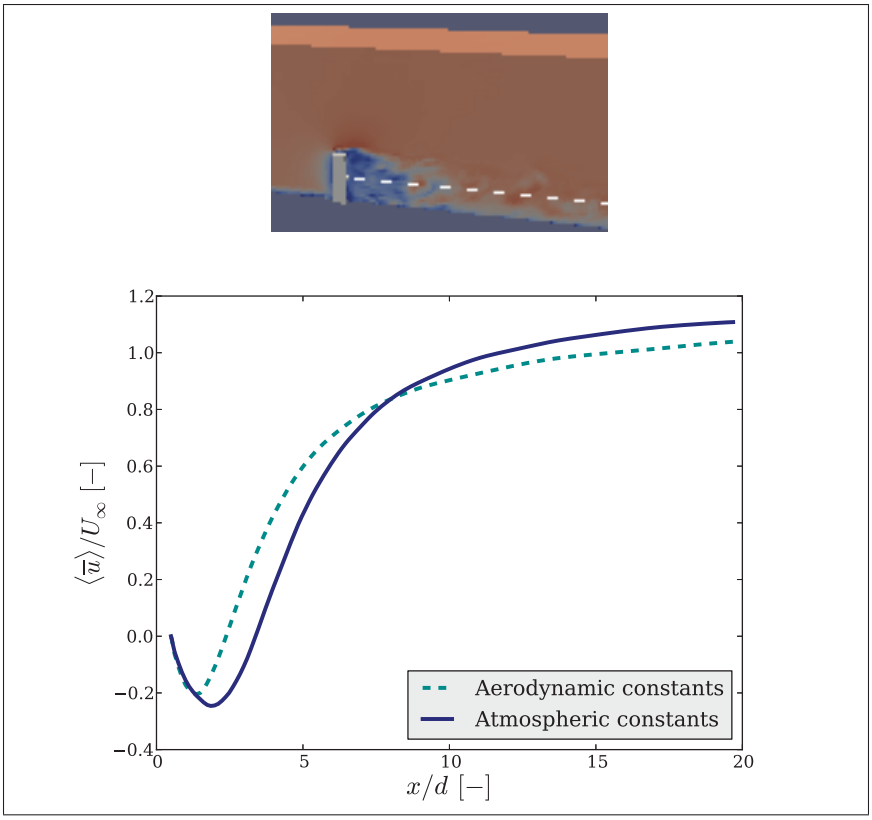

Figure 5.26 Time-averaged resolved downstream velocity at the centre-line and $z = 2d$ for the tick boundary layer upstream inflow using different model constants. Case B1 (aerodynamic constants) and B2 (atmospheric constants) with SIDDES.

ment and represent a more realistic inlet flow for the successor square-section cylinder case. Except from the different inlet condition, this successor simulation case (B3) was defined in the same way as case B2 (i.e. same boundary conditions, atmospheric constants, etc.)

The precursor simulation results are compared against the empty domain results from case B2 in Figure 5.28. Data shows that the appropriate logarithmic velocity profile is not achieved, and a 4.5% lower u^* value is obtained for case B3. To correct for the latter, a larger driving pressure gradient could have been used. The LLM is somewhat more visible for the DES precursor (or periodic) case, though the normalization used is not ideal to visualize it. Contrary to case B2, the LLM appears because the turbulence is not constrained or forced, thus it develops freely.

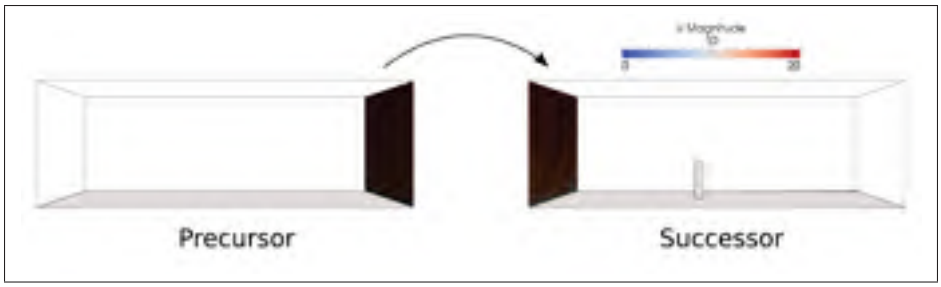

Figure 5.27 Schema of case B3

More importantly, these results show that indeed the resolved turbulence intensity obtained by a precursor simulation is rather larger that the one imposed on the thick boundary layer cases B1 and B2. With the results from the precursor simulations, a more accurate flow is used to represent the inlet condition for a ABL summered square cylinder obstacle. Only the SIDDES case is studied from now on.

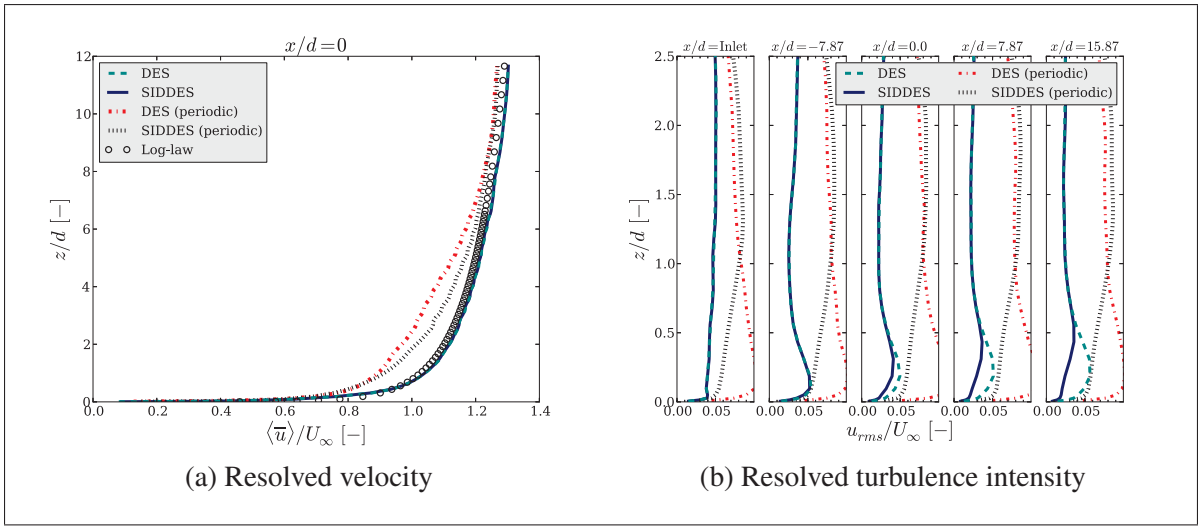

(a) Resolved velocity

(b) Resolved turbulence intensity

Figure 5.28 Profiles of the empty domain thick boundary layer cases. The precursor simulation of case B3 are labelled as periodic, while the DES and SIDDES (non-periodic) show the results from case B2.

Since experimental data is not available for this case, only a detailed qualitative analysis can be performed. First is it can be appreciated in Figure 5.29b, the square-section cylinder case B3 yield slightly different URANS/LES regions. A large URANS region is visible upstream of the

obstacle because the precursor time-averaged URANS region (Figure 5.29a) is also large. The URANS/LES regions obtained in this case are consistent with the flat terrain results. Next, the normalized time-averaged velocity at plane downstream of the obstacle is seen in Figure 5.30. It is evident that the wake is broader in the spanwise direction compared to the previous cases. This could be linked to the larger eddy structures present at the inlet boundary condition. As measured by Wang *et al.* (2006), two spanwise vortices are distinguished in Figure 5.30b at the top of the obstacle. The vortices have opposite spanwise velocity components. In that same figure, two base vortex is seen close to the wall. In a similar manner, two vortices are visible in the vertical direction in Figure 5.30c. The $\overline{u}_{i,\,rms}$ values and shear stresses at the same plane are shown in Figure 5.31. These results are in quantitative agreement with the lateral distributions measured by Wang *et al.* (2006). Also as it has been described in the literature (Wang *et al.*, 2006), the horseshoe vortex effect can be distinguished close to the wall at the side of the obstacle in Figure 5.32. The streamline also show that most of the flow leaves the wake vortex at a certain height approximately around $z/h \sim 2$. The same phenomena is seen in case A, thus the flow seems to escape the vortex at a much lower height (compare to Figure 5.15). This is also an indication that in the thick approaching boundary layer case, the base vortex is larger than in the thin boundary layer case as observed by Wang *et al.* (2006).

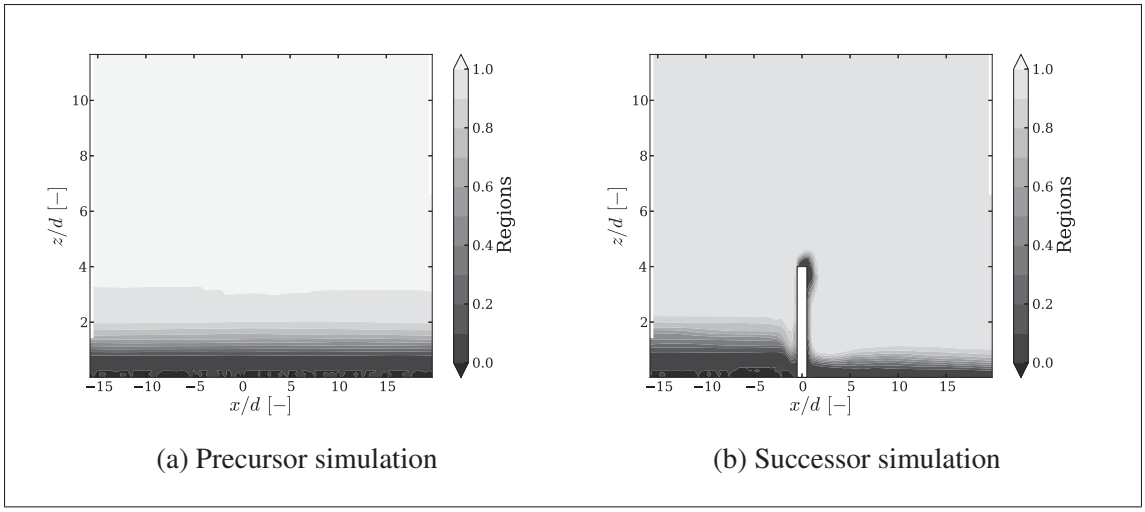

(a) Precursor simulation (b) Successor simulation

Figure 5.29 Time-averaged URANS and LES regions for the SIDDES case B3. A region of 1 represents a pure LES zone and 0 a pure URANS.

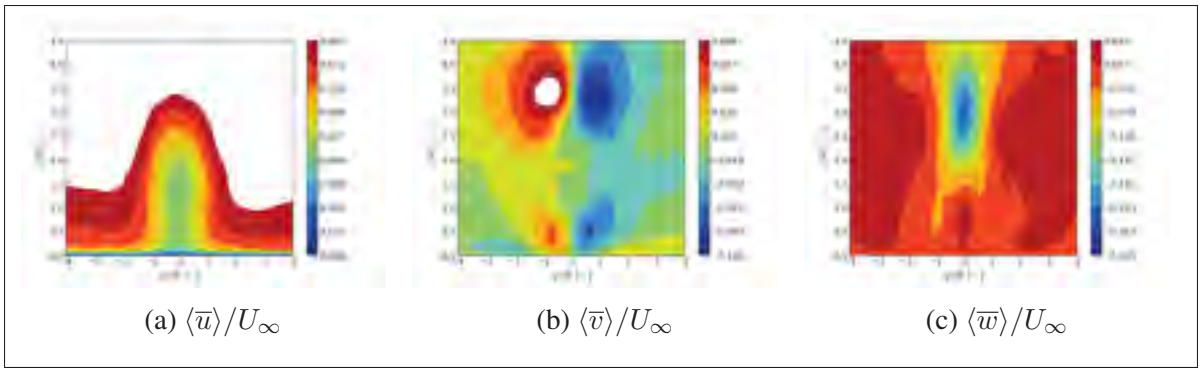

(a) $\langle \overline{u} \rangle / U_\infty$ (b) $\langle \overline{v} \rangle / U_\infty$ (c) $\langle \overline{w} \rangle / U_\infty$

Figure 5.30 Time-averaged velocity at a plane $x = 5d$ downstream from the obstacle on case B3 using SIDDES.

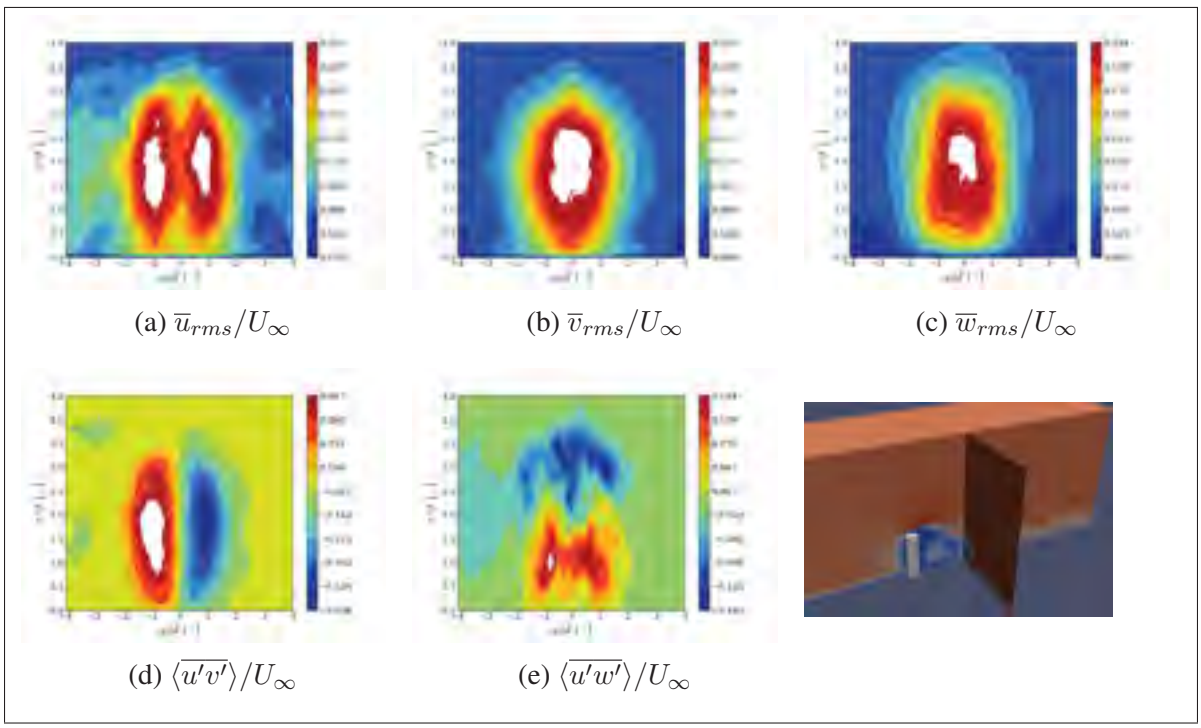

(a) $\overline{u}_{rms}/U_\infty$ (b) $\overline{v}_{rms}/U_\infty$ (c) $\overline{w}_{rms}/U_\infty$

(d) $\langle \overline{u'v'} \rangle / U_\infty$ (e) $\langle \overline{u'w'} \rangle / U_\infty$

Figure 5.31 $\overline{u}_{i,\,rms}$ and shear stresses for case B3 at $x = 5d$ using SIDDES.

The velocity vectors in the middle plane are shown in Figure 5.33. The upper and lower vortices behind the obstacle are visible. As for the thin boundary layer case, the saddle point exist and the recirculation bubble does not reattached at the wall. It has been demonstrated that the saddle point height is dependent on the approaching boundary layer flow. As the boundary layer thickness grows, the saddle point takes place further from the bottom wall and the upwash

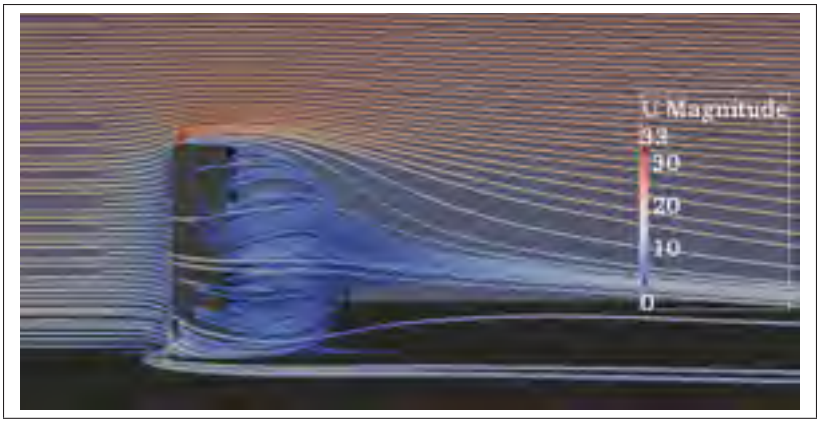

Figure 5.32 Time-averaged velocity streamlines visualization using SIDDES for case B3. Units: [m/s].

region becomes larger (Wang *et al.*, 2006). Comparing the case A (Figure 5.16) and the case B3 results, it can be observed that the saddle point does not necessarily takes place further away form the wall as the approaching boundary layer thickens. Nevertheless it is clear that contrary to case A, the base vortex in case B3 is smaller close to the bottom and it becomes larger further from the wall. This phenomena was also described by Wang *et al.* (2006) for upstream thick boundary layers.

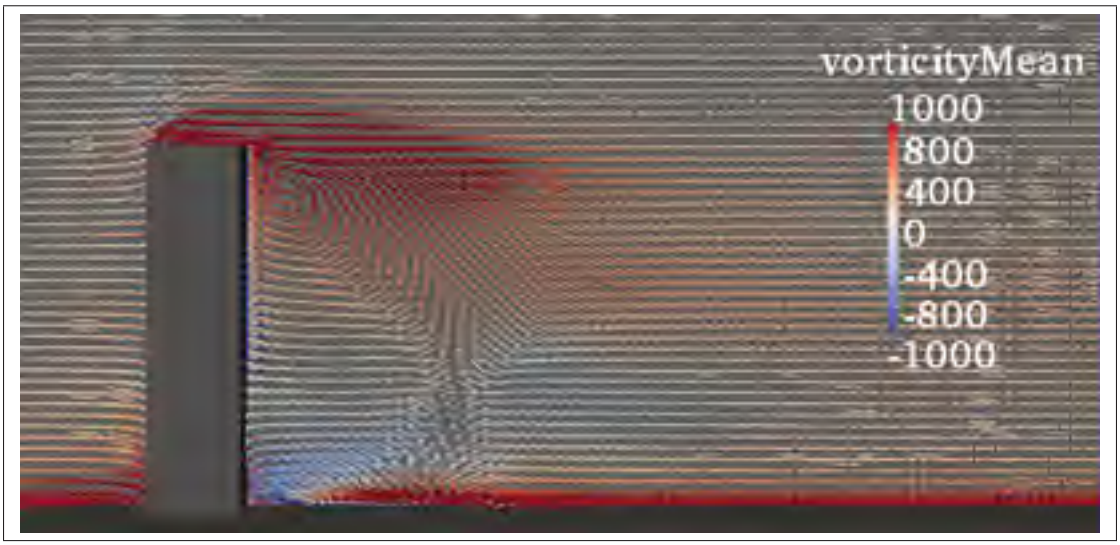

Figure 5.33 Case B3 time-averaged velocity vectors in the centre plane coloured by averaged spanwise vorticity on the SIDDES computation. Units: [1/s].

In Figure 5.34a, the shear stress visualization at the obstacle's front wall show that the flow deviates sideways in most of the cylinder. Up to to a certain height and exactly at the centre plane of the obstacle, the flow deviates downwards. Only a small part at the top of the obstacle displays shear stresses indicating that the flow deviates upwards. This reproduced behaviour is consistent with the shedding of a Kármán-type vortex (Sakamoto, 1983). Figure 5.34b shows the presence of upward and downward flow. The recirculation bubble can also be seen in the time-averaged wall shear stresses at the bottom wall displayed in Figure 5.35.

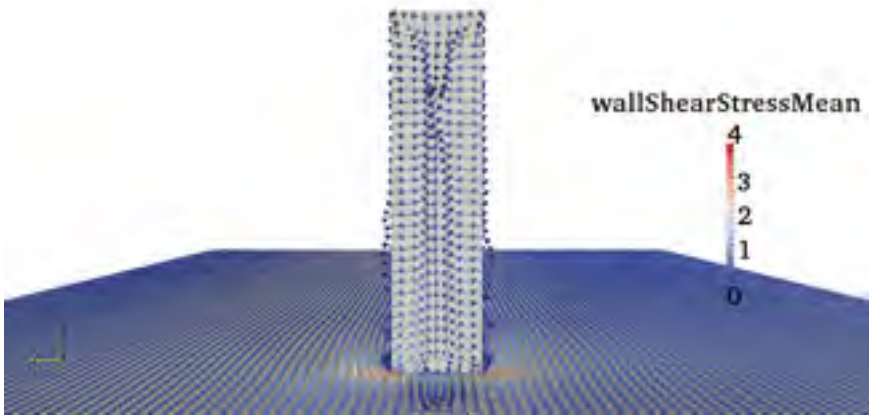

(a) Front face

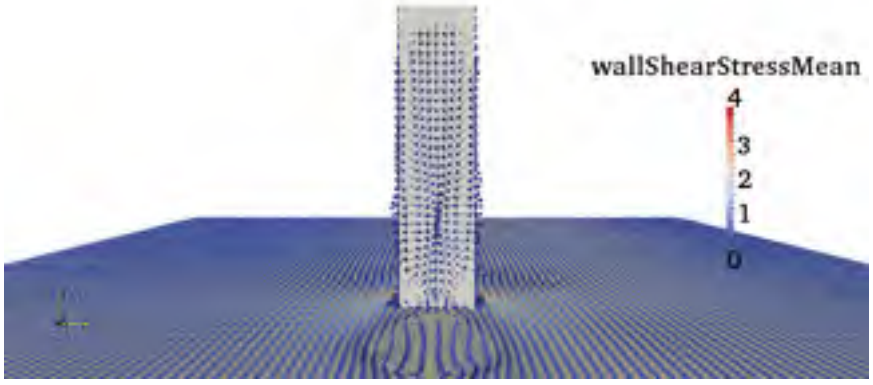

(b) Back face

Figure 5.34 Time-averaged wall shear stresses vectors on the cylinder for SIDDES case B3. Colour scale represents their magnitude. Units: $[\mathrm{m}^2/\mathrm{s}^2]$.

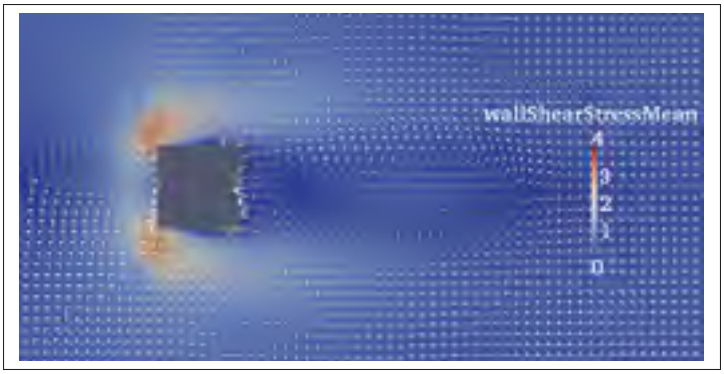

Figure 5.35 Time-averaged wall shear stresses at the bottom boundary for the thick boundary layer case B3. Units: $[\mathrm{m}^2/\mathrm{s}^2]$.

The flow behaviour can be more easily compared against case A in Figure 5.36. At the bottom wall behind the obstacle a small recirculation zone is visible on both thin and thick boundary layer cases. Further downstream a bigger recirculation bubble with negative streamwise velocity in the near-wall region can be seen. The thick boundary layer case bubble reattaches slightly after than the thin boundary layer case. At the front obstacle wall, the vertical shear stresses are rather different. The thick boundary layer case shows positive values in most of the obstacle, while this is not true in the thin boundary layer case. As for the back obstacle wall, the shear stresses change sign at exactly the same height. This is linked to the height of the saddle point, thus the SIDDES saddle point predictions are not consistent with Wang *et al.* (2006) results as pointed out previously. Lastly, the thin and thick boundary layer velocity statistics are compared in Figure 5.37. Contrary to Castro and Robins (1977) findings, the resolved turbulence intensity at the centre plane of the wake is not greatly affected by the approaching turbulence intensity.

5.1.3 Overview

The square-section cylinder cases present complex flow phenomena and overall the $k-\omega$ SST-SIDDES model was capable of reproducing such flow behaviour for different approaching flows. Unfortunately no experimental data was available for the thick boundary layer approaching flow, but a quantitative analysis yield successful results that could be di-

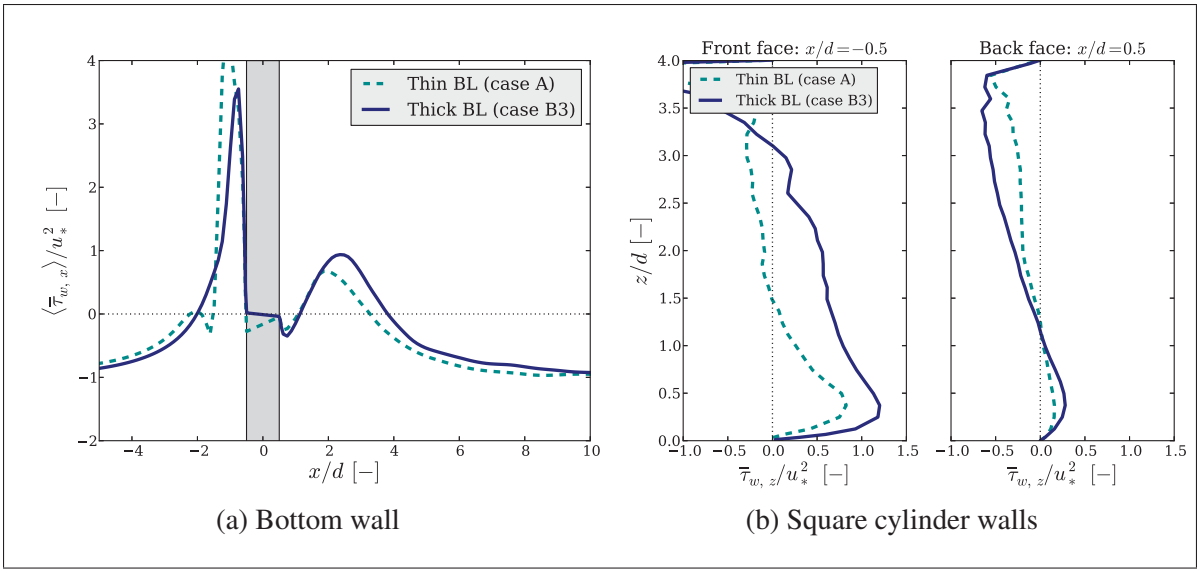

(a) Bottom wall (b) Square cylinder walls

Figure 5.36 Time-averaged wall shear stresses at the centre plane for cases A and B3 using SIDDES. The grey region represents the square-section cylinder.

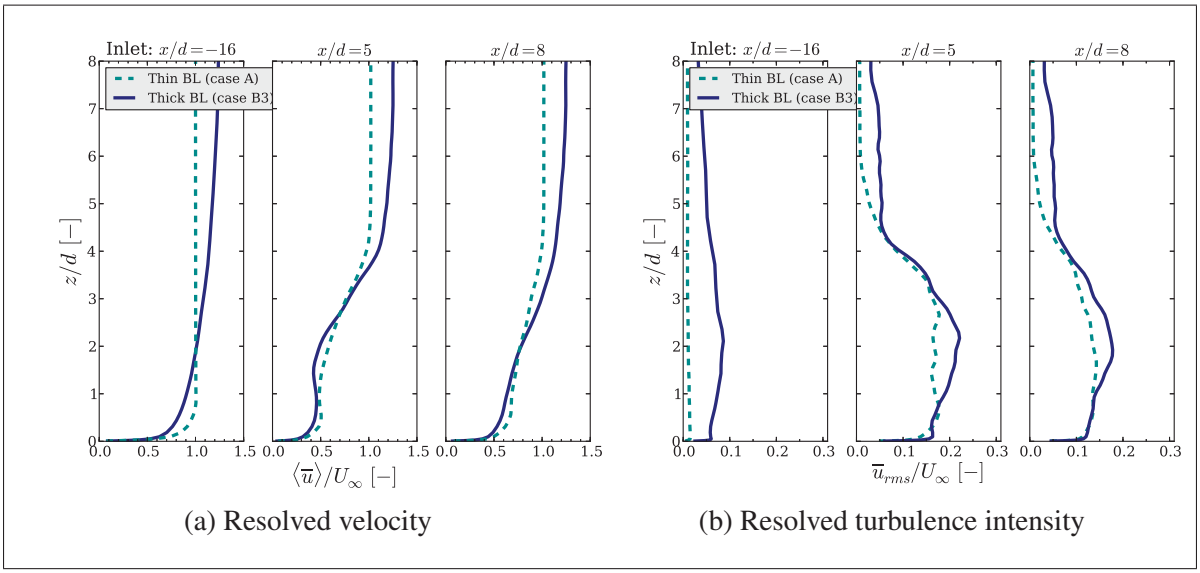

(a) Resolved velocity (b) Resolved turbulence intensity

Figure 5.37 Time-averaged velocity and turbulence intensity comparison between cases A and B3

rectly apply for obstacles completely submerged on atmospheric boundary layer flows. It is important to note that the bottom wall in this case was nevertheless defined as smooth and it is not representative of an atmospheric flow.

The inlet boundary condition prove to be a major challenge. The inlet for the thin boundary layer case (A) presented the correct mean velocity and turbulence intensity, but the information of the large turbulent structures might be missing. However, a good overall quantitative agreement with the results was obtained. As for the thick boundary layer cases, the correct definition of the inlet was problematic. For cases B1 and B2 even though the velocity profile was correct, an erroneous turbulence intensity was imposed. Only for case B3, it was assured that the inlet correctly reproduced a realistic approaching flow for thick boundary cases. This last case (B3) should be the most accurate representation of a square-section obstacle immersed in atmospheric boundary layer, nevertheless, experimental data is required to quantitatively verify these results.

5.2 Askervein hill measurement campaign

The Askervein experiment measured the atmospheric flow around an isolated hill of moderate and smooth slopes located on the island of South Uist in the Outer Hebrides in Scotland. Two extensive field campaign took place in 1982 (Taylor and Teunissen, 1983) and 1983 (Taylor and Teunissen, 1985). The experimental data is widely available and explained in great detailed. The Askervein hill has gentle slopes which likely caused weak flow recirculation regions (Taylor and Teunissen, 1985). For this reason, the terrain is considered only as mildly complex, but certain complex phenomena are indeed observed. This test case has been widely analyzed, but even more than thirty years later, the computational analysis still yield conflicting results (Silva Lopes *et al.*, 2007).

The Askervein hill has an almost elliptic shape with an approximately 1 km semi-minor axis and a 2 km long semi-major axis. The hill height is 116 m ($h = 126$ m above sea level). Their slopes are less than 20% for the most part, but can reach 30% in certain areas. A picture of the hill is shown in Figure 5.38. Wind speed measurement were taken with anemometers placed at a 10 m height along line A and line AA. This lines are parallel to the hill minor axis and oriented at approximately 223°N. Also measurements were carried out along the major axis (line B). To provide a vertical velocity profiles, taller towers were also placed at a reference

position (RS) upstream of the hill, at the hill top (HT), at the hill central point (CP) and at the base of the hill. These references are illustrated in Figure 5.39, but precise locations are given in Table 5.2 and in the original references. The field campaign also gather kite measurement data, temperature, humidity, among others atmospheric parameters.

Figure 5.38 Picture of the Askervein hill.
Reproduced with permission from P. Taylor,
www.yorku.ca/pat/research/Askervein/ASK5.JPG

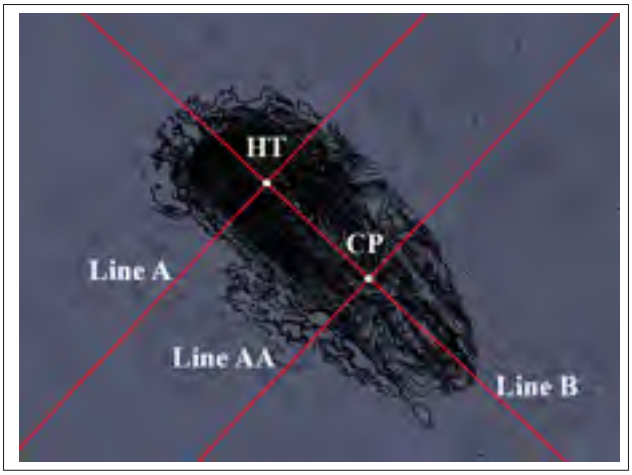

Figure 5.39 Askervein contour map and
reference points location

The prominent winds reach the hill at 210° from the North, and arrive from an upstream terrain which is fairly flat and has a uniform roughness of $z_0 = 0.03$ m. This wind direction is the most commonly studied and the classical reference case of the Askervein hill test case. Specifically, the results from run numbers TU03-B and MF03-D (Taylor and Teunissen, 1985) will be used to validate the hybrid simulation results. Those measurements took place under moderate to strong south-west winds in near-neutral atmospheric conditions on October 3rd 1983 (Taylor and W., 1987). In this two-hour data run, the average wind direction is 210°, and the average wind speed at a height of 10 m is $u_{\text{ref}} = 8.9$ m/s. A $u_* = 0.618$ m/s was obtained by fitting the log-law of the wall to the experimental data (Bechmann, 2006).

Table 5.2 Askervein case masts location

	Longitude [m]	Latitude [m]	
Reference point (RF)	74 300	20 980	undisturbed flow
Hill top (HT)	75 381	23 753	
Central hill point (CP)	75 678	23 465	

Numerous RANS simulations have been performed, including Kim and Patel (2000), Castro *et al.* (2003), and Sørensen (1995), while some of the LES simulations found in the literature are Bechmann (2006), Silva Lopes *et al.* (2007) and Katopodes Chow and Street (2009). The consequences of the topographic resolution, the domain dimensions, grid refinement and convergence, the boundary conditions, the roughness and turbulence models have been addressed in these previously mentioned studies. Overall, the mean flow behaviour in the upwind and hill top regions can be accurately predicted. This is true even when using some simple linear models and rather coarser grids. However the correct estimation of the flow proprieties at lee-side of the hill is more difficult (Castro *et al.*, 2003). RANS models tend to underestimate the downstream turbulence (Sanz Rodrigo, 2014) and fail to predict the recirculation region. URANS simulations performed by Castro *et al.* (2003) yield slightly better results which confirm the existence of a unsteady separation region. Nevertheless the separation estimated size increased considerably with grid refinement. In general, LES improves the Askervein test case results in the more complex area behind the hill.

The flow around the Askervein hill will be simulated using the $k-\omega$ SST-SIDDES model. The terrain elevation file has a resolution of 20 m and lacks the topographic information of the surrounding hills. This coarse resolution is not ideal and it might have some important repercussions, but it alleviates the meshing constrains and most important it allows for the use of periodic boundaries in the lateral direction. For simplicity, the topography was rotated to align the domain inlet/outlet boundaries to the streamwise direction. The domain size and terrain elevation used in the hybrid simulation are shown in Figure 5.40a. For comparison Figure 5.40b shows a topographic map of the area with a higher resolution. This more realistic representation of the terrain was obtained from the Wakebench project (Sanz Rodrigo, 2014). It was not used for these simulations because its fine resolution posses some challenges when defining the boundary conditions.

The domain used for the hybrid simulations covers 7.8×5.6 km and has a height of 1.5 km. This corresponds to $(L_x,\, L_y,\, L_z) = (5.2H,\, 3.7H,\, H)$. A correct meshing technique is crucial in complex terrain simulations and particularly with this hybrid model that requires an extremely small z_1^+. The mesh was defined with uniform cells in the stream and spanwise direction with a $\Delta_x/H = \Delta_y/H = 0.016$. As for the vertical cells up to $z_u/H = 1/3$, they were defined using the meshing technique and tools described by Jeannotte (2013). This technique adds layers in the vertical direction following the terrain elevation, gives more control over the height of the first cell, is capable of generating high aspect ratio cells, and reduces the possibility of errors in the cells (i.e. cells that are not orthogonal, skewed, collapsed, incorrectly oriented, or that do not pass the *checkMesh* utility in general). On the contrary the standard *snappyMesh* OpenFOAM meshing tool does not have such advantages (Jeannotte, 2013). Then a secondary portion of the mesh between $z/H = 1/3 - 1$ was generated separately with the same stream and spanwise resolution as the bottom part of the mesh, and a uniform $\Delta_z/H = 0.035$. The top mesh portion was then merged and stitch to the bottom mesh to generate a final mesh (See Appendix III.8 for coding details). The resulting mesh is display in Figure 5.41. Merging the two portions of the mesh was necessary to define a vertical expansion ratio of 1.12 up to z_u,

(a) Domain and terrain representation used in the hybrid simulations

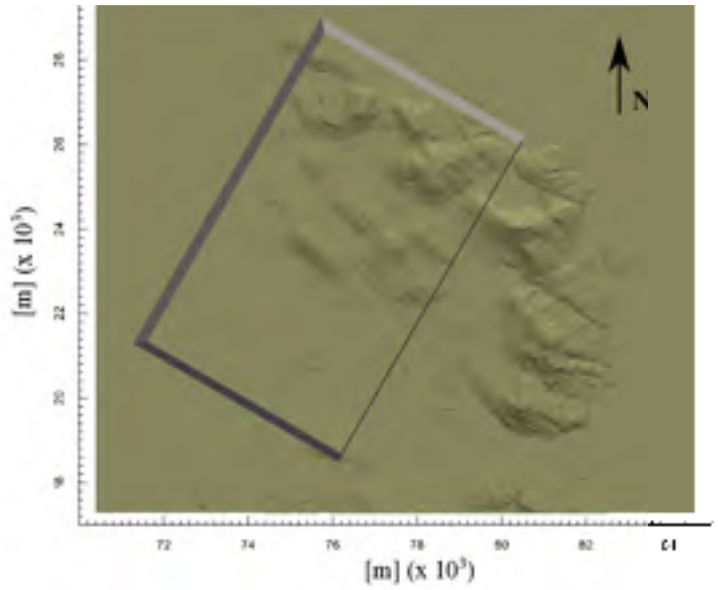

(b) A more realistic terrain. Not used in the hybrid simulations.

Figure 5.40 Top view of the Askervein hill

and also to avoid extremely elongated cells in the top two thirds of the domain which are not recommended in LES regions.

Two different meshes are analyzed. They both have the same number of cells in the stream and spanwise, but different z_1. The specific grid parameters are given in Table 5.3. Unfortunately even with the mentioned meshing technique, the required $z_1^+ \sim 1.0$ could not be attained with-

out having defective cells. The minimum z_1^+ that could be achieved was only approximately 160. However a finer resolution in the stream and spanwise direction will allow for smaller values of z_1^+. Nevertheless, the coarse mesh simulation used in this work will yield preliminary but insightful results. The more precise features that could be attained with a finer mesh will be explored in thorough study in a future work.

Table 5.3 Askervein mesh parameters

Mesh	N_x [−]	N_y [−]	N_z below z_u [−]	N_z above z_u [−]	z_1^+ [−]	z_1 [m]
A	335	240	79	19	~ 160	0.004
B	335	240	61	19	~ 1200	0.03

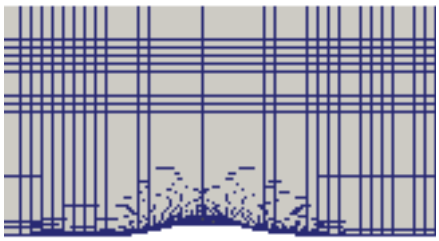

(a) Overall side view

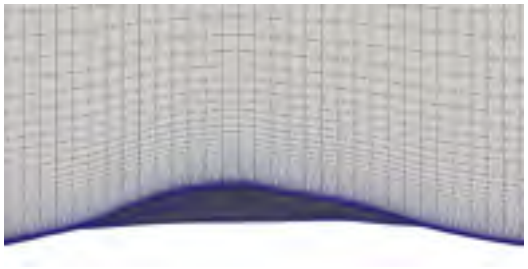

(b) Zoom around the hill

Figure 5.41 Askervein case mesh

A precursor simulation with the same roughness, orientation and mesh resolution as mesh B, but without conforming to the complex terrain was carried out first. To drive the precursor flow, a large scale pressure gradient was imposed based on $u_* = 0.618$ m/s. Then for the Askervein simulation (successor), the U, k and ω inlet boundary conditions were mapped from the precursor (as it was done for the square cylinder case B3 in Section 5.1.2.3). Also, zero-gradient boundary conditions were specified at the outlet. Even though the inlet/outlet boundary condition is fixed, a driving-pressure gradient was also imposed in the Askervein case to maintain a constant mass flow. If this pressure gradient was not imposed, the average velocity decreased with time. The bottom boundary was defined using Knopp's roughness

extension, while the top boundary was defined as stress-free. As for the lateral boundaries they were defined as periodic to avoid constraining the turbulence structures. The Coriolis force was not taken into consideration because $Ro \sim 10$. The discretization schemes were specified in the same manner as for the square-cylinder test case, and the atmospheric model constants were employed (See Table I-1). A maximum CFL of 0.7 was used. The simulations ran for 6 longitudinal flow-through-times and the time-averaged statistics were gathered for at least the following 5 flow-through-times.

Figure 5.42a shows that the URANS region extends far above the hill top with this mesh resolution. Additionally as seen in Figure 5.42b, the entire domain is solved by URANS at $z = 10$ m, the height at which most of the anemometers are placed. This is an important point that needs to be taken into consideration. Further studies are required to determine the resolution needed to develop sufficient LES content in the lee-side of the hill. However based on the flat terrain study, a mesh resolution of less than $\Delta_u/H = 0.010$ or $\Delta_u = 10$ m might be required for "mildly" complex terrains. It is also possible that on more complex terrain cases, the LES content downstream of an obstacle will be triggered even on coarser meshes. This can be observed for the square cylinder case on Figure 5.29.

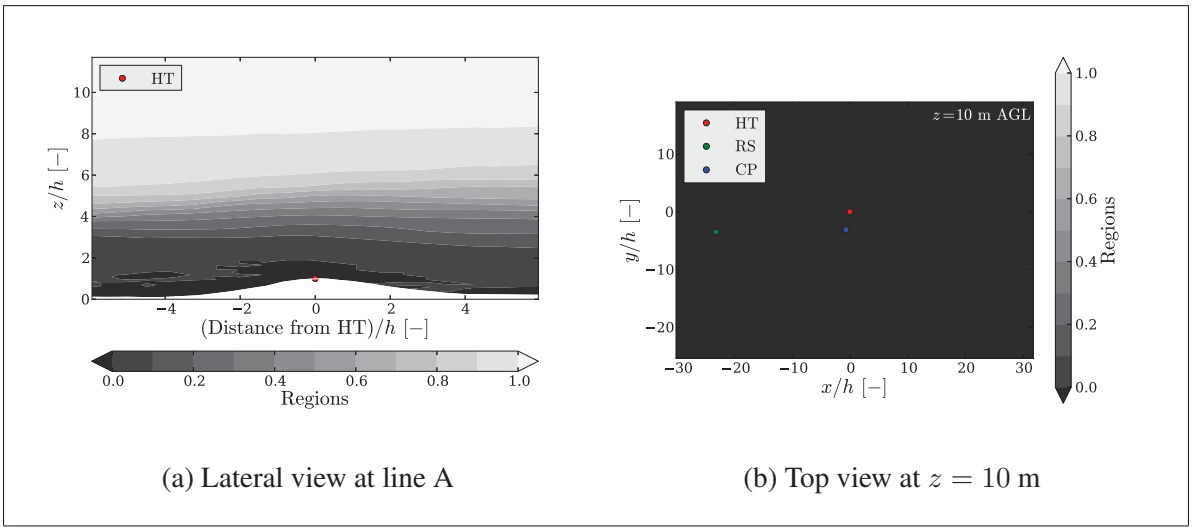

(a) Lateral view at line A

(b) Top view at $z = 10$ m

Figure 5.42 Time-averaged URANS/LES regions in the Askervein hill case. A pure LES region is identified as 1 and a pure URANS as 0.

The velocity obtained at the reference point RS is in agreement with the measurements as displayed in Figure 5.43a. However Figure 5.43b shows that the total turbulent kinetic energy (resolved plus modelled) simulated and the predicted by the Monin-Obukhov theory are greater than the measurement. Because both meshes are under resolved in the near-wall region, a turbulent kinetic energy peak is seen. The vertical velocity and turbulent kinetic energy profiles at RS and HT are given in Figures 5.44 and 5.45 respectively. The difference between the mesh A and mesh B results are minimal. As mentioned, the velocity at the RS is well reproduced and it is slightly underestimated at the hill top. Once again, the simulated turbulent kinetic energy value at HT is larger than in the measurements, notably the near-wall region is well estimated.

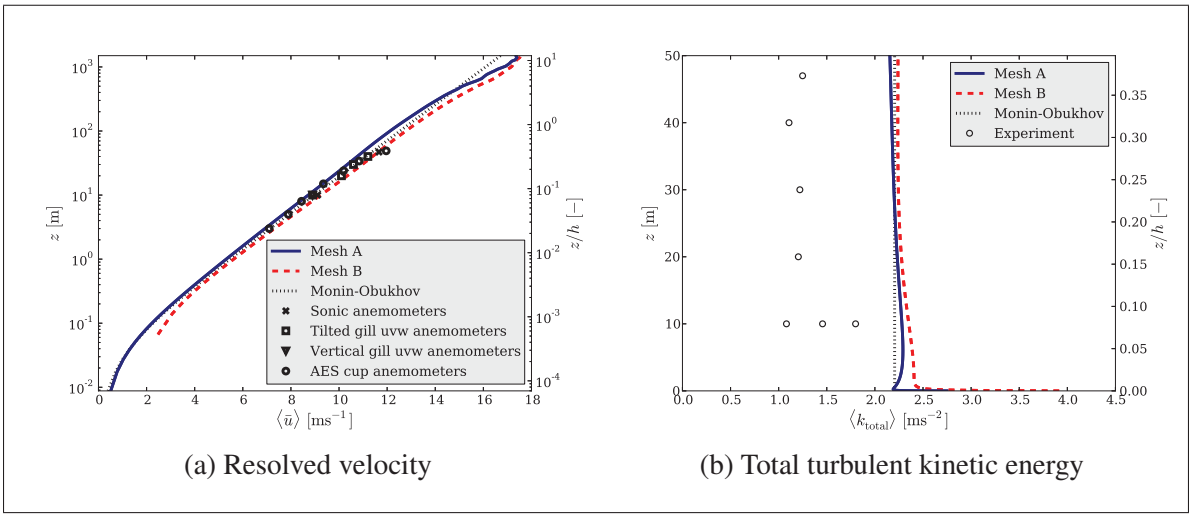

(a) Resolved velocity

(b) Total turbulent kinetic energy

Figure 5.43 Time-averaged vertical profiles at the reference point RS. Note the different scales of the vertical axis.

To better asses the accuracy of the Askervein hill simulations, the speed-up ratio

$$\Delta S(z) = \frac{|u(z)| - u_{\text{ref}}(z)}{u_{\text{ref}}(z)}. \tag{5.1}$$

is often calculated. The magnitude of the local and horizontal velocity $|u(z)|$ can then be compared against the undisturbed reference velocity at RS at the same height z. Figure 5.46 shows the vertical profile of ΔS at the hill top. Mesh A results are in better agreement with the experimental values in this case.

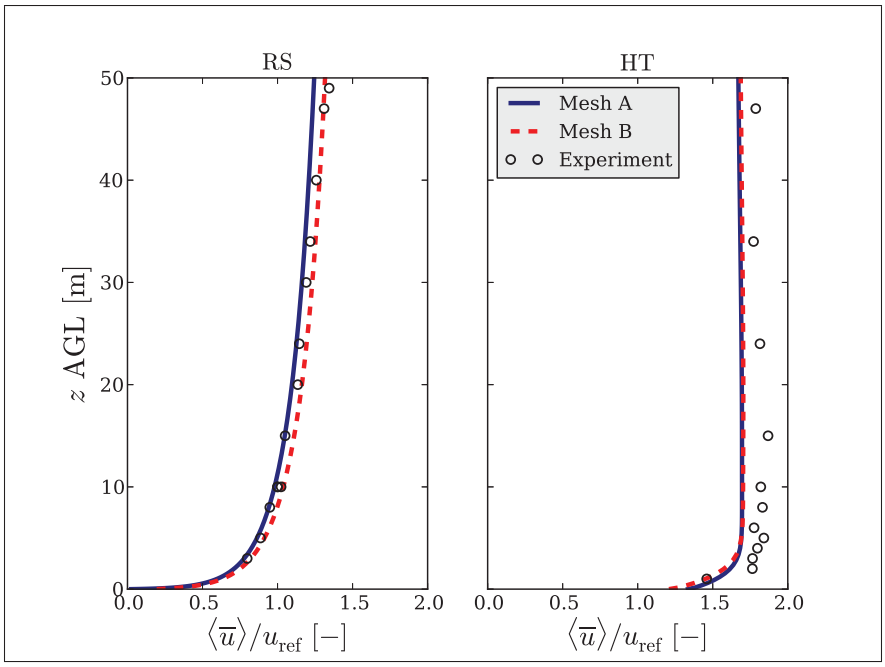

Figure 5.44 Time-averaged velocity profiles at RS and HT

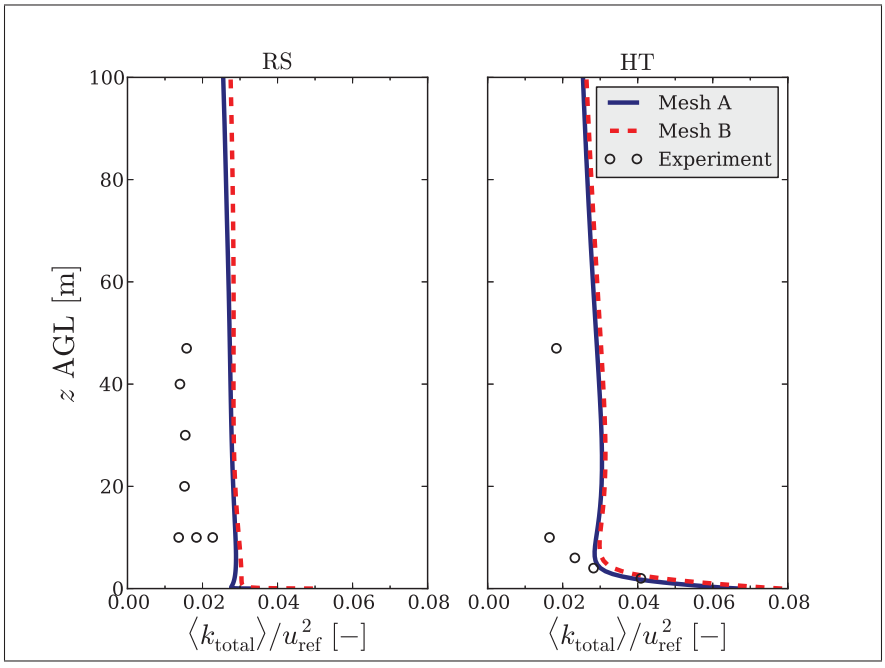

Figure 5.45 Total turbulent kinetic energy at RS and HT

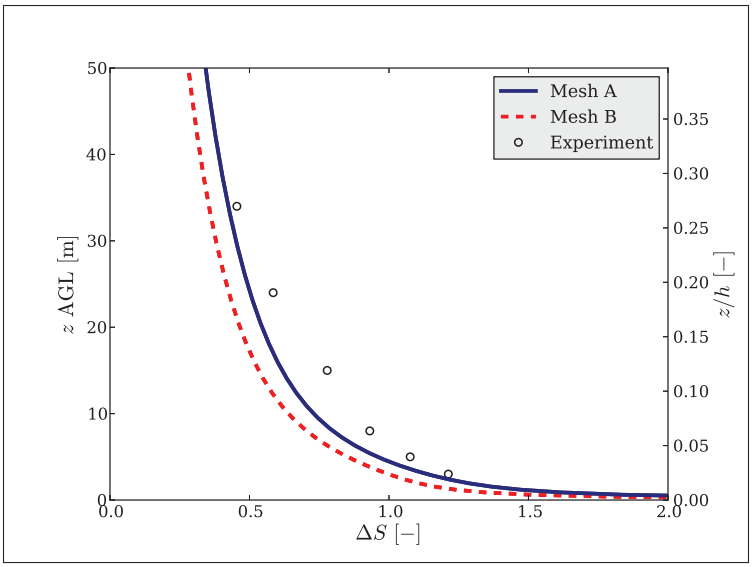

Figure 5.46 Vertical speed-up ratio at HT

Across the hill along line A and AA, the speed-up ratio at $z = 10$ m is rather accurately reproduced in the upstream region. This can be noticed in Figure 5.47. Nevertheless, the sharp deceleration in the lee-side of the hill along line A is not correctly predicted by the hybrid model. Downstream, the ΔS value can indicate the existence of a possible recirculation region (Katopodes Chow and Street, 2009). As for the normalized turbulent kinetic energy along line A and AA in Figure 5.48, the hybrid model results are not consistent with the experimental data. However in general, RANS models and even coarse mesh LES results (Silva Lopes *et al.*, 2007) tend to under estimate the turbulence downstream of the hill.

Finally, Figure 5.49a gives a global perception of the mean velocity field at a height of 10 m, while the instantaneous velocity field near the hill is shown in Figure 5.49b. These simulations do not indicate the presence of a recirculation region in the lee-side of the hill.

5.2.1 Overview

Even with a simplified terrain representation and a coarse topographic resolution, the neutral atmospheric flow around the Askervein hill was properly estimated by the $k - \omega$ SST-SIDDES hybrid model. Due to the coarse mesh refinement used, most of the results shown come from

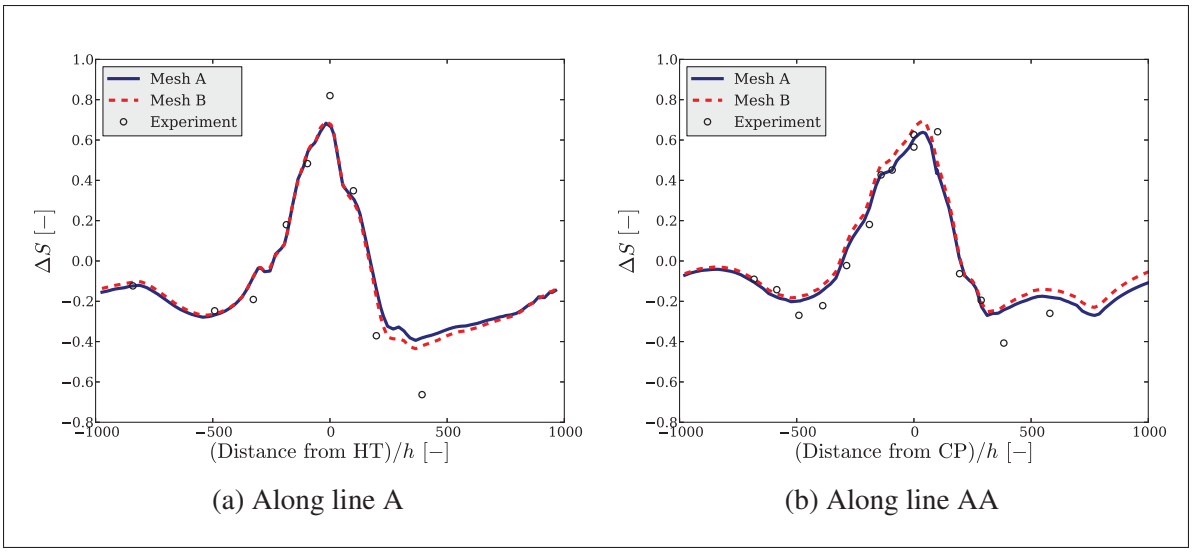

(a) Along line A (b) Along line AA

Figure 5.47 Speed-up across the Askervein hill at $z = 10$ m

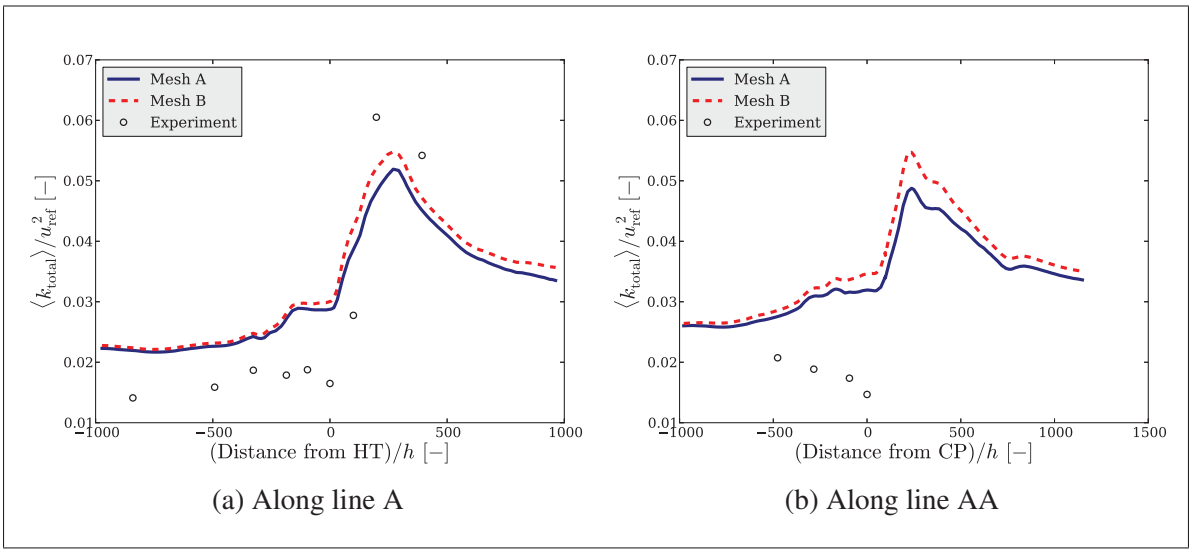

(a) Along line A (b) Along line AA

Figure 5.48 Turbulent kinetic energy across the Askervein hill at $z = 10$ m

URANS regions in the simulation. As it is often seen on RANS simulations, the hybrid results reproduce accurately the mean velocity field, but encounter difficulties to correctly estimate unsteady phenomena and turbulence statistics (i.e the turbulent kinetic energy and the recirculation region).

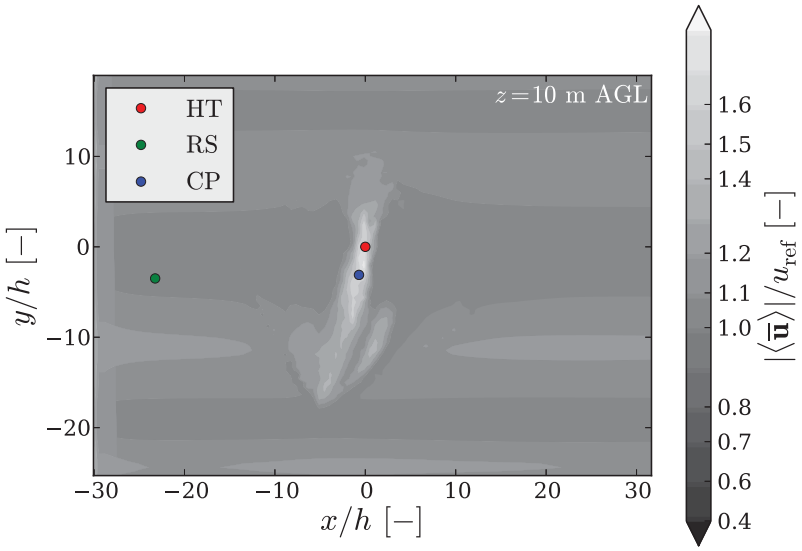

(a) Magnitude of the mean horizontal velocity

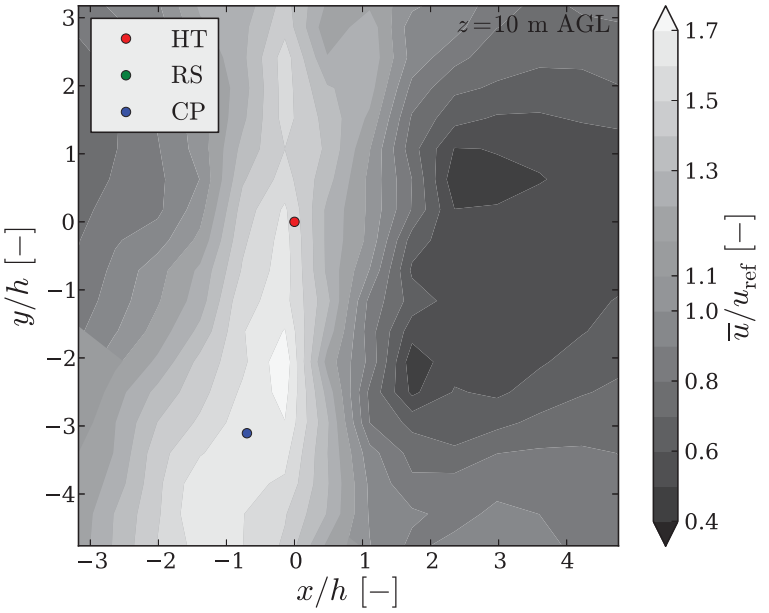

(b) Instantaneous streamwise velocity

Figure 5.49 Mesh A velocity field at $z = 10$ m

The hybrid model results could potentially be improved with a finer mesh. First, smaller cells will push the LES regions closer to the ground, possibly allowing the prediction of unsteady behaviour in the lee-side of the hill. Secondly, having a finer mesh will reduce the aspect ratio of the near-wall cells and alleviate the meshing constrains. Therefore, having smaller cells in the stream and spanwise direction will allow smaller values z_1 without introducing errors in the mesh and the required z_1^+ will be more easily attainable.

These results do not appear to indicate that having a large z_1^+ (without a wall function) could lead to any discrepancies or unphysical behaviour in the simulations. As shown on the flat terrain cases in Section 4.2, it might not be necessary to have $z_1^+ \sim 1.0$ for atmospheric flow simulations if its consequences are understood (i.e. peak in the turbulent kinetic energy profile and the inaccurate estimation of u_*). But to firmly corroborate that statement finer mesh test cases need to be analyzed.

On the other hand, Castro *et al.* (2003) considered that the inaccuracies in their Askervein RANS results could be related to the fact that equilibrium boundary layer assumptions are used in complex flows. Once more, a $k-\omega$ SST-SIDDES simulation of the Askervein case with a finer mesh and $z_1^+ \sim 1.0$ could help corroborate if wall functions and flat terrain assumptions are valid for complex terrain simulations.

CONCLUSION

A turbulence model based on the $k-\omega$ SST RANS model and the simplified improved delayed detached-eddy simulation (SIDDES) hybrid approach has been implemented in OpenFOAM v.2.2.2. The $k-\omega$ SST-SIDDES hybrid model is considered a good candidate for microscale simulations of the atmospheric boundary layer for two main reasons. First, its particular wall treatment is less dependent on flat terrain assumptions, therefore wall functions to model the Earth's surface can be avoided. This hybrid model might also provide some guidance to better understand the effects of using wall functions in complex terrain. And secondly, it is expected that the proposed hybrid model can result in a good compromise between the higher accuracy and lower computer cost needed by the wind energy industry.

The $k-\omega$ SST-SIDDES model is based on the standard DES hybrid approach, but its formulation is significantly more complex. However, the SIDDES can overcome certain drawbacks that arise when DES-type models are applied outside their original scope, specifically when they are used as a wall-modelled LES (WMLES). Because of the fine grid refinement (with respect to the boundary layer height) needed in microscale simulations, the DES approaches will always behave as a WMLES and the standard DES might most likely yield erroneous results as demonstrated by Nikitin *et al.* (2000) on channel flow cases. Subsequently, the SIDDES approach (or any other improvement or correction) is imperative for atmospheric boundary layer simulations with these type of hybrid models. In this thesis, the conclusions of Shur *et al.* (2008) and Gritskevich *et al.* (2012) concerning aerodynamic flows have been extended and the SIDDES has been proven valid on atmospheric flows with extremely rough walls and high Reynolds numbers.

Before being tested on atmospheric flows, this hybrid model has been extensively validated on canonical flows. This detailed process also provided an opportunity to properly explore certain modelling concepts and turbulence model limitations. To this end, decaying isotropic turbulence cased was used to properly calibrated the hybrid model constants within the specific numerical framework (i.e. OpenFOAM package, discretization schemes, etc.). It was also established that the model is capable of simulating correctly the turbulence energy cascade.

As well, a decaying turbulence subjected to rotation and a homogeneous shear turbulence test cases demonstrated that the rotation and mean shear effects are properly reproduced by the hybrid model. Next, several channel flow cases were analyzed to verify that the SIDDES model behaves well at the high Reynolds numbers and the large roughness lengths encountered in atmospheric flows. Also, blended discretization schemes were implemented to successfully improve the results and stability of the simulations. Overall, these canonical flow cases helped recognize and understand the proposed hybrid model capabilities and limitations.

Later, a rigorous analysis of the ideal atmospheric boundary layer over flat terrain with homogeneous roughness was carried out. The analysis brought forward the fact that the model requires a good quality mesh generator capable of properly defining the height of the fist node and handling high aspect ratio near-wall cells. Nevertheless, the fine grid refinement on the vertical direction required by the roughness extension might not be necessarily crucial at least for flat terrain. It was verified that DES indeed yields incorrect results on this particular type of simulations. To conclude, it was demonstrated that the hybrid model is able to reproduce the ideal atmospheric boundary layer characteristics. In particular, the velocity profiles shows a logarithmic behaviour and the turbulent kinetic energy is constant in the lower 20% of the domain. Additionally due to the URANS region that cover almost all of the ASL, the mean velocity gradient is correctly reproduced by the hybrid model. In other words, the overshoot commonly obtained by LES is absent. Lastly, a real flat terrain case was simulated. The SIDDES model yield realistic flow behaviour, but it overestimated the value of the spanwise component.

In this work, the $k-\omega$ SST-SIDDES turbulence model was thoroughly validated to assess its capabilities. The complete validation process could be used as a standard procedure for turbulence model verification on atmospheric flow. With $k-\omega$ SST-SIDDES, accurate results were obtained on canonical flows and atmospheric flows over flat terrain. It was shown that atmospheric boundary layer simulations over flat terrain can be carried out successfully without relying on the use of wall functions or on considerably large computing resources.

Finally, simulations of complex flow were performed. The massively separated flow around square-section cylinder and the full scale Askervein hill was studied. The fine mesh required appears to be the most important drawback and certain compromises had to be made. However, the results corroborate that the hybrid model is capable of capturing the physics of the complex turbulent flows without relying on the use of a wall function. Therefore the $k-\omega$ SST-SIDDES hybrid model is indeed a good candidate for studying complex flows and microscale wind energy simulations.

Proposed future work

Most of the thesis work was devoted to assure a proper hybrid model implementation, and to perform a very thorough and rigorous turbulence model validation within the OpenFOAM framework. All this testing was crucial to guarantee reliable simulations. However as in any research work, further studies and tests could always be performed to potentially enrich the current findings.

It is essential to develop a complete benchmark for testing complex terrain simulations that could become a standard for turbulence model verification on microscale atmospheric flow. This benchmark should consist of:

- Standard test cases to validate flow separation and reattachment.
- Recent and complete wind-tunnel experiments which are representative of atmospheric flows (i.e. thick boundary layer, rough surfaces, flow separation regions, etc).
- More challenging natural complex terrain cases where careful field measurement campaigns have taken place. For example, attempting to obtain accurate results of the Bolund experiment which presents a sharp escarpment.

More specifically in the case of atmospheric flow over complex terrain using the $k-\omega$ SST-SIDDES hybrid model, the future tests that should be considered must include:

- The analysis of the mentioned complex terrain benchmark. This type of studies will determine quantitatively and unquestionably the capabilities of the model. In particular, this type of analysis will corroborate if the $k-\omega$ SST-SIDDES surface treatment (without a wall function) can produce accurate results in complex terrain test cases.

- The study of the Askervein hill case using finer grids to push the LES regions closer to the ground surface. Having a smaller URANS region could possibly provide a more accurate estimation of the turbulent kinetic energy and other turbulence statistics, and modelled the unsteady behaviour of the flow in the lee-side of the hill. Additionally, a finer mesh will allow to reduce the height of the near-wall cells. Then it will be possible to corroborate if the used $k-\omega$ SST surface treatment can provide more accurate results in complex terrain than having a wall function.

- The study of variable roughness and canopy models to better model the ground heterogeneous surface.

- The inclusion of atmospheric stratification which has a considerable effect on the physics of the atmospheric flow.

APPENDIX I

$k-\omega$ SST-SIDDES HYBRID MODEL EQUATIONS

$$\begin{aligned}
\frac{\partial k}{\partial t}+\frac{\partial \overline{u}_j k}{\partial x_j}-\frac{\partial}{\partial x_j}\left[\left(\nu+\sigma_k \nu_t\right)\frac{\partial k}{\partial x_j}\right] =& P_k-\frac{k^{3/2}}{\tilde{l}} \\
\frac{\partial \omega}{\partial t}+\frac{\partial \overline{u}_j \omega}{\partial x_j}-\frac{\partial}{\partial x_j}\left[\left(\nu+\sigma_\omega \nu_t\right)\frac{\partial \omega}{\partial x_j}\right] =& \frac{\gamma}{\nu_t}P_k-\beta\omega^2+2(1-F_1)\frac{\sigma_{\omega 2}}{\omega}\frac{\partial k}{\partial x_j}\frac{\partial \omega}{\partial x_j}
\end{aligned} \tag{A I-1}$$

$$\begin{aligned}
P_k =& \min(\nu_t \mathcal{S}^2, c_1\,\beta_*\,k\,\omega) \\
\mathcal{S} =& \sqrt{S_{ij}S_{ij}} \\
\nu_t =& \frac{a_1 k}{\max(\mathrm{a_1}\omega, \mathcal{S}\mathrm{F}_2)}
\end{aligned} \tag{A I-2}$$

$k-\omega$ SST blending functions:

$$\begin{aligned}
F_1 =& \tanh\left(arg_1^4\right) \\
arg_1 =& \min\left(\max\left(\frac{\sqrt{k}}{\beta_*\,\omega\,d_w}, \frac{500\,\nu}{d_w^2\,\omega}\right), \frac{4\,\rho\,\sigma_{\omega 2}\,k}{CD_{k\omega}\,d_w^2}\right) \\
CD_{k\omega} =& \max\left(2\,\rho\,\sigma_{\omega 2}\frac{\nabla k\cdot\nabla\omega}{\omega}, 10^{-10}\right) \\
F_2 =& \tanh\left(arg_2^2\right) \\
arg_2 =& \max\left(\frac{2\sqrt{k}}{\beta_*\,\omega\,d_w}, \frac{500\,\nu}{d_w^2\,\omega}\right)
\end{aligned} \tag{A I-3}$$

SIDDES blending functions:

$$\tilde{l}_{SIDDES} = \tilde{f}_d \, l_{RANS} + (1 - \tilde{f}_d) l_{LES} \tag{A I-4}$$

$$\begin{aligned} l_{RANS} &= \frac{\sqrt{k}}{\beta_* \omega} \\ l_{LES} &= C_{DES} \Delta \\ C_{DES} &= (1 - F_1) C_{k-\epsilon} + F_1 C_{k-\omega} \\ \Delta_{IDDES} &= \min[\max(C_w d_w, C_w h_{max}, h_{wn}), h_{max}] \end{aligned} \tag{A I-5}$$

$$\begin{aligned} \tilde{f}_d &= \max[(1.0 - f_{dt}), f_b] \\ f_{dt} &= 1.0 - \tanh\left[(c_{d1} r_{dt})^{c_{d2}}\right] \\ r_{dt} &= \frac{\nu_t}{\kappa^2 d_w^2 \sqrt{0.5(\mathcal{S}^2 + \Omega^2)}} \\ f_b &= \min[2.0\, e^{-9.0\alpha^2}, 1.0] \\ \alpha &= 0.25 - d_w / h_{max} \end{aligned} \tag{A I-6}$$

Here, h_{max} is the maximum edge length of the cell, d_w is the distance to the nearest wall, h_{hw} is the grid step normal to the wall. Finally, $\mathcal{S}$ and Ω are the magnitude of the strain rate tensor and the magnitude of the vorticity tensor respectively.

The constants are calculated as $\phi = F_1\phi_1 + (1 - F_1)\phi_2$ based on the values from Table I-1.

Table-A I-1 Turbulence model constants.

$k-\omega$ SST constants for aerodynamic flows (Menter *et al.*, 2003):					
$\beta_1 = 0.075$	$\beta_2 = 0.0828$	$\sigma_{k1} = 0.85$	$\sigma_{k2} = 1.0$	$\kappa = 0.41$	$\beta_* = 0.09$
$\gamma_1 = 5/9$	$\gamma_2 = 0.44$	$\sigma_{\omega 1} = 0.5$	$\sigma_{\omega 2} = 0.856$	$a_1 = 0.31$	$c_1 = 10.0$
SIDDES constants for aerodynamic flows (Gritskevich *et al.*, 2012) (Travin *et al.*, 2002):					
$C_{k-\epsilon} = 0.61$	$C_{k-\omega} = 0.78$	$C_w = 0.15$	$C_{dt1} = 20.0$	$C_{dt2} = 3.0$	
$k-\omega$ SST constants for atmospheric flow (Boudreault, 2011):					
$\beta_1 = 0.0236$	$\beta_2 = 0.0276$	$\sigma_{k1} = 0.85$	$\sigma_{k2} = 1.0$	$\kappa = 0.40$	$\beta_* = 0.03$
$\gamma_1 = 0.3255$	$\gamma_2 = 0.3011$	$\sigma_{\omega 1} = 0.5$	$\sigma_{\omega 2} = 0.67$	$a_1 = 0.31$	$c_1 = 10.0$
SIDDES constants for atmospheric flow:					
$C_{k-\epsilon} = 0.61$	$C_{k-\omega} = 0.78$	$C_w = 0.15$	$C_{dt1} = 20.0$	$C_{dt2} = 3.0$	

APPENDIX II

FORMULATION OF THE DES, DDES AND IDDES MODELS

DES blending functions:

$$\tilde{l}_{DES} = \min(l_{RANS}, l_{LES}) \tag{A II-1}$$

$$\begin{aligned} l_{RANS} &= \frac{\sqrt{k}}{\beta_* \omega} \\ l_{LES} &= C_{DES}\Delta \\ C_{DES} &= (1 - F_1)C_{k-\epsilon} + F_1 C_{k-\omega} \\ \Delta &= \max(\Delta_x, \Delta_y, \Delta_z) \end{aligned} \tag{A II-2}$$

DDES blending functions:

$$\tilde{l}_{DDES} = l_{RANS} - f_d \max(0, l_{RANS} - l_{LES}) \tag{A II-3}$$

$$\begin{aligned} l_{RANS} &= \frac{\sqrt{k}}{\beta_* \omega} \\ l_{LES} &= C_{DES}\Delta \\ C_{DES} &= (1 - F_1)C_{k-\epsilon} + F_1 C_{k-\omega} \\ \Delta &= \max(\Delta_x, \Delta_y, \Delta_z) \end{aligned} \tag{A II-4}$$

$$
\begin{aligned}
f_d =& 1.0 - \tanh\left[(c_{d1} r_d)^{c_{d2}}\right] \\
r_d =& \frac{\nu + \nu_t}{\kappa^2 d_w^2 \sqrt{0.5(\mathcal{S}^2 + \Omega^2)}}
\end{aligned}
\tag{A II-5}
$$

IDDES blending functions:

$$
\tilde{l}_{IDDES} = \tilde{f}_d \left(1 + f_e\right) l_{RANS} + (1 - \tilde{f}_d) l_{LES} \tag{A II-6}
$$

$$
\begin{aligned}
l_{RANS} =& \frac{\sqrt{k}}{\beta_* \omega} \\
l_{LES} =& C_{DES} \Delta \\
C_{DES} =& (1 - F_1) C_{k-\epsilon} + F_1 C_{k-\omega} \\
\Delta_{IDDES} =& \min[\max(C_w d_w,\, C_w h_{max},\, h_{wn}),\, h_{max}]
\end{aligned}
\tag{A II-7}
$$

$$
\begin{aligned}
\tilde{f}_d =& \max[(1.0 - f_{dt}), f_b] \\
f_{dt} =& 1.0 - \tanh\left[(c_{d1} r_{dt})^{c_{d2}}\right] \\
r_{dt} =& \frac{\nu_t}{\kappa^2 d_w^2 \sqrt{0.5(\mathcal{S}^2 + \Omega^2)}} \\
f_b =& \min[2.0\, e^{-9.0\alpha^2}, 1.0] \\
\alpha =& 0.25 - d_w / h_{max}
\end{aligned}
\tag{A II-8}
$$

$$
\begin{aligned}
f_e =& f_{e2} \max[(f_{e1} - 1.0), 0.0] \\
f_{e1} =& \begin{cases} 2e^{-11.09\alpha^2} & \text{if } \alpha \geq 0 \\ 2e^{-9.00\alpha^2} & \text{if } \alpha < 0 \end{cases} \\
f_{e2} =& 1.0 - \max(f_t, f_l) \\
f_t =& \tanh\left[(C_t^2\, r_{dt})^3\right] \\
f_l =& \tanh\left[(C_l^2\, r_{dl})^{10}\right] \\
r_{dl} =& \frac{\nu}{\kappa^2 d_w^2 \sqrt{0.5(\mathcal{S}^2 + \Omega^2)}}
\end{aligned}
\tag{A II-9}
$$

Here, $C_l = 5.0$ and $C_t = 1.87$, h_{max} is the maximum edge length of the cell, d_w is the distance to the nearest wall, h_{hw} is the grid step normal to the wall. Finally, $\mathcal{S}$ and Ω are the magnitude of the strain rate tensor and the magnitude of the vorticity tensor respectively.

APPENDIX III

OPENFOAM CODE

1. Implementing the k and ω equations for the hybrid model

```
// Turbulent frequency equation
tmp<fvScalarMatrix> omegaEqn
(
    fvm::ddt(omega_)
  + fvm::div(phi_, omega_)
  - fvm::Sp(fvc::div(phi_), omega_)
  - fvm::laplacian(DomegaEff(F1), omega_)
 ==
 // gamma(F1)*S2   //See Gritskevich2011
    gamma(F1)*min(G, c1_*betaStar_*k_*omega_)/max(nuSgs_,
            dimensionedScalar("SMALL", nuSgs_.dimensions(), SMALL))
  - fvm::Sp(beta(F1)*omega_, omega_)
  - fvm::SuSp
    (
       (F1 - scalar(1))*CDkOmega/omega_, omega_
    )
);



.....



// Turbulent kinetic energy equation
tmp<fvScalarMatrix> kEqn
(
    fvm::ddt(k_)
  + fvm::div(phi_, k_)
  - fvm::Sp(fvc::div(phi_), k_)
  - fvm::laplacian(DkEff(F1), k_)
 ==
    min(G, c1_*betaStar_*k_*omega_)
//- fvm::Sp(betaStar_*omega_, k_)          // Original kwSST code
  - fvm::Sp(pow(k_,1.0/2.0)/dTilda_, k_)  // Modified for SIDDES
);
```

2. Implementing the equations for the free homogeneous flow case

```
fvVectorMatrix UEqn
(
    fvm::ddt(U)
  + fvm::div(phi, U)
  + turbulence->divDevReff(U)
//Added terms
  + fvc::div(Ushearphi, Ushear)
  + fvc::div(phi, Ushear)
  + fvm::div(Ushearphi, U)
  - fvc::laplacian(nu, Ushear)
);
```

This equation is being solved for `U` which (only for this case) represents the velocity fluctuations. `Ushear` is the mean velocity calculated as:

```
   forAll(Ushear,cellI)
    {
        scalar z = mesh.C()[cellI].z();
        Ushear[cellI].x()=dudz*z;
    }
```

based on `dudz`, the imposed mean gradient. Also `surfaceScalarField Ushearphi = fvc::interpolate(Ushear) & mesh.Sf()`. Finally `UTotal=U+Ushear`.

3. Adding a pressure gradient to drive the flow

The constant pressure gradient is added to the momentum predictor matrix `UEqn`. The term `gradP` is read directly from the input files of the simulation case.

```
fvVectorMatrix UEqn
(
     fvm::ddt(U)
     + fvm::div(phi, U)
     + turbulence->divDevReff(U)
     + gradP                              // Large scale pressure gradient
);
```

4. Adding the Coriolis force

Based on the SOWFA code (Churchfield *et al.*, 2014), the Coriolis term is calculated as:

```
fCoriolis = -2.0*(Omega^U);
```

The variable `Omega` represents the angular velocity vector that could be read directly from the case input files or it can be calculated inside the code using the planetary rotation period. Then the term `fCoriolis` is added inside the PISO loop in the **.C* file.

```
// Pressure-velocity PISO corrector
#include "computeCoriolisForce.H"

// Momentum predictor
fvVectorMatrix UEqn
(
     fvm::ddt(U)
   + fvm::div(phi, U)
   + turbulence->divDevReff(U)
   - fCoriolis                          // Coriolis force
   + gradP                              // Large scale pressure gradient
);
```

5. Blending schemes

Lines added to the turbulence model code *SIDDES.C*. A field variable called `region` calculated each time step defines if a cell is solved in URANS or LES mode.

```
//Returns 0 in pure RANS-Regions an 1 in pure LES-regions
volScalarField SIDDES::region(const volScalarField& S) const
{
   volScalarField region
   (
        IOobject
        (
            "region",
            runTime_.timeName(),
            mesh_,
            IOobject::READ_IF_PRESENT,
            IOobject::NO_WRITE
        ),
        mesh_,
        dimensionedScalar("region", dimensionSet(0, 0, 0, 0, 0, 0, 0), 0)
    );
```

```
    const volScalarField expTerm(exp(sqr(this->alpha())));
    tmp<volScalarField> fb = min(2*pow(expTerm, -9.0), scalar(1));
    const volScalarField fdTilda(max(1 - fdt(S), fb));

   forAll(fdTilda, cellI)
   {
       region[cellI]=1-fdTilda[cellI];
   }

   return region;
}
```

Lines of code added to *pisoFoamABL.C* file in the solver application. This lines are placed at the end of the PISO loop to obtain the value of the `region` from the turbulence model code, then calculate the blending factors for each needed variable. The blending factor will define the discretization scheme to use during the following PISO loop.

```
volScalarField getRegion=mesh.lookupObject<volScalarField>("region");
//UBlendingFactor=fvc::interpolate(getRegion);
omegaBlendingFactor=fvc::interpolate(getRegion);
kBlendingFactor=fvc::interpolate(getRegion);
```

6. system/fvSchemes file

```
/*--------------------------------*- C++ -*----------------------------*\
| =========                 |                                           |
| \\      /  F ield         | OpenFOAM: The Open Source CFD Toolbox     |
|  \\    /   O peration     | Version:  2.2.0                           |
|   \\  /    A nd           | Web:      http://www.OpenFOAM.org         |
|    \\/     M anipulation  |                                           |
\*---------------------------------------------------------------------*/
FoamFile
{
    version     2.0;
    format      ascii;
    class       dictionary;
    object      fvSchemes;
}
// * * * * * * * * * * * * * * * * * * * * * * * * * * * * * * * * * * * * //

ddtSchemes
{
 default            backward;
}

gradSchemes
{
    default       Gauss linear 1.0;
    grad(U)       Gauss linear;
    grad(k)       cellLimited leastSquares 1.0;
    grad(omega)   cellLimited leastSquares 1.0;
}

divSchemes
{
    default         none;
    div(phi,U)      Gauss linear;
    div(phi,k)      Gauss localBlended linear linearUpwind grad(k);
    div(phi,omega)  Gauss localBlended linear linearUpwind grad(omega);
    div((nuEff*dev(T(grad(U)))))    Gauss linear;
}

laplacianSchemes
{
    default                     none;
    laplacian(nuEff,U)          Gauss linear uncorrected;
    laplacian((1|A(U)),p)       Gauss linear uncorrected;
    laplacian(DomegaEff,omega)  Gauss linear uncorrected;
    laplacian(DkEff,k)          Gauss linear uncorrected;
}

interpolationSchemes
{
    default         linear;
}

snGradSchemes
{
    default         uncorrected;
}

fluxRequired
{
    default         no;
    p;
}

// ************************************************************************* //
```

7. system/fvSolution file:

```
/*--------------------------------*- C++ -*----------------------------*\
| =========                 |                                           |
| \\      /  F ield         | OpenFOAM: The Open Source CFD Toolbox     |
|  \\    /   O peration     | Version:  2.2.0                           |
|   \\  /    A nd           | Web:      www.OpenFOAM.com                |
|    \\/     M anipulation  |                                           |
\*---------------------------------------------------------------------*/
FoamFile
{
    version     2.0;
    format      ascii;
    class       dictionary;
    location    "system";
    object      fvSolution;
}
// * * * * * * * * * * * * * * * * * * * * * * * * * * * * * * * * * * * * //

solvers
{
    p
    {
        solver          GAMG;
        tolerance       1e-6;
        relTol          0.001;
        smoother        DICGaussSeidel;
        nPreSweeps      0;
        nPostSweeps     2;
        nFinestSweeps   2;
        cacheAgglomeration true;
        nCellsInCoarsestLevel 1000;
        agglomerator    faceAreaPair;
        mergeLevels     2;
    }

    pFinal
    {
        solver          GAMG;
        tolerance       1e-6;
        relTol          0;
        smoother        DICGaussSeidel;
        nPreSweeps      0;
        nPostSweeps     2;
        nFinestSweeps   2;
        cacheAgglomeration true;
        nCellsInCoarsestLevel 1000;
        agglomerator    faceAreaPair;
        mergeLevels     2;
        minIter         1;
    }

    U
    {
        solver          smoothSolver;
        smoother        GaussSeidel;
        nSweeps         1;
        tolerance       1e-6;
        relTol          0;
        minIter         1;
    }

    k
    {
        solver          smoothSolver;
```

```
        smoother        GaussSeidel;
        nSweeps         1;
        tolerance       1e-6;
        relTol          0;
        minIter         1;
    }

    omega
    {
        solver          smoothSolver;
        smoother        GaussSeidel;
        nSweeps         1;
        tolerance       1e-6;
        relTol          0;
        minIter         1;
    }
}
PISO
{
    nCorrectors     3;
    nNonOrthogonalCorrectors 0;
    pRefPoint       (50 50 50);
    pRefValue       0;
}

// ************************************************************************* //
```

Certain observations:

- If the preconditioned biconjugate gradient solver method (`PBiCG`) was used for the linearized U, k and ω equations instead of the `smoothSolver` method, the simulations became really unstable when run in parallel and the number of pressure iterations needed to reach the defined tolerance increased considerably.

- The PISO algorithm with three corrector loops (`nCorrectors`) for the pressure needed less iterations in total to converge than when only two `nCorrectors` were used.

- To minimize the execution time of a simulation, it was found that 90 000 cells/CPU cores was the optimal value for flat terrain cases. However, this number varied greatly for complex terrain cases. This test was carried out in the Guillimin supercomputer using only the nodes that have 16 CPU cores.

8. Meshing technique in OpenFOAM for complex topography

This meshing technique is based on Jeannotte (2013). To create the Askervien case mesh, two cases were used: *bottomMesh* and *topMesh*. The *constant/blockMesh* file in the bottom case is defined as:

```
*---------------------------------*- C++ -*----------------------------------*\
| =========                 |                                                 |
| \\      /  F ield         | OpenFOAM: The Open Source CFD Toolbox           |
|  \\    /   O peration     | Version:  2.2.0                                  |
|   \\  /    A nd           | Web:      http://www.OpenFOAM.org               |
|    \\/     M anipulation  |                                                 |
\*---------------------------------------------------------------------------*/
FoamFile
{
    version     2.2.0;
    format      ascii;
    class       dictionary;
    object      blockMeshDict;
}
// * * * * * * * * * * * * * * * * * * * * * * * * * * * * * * * * * * * * //

convertToMeters 1;

// ******Coordinates of blocks
x0 -3800;
x1  4000;
x2  4000;
x3 -3800;

y0 -3200;
y1 -3200;
y2  2400;
y3  2400;

z0  400;   //Not really important
z1  500;

//*****Number of cells*****
Nx 335;  // Number of x-cells
Ny 240;  // Number of y-cells
Nz1 1;   // Number of z-cells


//*****Grading values******
Gx  1.0;   //x-grading
Gy  1.0;   //y-grading
Gz1 1.0 ;  //z-grading

vertices
(
    ($x0 $y0 $z0)  //0
    ($x1 $y1 $z0)  //1
    ($x2 $y2 $z0)  //2
    ($x3 $y3 $z0)  //3
    ($x0 $y0 $z1)  //4
    ($x1 $y1 $z1)  //5
    ($x2 $y2 $z1)  //6
    ($x3 $y3 $z1)  //7
);
```

```
blocks
(
    hex (0 1 2 3 4 5 6 7) ($Nx $Ny $Nz1) simpleGrading ($Gx $Gy $Gz1)
);

...

boundary
(
    inlet
    {
        type patch;

        faces
        (
        (0 4 7 3)
        );
    }
    outlet
    {
        type patch;

        faces
        (
        (1 2 6 5)
        );
    }
    bottom
    {
        type wall;
        faces
        (
        (0 3 2 1)
        );
    }
    tmp_bottom
    {
        type slip;
        faces
        (
        (4 5 6 7)
        );
    }
    front
    {
        type patch;
        faces
        (
        (0 1 5 4)
        );
    }
    back
    {
        type patch;
        faces
        (
        (3 7 6 2)
        );
    }
);

mergePatchPairs
(
);

// ************************************************************************* //
```

While the file *constant/blockMesh* in the *topMesh* case is defined as:

```
*---------------------------------*- C++ -*----------------------------------*\
| =========                 |                                                 |
| \\      /  F ield         | OpenFOAM: The Open Source CFD Toolbox           |
|  \\    /   O peration     | Version:  2.2.0                                 |
|   \\  /    A nd           | Web:      http://www.OpenFOAM.org               |
|    \\/     M anipulation  |                                                 |
\*---------------------------------------------------------------------------*/
FoamFile
{
    version     2.2.0;
    format      ascii;
    class       dictionary;
    object      blockMeshDict;
}
// * * * * * * * * * * * * * * * * * * * * * * * * * * * * * * * * * * * * //

convertToMeters 1;

// ******Coordinates of blocks
x0 -3800;
x1  4000;
x2  4000;
x3 -3800;

y0 -3200;
y1 -3200;
y2  2400;
y3  2400;

z0  400;   //Not really important
z1  500;

//*****Number of cells*****
Nx 335;  // Number of x-cells
Ny 240;  // Number of y-cells
Nz1 19;  // Number of z-cells

//*****Grading values******
Gx  1.0;   //x-grading
Gy  1.0;   //y-grading
Gz1 1.0;   //z-grading


....

boundary
(
    inlet
    {
        type patch;
        faces
        (
        (0 4 7 3)
        );
    }
    outlet
    {
        type patch;
        faces
        (
        (1 2 6 5)
        );
    }
```

```
    tmp_top
    {
        type patch;
        faces
        (
        (0 3 2 1)
        );
    }
    top
    {
        type slip;
        faces
        (
        (4 5 6 7)
        );
    }
    front
    {
        type patch;
        faces
        (
        (0 1 5 4)
        );
    }
    back
    {
        type patch;
        faces
        (
        (3 7 6 2)
        );
    }
);

mergePatchPairs
(
);

// ************************************************************************* //
```

Then the complete mesh is generated with the following script:

```
cd bottomMesh
echo "Generating bottomMesh..."
blockMesh > log.mesh
moveDynamicMesh >> log.mesh    //Based on constant/dynamicMeshDict and 0/pointDisplacement,
the cells are elongated in the z-direction until they intersect with Askervein.stl terrain
elevation file.

...
refineWallLayer bottomMesh $Ratio -overwrite  >> log.mesh
...
refineWallLayer bottomMesh $Ratio -overwrite  >> log.mesh
....

cd ../topMesh
echo "Generating topMesh..."
blockMesh > log.mesh

cd ..
echo "Merging..."
mergeMeshes topMesh bottomMesh >> log.mesh
```

```
cd topMesh
echo "Stitching..."
stitchMesh -overwrite -perfect tmp_top tmp_bottom >> log.mesh

echo "Remove tmp patches from constant/polyMesh/boundary file manually!!!!"
.....

echo "Renumbering ..."
renumberMesh >> log.mesh

cp [lastTime]/polyMesh/* constant/polyMesh/
rm -rf [lastTime]

echo "The mesh is ready!. Just copy constant/polyMesh/* into the Askervein test case"
```

This meshing technique can take up to a couple hours to complete for the Askervein case in a desktop computer.

BIBLIOGRAPHY

Anderson, J. D., 1995. *Computational fluid dynamics: the basics with applications*. USA : McGraw-Hill.

Andren, A., A. R. Brown, J. Graf, P. J. Mason, C-H. Moeng, F. T. M. Nieuwstadt, and U. Schumann. 1994. "Large-eddy simulation of a neutrally stratified boundary layer: A comparison of four computer codes". *Quarterly Journal of the Royal Meteorological Society*, vol. 120, p. 1457–1484.

Apsley, D. D. and I. P. Castro. 1997. "Flow and dispersion over hills: Comparison between numerical predictions and experimental data". *Journal of Wind Engineering and Industrial Aerodynamics*, vol. 67 & 68, p. 375–386.

Athanassiadou, M. and I. P. Castro. 2001. "Neutral flow over a series of rough hills: A laboratory experiment". *Boundary-Layer Meteorology*, vol. 101, p. 1–30.

Ayotte, K. W. 2008. "Computational modelling for wind energy assessment". *Journal of Wind engineering and Industrial Aerodynamics*, vol. 96, p. 1571-1590.

Bardina, J., J. H. Ferziger, and W. C. Reynolds. May 1983. *Improved turbulence models based on large eddy simulation of homogeneous, incompressible, turbulent flows*. Technical Report TF-19. USA : Thermosciences Division. Department of Mechanical Engineering. Stanford University.

Bardina, J., J. H. Ferziger, and R. S. Rogallo. 1985. "Effect of rotation on isotropic turbulence: computation and modelling". *Journal of Fluid Mechanics*, vol. 154, p. 321–336.

Bartello, P., O. Métais, and M. Lesieur. 1994. "Coherent structures in rotating three-dimensional turbulence". *Journal of Fluid Mechanics*, vol. 273, p. 1–29.

Batchelor, G. K., 1967. *An introduction to fluid dynamics*. Cambridge : Cambridge University Press.

Bechmann, A. November 2006. "Large-eddy simulation of atmospheric flow over complex terrain". PhD thesis, Risø National Laboratory. Technical University of Denmark, Roskilde, Denmark. Risø-PhD-28(EN).

Bechmann, A. and N. N. Sørensen. 2010. "Hybrid RANS/LES method for wind flow over complex terrain". *Wind Energy.*, vol. 13, p. 36-50.

Berg, J., J. Mann, A. Bechmann, M. S. Courtney, and H. E. Jørgensen. 2011. "The Bolund experiment, Part I: Flow over a steep, three-dimensional hill". *Boundary-Layer Meteorology*, vol. 141, p. 219–243.

Blocken, B., T. Stathopoulos, and J. Carmeliet. 2007. "CFD simulations of the atmospheric boundary layer: wall function problems". *Atmospheric Environment*, vol. 41, p. 238-252.

Boudreault, L-É. 2011. "Modélisation numérique de la séparation de l'écoulement atmosphérique". M.Ing thesis, École de Technologie Supérieure, Montreal, QC. Canada.

Bourgeois, J. A., P. Sattari, and R. J. Martinuzzi. 2011. "Alternating half-loop shedding in the turbulent wake of a finite surface-mounted square cylinder with a thin boundary layer". *Physics of Fluids*, vol. 23, n° 9, p. 095101.

Boussinesq, M. J., 1897. *Théorie de l'écoulement tourbillonnant et tumultueux des liquides dans les lits rectilignes a grande section*. Paris : Gauthier-Villars et fils.

Brasseur, J. G. and T. Wei. 2010. "Designing large-eddy simulation of the turbulent boundary layer to capture law-of-the-wall scaling". *Physics of Fluids*, vol. 22, n° 2, p. 021303.

Bunge, U., C. Mockett, and F. Thiele. 2007. "Guidelines for implementing detached-eddy simulation using different models". *Aerospace Science and Technology*, vol. 11, p. 376–385.

Castro, F. A., J. M. L. M. Palma, and A. Silva Lopes. 2003. "Simulation of the Askervein flow. Part 1: Reynolds averaged Navier-Stokes equations ($k - \varepsilon$ Turbulence Model)". *Boundary-Layer Meteorology*, vol. 107, p. 501-530.

Castro, I. P. and M. Dianat. 1983. "Surface flow patterns on rectangular bodies in thick boundary layers". *Journal of Wind Engineering and Industrial Aerodynamics*, vol. 11, p. 107–119.

Castro, I. P. and A. G. Robins. 1977. "The flow around a surface-mounted cube in uniform and turbulent streams". *Journal of Fluid Mechanics*, vol. 79, n° 02, p. 307.

Chow, F. K. July 2004. "Subfilter-scale turbulence modeling for large-eddy simulation of the atmospheric boundary layer over complex terrain". PhD thesis, Department of Civil and Environmental Engineering, Stanford University, California, USA.

Churchfield, M. J., P. J. Moriarty, G. Vijayakumar, and J. G. Brasseur. August 2-6 2010. "Wind energy-related atmospheric boundary layer large-eddy simulation using OpenFOAM". In *19th Symposium on Boundary Layers and Turbulence*. (Keystone, Colorado 2010).

Churchfield, M. J., S. Lee, and P. J. Moriarty. 2014. "NREL-NWTC information portal (SOWFA)". *https://nwtc.nrel.gov/SOWFA*.

Clifton, A, M H Daniels, and M Lehning. 2014. "Effect of winds in a mountain pass on turbine performance". *Wind Energy*, vol. 17, n° August 2013, p. 1543–1562.

Comte-Bellot, G. and S. Corrsin. 1971. "Simple eulerian time correlation of full and narrow-band velocity signals in grid-generated, 'isotropic' turbulence". *Journal of Fluid Mechanics*, vol. 48, n° 2, p. 273-337.

Davidson, P. A., 2004. *Turbulence. An introduction for scientists and engineers*. Oxford : Oxford University Press, 657 p.

Deardorff, J. W. 1972. "Numerical investigation of neutral and unstable planetary boundary layers". *Journal of the Atmospheric Sciences*, vol. 29, p. 91–115.

Detering, H.W. and D. Etling. 1985. "Application of the E-ε turbulence model to the atmospheric boundary layer". *Boundary-Layer Meteorology*, vol. 33, n° 2, p. 113–133.

Drobinski, P. and R. C. Foster. 2003. "On the origin of near-surface streaks in the neutrally-stratified planetary boundary layer". *Boundary-Layer Meteorology*, vol. 108, p. 247–256.

Drobinski, P., P. Carlotti, R. K. Newsom, R. M. Banta, R. C. Foster, and J-L. Redelsperger. 2004. "The structure of the near-neutral atmospheric surface layer". *Journal of Atmospheric Sciences*, vol. 61, p. 699–714.

Drobinski, P., P. Carlotti, J-L. Redelsperger, V. Masson, R. M. Banta, and R. K. Newsom. 2007. "Numerical and experimental investigation of the neutral atmospheric surface layer". *Journal of the Atmospheric Sciences*, vol. 64, n° 1, p. 137–156.

Emeis, Stefan, 2013. *Wind energy meteorology. Atmospheric physics for wind power generation*. Berlin : Springer-Verlag.

Ferziger, J.H and M. Perić, 2002. *Computational methods for fluid dynamics*. ed. 3rd. Berlin : Springer, 423 p.

Finnigan, J. J. 1988. "Air flow over complex terrain". In *Flow and transport in the natural environment: Advances and applications*. (Berlin, Germany 1988), p. 183-229. Springer-Verlag.

Franke, J., A. Hellsten, H. Schlünzen, and B. Carissimo. 2007. *Best practice guideline for the CFD simulation of flows in the urban environment*. Technical Report COST Action 732. Quality assurance and improvement of microscale meteorological models. Hamburg, Germany : University of Hamburg. Meteorological Institute Centre for Marine and Atmospheric Sciences.

Garrat, J. R., 1994. *The atmospheric boundary layer*. Cambridge : Cambridge University Press.

Godeferd, F. S. 2012. "Relating statistics to dynamics in axisymmetric homogeneous turbulence". *Physica D: Nonlinear Phenomena*, vol. 241, p. 794–802.

Grant, A. L. M. 1986. "Observations of boundary layer structure made during the 1981 KONTUR experiment". *Quarterly Journal of the Royal Meteorological Society*, vol. 112, p. 825–841.

Grant, A. L. M. 1991. "The structure of the turbulence in the near neutral atmospheric boundary layer". *Journal of Atmospheric Sciences*, vol. 49, n° 3, p. 226–239.

Gritskevich, M. S., A. V. Garbaruk, J. Schütze, and F. R. Menter. 2012. "Development of DDES and IDDES formulations for the $k-\omega$ shear stress transport model". *Flow, Turbulence and Combustion*, vol. 88, p. 431–449.

Gungor, A. G. and S. Menon. 2010. "A new two-scale model for large eddy simulation of wall-bounded flows". *Progress in Aerospace Sciences*, vol. 46, p. 28-45.

Hargreaves, D. M. and N. G. Wright. 2007. "On the use of the $k-\varepsilon$ model in commercial CFD software to model the neutral atmospheric boundary layer". *Journal of Wind Engineering and Industrial Aerodynamics*, vol. 95, p. 3555-369.

Hinze, J. O., 1975. *Turbulence*. ed. 2nd. USA : McGraw-Hill.

Hossain, J. and the WWEA Technical Committee. December 2014. *World wind resource assessment report*. WWEA Technical Paper Series TP-01-14. Germany : World Wind Energy Association.

Issa, R. I. 1985. "Solution of the implicitly discretised fluid flow equations by operator-splitting". *Journal of Computational Physics*, vol. 62, p. 40–65.

Jackson, P. S. and J. C. R. Hunt. 1975. "Turbulent wind flow over a low hill". *Q. J. R. Meteorol. Soc.*, vol. 101, p. 929–955.

Jeannotte, E. 2013. "Estimation of LIDAR bias over complex terrain using numerical tools". M.Ing thesis, École de Technologie Supérieure, Montreal, QC. Canada.

Jimenez, A., A. Crespo, and E. Migoya. 2010. "Application of a LES technique to characterize the wake deflection of a wind turbine in yaw". *Wind Energy*, vol. 13, p. 559–572.

Jimenez J. (Ed.). 1997. *A selection of test cases for the validation of large-eddy simulations of turbulent flows*. Technical Report AGARD Advisory Report No.345. The Fluid Dynamics Panel : Working Group 21. *ftp://torroja.dmt.upm.es/AGARD/*.

Kaimal, J. C. and J. J. J. Finnigan, 1994. *Atmospheric boundary layer flows. Their structure and measurement*. Oxford : Oxford University Press, 283 p.

Kang, H. S., S. Chester, and C. Meneveau. 2003. "Decaying turbulence in an active-grid-generated flow and comparisons with large-eddy simulation". *Journal of Fluid Mechanics*, vol. 480, p. 129–160.

Katopodes Chow, F. and R. L. Street. 2009. "Evaluation of turbulence closure models for large-eddy simulation over complex terrain: Flow over Askervein hill". *Journal of Applied Meteorology and Climatology*, vol. 48, n° 5, p. 1050–1065.

Kim, H. G. and V. C. Patel. 2000. "Test of turbulence models for wind flow over terrain with separation and recirculation". *Boundary-Layer Meteorology*, vol. 94, p. 5–21.

Knopp, T., B. Eisfeld, and J. B. Calvo. 2009. "A new extension for k-ω turbulence models to account for wall roughness". *International Journal of Heat and Fluid Flow*, vol. 30, n° 1, p. 54–65.

Koblitz, T., A. Bechmann, A. Sogachev, N. N. Sørensen, and P. E. Réthoré. 2013. "Computational fluid dynamics model of stratified atmospheric boundary-layer flow". *Wind Energy*, vol. 18, p. 75–89.

Kolmogorov, A. N. 1941. "The local structure of turbulence in incompressible viscous fluid for very large Reynolds numbers". *Doklady ANSSSR*, vol. 30, p. 301-304. (Cited from Pope, 2000).

Langreder, W., K. Kaiser, H. Hohlen, and J. Hojstrup. 2004. "Turbulence correction for power curves". *EWEC London*.

Lee, M. J., J. Kim, and P. Moin. 1990. "Structure of turbulence at high shear rate". *Journal of Fluid Mechanics*, vol. 216, p. 561–583.

Leonard, A. 1974. "Energy cascade in large-eddy simulations of turbulent fluid flows". *Adv. in Geophysics A*, vol. 18, p. 237-248.

Lesieur, M. and O. Métais. 1996. "New trends in large-eddy simulations of turbulence". *Annual Review of Fluid Mechanics*, vol. 28, p. 45–82.

Lim, H. C., I. P. Castro, and R. P. Hoxey. 2007. "Bluff bodies in deep turbulent boundary layers: Reynolds-number issues". *Journal of Fluid Mechanics*, vol. 571, p. 97–118.

Lim, H. C., T. G. Thomas, and I. P. Castro. 2009. "Flow around a cube in a turbulent boundary layer: LES and experiment". *Journal of Wind Engineering and Industrial Aerodynamics*, vol. 97, p. 96–109.

Manwell, J. F., J. G. McGowan, and A. L. Rogers, 2002. *Wind energy explained. Theory, design and application*. Chippenham, Wiltshire : John Wiley and Sons, LTD.

Mason, P.J. and D J Thomson. 1987. "Large-eddy simulations of the neutral-static-stability planetary boundary layer". *Quarterly Journal of the Royal Meteorological Society*, vol. 113, n° 476, p. 413–443.

Menter, F. R. 1992. *Improved two-equation k-ω turbulence models for aerodynamic flows*. Technical Report NASA-TM-103975. USA : NASA.

Menter, F. R. 1993. "Zonal two equation $k - \omega$ turbulence models for aerodynamic flows". *AIAA*, vol. 93, p. 2906.

Menter, F. R. 1994. "Two-equation eddy viscosity turbulence models for engineering applications". *AIAA*, vol. 32, n° 8, p. 1598–1605.

Menter, F. R., M. Kuntz, and R. Langtry. 2003. "Ten years of industrial experience with the SST turbulence model". *Turbulence, Heat and Mass Transfer 4*, vol. 4, p. 625-632.

Mockett, C., M. Fuchs, and F. Thiele. 2012. "Progress in DES for wall-modelled LES of complex internal flows". *Computers & Fluids*, vol. 65, p. 44–55.

Monin, A. S. and A. M. Obukhov. 1954. "Basic laws of turbulent mixing in the atmospheric surface layer". *Trudy Geofiz. Inst. Acad. Sci. U.S.S.R.*, vol. 24, n° 151, p. 163-187.

Muller, Y.-A., Aubrun S., Loyer S., and Masson C. February 4-7th 2013. "Time resolved tracking of the far wake meandering of of a wind turbine model in wind tunnel conditions". In *European Wind Energy Association*. (Vienna 2013).

Munson, B. R., D. F. Young, and T. H. Okiishi, 2006. *Fundamentals of fluid mechanics*. ed. 5th. USA : John Wiley & Sons, Inc.

Nikitin, N. V., F. Nicoud, B. Wasistho, K. D. Squires, and P. R. Spalart. 2000. "An approach to wall modeling in large-eddy simulations". *Physics of Fluids*, vol. 12, n° 7, p. 1629–1632.

Oberkampf, W. L. and T. G. Trucano. 2002. "Verification and validation in computational fluid dynamics". *Progress in Aerospace Sciences*, vol. 38, p. 209-272.

Panofsky, H. A. and J. A. Dutton, 1984. *Atmospheric turbulence. Models and methods for engineering applications.* USA : John Wiley & Sons, Inc.

Panton, R. L., 1995. *Incompressible flow*. ed. 2nd. USA : Wiley-Interscience Publication, 837 p.

Patankar, S. V., 1980. *Numerical heat transfer and fluid flow*. USA : Taylor & Francis.

Patel, V. C. 1998. "Perspective: flow at high Reynolds number and over rough surfaces - Achilles heel of CFD". *Journal of Fluid Engineering*, vol. 120, p. 434–444.

Patel, V. C. and J. Y. Yoon. 1996. "Application of turbulence models to separated flow over rough surfaces". *Journal of Fluid Engineering*, vol. 117, p. 234 – 241.

Peña, A., R. Floors, and S-E. Gryning. 2014. "The Høvsøre tall wind-profile experiment: A description of wind profile observations in the atmospheric boundary layer". *Boundary-Layer Meteorology*, vol. 150, p. 69–89.

Peinke, J., S. Barth, F. B ottcher, D. Heinemann, and B. Lange. 2004. "Turbulence, a challenging problem for wind energy". *Physics A*, vol. 338, p. 187-193.

Peng-Karrholm, Fabian. 2006. *Rhie-Chow interpolation in OpenFOAM*. Technical report. Göteborg, Sweden : Chalmers University of Technology.

Petersen, E. L., N. G. Mortensen, L. Landberg, J. Højstrup, and H. P. Frank. 1998. "Wind power meteorology. Part II: Sitting and models". *Wind Energy*, vol. 1, p. 55-72.

Piomelli, U., J. Ferziger, and P. Moin. 1989. "New approximate boundary conditions for large eddy simulations of wall-bounded flows". *Phys. Fluids A*, vol. 1, n° 6, p. 1061–1068.

Pope, S. B. 1975. "A more general effective-viscosity hypothesis". *Journal of Fluid Mechanics*, vol. 72, p. 331–340.

Pope, S. B., 2000. *Turbulent flows*. Cambridge : Cambridge University Press, 771 p.

Porté-Agel, F., C. Meneveau, and M. B. Parlange. 2000. "A scale-dependent dynamic model for large-eddy simulation: application to a neutral atmospheric boundary layer". *Journal of Fluid Mechanics*, vol. 415, p. 261-284.

Pumir, A. 1996. "Turbulence in homogeneous shear flows". *Physics of Fluids*, vol. 8, n° 11, p. 3112–3127.

Reichardt, H. 1951. "Vollständige darstellung der turbulenten geschwindigkeitsverteilung in glatten leitungen". *ZAMM - Journal of Applied Mathematics and Mechanics. Zeitschrift für Angewandte Mathematik und Mechanik*, vol. 31, n° 7, p. 208–219.

Reynolds, O. 1895. "On the dynamical theory of incompressible viscous fluids and the determination of the criterion". *Phil Trans. R. Lond. Soc. A.*, vol. 186, p. 123–164.

Richards, P. and R. Hoxey. 1993. "Appropriate boundary conditions for computational wind engineering models using the $k-\varepsilon$ model". *Journal of Wind Engineering and Industrial Aerodynamics*, vol. 46 & 47, p. 145-153.

Riziotis, V. A. and S. G. Voustsinas. 2000. "Fatigue loads on wind turbines of different control strategies operating in complex terrain". *Journal of Wind Engineering and Industrial Aerodynamics*, vol. 85, p. 211-240.

Rogallo, S. 1981. *Numerical experiments in homogeneous turbulence*. Technical Report NASA-TM-81315. USA : NASA.

Rogers, M. M. and P. Moin. 1987. "The structure of the vorticity field in homogeneous turbulent flows". *Journal of Fluid Mechanics*, vol. 176, p. 33–66.

Roy, C. J., L. J. Dechant, J. L. Payne, and F. G. Blottner. 2003. "Bluff-body flow simulations using hybrid RANS/LES". *AIAA Journal*, vol. 3889.

Sagaut, P., 2006. *Large eddy simulations for incompressible flows: An introduction*. ed. 3rd. Berlin : Springer.

Sagaut, P. and C. Cambon, 2008. *Homogeneous turbulence dynamics*. Cambridge : Cambridge University Press, 460 p.

Sakamoto, H. 1983. "Vortex shedding from a rectangular prism and a circular cylinder placed vertically in a turbulent boundary layer". *Journal of Fluid Mechanics*, vol. 126, p. 147–165.

Salmon *et. al.*, J. R. 1988. "The Askervein hill project: mean wind variations at fixed heights above ground". *Boundary-Layer Meteorology*, vol. 43, p. 247-271.

Sanz Rodrigo, J. *et al.* 2014. "IEA-Task 31 Wakebench: Towards a protocol for wind farm flow model evaluation. Part 1: Flow-over-terrain models". *The Science of Making Torque from Wind 2014. Journal of Physics: Conference Series.*, vol. 524, p. 012105.

Sanz Rodrigo, J. *et al.* 2014. "IEA-Wind Task 31 "Wakebench" project. Windbench portal.". *https://windbench.net*.

Sattari, P., J. A. Bourgeois, and R. J. Martinuzzi. 2011. "On the vortex dynamics in the wake of a finite surface-mounted square cylinder". *Experiments in Fluids*, vol. 52, n° 5, p. 1149–1167.

Schlichting, H. and K. Gersten, 2000. *Boundary layer theory*. ed. 8th. Berlin : Springer.

Senocak, I., A. S. Ackerman, M. P. Kirkpatrick, D. E. Stevens, and N. N. Mansour. 2007. "Study of near-surface models for large-eddy simulations of a neutrally stratified atmospheric boundary layer". *Boundary-Layer Meteorology*, vol. 124, p. 405-424.

Shur, M. L., P. R. Spalart, M. Kh. Strelets, and A. K. Travin. 2008. "A hybrid RANS-LES approach with delayed-DES and wall-modelled LES capabilities". *International Journal of Heat and Fluid Flow*, vol. 29, n° 6, p. 1638–1649.

Silva Lopes, A., J. M. L. M. Palma, and F. A. Castro. 2007. "Simulation of the Askervein flow. Part 2: Large-eddy simulations". *Boundary-Layer Meteorology*, vol. 125, p. 85-108.

Sørensen, N. N. 1995. *General purpose flow solver applied to flow over hills*. Risø-R-827(EN). Roskilde, Denmark : RisøNational Laboratory.

Spalart, P. R. July 2001. *Young-person's guide to detached-eddy simulation grids*. Technical Report CR-2001-211032. USA : NASA.

Spalart, P. R., W-H. Jou, M. Strelets, and S.R. Allmaras. August 4-8 1997. "Comments on the feasibility of LES for wings, and on a hybrid RANS/LES approach". In *Proceedings of the first AFOSR international conference on DNS/LES*. (Ruston, Louisiana 1997). Louisiana Tech University.

Spalart, P. R., S. Deck, M. L. Shur, K. D. Squires, M. K. Strelets, and A. Travin. 2006. "A new version of detached-eddy simulation, resistant to ambiguous grid densities". *Theoretical and Computational Fluid Dynamics*, vol. 20, n° 3, p. 181-195.

Stoll, R. and F. Porté-Agel. 2006. "Effect of roughness on surface boundary conditions for large-eddy simulation". *Boundary-Layer Meteorology*, vol. 118, p. 169–187.

Stull, R. B., 1988. *An introduction to boundary layer meteorology*. Dordrecht : Kluwer Academic Publishers.

Sukheswalla, P., T. Vaithianathan, and L. R. Collins. 2013. "Simulation of homogeneous turbulent shear flows at higher Reynolds numbers: numerical challenges and a remedy". *Journal of Turbulence*, vol. 14, n° 5, p. 60–97.

Sullivan, P. P. 1994. "A subgrid-scale model for large-eddy simulation of planetary boundary-layer flows". *Boundary-Layer Meteorology*, vol. 71, p. 247–276.

Sumner, J. and C. Masson. 2012. "The Apsley and Castro limited-length-scale $k - \varepsilon$ model revisited for improved performance in the atmospheric surface Layer". *Boundary-Layer Meteorology*, vol. 144, n° 2, p. 199-215.

Sumner, J., C. S. Watters, and C. Masson. 2010. "Review. CFD in wind energy: The virtual, multiscale wind tunnel". *Energies*, vol. 3, p. 989-1013.

Tavoularis, S. and U. Karnik. 1989. "Further experiments on the evolution of turbulent stresses and scales in uniformly sheared turbulence". *Journal of Fluid Mechanics*, vol. 204, p. 457–478.

Taylor, P. A. and H. W. Teunissen. November 1983. *Askervein '82: Report on the September/October 1982 experiment to study boundary-layer flow over Askervein, South Uist*. Technical Report MSRB-83-8. Canada : Environment Canada. Atmospheric Environment Service.

Taylor, P. A. and H. W. Teunissen. December 1985. *The Askervein hill project: Report on the Sept./Oct. 1983, Main field experiment*. Technical Report MSRB-84-6. Canada : Environment Canada. Atmospheric Environment Service.

Taylor, P. A. and Teunissen H. W. 1987. "The Askervein hill project: Overview and background data". *Boundary-Layer Meteorology*, vol. 39, p. 15-39.

Tennekes, H. and J. L. Lumley, 1972. *A first course in turbulence*. Cambridge, Massachusetts : The MIT Press, 300 p.

The OpenFOAM Foundation. 28th September 2013. "OpenFOAM® - The open source CFD toolbox. User guide". *http://www.openfoam.org*.

The WRF community. 2015. "The weather research and forecasting model website". *http://www.wrf-model.org/*.

Travin, A., M. L. Shur, M. Strelets, and P. R. Spalart. 2002. "Physical and numerical upgrades in the detached-eddy simulation of complex turbulent flows.". In *Advances in LES of Complex Flows Conference Proceedings*. (Printed in the Netherlands 2002), p. 239-254. KluwerAcademic Publishers.

Troldborg, N. June 2008. "Actuator line modeling of wind turbine wakes". PhD thesis, Department of Mechanical Engineering, Technical University of Denmark, Lyngby, Denmark.

Uchida, T. and Y. Ohya. 2003. "Large-eddy simulation of turbulent airflow over complex terrain". *Journal of Wind Engineering and Industrial Aerodynamics*, vol. 91, p. 219-229.

Versteeg, H. K. and W. Malalasekera, 2007. *An introduction to computational fluid dynamics. The finite volume method*. ed. 2nd. Harlow : Pearson Education Limited, 503 p.

Wang, H. F., Y. Zhou, C. K. Chan, and K. S. Lam. 2006. "Effect of initial conditions on interaction between a boundary layer and a wall-mounted finite-length-cylinder wake". *Physics of Fluids*, vol. 18, p. 065106.

Welch, P. D. 1967. "The use of fast Fourier transform for the estimation of power spectra: A method based on time averaging over short, modified periodograms". *IEEE Transactions on Audio and Electroacoustics*, vol. AU-15, p. 70–73.

White, F. M., 1991. *Viscous fluid flow*. McGraw-Hill Series in Mechanical Engineering. ed. 2nd. Boston : McGraw-Hill.

Wilcox, D. C., 2004. *Turbulence modeling for CFD*. ed. 2nd. San Diego, California : Birmingham Press, Inc., 540 p.

Wood, N. 2000. "Wind Flow over Complex Terrain: A Historical perspective and the prospect for Large-Eddy Modelling". *Boundary-Layer Meteorology*, vol. 96, p. 11-32.

World Wind Energy Association. 2014. "World wind energy half-year report 2014". *http://www.wwindea.org*.

Yu, H., S. S. Girimaji, and L-S. Luo. 2005. "DNS and LES of decaying isotropic turbulence with and without frame rotation using lattice Boltzmann method". *Journal of Computational Physics*, vol. 209, p. 599–616.